Effizientes Abtasten der Gleichgewichtsensembles gelöster Polypeptide: Neue Methoden und ihre Anwendungen

Robert Denschlag

SIGILL. UNIVERSITAT. LUDOVIC. MAXIM.

München 2010

Effizientes Abtasten der Gleichgewichtsensembles gelöster Polypeptide: Neue Methoden und ihre Anwendungen

Robert Denschlag

Dissertation
an der Fakultät für Physik
der Ludwig-Maximilians-Universität
München

vorgelegt von
Robert Denschlag
aus Worms

München, im Juni 2010

Erstgutachter: Prof. Dr. Paul Tavan
Zweitgutachter: Prof. Dr. Martin Zacharias
Tag der mündlichen Prüfung: 21.07.2010

Inhaltsverzeichnis

Zusammenfassung vi

1 Einführung 1
- 1.1 Lichtinduzierte Dynamik 1
- 1.2 Aufbau und Struktur von Proteinen 5
- 1.3 Computersimulationen an Biomolekülen 8
  - 1.3.1 Molekularmechanische Kraftfelder 8
  - 1.3.2 Simulationsmethoden 10
  - 1.3.3 Schwachstellen von MM Computersimulationen 11
- 1.4 Verallgemeinerte-Ensemble Abtasttechniken 12
  - 1.4.1 Simulated Tempering 14
  - 1.4.2 Replica Exchange 18
  - 1.4.3 Solute Tempering 19
- 1.5 Die Struktur dieser Arbeit 21

2 Effizienzreduktion durch RE Simulationen 23

3 Optimierte Replica Exchange Protokolle 31
- 3.1 Optimale Temperaturleitern 31
- 3.2 Vergleich verschiedener Austauschschemata 36

4 Simulated Solute Tempering 43

5 Relaxation eines lichtschaltbaren Peptides 57

6 Resümee und Ausblick 87

Literaturverzeichnis 95

Danksagung 103

Zusammenfassung

Aussagekräftige Molekulardynamik (MD) Simulationen von Biomolekülen in kondensierter Phase stellen hohe Anforderungen an die Genauigkeit des Kraftfeldes und die Dauer der simulierten Zeitspanne. Letztere muss lang genug sein, damit das Zeitmittel der im Blickpunkt stehenden Observablen dem entsprechenden Ensemblemittel entspricht. Ferner ist es wegen der geforderten Genauigkeit in der Regel notwendig, das Lösungsmittel atomar zu beschreiben.

Trotz der raschen Fortschritte der Computertechnik verhindert auch heute noch der damit verbundene Rechenaufwand schon bei kleinen Peptiden das ergodische Abtasten ihrer Konformationsräume, solange lediglich herkömmliche Verfahren der MD Simulation eingesetzt werden. Dagegen können moderne MD Techniken das Abtastproblem durch die Verwendung sogenannter „verallgemeinerter Ensembles“ abmildern. Ein populäres Verfahren ist die „Replica Exchange“ (RE) Methode, deren verallgemeinertes Ensemble im einfachsten Fall aus einem Satz bis auf die Temperatur identischer Simulationsssysteme (Replikate) besteht. Die Interpretation, Optimierung und Weiterentwicklung solcher Techniken stehen im Zentrum dieser Arbeit.

Dazu stellt sie vier Publikationen aus den vergangenen zwei Jahren vor /3-6/. Hier wird zunächst anhand eines einfachen Modells für ein β-Hairpinpeptid gezeigt, dass und unter welchen Bedingungen RE Methoden die Abtasteffizienz sogar reduzieren können /3/. Es wird dabei der Zusammenhang zwischen den Kinetiken simulierter Faltungs-Entfaltungsgleichgewichte und der Geschwindigkeit der Durchmischung des verallgemeinerten Ensembles andiskutiert. In Nachfolgearbeiten /4,5/ wird diese Frage aufgegriffen und gezeigt, wie die Mischungsgeschwindigkeit maximiert werden kann, so dass die Abtasteffizienz durch eine geeignet gewählte Temperaturleiter optimiert wird. Schließlich wird eine neue Abtastmethode vorgeschlagen /6/, welche eine deutlich effizientere Simulation der Gleichgewichtsensembles gelöster Polypeptide ermöglicht. Die neue „Simulated Solute Tempering“ (SST) Methode verwandelt das von Liu et al. (*Proc. Natl. Acad. Sci. USA* 102, 13749, 2005) vorgeschlagene „Replica Exchange with Solute Tempering“ (REST) Verfahren in einen sequentiellen Zugang. Dabei übernimmt SST von REST die im Vergleich zu RE schon ausgedünnten Temperaturleitern. Wie anhand eines Oktapeptids in Lösung demonstriert wird, ist die Abtasteffizienz von SST nicht nur größer als jene von RE, sondern sogar jener von REST deutlich überlegen.

Darüber hinaus demonstriert diese Dissertation anhand einer Anwendung /9/ den Nutzen der angesprochenen Verfahren. Diese Anwendung behandelt ein zyklisches, lichtschaltbares Modellpeptid namens cAPB, dessen Gleichgewichtsensembles bei Zimmertemperatur mit RE Methoden berechnet werden. Darauf aufbauend wird die durch *cis/trans* Photoisomerisierung des kovalent integrierten Azobenzolfarbstoffs ausgelöste Relaxation des Peptidrückgrats simuliert und kinetisch charakterisiert. Die Ergebnisse der Simulationen werden zur Analyse experimenteller Daten genutzt. Für die langsamste, experimentell bislang nicht zugängliche Relaxationskinetik liefern die Simulationen eine Vorhersage von 23 ns. Weitere Anwendungen /1,7,8/ und methodische Beiträge /2/ wurden vor allem deshalb nicht in den Text integriert, um das Hauptanliegen dieser Dissertation zur Geltung zu bringen, das in der Analyse und Optimierung von RE Methoden besteht.

Verzeichnis der unter meiner Mitwirkung entstandenen Publikationen

/1/ TE Schrader, WJ Schreier, T Cordes, FO Koller, G Babitzki, R Denschlag, C Renner, S-L Dong, M Löweneck, L Moroder, P Tavan, and W Zinth (2007). Light triggered ß-hairpin folding and unfolding. *Proc. Natl. Acad. Sci. USA* 104, 15729-15734.

/2/ M Lingenheil, R Denschlag, R Reichold, and P Tavan (2008). The "Hot-Solvent/Cold-Solute" problem revisited. *J. Chem. Theory Comput.* 4, 1293-1306.

/3/ **R Denschlag, M Lingenheil, and P Tavan (2008). Efficiency reduction and pseudo-convergence in replica exchange sampling of peptide folding-unfolding equilibria. *Chem. Phys. Lett.* 458, 244-248.**

/4/ **R Denschlag, M Lingenheil, and P Tavan (2009). Optimal temperature ladders in replica exchange simulations. *Chem. Phys. Lett.* 473, 193-195.**

/5/ **M Lingenheil, R Denschlag, G Mathias, and P Tavan (2009). Efficiency of exchange schemes in replica exchange. *Chem. Phys. Lett.* 478, 80-84.**

/6/ **R Denschlag, M Lingenheil, P Tavan, and G Mathias (2009). Simulated solute tempering. *J. Chem. Theory Comput.* 5, 2847-2857.**

/7/ G Babitzki, R Denschlag, and P Tavan (2009). Polarization effects stabilize bacteriorhodopsin's chromophore binding pocket: A molecular dynamics study. *J. Phys. Chem. B* 113, 10483-10495.

/8/ M Lingenheil, R Denschlag, and P Tavan (2010). The polarity of the environment steers the stability of PrP^c helix 1. *Eur. Biophys. J.* DOI: 10.1007/s00249-009-0570-6.

/9/ **R Denschlag, WJ Schreier, B Rieff, TE Schrader, FO Koller, L Moroder, W Zinth, P Tavan (2010). Relaxation time prediction for a light switchable peptide by molecular dynamics. *Phys. Chem. Chem. Phys.* 12, 6204 - 6218**

Die durch **Fettdruck** hervorgehobenen Arbeiten sind in den Text der Dissertation eingearbeitet und dort nachgedruckt.

1 Einführung

Mit einem Anteil von über 50% an der Trockenmasse stellen die Proteine die dominante Klasse der in einer Zelle vorkommenden Makromoleküle dar [1]. Dort haben sie vielfältige Funktionen. So bestimmen sie beispielsweise als Strukturelemente die Beschaffenheit des Gewebes, steuern als Enzyme lebensnotwendige biochemische Reaktionen, regeln als Membrankanäle die Aktivität von Nervenzellen, übernehmen als Verpackungsmaterial den Transport wichtiger Substanzen, steuern als Hormone Vorgänge im Körper oder dienen als Antikörper dem Immunsystem [1, 2]. Maßgeblich für die Funktion eines Proteins ist dessen 3-dimensionale Struktur. Diese Struktur hängt nicht nur von der chemischen Zusammensetzung des Proteins ab, sondern auch von der Umgebung, in der es sich befindet. Daher kann sich die Struktur durch umfeldgesteuerte Umfaltung ändern. Gerade diese Steuerbarkeit der Proteinstruktur durch das physikalisch-chemische Umfeld ermöglicht es Proteinen, in der Zelle als biomolekulare Maschinen zu fungieren.

Die Entwicklung und Anwendung von Methoden, welche erweiterte Einblicke in die Struktur und Dynamik von Proteinen liefern, kann zu einem verbesserten Verständnis ihrer Funktionsweise führen und sind daher Gegenstand aktueller Forschung. Diesem übergeordneten Ziel war auch der Sonderforschungsbereich 533 „Lichtinduzierte Dynamik von Biopolymeren“ gewidmet, durch den meine Arbeit hauptsächlich finanziert wurde.

1.1 Lichtinduzierte Dynamik

Zu Beginn meiner Doktorarbeit war mir die Aufgabe gestellt worden, ein von Heiko Carstens begonnenes und in das Teilprojekt C1 „Theorie und Computersimulation der Konformationsdynamik von Peptiden und Proteinen in natürlicher Umgebung“ des SFB 533 eingebettetes Forschungsvorhaben fortzuführen. Dieses Vorhaben befasste sich mit der *in silico* Untersuchung der Konformationsdynamik lichtschaltbarer Modellpeptide [3]. Da es sich bei diesen Modellpeptiden um vergleichsweise kleine Moleküle handelt, hatten schon die Voruntersuchungen von Heiko Carstens gezeigt, dass sie sich hervorragend für aufeinander abgestimmte theoretische und experimentelle Untersuchungen eignen [4, 5].

Gerade bei komplex geordneten, aber gleichzeitig auch flexiblen Makromolekülen wie den Polypeptiden kann ein genaues Verständnis der ablaufenden Prozesse nur durch ein enges Zusammenwirken von Experiment und Theorie gewonnen werden [6–8]. Zum einen sind ohne weitere Zusatzinformationen eindeutige Interpretationen experimenteller Daten häufig schwierig. Hier können theoretische Ansätze in Form von Computersimulationen wichtige noch fehlende Informationen liefern. Zum anderen liefert der Vergleich mit dem Experiment Aufschluss über die Qualität der Modelle, die den Computersimulationen zugrundeliegen, und kann dadurch deren Verfeinerung und Weiterentwicklung inspirieren.

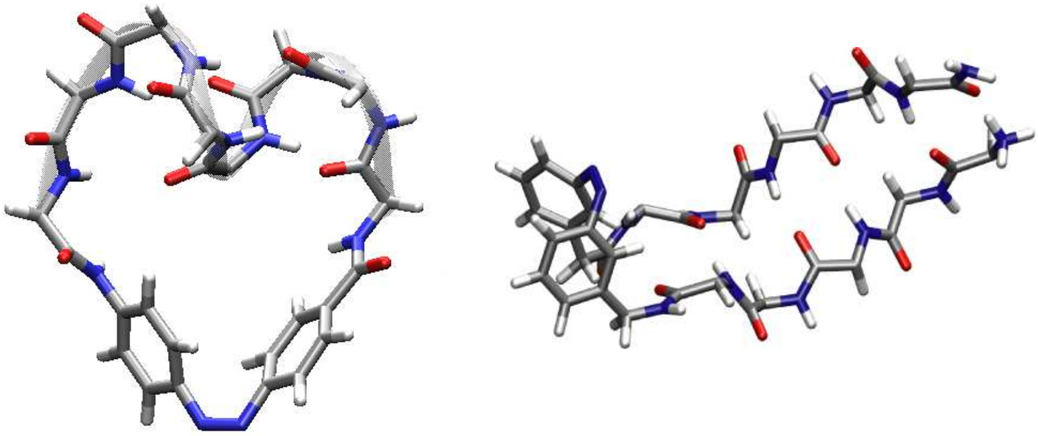

Abbildung 1.1: Azopeptide. Links ist das zyklische Peptid cAPB [9] in einer α-helikalen Struktur dargestellt, die zeitweise während ausgedehnter Computersimulationen [10] angenommen wurde. Die helikale Struktur wird dabei durch ein graues Band hervorgehoben. Rechts erkennt man das β-Hairpinpeptid, welches mit seinen zwei Strängen eine Haarnadelstruktur ausbildet [11]. Beide Konformationen (Helix und Haarnadel) setzen voraus, dass sich der Azobenzolfarbstoff in der *cis* Konfiguration befindet.

Im Mittelpunkt meiner Untersuchungen standen die beiden in der Abbildung 1.1 dargestellten Modellpeptide. Es waren dies ein durch ein Azobenzolderivat namens APB [(4-AminoPhenyl)azoBenzolsäure] zyklisiertes Peptid namens cAPB [9] (links) und ein β-Hairpinpeptid [11] (rechts), dessen Turn-Struktur durch das Azobenzolderivat AMPP [3-(3-AminoMethylPhenylazo)Phenylacetatsäure] gebildet wird. Die hier in das jeweilige Peptidrückgrat kovalent integrierten Azobenzolfarbstoffe können nach Absorption von Licht mit der Wellenlänge $\lambda \approx 500$ nm durch Photoisomerisierung ultraschnell (≈ 300 fs) von den im Bild dargestellen *cis* Konfigurationen in die zugehörigen *trans* Zustände übergehen.

Die mit dieser *cis-trans* Isomerisierung verbundene Geometrieänderung des Farbstoffs ist in Abbildung 1.2 hervorgehoben. Sie besteht sowohl in einer Streckung des Farbstoffs um etwa 3 Å als auch in einer Änderung des Winkels zwischen den beiden Phenylgruppen, an welche die jeweiligen Peptidstränge kovalent gebunden sind. Daher löst die lichtinduzierte *cis-trans* Isomerisierung zunächst starke Zugkräfte auf die angrenzenden Peptidreste aus, welche von dort in das restliche Peptid propagiert werden. Insgesamt lenkt die dadurch getriebene Konformationsdynamik die Moleküle aus den nun gestörten Gleichgewichtsensembles der *cis* Zustände in die relaxierten Gleichgewichtsensembles der *trans* Zustände.

Hier stellen sich nun die Fragen, wie die angesprochenen Konformerenensembles zusammengesetzt sind, welche Wege in den hochdimensionalen Konfigurationsräumen im Verlaufe der lichtinduzierten *cis-trans* Relaxation eingeschlagen werden und auf welchen

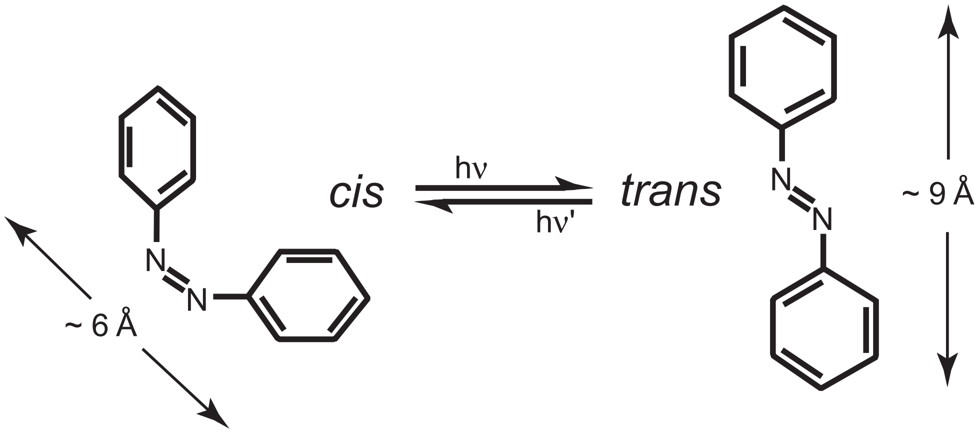

Abbildung 1.2: Geometrieänderung von Azobenzol durch Photoisomerisierung. Durch Lichteinfall kann Azobenzol vom *cis*- zum *trans*-Isomer und *vice versa* geschaltet werden, was starke Geometrieänderungen mit sich bringt.

Zeitskalen die Relaxationsprozesse ablaufen. Es war das Hauptziel der vorliegenden Dissertation, diese Fragen mit Mitteln der Molekulardynamik-(MD-)Simulation [7, 8, 12], in enger Kooperation mit laufenden spektroskopischen Untersuchen in der Arbeitsgruppe Zinth, zu beantworten. Trotz der stark reduzierten Komplexität der beiden recht kleinen Modellpeptide zeigte sich im Laufe meiner Arbeit relativ schnell, dass der notwendige Rechenaufwand zur Beantwortung der angesprochenen Fragestellungen selbst mit den vorhandenen, sehr effizienten und parallelisierten MD-Simulationsprogrammen EGO/MMII [13] und GROMACS [14], sowie unter Einsatz moderner Linux-Rechnercluster, kaum zu bewältigen war. So konnte ich im Verlaufe meiner Arbeit zeigen [15], dass der Rechenaufwand, der durch die *Faltungsreaktion* unseres β-Haarnadelpeptids aufgeworfen wird, mit gegenwärtigen Mitteln der MD-Simulation nicht zu bewältigen ist.

Dieser Faltungsprozess kann durch *trans-cis* Photoisomerisierung mit Licht der Wellenlänge $\lambda \approx 400$ nm ausgelöst werden und ist nach zeitaufgelöster Spektroskopie [16] erst auf einer Zeitsakala von etwa 30 μs abgeschlossen. Solche Zeitskalen sind durch MD Simulationen mit explizitem Lösungsmittel derzeit noch nicht erreichbar, zumal für statistisch valide Aussagen dutzende Simulationen notwendig sind. Beispielsweise liegt der kürzlich erreichte ”Weltrekord” für die Simulationsdauer einer einzelnen Simulation eines in Lösung simulierten Peptids bei 10 μs [17]. Entsprechend konzentrierte ich mich auf die durch *cis-trans* Photoisomerisierung ausgelöste Entfaltungsdynamik, die auf sehr viel kürzeren Zeitskalen abläuft. Allerdings müssen für eine simulationsgestützte Beschreibung dieser Dynamik zunächst die stationären *cis*- und *trans*-Konformerenensembles des in Methanol gelösten β-Haarnadelpeptids berechnet werden, um damit (i) die Start- und Endpunkte der lichtinduzierten Dynamik zu kennen und (ii) den Fortschritt der Relaxation messen zu können. Da ein statistisch valides Abtasten der Konformerenensembles mittels konventioneller MD wegen den angesprochenen Faltungszeiten aber aussichtslos ist, wurde zur Lösung des Abtastproblems die Verwendung von Verallgemeinerte-Ensemble

Techniken vom Replica-Exchange (RE) Typ [18–20] angedacht. Hier setzte nun meine oben erwähnte und im Kapitel 2 abgedruckte Arbeit an, in der ich zeigen konnte, dass RE-Techniken im gegebenen Falle von β-Haarnadelpeptiden bedauerlicherweise keinen Vorteil gegenüber konventionellen Simulationstechniken aufweisen.

Durch das bisher Gesagte drängt sich der Eindruck auf, dass das von meinem Doktorvater vorgeschlagene und oben skizzierte Projekt von vornherein zum Scheitern verurteilt war. In Teilen, nämlich bei dem angesprochenen β-Haarnadel Peptid, war dies tatsächlich der Fall. Dennoch trugen die wenigen zu diesem Haarnadelpeptid durch MD Simulationen erzielten Resultate zu einer hochrangig publizierten Arbeit bei [16] und führten außerdem zu einem besseren Verständnis der RE-Abtasttechniken [15], welches kurzgefasst darin besteht, dass Temperaturerhöhung nicht notwendigerweise zu einem beschleunigten Abtasten führen muss.

Aufgrund der geschilderten Schwierigkeiten verwendete ich die mir zur Verfügung stehenden Computerressourcen zur Beschreibung des zyklischen cAPB Peptids. Auch für dieses Peptid besteht unter Verwendung konventioneller MD das Abtastproblem, weshalb mein Vorgänger, Heiko Carstens, dazu übergegangen war, die Ensembles der Gleichgewichtskonformere durch drastische Temperaturerhöhung auf 500 K zu berechnen. Seinem Vorgehen lag die Annahme zugrunde, dass das Abtastproblem bei cAPB durch enthalpischen Barrieren zwischen den einzelnen Konformationen hervorgerufen wird und diese Barrieren daher durch Temperaturerhöhung schneller überwunden werden, so dass das Abtasten des Konformationsraumes erheblich beschleunigt wird [5].

Trotz guter Übereinstimmung der bei 500 K simulierten Konformerengemische mit bei 300 K gewonnenen NMR Daten [9], musste aber befürchtet werden, dass die berechneten Hochtemperaturensembles stark von den bei Raumtemperatur zu erwartenden Simulationsergebnissen abweichen. Zur Begründung sei festgestellt [10], dass die beobachtete Übereinstimmung [5] mit den NMR Daten ein zwar notwendiges nicht aber hinreichendes Kriterium für die Realitätsnähe eines durch Simulation bestimmten Ensembles von Peptidstrukturen ist. Wie ich weiter oben bereits erklärt habe, ist die genaue Kenntnis der Konformerenensembles bei Raumtemperatur aber eine entscheidende Voraussetzung für eine simulationsgestützte Beschreibung des lichtinduzierten Übergangs von dem einen (z.B. *cis*) in das andere (z.B. *trans*) Ensemble. Aufgrund der relativ guten Konvergenz der 500 K Simulationen [5] bestand im Fall von cAPB die begründete Hoffnung, dass die 300 K Konformerenensembles mit RE-Techniken statistisch valide berechnet werden können, da diese Methoden Hochtemperatursimulationen nutzen, um den Konformationsraum bei Raumtemperatur beschleunigt abzutasten.

Aus diesen Gründen stellte sich mir zu Beginn meiner Dissertation die spezielle Aufgabe, die in der Literatur vorgeschlagenen RE-Techniken für die Arbeitsgruppe technisch verfügbar zu machen, um sie dann für cAPB und andere Systeme einsetzen zu können. Diese Aufgabe entwickelte sich nach und nach zu einem eigenen Projekt, in dem über die Sichtung und Implementierung vorhandener RE-Methoden hinaus deren Verbesserung und Weiterentwicklung auf der Agenda stand. Aufgrund der erzielten Erfolge stellen die Ergebnisse dieser Untersuchungen den Grundpfeiler meiner kumulativen Dissertation dar. Um das Verständnis der nachfolgend im Hauptteil dieser Arbeit abgedruckten Publikatio-

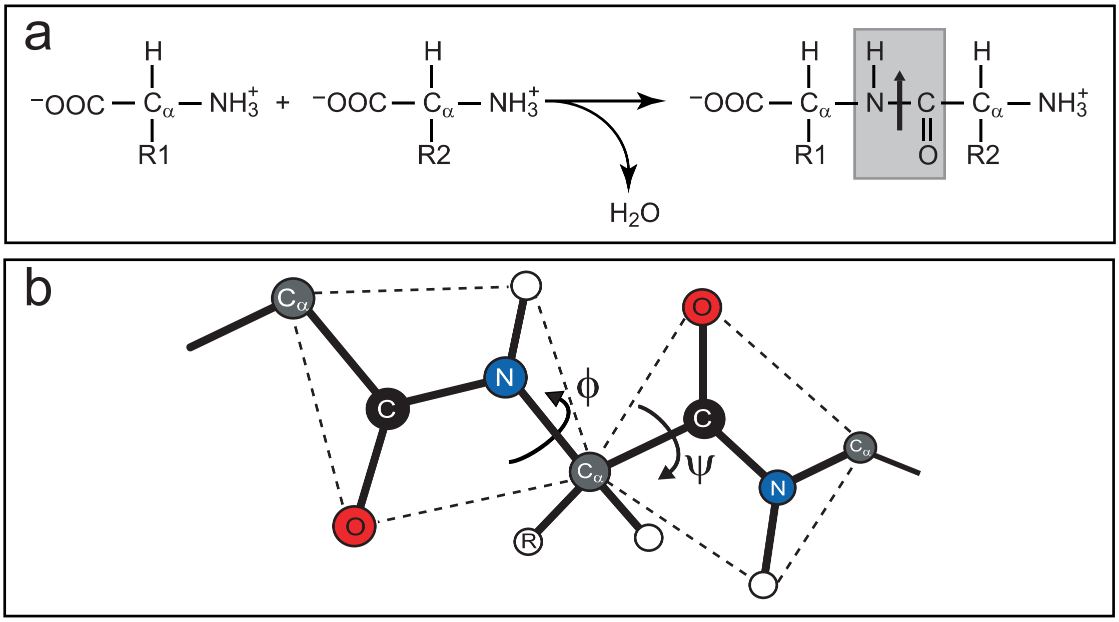

Abbildung 1.3: a) Peptidsynthese: Zwei Aminosäuren verbinden sich unter Abspaltung von Wasser zu einem Dipeptid. Das durch die Peptidbindung entstehende torsionsstabile und polare Peptidplättchen ist durch den rautenförmigen gestrichelten Rahmen gekennzeichnet. Die Polarität des Plättchens wird durch den eingezeichneten Dipol (Pfeil) angezeigt. Das Peptidrückgrat ist grau unterlegt. b) Die ϕ/ψ Diederwinkel bestimmen die relative Lage der Peptidplättchen zueinander. Sie stellen die wesentlichen Freiheitsgrade des Peptidrückgrats dar.

nen zu erleichtern, möchte ich einleitend zunächst noch auf einige grundlegende Begriffe zum Aufbau und zur Struktur von Proteinen sowie zu deren theoretischer Beschreibung durch Computersimulationen eingehen. Anschließend werde ich einen Überblick über die sog. Verallgemeinerte-Ensemble Abtasttechniken geben und mit der *Simulated Tempering* und der *Replica Exchange* Methode die Grundlagen zweier populärer Vertreter dieser Verfahren ausführlich darstellen.

1.2 Aufbau und Struktur von Proteinen

Die molekularen Grundbausteine der Proteinen sind die Aminosäuren, deren chemische Zusammensetzung in Abbildung 1.3a dargestellt ist. Neben dem zentralen C_α Atom besteht eine Aminosäure aus einer Aminogruppe (NH_3^+), einer Carboxylgruppe (COO^-), einem Wasserstoffatom (H) und einer aminosäurespezifischen Seitengruppe (R), dem sog. Rest. Durch die in Abbildung 1.3a dargestellte Peptidbindung, an der die beiden funktionellen Gruppen COO^- und NH_3^+ beteiligt sind, können Aminosäuremonomere sukzessive unter Abspaltung von Wasser zu einem Polypeptid synthetisiert werden, wobei Peptide mit mehr als etwa 100 Aminosäuren generell als Proteine bezeichnet werden [2].

Durch die Peptidbindung entsteht die in der Abb. 1.3a grau unterlegte flache und torsionsstabile Peptideinheit, das sog. Peptidplättchen. Eine weitere, besonders wichtige Eigenschaft des Peptidplättchens ist seine große Polarität, die durch die hohe Elektronegativität des Sauerstoffes verursacht wird. Die resultierende Ladungsverteilung erzeugt ein elektrisches Dipolmoment, welches in Abb. 1.3a durch einen senkrechten Pfeil angedeutet wird. Aufgrund der Steifigkeit der Peptidplättchen wird die Struktur des Peptidrückgrats im Wesentlichen durch die relative Orientierung der Plättchen bestimmt. Deren relative Ausrichtung wird durch die in Abb. 1.3b dargestellten ϕ/ψ-Diederwinkel beschrieben. Bei Vernachlässigung der Seitengruppen stellen diese Winkel die wesentlichen Freiheitsgrade des Peptids dar.

In den Zellen werden die Proteine in den Ribosomen synthetisiert [2]. Dabei greift die Natur auf einen Satz aus 20 verschiedenen Aminosäuren zurück, deren Abfolge die Primärstruktur des Proteins definiert und im Genom festgelegt ist [2]. Während und nach der Synthese faltet ein Protein in seine native 3-dimensionale Struktur, die sog. Tertiärstruktur, die seine Funktion bestimmt [21]. Die Tertiärstruktur ist üblicherweise die Struktur mit minimaler freier Energie (Beispiele für Ausnahmen findet man in [22, 23]) und ist eindeutig durch die Primärstruktur und durch die Umgebung, in die das Protein eingebettet ist, festgelegt [24–26]. Über die Tertiärstruktur hinaus können sich mehrere Proteine auch zu einem Proteinkomplex zusammensetzen. Die dann aus verschiedenen Tertiärstrukturen zusammengesetzte Struktur des Proteinkomplexes wird als Quartärstruktur bezeichnet. Aufgrund der schon eingangs angesprochenen hohen Proteinkonzentration in der Zelle besteht insbesondere während des Aufbaus sehr komplex zusammengesetzter Proteine das Risiko der unkontrollierten Aggregation von metastabilen Faltungszwischenzuständen [27]. Die damit verbundene Fehlfaltung [21, 28] kann Krebs, Alzheimer, Parkinson und andere schwere Krankheiten auslösen [28]. Um das Risiko der Fehlfaltung zu vermindern wird daher der Faltungsprozess in der Zelle durch Helferproteine, die sog. Chaperone, unterstützt [29].

Allen nativen Proteinstrukturen ist gemein, dass sie sich aus rigiden Untereinheiten, den sog. Sekundärstrukturelementen, zusammensetzen. Die beiden häufigsten Sekundärstrukturen sind die α-Helix und das antiparallele β-Faltblatt, die uns schon im letzten Kapitel als mögliche Strukturen des cAPB und des Haarnadel Modellpeptids begegnet sind. Beide Strukturelemente wurden Anfang der 1950er Jahre von Linus Pauling und Kollegen als mögliche Strukturuntereinheiten der Proteine wegen der besonders günstigen elektrostatischen Anordnung der Dipole vorgeschlagen [30, 31]. In Abbildung 1.4 sind diese beiden Sekundärstrukturen mit Blick auf die Anordnung der Dipole schematisch dargestellt. Während die Dipole des Faltblattes (Abb. 1.4 rechts) entlang des Rückgrats abwechselnd in entgegengesetzte Richtungen zeigen und mit durch viele Residuen getrennten Dipolen bindend in Wechselwirkung treten, richten sich die Dipole einer α-Helix (Abb. 1.4 links) parallel aus und binden an Dipole, die entlang des Rückgrats nur wenige Residuen entfernt liegen. Diese „lokale“ bzw. „nichtlokale“ Wechselwirkung der Dipole in der Helix bzw. im Faltblatt hat Auswirkungen auf die Zeitskalen, auf denen sich diese Sekundärstrukturelemente bilden. Während die Faltung einer ungeordneten Peptidkette zu einer α-Helix in weniger als 0.1 μs erfolgen kann, dauert die Bildung von Faltblättern mit mindestens 1 μs erheblich länger [21, 32, 33]. Entsprechend falten Proteine je nach Helix- und Falt-

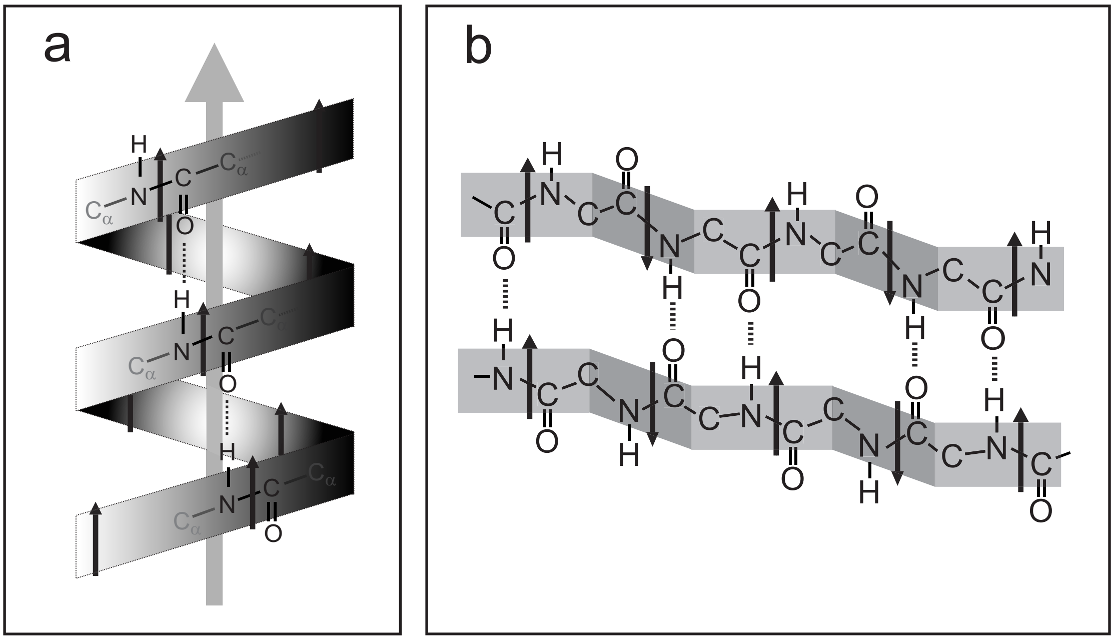

Abbildung 1.4: Sekundärstrukturmotive. a) Schematische Darstellung einer α-Helix. Die kollinear-parallele Anordnung der Dipole führt zur Stabilisierung dieses Strukturmotivs und zur Ausbildung eines makroskopischen Dipolmoments. b) Antiparalleles β-Faltblatt. Energetisch stabilisierend wirken hier die kollinear-parallel ausgerichteten Dipole verschiedener Peptidstränge und die axial-antiparallel ausgerichteten Dipole im Strang benachbarter Peptidgruppen.

blattanteil unterschiedlich schnell. Kurze Faltungszeiten von weniger als 100 μs sind für helixreiche Proteine möglich [34–36], während heterogener zusammengesetzte Proteine üblicherweise auf Zeitskalen von dutzenden Millisekunden bis Minuten falten [37–39].

In vielen Fällen kann die 3-dimensionale Struktur eines Proteins unter kontrollierten Bedingungen außerhalb der Zelle durch experimentelle Methoden wie die Röntgenkristallographie [40–42] oder die Kernspinresonanzspektroskopie (NMR) [42–44] recht genau aufgeklärt werden. Die detaillierte Aufklärung dynamischer Prozesse wie Faltung und Umfaltung gestaltet sich hingegen trotz vielfältiger experimenteller Methoden [45–52] als extrem schwierig. Dies liegt an den hohen Anforderungen, die an die zeitliche und räumliche Auflösung gestellt werden müssen, um ein detailliertes Bild der Proteindynamik zu gewinnen. Im Prinzip können Computerexperimente diesen hohen Anforderungen gerecht werden und somit wichtige Einsichten in die Struktur und Dynamik von Proteinen liefern. Für den Fall einer unbekannten Proteinstruktur können Computersimulationen beispielsweise Informationen zur Stabilität potentieller Molekülstrukturen liefern [53–55], oder Hinweise auf Faltungsdynamiken geben, aus denen sich mögliche Faltungsszenarien [42] ableiten lassen [56, 57].

1.3 Computersimulationen an Biomolekülen

Wie ich im vorangegangenen Abschnitt bereits angedeutet habe, können Computersimulationen Einblicke in die Struktur und Dynamik von Biomolekülen in einer räumlichen und zugleich zeitlichen Auflösung vermitteln, die bislang mit experimentellen Methoden nicht erreicht wird [58]. So konnte im Jahr 1977 die bis dahin verbreitete Vorstellung, es handele sich bei Proteinen im nativen Zustand um recht rigide Strukturen, durch eine Molekulardynamik (MD) Simulation an einem Protein widerlegt werden [12, 59]. Dieser Simulation lag ein Modell zugrunde, in dem die Wechselwirkung der Atome durch eine semi-empirische Energiefunktion beschrieben wurde [59, 60]. Die Bauart dieser auch als molekularmechanisches (MM) Kraftfeld bezeichneten Energiefunktion findet sich im Wesentlichen noch heute in modernen MM Kraftfeldern wie CHARMM [61, 62], AMBER [63], GROMOS [64] oder OPLS [65] wieder und wird im nachfolgenden Abschnitt näher erläutert.

1.3.1 Molekularmechanische Kraftfelder

Die Wechselwirkungen zwischen den Atomen werden in einem MM Kraftfeld durch eine Energiefunktion der Form

$$\begin{aligned} E(\mathbf{R};\mathbf{A}) &= \sum_{\text{bond}} k_b^{(ij)}(r_{ij}-\hat{r}_{ij})^2 + \sum_{\text{angle}} k_\theta^{(ijk)}(\theta_{ijk}-\hat{\theta}_{ijk})^2 \\ &+ \sum_{\text{torsion}} k_{\phi,h}^{(ijkl)}[1-\cos(n_h\phi_{ijkl}-\hat{\phi}_{ijkl})] \\ &+ \sum_{\text{vdW}} \left[\left(\frac{A_{ij}}{r_{ij}}\right)^{12} - \left(\frac{B_{ij}}{r_{ij}}\right)^{6}\right] + \sum_{\text{coul.}} \frac{q_i q_j}{r_{ij}} \end{aligned} \tag{1.1}$$

beschrieben[1] [59, 60]. Hierin bezeichnet $\mathbf{R} \equiv (\mathbf{r}_1, \mathbf{r}_2, \ldots, \mathbf{r}_n)$ die Konfiguration der n Atome des Simulationssystems. Die Ausdrücke $r_{ij} \equiv |\mathbf{r_j} - \mathbf{r_i}|$, $\theta_{ijk} \equiv \theta(\mathbf{r}_i, \mathbf{r}_j, \mathbf{r}_k)$ und $\phi_{ijkl} \equiv \phi(\mathbf{r}_i, \mathbf{r}_j, \mathbf{r}_k, \mathbf{r}_l)$ bezeichnen die in Abbildung 1.5 dargestellten internen Koordinaten. Das Symbol $\mathbf{A}$ steht für einen Satz kraftfeldspezifischer Parameter die entweder empirisch aus experimentellen Daten oder *ab inito* aus quantenmechanischen Rechnungen gewonnen werden.

Bis auf eine für die Kraftberechnung irrelevante Konstante bestimmen die ersten drei Summenterme in Gleichung (1.1) den bindenden Anteil der potentiellen Energie $E(\mathbf{R};\mathbf{A})$. Dieser Anteil umfasst die Wechselwirkungsenergie kovalent gebundener Atome, die durch höchstens drei Bindungen voneinander getrennt sind. Durch die Parameter $\hat{r}_{ij}$, $\hat{\theta}_{ijk}$ und $\hat{\phi}_{ijkl}$ wird die Gleichgewichtsgeometrie festgelegt. Abweichungen der Bindungsabstände r_{ij} von den Gleichgewichtsabständen $\hat{r}_{ij}$ werden energetisch durch den ersten Summenterm „bestraft“. Der zweite bzw. dritte Summenterm bestraft Abweichungen der Bindungswinkel θ_{ijk} bzw. Diederwinkel ϕ_{ijkl} von den zugehörigen Gleichgewichtswinkeln

---

[1] Die Abhängigkeit des Indexes h von i, j, k, l wurde der Übersicht wegen unterdrückt.

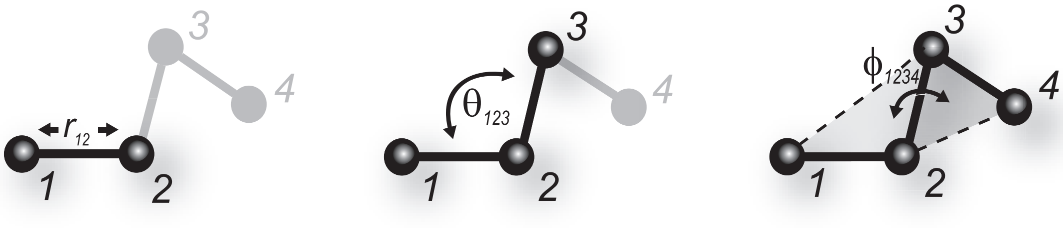

Abbildung 1.5: Interne Koordinaten eines MM Kraftfeldes. Stellvertretend für die Bindungslängen r_{ij}, Bindungswinkel θ_{ijk} und Diederwinkel ϕ_{ijkl} sind in der Abbildung die Bindungslänge r_{12} (links), der Bindungswinkel θ_{123} (Mitte) und der Diederwinkel ϕ_{1234} (rechts) eingezeichnet.

$\hat{\theta}_{ijk}$ und $\hat{\phi}_{ijkl}$. Die Stärke der energetischen Bestrafung wird hierbei durch die jeweiligen Kraftkonstanten $k^{(ij)}$, $k^{(ijk)}$ und $k^{(ijkl)}$ festgelegt. Dabei sind die Kraftkonstanten $k^{(ij)}$ und $k^{(ijk)}$ der Bindungsabstände und Bindungswinkel recht groß, so dass in diesen Freiheitsgraden Veränderungen der Molekülgeometrie gegenüber der Gleichgewichtsgeometrie nur sehr begrenzt möglich sind. Insbesondere ist das Aufbrechen von Bindungen wegen der harmonischen Potentiale $k_b^{(ij)}(r_{ij} - \hat{r}_{ij})^2$ gänzlich ausgeschlossen. Im Gegensatz zu $k^{(ij)}$ und $k^{(ijk)}$ haben die Kraftkonstanten $k^{(ijkl)}$ vereinzelter Diederwinkel kleine bis moderate Werte, was in Verbindung mit den beschränkten Termen $[1 - \cos(n_h\phi_{ijkl} - \hat{\phi}_{ijkl})]$ im dritten Summenterm zu einer großen Flexibilität in den entsprechenden Diederwinkeln führen kann. Als Beispiel für sehr flexible Diederwinkel denke man an die schon besprochenen ϕ/ψ-Diederwinkel des Peptidrückgrats (vgl. Abb. 1.3).

Die Wechselwirkungsenergien zweier Atome, die innerhalb eines Moleküls durch mehr als drei kovalente Bindungen voneinander getrennt sind oder zu verschiedenen Molekülen gehören, werden durch die beiden letzten Summenterme in Gleichung (1.1) erfasst und stellen den nichtbindenden Anteil der potentiellen Energie $E(\mathbf{R}; \mathbf{A})$ dar. Dabei wird die kurzreichweitige van-der-Waals Wechselwirkung durch ein Lennard-Jones Potential mit den Parametern A_{ij} und B_{ij} beschrieben. Während einzelne, nichtionisierte Atome ungeladen sind, kommt es in einem Molekül aufgrund der unterschiedlichen Elektronegativitäten der aneinander gebundenen Atome zu mehr oder minder großen Verschiebungen der Elektronendichte. Im einfachsten Fall wird dieser Sachverhalt pauschal durch sog. Partialladungen q_i beschrieben, die sich an den Kernorten $\mathbf{r}_i$ befinden. Die elektrostatische Energie zweier partiell geladener Atome i und j ergibt sich dann aus der Coulombwechselwirkung, die durch den letzten Summenterm in der Gleichung (1.1) berücksichtigt wird.

Mögliche, auf dem soeben beschriebenen Kraftfeld $E(\mathbf{R}; \mathbf{A})$ beruhende Simulationstechniken sind die bereits erwähnte MD Methode sowie das Monte-Carlo (MC) Verfahren. Nachfolgend werde ich, beginnend mit der MD Methode, die Grundprinzipen dieser beiden Simulationstechniken darstellen.

1.3.2 Simulationsmethoden

In MD Simulationen wird die Dynamik der Kerne (und damit der Atome) eines Molekülsystems klassisch durch die Newtonschen Bewegungsgleichungen

$$m_i \frac{d^2}{dt^2}\mathbf{r}_i(t) = -\nabla_i E[\mathbf{R}(t); \mathbf{A}] \tag{1.2}$$

beschrieben, wobei m_i die Masse und $-\nabla_i E[\mathbf{R}(t); \mathbf{A}]$ die auf das Atom i wirkende Kraft bezeichnet. Diese Bewegungsgleichungen lassen sich numerisch effizient und genau durch den sog. Verlet Algorithmus [66] lösen. Nach dem Verlet Schema wird der neue Ort

$$\mathbf{r}_i(t + \Delta t) = 2\mathbf{r}_i(t) - \mathbf{r}_i(t - \Delta t) - \nabla_i E[\mathbf{R}(t); \mathbf{A}](\Delta t)^2/m_i + \mathcal{O}(\Delta t^4) \tag{1.3}$$

des Atomes i zum Zeitpunkt $t + \Delta t$ durch die aktuelle und vergangene Position $\mathbf{r}_i(t)$ und $\mathbf{r}_i(t - \Delta t)$ bis auf die 3. Ordnung in Δt genau bestimmt. Der Zeitschritt Δt wird mit einer Femtosekunde so gewählt, dass selbst die schnellen CH-Streckschwingungen noch hinreichend glatt diskretisiert werden [67].

Sieht man von numerischen Ungenauigkeiten ab, so bleibt in einer MD Simulation die Energie E erhalten. Um Oberflächeneffekte bei der Beschreibung von Protein-Lösungsmittel-Systemen zu vermeiden und den Druck kontrollieren zu können, wird das endliche Simulationssystem üblicherweise periodisch fortgesetzt. Demnach ist neben der Energie auch das Simulationsvolumen V und die Teilchenzahl N konstant, so dass eine derartige MD Simulation ein mikrokanonisches (NVE) Ensemble generiert. Dabei wird die sog. Ergodenhypothese unterstellt, die besagt, dass im Grenzfall unendlich langer Simulationszeiten das Zeitmittel mit dem Ensemblemittel übereinstimmt. Entsprechend lassen sich durch hinreichend lange MD Simulationen neben dynamischen Systemeigenschaften auch Ensembleeigenschaften berechnen. In den meisten MD Simulationen wird allerdings anstatt der Energie E die Temperatur T konstant gehalten, da sich Proteine in Körperzellen näherungsweise in einem kanonischen (NVT) Ensemble befinden.

Ist man nicht an den dynamischen Eigenschaften sondern ausschließlich an Ensembleeigenschaften eines Simulationssystems interessiert, dann stellt die MC Simulationsmethode eine Alternative zu MD dar. In einer MC Simulation wird in jedem Simulationsschritt eine neue Systemkonfiguration $\mathbf{R}_{\text{neu}} = \mathbf{R}_{\text{alt}} + \delta\mathbf{R}$ durch eine zufällige Änderung $\delta\mathbf{R}$ erzeugt, welche die alte Konfiguration $\mathbf{R}_{\text{alt}}$ mit einer zu ermittelnden Wahrscheinlichkeit P ersetzt. Für den Fall, dass mit einer MC Simulation ein kanonisches Ensemble simuliert werden soll, ergibt sich die Übergangswahrscheinlichkeit aus dem Metropolis Kriterium [68]

$$P = \min\left\{1, \exp\left[\frac{E(\mathbf{R}_{\text{alt}}; \mathbf{A}) - E(\mathbf{R}_{\text{neu}}; \mathbf{A})}{k_{\text{B}}T}\right]\right\}, \tag{1.4}$$

wobei k_{B} die Boltzmann Konstante bezeichnet.

Tatsächlich bieten die im weiteren Verlauf dieser Arbeit vorgestellten Verallgemeinerte-Ensemble Abtasttechniken die Möglichkeit, die MD und MC Methoden miteinander zu verbinden. Dahinter steckt das Ziel, die statistische Aussagekraft und damit die Qualität von Computersimulationen zu verbessern. Bevor ich aber auf die Verallgemeinerte-Ensemble Abtasttechniken eingehe, werde ich im folgenden Abschnitt die qualitätsbegrenzenden Faktoren von MM Computersimulationen diskutieren.

1.3.3 Schwachstellen von MM Computersimulationen

Einem gemäß Gleichung (1.1) definierten MM Kraftfeld liegen zahlreiche Näherungen zugrunde. Eher unproblematisch ist die Verwendung harmonischer Potentiale zur Beschreibung der Streck- und Bindungswinkelschwingungen, obschon bei Raumtemperatur die schnellsten Streckschwingungen nach der Quantenmechanik im Grundzustand sind, weshalb die entsprechenden Freiheitsgrade quantenmechanisch „eingefroren“ sind. Diesem Sachverhalt wird allerdings häufig Rechnung getragen, indem die Auslenkungen der Bindungslängen aus den Gleichgewichtslagen durch den sog. Shake-Algorithmus [69] unterbunden werden. Problematischer ist die Näherung der Ladungsverteilung in einem Molekül durch fixe Partialladungen q_i, da hierdurch Ladungsverschiebungen in polarisierbaren Molekülen, die durch komplex geordnete Umgebungsstrukturen — wie sie in Proteinen generell anzutreffen sind — in spezifischer Weise erzeugt werden, unberücksichtigt bleiben müssen [7]. Weiterhin kann eine adäquate Beschreibung der ϕ/ψ Diederwinkelpotentiale durch trigonometrische Funktionen schwierig sein. Für das CHARMM Kraftfeld weiß man beispielsweise, dass die dort verwendete Parametrisierung der Diederwinkelpotentiale fälschlicherweise die sog. π-Helix Struktur präferiert. Um dieses Verhalten zu korrigieren, wurde die Parametrisierung der CHARMM Diederwinkelpotentiale durch eine als CMAP bezeichnete Korrekturkarte erweitert [70].

Neben der Genauigkeit des Kraftfeldes ist die statistische Güte einer Simulation entscheidend für deren Aussagekraft. Statistisch aussagekräftig ist eine Computersimulation genau dann, wenn deren Ergebnisse auch durch eine beliebige Verlängerung der Rechenzeit keine bzw. nur unwesentliche Veränderungen erfahren. Tatsächlich stellt diese Konvergenzforderung eine große Herausforderung dar. Insbesondere für den Fall sehr großer Simulationssysteme mit abertausenden Atomen ist diese Bedingung auch mit moderner Computertechnik trotz monatelanger Rechenzeiten häufig nicht zu erfüllen. Je nach Systemgröße sind heutzutage etwa 10^8 bis 10^{10} Simulationsschritte möglich [17, 71–73], was bei einer MD Simulation mit Femtosekundenzeitschritt einer Simulationszeit von einer zehntel bis zehn Mikrosekunden entspricht. Entsprechend lassen sich nur sehr schnelle Dynamiken durch vielfache Wiederholung mit hoher statistischer Güte simulieren.

Um Simulationszeiten jenseits von zehn Mikrosekunden zu erreichen, sind weitere, im obigen Modell nicht enthaltene Näherungen notwendig. Hierzu muss man wissen, dass eine realistische Computersimulation eines Proteins das umgebende Lösungsmittel mit einbeziehen muss. Geschieht dies explizit, so besteht das Simulationssystem typischerweise zu mehr als 90% aus Lösungsmittelatomen [7, 58]. Daher lässt sich der Rechenaufwand erheblich reduzieren, falls die durch das Lösungsmittel hervorgerufene elektrostatische Wechselwirkungsenergie implizit beschrieben wird [7, 58].

Eine populäre Methode zur impliziten Beschreibung des Lösungsmittel ist die sog. *Ge-*

neralized Born (GB) Methode [74, 75]. Allerdings ist diese Methode dafür bekannt, andere freie Energielandschaften zu erzeugen als Simulationen mit explizitem Lösungsmittel [76, 77] und Salzbrücken zu überstabilisieren [78]. Ferner kann das Fehlen der Lösungsmittelviskosität zu falschen Zeitskalen dynamischer Prozesse führen [79]. Darüber hinaus fußt die GB Kontinuumsbehandlung des Lösungsmittel nicht auf der Poisson Gleichung [80], weshalb es dieser Methode an physikalischer Stringenz fehlt [81]. Trotzdem sind die mit Kontinuumselektrostatik erreichbaren Simulationszeiten von mittlerweile über einer Millisekunde [75] sehr beeindruckend, weshalb auch in unserer Arbeitsgruppe seit einigen Jahren an der Entwicklung einer auf der Poisson Gleichung basierenden impliziten Lösungsmittelmethode [82–84] gearbeitet wird. Allerdings ist diese Entwicklung noch nicht abgeschlossen und damit ist die Methode derzeit noch nicht einsetzbar.

Aus den geschilderten Gründen sah ich in meiner Arbeit von der Anwendung impliziter Lösungsmittelmethoden ab und konzentrierte mich auf Methoden, die die statistische Güte einer Simulation erhöhen, ohne dabei zusätzliche Näherungen in Kauf nehmen zu müssen. Im nachfolgenden Abschnitt werde ich näher auf diese Methoden eingehen.

1.4 Verallgemeinerte-Ensemble Abtasttechniken

Die zur Bestimmung der strukturellen NVT Gleichgewichtsensembles von Peptiden und Proteinen mittels konventioneller MD (oder MC) nötigen Simulationszeiten werden stark durch die jeweilige Form der freien Energielandschaft beeinflusst, weil die Geschwindigkeit, mit der eine freie Energiebarriere bei der Temperatur T überwunden wird, proportional zu dem sog. Arrheniusfaktor $\exp[-\Delta F/k_\mathrm{B}T]$ mit

$$\Delta F = \Delta E - T\Delta S \tag{1.5}$$

ist [85]. Hierin bezeichnet $T\Delta S$ den entropischen Anteil und ΔE den enthalpischen Anteil der freien Energiebarriere ΔF und k_B die Boltzmann Konstante. Hohe Barrieren verursachen daher lange Verweildauern des Simulationssystems in Konformationszuständen mit niedriger freier Energie. Entsprechend lange Simulationszeiten können notwendig werden, damit die wesentlichen Konformationen des Simulationssystems hinreichend oft besucht werden, was eine Grundvoraussetzung für das ergodisches Abtasten des Konformerenensembles darstellt.

Tatsächlich lässt sich die Abtastgeschwindigkeit mit einem Trick steigern. Der Trick besteht darin, die Simulation bei einer geänderten Temperatur und/oder unter Verwendung eines Kraftfeldes $E(\mathbf{R}; \mathbf{A}')$ mit modifizierten Parametern $\mathbf{A}'$ durchzuführen. Dabei müssen die Änderungen derart vorgenommen werden, dass die dimensionslosen freien Energiebarrieren $\Delta F/k_\mathrm{B}T$ des Simulationssystems verkleinert werden. Allerdings simuliert die so modifizierte Simulation anstelle des ursprünglichen (physikalischen) Boltzmannensembles ein neues, mehr oder minder unphysikalisches Ensemble, das als verallgemeinertes Ensemble bezeichnet wird [86]. Die Eigenschaften des physikalischen Boltzmannensembles können am Ende der Simulation durch eine sog. Regewichtung [87] aus den

Temperatur	2 kcal/mol	4 kcal/mol	6 kcal/mol	8 kcal/mol	10 kcal/mol
300 K	1.0	1.0	1.0	1.0	1.0
400 K	2.3	5.3	12.3	28.5	65.8
500 K	3.8	14.6	55.6	212.3	810.6
600 K	5.3	28.5	151.9	810.6	4325

Tabelle 1.1: Faktoren, um die sich die Abtastgeschwindigkeit für verschiedenen Temperaturen und enthalpische Barrieren erhöht. Die Referenztemperatur ist 300 K.

Daten des verallgemeinerten Ensemble berechnet werden. Dabei werden statistische Fehler des verallgemeinerten Ensembles durch das „Zurückrechnen“ umso größer, je stärker das Kraftfeld und/oder die Temperatur modifiziert wurden. Daher liefert eine Regewichtung nur dann gute Ergebnisse, wenn (i) eine hohe statistische Qualität im verallgemeinerten Ensemble erreicht wurde und (ii) das verallgemeinerte Ensemble nicht „zu weit“ vom physikalischen Ensemble entfernt ist. Insbesondere müssen die wesentlichen Konformationen im urprünglichen Boltzmannensemble auch wesentlich im verallgemeinerten Ensemble sein, da auch eine Regewichtung keine statistischen Aussagen über Bereiche liefern kann, die von der Simulation nicht abgetastet wurden.

In den vergangenen drei Jahrzehnten wurden zahlreiche verallgemeinerte Ensembleabtasttechniken [18–20, 88–103] entwickelt.[1] Trotz der Vielfalt an Ansätzen lassen sich diese Techniken allesamt den beiden bereits oben angesprochenen Strategien zuordnen: Erhöhung der Abtastgeschwindigkeit durch (i) die Modifikation des Kraftfeldes [88–97] oder durch (ii) die Erhöhung der Temperatur [18–20, 98–103].

Mit der sogenannten *Umbrella Sampling* (US) Methode von Torrie und Valleau [88] wurde die Strategie (i) erstmals vor etwa 30 Jahren umgesetzt. Deutlich jünger ist die erste auf Temperaturerhöhung basierende Abtasttechnik, die sogenannte *Simulated Tempering* (ST) [99, 100] Methode, die entgegen einfacher Hochtemperatursimulationen auch für Simulationssysteme mit einer hohen Anzahl an Freiheitsgraden noch praktikabel ist und aus der sich später die sehr populäre *Replica Exchange* (RE) Methode [18–20] entwickelt hat. Der Vorteil von ST und RE gegenüber der US Methode ist, dass am Ende einer Simulation keine Regewichtung notwendig ist, da diese schon während der Simulation durch den dort implementierten Wechsel- bzw. Austauschprozess ganz automatisch stattfindet. Zudem basiert die US Methode auf einer geeigneten Modifikation des Kraftfeldes, während die ursprünglichen ST und RE Verfahren ausschließlich auf einer sehr viel einfacher umzusetzenden Temperaturerhöhung beruhen. Aus diesem Grund habe ich mich in meiner Arbeit auf die Untersuchung und Anwendung der beiden letzt genannten Methoden konzentriert, deren Funktionsweise ich im Folgenden darstelle.

---

[1] Eine sehr umfangreiche Auflistung und Klassifizierung bislang entwickelter Abtasttechniken findet der Leser in einer Arbeit von Hansen und Hünenberger [97].

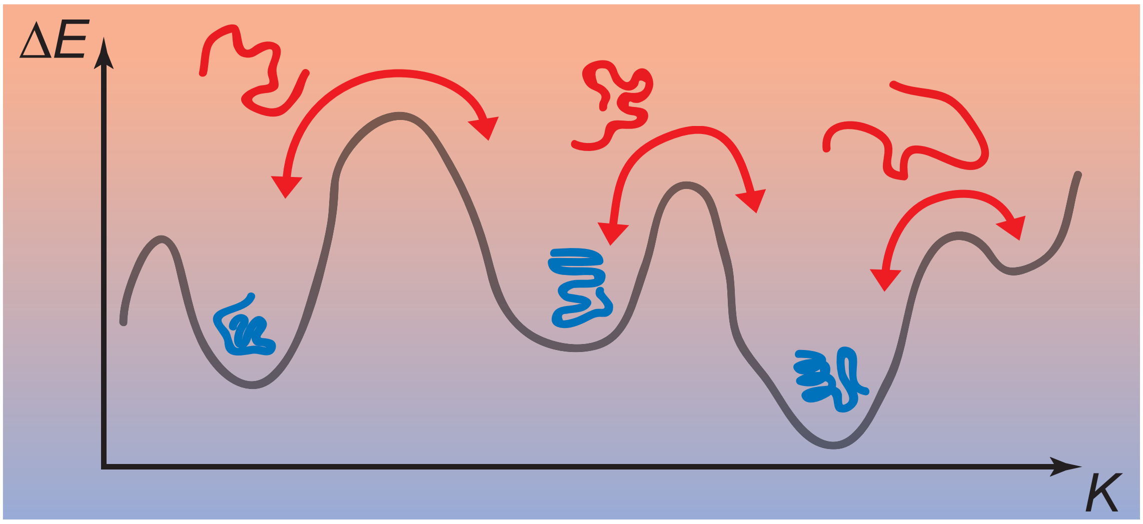

Abbildung 1.6: Illustration der *Simulated Tempering* Strategie. Temperaturerhöhung ermöglicht dem Simulationssystem das beschleunigte Überwinden von Energiebarrieren ΔE und damit ein schnelleres Abtasten des Konformationsraumes K.

1.4.1 Simulated Tempering

Werden die freien Energiebarrieren $\Delta F = \Delta E - T\Delta S$ eines Simulationssystems überwiegend durch deren enthalpische Beiträge ΔE bestimmt, so lässt sich durch Temperaturerhöhung der Quotient $\Delta F/\mathrm{k}_B T$ deutlich verkleinern, was nach den obigen Ausführungen zu einer Steigerung der Abtastgeschwindigkeit führt. Um eine Vorstellung zu bekommen, wie sich verschiedene Temperaturerhöhungen von ursprünglich 300 K für unterschiedliche enthalpische Barrieren auf die Abtastgeschwindigkeit auswirken, habe ich in der Tabelle 1.1 den nach dem Arrheniusfaktor zu erwartenden Geschwindigkeitszuwachs für mehrere Szenarien angegeben. Aus der Tabelle 1.1 geht hervor, dass eine Temperaturerhöhung für den Fall hoher Barrieren ΔE besonders effektiv ist. Das *Simulated Tempering* (ST) Verfahren nutzt genau diesen Sachverhalt aus, indem dem Simulationssystem die Möglichkeit gegeben wird, während der Simulation zu unterschiedlichen Temperaturen einer vorgegebenen Temperaturleiter $T_0 < T_1 < \cdots < T_{N-1}$ hin und her zu wechseln, um letztendlich eine verbesserte Ensemblestatistik bei der Zieltemperatur T_0 zu erzeugen. Dazu wird das Simulationssystem einer MD (oder MC) Simulation unterworfen, deren Temperatur T_i in zeitlich vorgegebenen Intervallen gegebenenfalls durch eine neue Temperatur T_j ersetzt wird. Durch häufige Temperaturwechsel befindet sich das Simulationssystem gelegentlich auch bei hohen Temperaturen, bei denen das System, wie in Abbildung 1.6 illustriert wird, enthalpische Barrieren leichter überwinden kann.

Damit ein Temperaturwechsel von T_i nach T_j keinen Einfluss auf die von der Simulation erzeugten kanonischen Ensemblestatistiken bei den einzelnen Temperaturen (insbesondere bei T_0) hat, muss dieser Prozess ein Flussgleichgewicht zwischen dem Zustand vor dem Wechsel $(\mathbf{R}, T_i)$ und dem Zustand nach dem Wechsel $(\mathbf{R}, T_j)$ darstellen [104].

Diese Forderung wird durch die sog. detaillierte Bilanz

$$P_i(\mathbf{R})P_{i\to j} = P_j(\mathbf{R})P_{j\to i} \tag{1.6}$$

sichergestellt, wobei $P_{i\to j}$ die Akzeptanzwahrscheinlichkeit für einen Temperaturwechsel von T_i nach T_j bezeichnet.[1] $P_i(\mathbf{R})$ ist die Boltzmannwahrscheinlichkeit die Konfiguration $\mathbf{R}$ bei der Temperatur T_i zu finden:

$$P_i(\mathbf{R}) = \frac{\exp[-E(\mathbf{R};\mathbf{A})/k_\mathrm{B}T_i]}{Z}. \tag{1.7}$$

Hierin bezeichnet $Z = \sum_k Z_k$ die kanonische Zustandssumme des verallgemeinerten Ensembles, welches sich aus den einzelnen kanonischen Ensembles k ($k \in \{0,\dots,N-1\}$) mit den Zustandssummen $Z_k = \sum_{\mathbf{R}'} \exp(-E(\mathbf{R}',\mathbf{P})/k_\mathrm{B}T_k)$ zusammensetzt. Akzeptanzwahrscheinlichkeiten, die im Einklang mit der Bilanzgleichung (1.6) stehen, lassen sich mithilfe des Metropolis Kriteriums [68] wie folgt angeben:

$$P_{i\to j} \equiv \min\{1, P_j(\mathbf{R})/P_i(\mathbf{R})\} \quad \text{und} \quad P_{j\to i} \equiv \min\{1, P_i(\mathbf{R})/P_j(\mathbf{R})\}. \tag{1.8}$$

Tatsächlich hat die ST Methode noch einen „Haken“. Um dieses Problem zu erkennen, muss man die Wahrscheinlichkeiten $P_k = \sum_{R'} P_k(R')$, das Simulationssystem bei einer Temperatur T_k zu finden, genauer betrachten. Die Wahrscheinlichkeiten P_k ergeben sich gerade als Quotienten Z_k/Z aus den Zustandssummen Z_k und Z. An diesen „Aufenthaltswahrscheinlichkeiten“ ändert auch der Wechselprozess der Temperaturen nichts, solange die geforderte Bilanzgleichung (1.6) erfüllt ist. Da die einzelnen Zustandssummen Z_k im Allgemeinen sehr unterschiedlich ausfallen, gilt dies auch für die Wahrscheinlichkeiten P_k, was dazu führen kann, dass sich das Simulationssystem während einer Simulation *de facto* nie bei der Zieltemperatur T_0 befindet ($P_0 \approx 0$). In einem solchen Fall hätte man keine Simulationsdaten bei T_0 und die Simulation wäre nutzlos.

Glücklicherweise lassen sich die Wahrscheinlichkeiten P_k durch eine temperaturspezifische Anpassung des Kraftfeldes $E(\mathbf{R};\mathbf{A})$ neu justieren. Für jede Temperatur T_k wird ein neues Kraftfeld

$$\tilde{E}_k(\mathbf{R};\mathbf{A}) \equiv E(\mathbf{R};\mathbf{A}) + w_k k_\mathrm{B} T_k \tag{1.9}$$

eingeführt, welches in einfacher Weise aus dem Orginalkraftfeld $E(\mathbf{R};\mathbf{A})$ und einer für die Kräfteberechnung unwesentlichen Konstanten $w_k k_\mathrm{B} T_k$ hervorgeht. Die Konstanten w_k nennt man Gewichte. Diese werden durch $w_k = -\ln Z_k$ für gewöhnlich so gewählt, dass die Zustandssummen $\tilde{Z}_k = \sum_{\mathbf{R}'} \exp[-\tilde{E}_k(\mathbf{R}',\mathbf{P})/k_\mathrm{B}T_k]$ des neuen verallgemeinerten Ensembles allesamt den Wert 1 annehmen [105]. Entsprechend haben die neuen „Aufenthaltswahrscheinlichkeiten“ $\tilde{P}_k$ allesamt den gleichen Wert $1/N$, was zu einem uniformen Abtasten des Temperaturraumes führt. Da sich durch die temperaturspezifischen Kraftfeldmodifikationen die Boltzmannwahrscheinlichkeiten $P_k(\mathbf{R})$ aus Gleichung (1.7) zu

$$\tilde{P}_k(\mathbf{R}) = \frac{\exp[-\tilde{E}_k(\mathbf{R};\mathbf{A})/k_\mathrm{B}T_k]}{\tilde{Z}} \tag{1.10}$$

---

[1] Demnach wird ein Temperaturwechsel von T_i nach T_j mit der Wahrscheinlichkeit $P_{i\to j}$ ausgewürfelt und stellt damit einen MC Schritt dar.

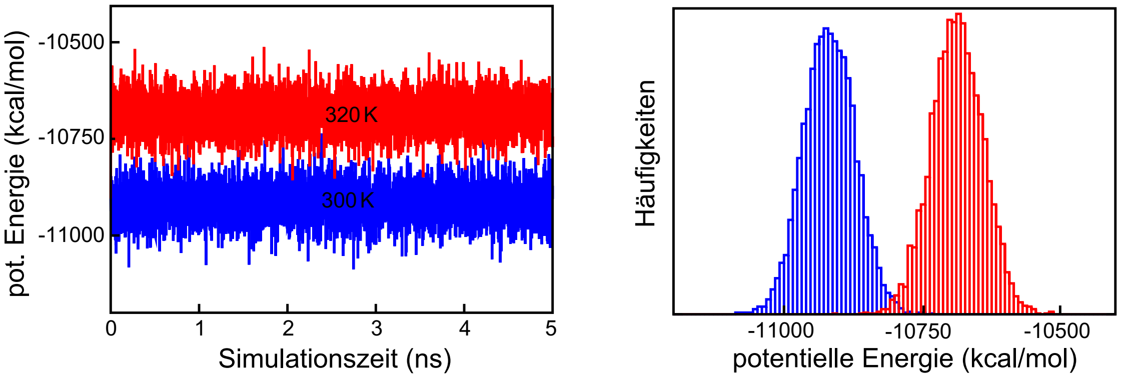

Abbildung 1.7: Schwankungen der potentiellen Energie während einer MD Simulation. Links: Zeitliche Entwicklung der potentiellen Energie für ein Simulationssystem bestehend aus rund 1000 Wassermolekülen und einem darin gelösten Oktapeptid simuliert bei zwei unterschiedlichen Systemtemperaturen (300 K, 320 K). Rechts: Die durch Histogramme dargestellten Verteilungen der potentiellen Energien der 300 K Simulation (blau) und der 320 K Simulation (rot). Trotz eines vergleichsweisen geringen Temperaturunterschieds haben die beiden Verteilungen nur einen kleinen Überlapp.

ändern, verändern sich auch die Akzeptanzwahrscheinlichkeiten aus Gleichung (1.8). Mittels Gleichung (1.10) erhält man die neuen Akzeptanzwahrscheinlichkeiten

$$\tilde{P}_{i \to j} = \min\{1, \exp(\Delta_{i \to j})\} \quad \text{mit} \quad \Delta_{i \to j} = \frac{\tilde{E}_i(\mathbf{R}; \mathbf{A})}{k_{\mathrm{B}} T_i} - \frac{\tilde{E}_j(\mathbf{R}; \mathbf{A})}{k_{\mathrm{B}} T_j}, \tag{1.11}$$

wobei $\Delta_{i \to j}$ durch Gleichung (1.9) auf die Form

$$\Delta_{i \to j} = \left(\frac{1}{k_{\mathrm{B}} T_i} - \frac{1}{k_{\mathrm{B}} T_j} \right) E(\mathbf{R}, \mathbf{A}) - (w_j - w_i), \tag{1.12}$$

gebracht werden kann.

Nachdem bis hierhin die Theorie zu ST eingehend dargestellt wurde, möchte ich abschließend noch einige Anmerkungen zu verschiedenen Details der ST Methode machen, über die ich bislang stillschweigend hinweggegangen bin, die aber für das Verständnis der Methode und deren praktische Umsetzung wichtig sind. In Bezug auf die Umsetzung einer ST Simulation ist es nützlich zu erkennen, dass sich die Kraftfeldmodifikationen aus Gleichung (1.9) nur während des Temperturwechsels durch veränderte Akzeptanzwahrscheinlichkeiten auf die Simulation auswirken. Zwischen den Wechselversuchen haben die Konstanten $w_k k_{\mathrm{B}} T_k$ in Gleichung (1.9) keinen Einfluss auf die Dynamik des Simulationssystems, so dass dort weiterhin das Orginalkraftfeld $E(\mathbf{R}, \mathbf{A})$ verwendet werden darf.

In den bisherigen Ausführungen zu ST wurde ausschließlich die potentielle Energie $E(\mathbf{R}; \mathbf{A})$ anstelle der Gesamtenergie berücksichtigt. Für den Fall von MC Simulationen stellt dies kein Problem dar, da dort die potentielle Energie und die Gesamtenergie identisch sind. Dies gilt allerdings nicht für MD Simulationen, da dort die kinetische Energie für die Dynamik des Systems verantwortlich ist. In einer wegweisenden Arbeit von Sugita und Okamoto [20] wurde aber gezeigt, dass bei einem Wechselprozess die kinetische Energie keine Rolle spielt, solange der Temperaturwechsel, beispielsweise von T_i nach T_j, von einer Skalierung der Atomgeschwindigkeiten durch $\sqrt{T_j/T_i}$ begleitet wird [20].[1]

Ein weiterer, noch nicht angesprochender Punkt ist die Wahl der Temperaturleiter. Diese darf nicht völlig willkürlich gewählt werden. Vielmehr müssen die Verteilungen der potentiellen Energien benachbarter Temperaturen T_i und $T_{i\pm1}$ einen deutlichen Überlapp besitzen, da dieser Überlapp ein Maß für die Akzeptanzwahrscheinlichkeiten $P_{i\to i\pm1}$ darstellt [106]. Aus diesem Grund beschränkt man sich gewöhnlich auf Wechselversuche zwischen benachbarten Temperaturen, da Temperaturwechsel zwischen nicht benachbarten Temperaturen deutlich unwahrscheinlicher sind.

Wie sensibel die Verteilungen der potentiellen Energien auf Temperaturänderungen reagieren, wird durch Abbildung 1.7 deutlich. Hier bewirkt eine Temperaturerhöhung von nur $\Delta T = 20$ K schon eine derart große Verschiebung der Energieverteilung, dass der Überlapp zwischen den Energieverteilungen fast verschwindet. Entsprechend klein würden in diesem Fall die Akzeptanzwahrscheinlichkeiten ausfallen. Dabei ist das Simulationssystem, auf die sich Abbildung 1.7 bezieht, mit ca. 3000 Atomen vergleichsweise klein. Für Simulationssysteme mit einer sehr viel größeren Teilchenzahl n fällt der Überlapp der potentiellen Energieverteilungen noch deutlich geringer aus, da die Verschiebung $\Delta\bar{E}$ des potentiellen Energiemittelwertes $\bar{E}$ proportional zu n ausfällt, während die Breite σ_E der Verteilung nur mit $\sqrt{n}$ anwächst.[2] Daher liegen in ST Simulationen mit hinreichend großen Akzeptanzwahrscheinlichkeiten die Temperaturdifferenzen benachbarter Temperatursprossen üblicherweise bei nur wenigen Grad Kelvin, was eine große Anzahl N an Sprossen notwendig macht, damit das verallgemeinerte Ensemble einen hinreichend großen Temperaturbereich abdecken kann. Eine hohe Sprossenzahl N führt allerdings dazu, dass nur ein Bruchteil der im verallgemeinerten Ensemble simulierten Information zur Ensemblestatistik bei T_0 beiträgt, was sich negativ auf die Abtasteffizienz auswirkt.

Ein möglicher Kompromiss zwischen nicht zu kleinen Akzeptanzwahrscheinlichkeiten und einer nicht zu großen Anzahl an Temperatursprossen besteht darin, die Temperaturleiter so zu wählen, dass die mittlere Dauer, die das Simulationssystem für eine Wanderung von T_0 nach T_{N-1} und zurück benötigt (die sog. *round-trip* Zeit), minimiert wird. Dieser Strategie liegt die Annahme zugrunde, dass eine Minimierung der *round-trip* Zeit eine Maximierung der Abtastgeschwindigkeit bei T_0 bewirkt. Mit der Frage, wie und unter welchen Voraussetzungen eine solche Temperaturleiter für ein Simulationssystem konstruiert werden kann, beschäftigt sich das 3. Kapitel dieser Dissertation. Tatsächlich lässt sich durch eine geeignete, über die Energieverschiebung aus Gleichung (1.9) hinausgehende Modifikation des Kraftfeldes die Anzahl N der Temperatursprossen reduzieren und damit die Abtasteffizienz der ST Methode steigern. In diesem Zusammenhang wird in Kapitel 4 eine neue ST Variante, das sog. *Simulated Solute Tempering* vorgestellt. Dort wird auch ausführlich erläutert, wie die *a priori* unbekannten Gewichte $w_k = -\ln Z_k$ (genau genommen die entsprechenden Differenzen $w_j - w_i$) durch Vorabsimulationen bei den einzelnen Temperaturen T_k abgeschätzt werden können.

---

[1] Zwar bezieht sich die Arbeit von Sugita und Okamoto direkt auf die im nächsten Abschnitt dargestellte *Replica Exchange* Methode, die dargelegte Theorie kann aber direkt auf ST übertragen werden.

[2] Diese Argumentation beruht darauf, dass n proportional zur extensiven Wärmekapazität $C \approx \Delta\bar{E}/\Delta T$ ist und im kanonischen Ensemble die Beziehung $\sigma_E = T\sqrt{k_\mathrm{B}C}$ gilt [107].

Obwohl es sich herausgestellt hat, dass die Gewichte durch recht kurze Vorabsimulationen schon recht gut abgeschätzt werden können [105], bleibt immer eine gewisse Restunsicherheit, zumal der Erfolg einer ST Simulation sehr sensibel von den Gewichten abhängt. Im nächsten Abschnitt werde ich daher zeigen, wie eine fast zwanglose Erweiterung der ST Methodik zu der sog. *Replica Exchange* Methode führt, in der aber, im Unterschied zu ST, die Gewichte w_k keine Rolle mehr spielen.

1.4.2 Replica Exchange

Die *Replica Exchange* (RE) Methode [18–20], die manchmal auch als *Parallel Tempering* bezeichnet wird [108], übernimmt die Grundidee von ST, nämlich dem Simulationssystem einen Temperaturwechsel entlang einer Temperaturleiter $T_0 < T_1 < \cdots < T_{N-1}$ zu ermöglichen. Im Gegensatz zum ST Verfahren, bei dem nur eine Simulation durch den Temperaturraum wandert, besteht eine RE Simualtion jedoch aus N identischen Simulationssystemen (Replikaten), die jeweils exklusiv bei einer Temperatur T_i ($i \in \{0, \ldots, N-1\}$) simuliert werden. In zeitlich vorgegebenen Intervallen kommunizieren jeweils Paare von Replikaten miteinander, indem sie gegebenenfalls ihre Temperaturen T_i und T_j untereinander austauschen.[1] Damit wird auch nach einem Austausch jede Temperatur der Temperaturleiter von genau einem Replikat bevölkert. Anstelle einer Akzeptanzwahrscheinlichkeit $P_{i\to j}$ für einen Temperaturwechsel hat man es nun mit einer Akzeptanzwahrscheinlichkeit P_{ij} für einen gegenseitigen Temperaturaustausch zu tun, von der man — analog zu ST — die Erfüllung der detaillierten Bilanz

$$P_i(\mathbf{R}_i)P_j(\mathbf{R}_j)P_{ij} = P_i(\mathbf{R}_j)P_j(\mathbf{R}_i)P_{ji} \tag{1.13}$$

fordert, wobei P_i und P_j Boltzmannwahrscheinlichkeiten analog zu Gleichung (1.7) bezeichnen. Wiederum liefert das Metropolis Kriterium [68]

$$P_{ij} = \min\{1, \frac{P_i(\mathbf{R}_j)P_j(\mathbf{R}_i)}{P_i(\mathbf{R}_i)P_j(\mathbf{R}_j)}\} \quad \text{und} \quad P_{ji} = \min\{1, \frac{P_i(\mathbf{R}_i)P_j(\mathbf{R}_j)}{P_i(\mathbf{R}_j)P_j(\mathbf{R}_i)}\} \tag{1.14}$$

eine Lösung der Bilanzgleichung (1.13). Durch Einsetzen der Boltzmannwahrscheinlichkeiten P_i und P_j ergibt sich

$$P_{ij} = \min\{1, \exp(\Delta_{ij})\} \tag{1.15}$$

mit

$$\Delta_{ij} = (1/k_\mathrm{B}T_i - 1/k_\mathrm{B}T_j)[E(\mathbf{R}_i) - E(\mathbf{R}_j)]. \tag{1.16}$$

Wie stark RE mit der ST Methode verwandt ist, zeigt der einfache Zusammenhang zwischen Δ_{ij} aus Gleichung (1.16) und $\Delta_{i\to j}$ aus Gleichung (1.12)

$$\Delta_{ij} = \Delta_{i\to j}\Delta_{j\to i}, \tag{1.17}$$

---

[1] T_j ist üblicherweise eine benachbarte Temperatur $T_{i\pm1}$.

wobei zur Bestimmung der $\Delta_{i\to j}$ bzw. $\Delta_{j\to i}$ die Energie $E(\mathbf{R}, \mathbf{A})$ in der Gleichung (1.12) trivialerweise durch $E(\mathbf{R}_i, \mathbf{A})$ bzw. $E(\mathbf{R}_j, \mathbf{A})$ ersetzt werden muss. Die Interpretation dieser Beziehung wird besonders einfach, wenn man von Akzeptanzwahrscheinlichkeiten kleiner als eins ausgeht, so dass $P_{ij} = \exp(\Delta_{ij})$ und $P_{i\to j} = \exp(\Delta_{i\to j})$ gilt. Damit folgt aus Gleichung (1.17) $P_{ij} = P_{i\to j}P_{j\to i}$, d.h. die Akzeptanzwahrscheinlichkeit P_{ij} für einen Temperaturaustausch zwischen zwei Replikaten ist gleich dem Produkt der beiden Wechselwahrscheinlichkeiten $P_{i\to j}$ und $P_{j\to i}$. Mithin ist damit $P_{ij} \leq P_{i\to j}$, woraus abgeleitet werden kann, dass die Replikate einer RE Simulation längere *round-trip* Zeiten besitzen als das Simulationssystem einer entsprechenden ST Simulation. In der in Kapitel 4 dieser Dissertation abgedruckten Publikation werden neben der Einführung der SST Methode die Auswirkungen unterschiedlicher *round-trip* Zeiten auf die Abstastgeschwindigkeit untersucht. Dabei wird neben der SST Methode die *Replica Exchange with Solute Tempering* Methode [101] angewendet, die das RE Pendant zu SST darstellt. Beide Methoden beruhen auf dem von Liu und Co-Autoren vorgestellten *Solute Tempering* Konzept [101], auf welches ich im Folgenden kurz eingehen werde, da dieses Konzept in unserer Arbeitsgruppe mithilfe meiner Expertise vielfach angewendet wurde [16, 55, 102, 109].

1.4.3 Solute Tempering

Die ursprüngliche Idee des *Solute Tempering* Konzepts besteht darin, nur das gelöste Molekül (engl. *solute*) nicht aber das Lösungsmittel einer Temperaturerhöhung zu unterwerfen. Damit wirkt eine Temperaturerhöhung auf nur noch vergleichsweise wenige Atome des Simulationssystems. Da identische Simulationssysteme, die sich nur in der Temperatur weniger Atome unterscheiden, einen deutlich größeren Energieüberlapp besitzen als solche, bei denen der selbe Temperaturunterschied alle Atome betrifft, können mit dieser Strategie ST und RE Simulationen durchgeführt werden, deren Temperaturleitern deutlich weniger Sprossen zur Abdeckung eines vorgegebenen Temperaturbereichs benötigen und die dennoch große Akzeptanzwahrscheinlichkeiten haben.

Eine intuitive aber dennoch naive Umsetzung dieser Strategie könnte darin bestehen, das gelöste Molekül einfach durch einen Thermostaten auf die gewünschte Temperatur T_i zu bringen, während man durch einen zweiten Thermostaten das Lösungsmittel auf der Zieltemperatur T_0 hält. Eine derart ablaufende Simulation erzeugt jedoch kein kanonisches Ensemble bei der Temperatur T_i und verstößt somit gegen die Grundannahme, die der ST und der RE Methode zugrunde liegt. Entsprechend würde das geschilderte Vorgehen, eingebunden in eine ST oder RE Simulation, kein kanonisches Ensemble bei der Zieltemperatur T_0 erzeugen.

Daher schlugen Liu und Co-Autoren [101] einen anderen Weg ein, der auf einem einfachen Sachverhalt beruht: Ein Simulationssystem unter der Wirkung eines skalierten Kraftfeldes $\tilde{E}(\mathbf{R}; \mathbf{A}) = E(\mathbf{R}; \mathbf{A}) \cdot T/T_0$ generiert wegen

$$\exp(-\tilde{E}(\mathbf{R}; \mathbf{A})/k_\mathrm{B}T) = \exp(-E(\mathbf{R}; \mathbf{A})/k_\mathrm{B}T_0)$$

die gleiche Boltzmannstatistik bei der Temperatur T wie das unskalierte System bei der Temperatur T_0. Damit ist das skalierte System auch bei der erhöhten Temperatur $T > T_0$

seitens der Statistik effektiv „kalt“. Diesem Ansatz folgend schlugen die Autoren speziell für die Anwendung auf eine RE Simulation eine temperaturabhängige Skalierung

$$E_k(\mathbf{R};\mathbf{A}) = \lambda_{k,0}E^{PP}(\mathbf{R};\mathbf{A}) + \lambda_{k,1}E^{LL}(\mathbf{R};\mathbf{A}) + \lambda_{k,2}E^{PL}(\mathbf{R};\mathbf{A}) \tag{1.18}$$

der Protein-Protein E^{PP}, Lösungsmittel-Lösungsmittel E^{LL} und Protein-Lösungsmittel E^{PL} Wechselwirkungsanteile des unskalierten Kraftfeldes $E = E^{PP} + E^{LL} + E^{PL}$ mit den Skalierungsfaktoren

$$\lambda_{k,0} = 1, \quad \lambda_{k,1} = \frac{T_k}{T_0} \quad \text{und} \quad \lambda_{k,2} = \frac{T_0 + T_k}{2T_0} \tag{1.19}$$

vor und bezeichneten dieses Verfahren als *Replica Exchange with Solute Tempering* (REST) [101]. Entsprechend weist ein Replikat, dass bei der Temperatur $T_k > T_0$ mit dem modifizierten Kraftfeld $E_k(\mathbf{R};\mathbf{A})$ simuliert wird, ein effektiv kaltes (T_0) Lösungsmittel auf, wohingegen das von der Skalierung unberührte Protein die Temperatur T_k besitzt. Da das Kraftfeld bei T_0 unskaliert bleibt, erzeugt REST bei der Zieltemperatur T_0 das gesuchte Boltzmannensemble, während die restlichen Ensembles ($T_k > T_0$) wegen der Skalierung unphysikalische Boltzmannensembles sind. Allerdings müssen die Δ_{ij} aus Gleichung (1.16) angepasst werden, da die Replikate nun neben den Temperaturen auch ihre temperaturspezifischen Energiefunktionen austauschen. REST wird daher der Familie der sog. *Hamiltonian Replica Exchange* Methoden [94, 95] zugerechnet [10]. Das Δ_{ij} aus Gleichung (1.16) ist nun durch

$$\Delta_{ij} = \frac{1}{k_\mathrm{B}T_i} \cdot [E_i(\mathbf{R}_j;\mathbf{A}) - E_i(\mathbf{R}_i;\mathbf{A})] + \frac{1}{k_\mathrm{B}T_j} \cdot [E_j(\mathbf{R}_i;\mathbf{A}) - E_j(\mathbf{R}_j;\mathbf{A})] \tag{1.20}$$

zu ersetzen. Diese Beziehung lässt sich wieder über eine Bilanzgleichung analog zur Gleichung (1.13) ableiten.[1]

Ich musste allerdings feststellen, dass die Implementierung der von Liu und Co-Autoren vorgeschlagenen Skalierung (1.19) mit einem erheblichen programmiertechnischen Aufwand verbunden ist. Dieser Aufwand lässt sich gänzlich umgehen, wenn man für $\lambda_{k,2}$ anstelle des arithmetischen Mittels aus $\lambda_{k,0}$ und $\lambda_{k,1}$ das geometrische Mittel verwendet. Entsprechend wird in unserer Arbeitsgruppe die alternative *Solute Tempering* Skalierung

$$\lambda_{k,0} = 1, \quad \lambda_{k,1} = \frac{T_k}{T_0} \quad \text{und} \quad \lambda_{k,2} = \sqrt{T_k/T_0} \tag{1.21}$$

verwendet, die durch eine einfache Modifikationen von Kraftfeldparametern herbeigeführt werden kann.[2] Beispielsweise führt die Skalierung der Partialladungen der Lösungsmittelatome mit dem Faktor $\sqrt{T_k/T_0}$ dazu, dass alle drei elektrostatischen Energieanteile $E^{PP}_{k,elec}$, $E^{LL}_{k,elec}$ und $E^{PL}_{k,elec}$ automatisch die Skalierungen (1.21) erfahren. Weiterführende Informationen hierzu können im Methodenteil der in Kapitel 5 abgedruckten Publikation nachgelesen werden.

---

[1] Oder aber man nutzt die im letzten Abschnitt aufgezeigte Gleichung (1.17), in der $\Delta_{i\to j}$ durch Gleichung (1.11) gegeben ist, wobei dort $\tilde{E}_i(\mathbf{R};\mathbf{A})$ durch $E_i(\mathbf{R_i};\mathbf{A}) + w_i k_\mathrm{B} T_i$ ersetzt werden muss (analoges gilt für $\Delta_{j\to i}$).

[2] Formal bedeutet dies, es lässt sich ein Parametersatz $\mathbf{A}_k$ finden, so dass $E_k(\mathbf{R}_k;\mathbf{A}) \equiv E(\mathbf{R}_k;\mathbf{A}_k)$ gilt.

1.5 Die Struktur dieser Arbeit

Den Hauptteil meiner Dissertation bilden die Kapitel 2 bis 5. In jedem dieser Kapitel ist eine Publikation abgedruckt. Eine Ausnahme ist Kapitel 2, welches zwei meiner Publikationen umfasst. Jeder Publikation geht eine in deutsch verfasste Zusammenfassung voraus, in der die Hintergründe und Ziele der nachfolgenden Veröffentlichung dargestellt werden. Die Kapitel 2 und 3 befassen sich mit methodischen Aspekten von RE und ST Simulationen. Das im letzten Abschnitt vorgestellte *Solute Tempering* Konzept und Erkenntnisse aus Kapitel 3 führten dann zur Entwicklung einer neuen ST Variante, die in Kapitel 4 vorgestellt wird und deren Abtasteffizienz dort mit bereits etablierten Abtasttechniken verglichen wird. Im letzten Kapitel des Hauptteils steht dann die Untersuchung von Nichtgleichgewichtsdynamiken im Vordergrund, wobei grundlegend für diese Arbeit die genaue Bestimmung der zugehörigen strukturellen Start- und Zielensembles mittels RE Simulationen waren. Den Schlussteil meiner Arbeit bildet das Kapitel 6, in dem die Ergebnisse des Hauptteils noch einmal zusammengefasst werden und darüber hinaus — an geeigneter Stelle — ein Blick auf zukünftige Entwicklungen gegeben wird.

2 Effizienzreduktion durch RE Simulationen

Die Anwendung der *Replica Exchange* Methode beruht auf der Erwartung, dadurch die Abtasteffizienz der Computersimulation steigern zu können. Der nachfolgend abgedruckte Artikel[1]

> Robert Denschlag, Martin Lingenheil, Paul Tavan:
> „Efficiency reduction and pseudo-convergence in replica exchange sampling of peptide folding-unfolding equilibria“
> *Chem. Phys. Lett.* **458**, 244-248 (2008),

den ich zusammen mit Martin Lingenheil und Paul Tavan verfasst habe, zeigt erstmals, dass dies nicht zwangsläufig der Fall ist. Hierzu wird die Faltungs-Entfaltungsdynamik eines 3-Zustandssystems simuliert, welches aufgrund der gewählten freien Energiedifferenzen zwischen den einzelnen Zuständen ein Modell für ein β-Hairpin darstellt. Es zeigt sich, dass Temperaturerhöhung die Faltungsdynamik des Modellsystems derart verlangsamt, dass sich in der Summe auch die Faltungs-Entfaltungsdynamik des Modellsystems verlangsamt und als Folge die Abtasteffizienz durch die Anwendung der *Replica Exchange* Methode reduziert wird. Zusätzlich werden in diesem Artikel die Fragen beantwortet, wie die Qualität der Konvergenz einer *Replica Exchange* Simulation abgeschätzt werden kann und welche Fehler bei der Konvergenzanalyse gemacht werden können.

---

[1] Mit freundlicher Genehmigung des Elsevier Verlags (Lizenznummer: 2415941044663).

Chemical Physics Letters 458 (2008) 244–248

Contents lists available at ScienceDirect

Chemical Physics Letters

journal homepage: www.elsevier.com/locate/cplett

Efficiency reduction and pseudo-convergence in replica exchange sampling of peptide folding–unfolding equilibria

Robert Denschlag, Martin Lingenheil, Paul Tavan *

Lehrstuhl für Biomolekulare Optik, Ludwig-Maximilians-Universität, Oettingenstr. 67, 80538 München, Germany

ARTICLE INFO

Article history:
Received 20 March 2008
In final form 25 April 2008
Available online 3 May 2008

ABSTRACT

Replica exchange (RE) molecular dynamics (MD) simulations are frequently applied to sample the folding–unfolding equilibria of β-hairpin peptides in solution, because efficiency gains are expected from this technique. Using a three-state Markov model featuring key aspects of β-hairpin folding we show that RE simulations can be less efficient than conventional techniques. Furthermore we demonstrate that one is easily seduced to erroneously assign convergence to the RE sampling, because RE ensembles can rapidly reach long-lived stationary states. We conclude that typical REMD simulations covering a few tens of nanoseconds are by far too short for sufficient sampling of β-hairpin folding–unfolding equilibria.

© 2008 Elsevier B.V. All rights reserved.

Replica exchange molecular dynamics (REMD) is considered to be a method for the efficient canonical sampling of biomolecular properties. Therefore, the REMD simulation technique has been frequently applied to generate equilibrium ensembles of biomolecules in solution [1–12]. Here, systems of particular interest were peptides folding into a β-hairpin. Reported simulation times covered the range from a few nanoseconds up to a few tens of nanoseconds [9–12]. As an important result, free energy differences ΔF between various conformational states were given [9–11]. A reliable calculation of these values requires that the REMD simulations generate approximately the associated conformational equilibrium ensembles.

It is not easy to judge whether a necessarily finite simulation time was actually long enough to sample the most important regions of conformational space. As an indication of convergence one may take the observation that the calculated ΔF values do not change too much upon a substantial elongation of the simulation time. Particularly for a β-hairpin peptide, which folds on time scales of μs at ambient temperatures [13,14], one may ask whether the equilibrium folding–unfolding ensemble can be sampled by REMD within simulation times spanning a few tens of nanoseconds. In this Letter, we will address this question by constructing a Markovian three-state model for β-hairpin folding–unfolding and by executing extended replica exchange Monte Carlo (REMC) simulations for this model. In addition, we check to what extent replica exchange can help to speed up the sampling in the given case.

Our three-state model system consists of a folded state $\mathfrak{f}$, a transition state $\mathfrak{t}$, and an unfolded state $\mathfrak{u}$. For a β-hairpin peptide in solution, $\mathfrak{f}$ will cover a small and compact region in the peptide's configurational space. Correspondingly, $\mathfrak{f}$ is characterized by a small entropy $S_\mathfrak{f}$ and a low energy $U_\mathfrak{f}$, which accounts for the hydrogen bonds linking the β-strands. We assume that the configurational space covered by the transition state $\mathfrak{t}$ is not much larger. Thus, $S_\mathfrak{t}$ is also small. However, the energy $U_\mathfrak{t}$ must be higher because some inter-strand hydrogen bonds will be broken. The unfolded state $\mathfrak{u}$ is extended and highly flexible with a large entropy $S_\mathfrak{u}$ and a large energy $U_\mathfrak{u}$ because of the broken hydrogen bonds.

The concepts sketched above can be immediately transferred into the set-up of a three-state Markov model for β-hairpin folding–unfolding. Table 1 lists our choice for the model parameters S_i and U_i, $i \in \{\mathfrak{f}, \mathfrak{t}, \mathfrak{u}\} \equiv \{1, 2, 3\}$. According to this choice, the free energies $F_\mathfrak{f}$ and $F_\mathfrak{u}$ are equal at the temperature $T = T_0$. Note that the equilibrium probability $P_i(T)$ of a state i at temperature T is $\exp(-F_i/k_BT)/[\sum_k \exp(-F_k/k_BT)]$, where k_B is the Boltzmann constant. Consequently, $P_\mathfrak{f}(T_0)$ equals $P_\mathfrak{u}(T_0)$.

Fig. 1 specifies the structure of the transition matrix $\widehat{T} = (t_{ij})$ defining the Markov model and illustrates the energetics of the model at a temperature $T > T_0$. Direct transitions from $\mathfrak{f}$ to $\mathfrak{u}$ and vice versa are forbidden. Therefore, t_{13} and t_{31} vanish. Furthermore, we have chosen $t_{22} = 0$ implying that the transition state $\mathfrak{t}$ cannot be occupied for more than one Markov step. We have chosen $t_{12} = t_{32} = 1/2$, which is plausible for all temperatures $T > (2/3)T_0$ because at these temperatures $F_\mathfrak{f}$ and $F_\mathfrak{u}$ are smaller than $F_\mathfrak{t}$ (cf. Table 1). We assume detailed balance implying that $t_{21}P_\mathfrak{f} = t_{12}P_\mathfrak{t}$ and $t_{23}P_\mathfrak{u} = t_{32}P_\mathfrak{t}$, where $P_\mathfrak{f}$, $P_\mathfrak{t}$, and $P_\mathfrak{u}$ are the equilibrium probabilities of the states i. One gets $t_{21} = \exp[(F_\mathfrak{f} - F_\mathfrak{t})/k_BT]/2$ and $t_{23} = \exp[(F_\mathfrak{u} - F_\mathfrak{t})/k_BT]/2$. $\widehat{T}$ becomes a stochastic matrix for $t_{11} = 1 - t_{21}$ and $t_{33} = 1 - t_{23}$. The associated stationary distribution is then $(P_\mathfrak{f}, P_\mathfrak{t}, P_\mathfrak{u})^T$ at all $T > 2T_0/3$.

---

* Corresponding author. Fax: +49 89 2180 9220.
E-mail address: tavan@physik.uni-muenchen.de (P. Tavan).

0009-2614/$ - see front matter © 2008 Elsevier B.V. All rights reserved.
doi:10.1016/j.cplett.2008.04.114

Table 1
Energy terms of a three-state Markov model for β-hairpin folding–unfolding

State	$F = U - T \cdot S$	U	$T \cdot S$
$\mathfrak{f}$	0	0	0
$\mathfrak{t}$	$2E_{\mathfrak{u}}/3$	$2E_{\mathfrak{u}}/3$	0
$\mathfrak{u}$	$E_{\mathfrak{u}} \cdot (1 - T/T_0)$	$E_{\mathfrak{u}}$	$E_{\mathfrak{u}} \cdot T/T_0$

The free energy F, the energy U, and the entropy S are given in terms of the unfolding energy $E_{\mathfrak{u}}$ and a temperature T_0 defining the mid-point of the unfolding transition through $F_{\mathfrak{f}} = F_{\mathfrak{u}} = 0$.

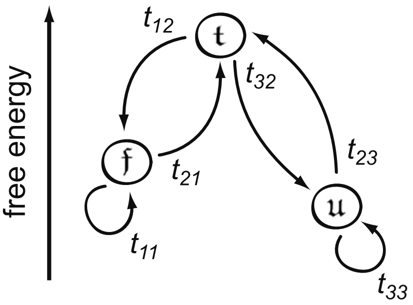

Fig. 1. Illustration of the transition matrix $\widehat{T}$ defining our Markov model for β-hairpin folding–unfolding. States are ordered according to their free energies at a temperature $T > T_0$. The state energies are specified in Table 1 and the matrix elements t_{ij} in the text.

The transition matrix $\widehat{T}$ determines the folding and unfolding rates $k_{\mathrm{f}} = t_{12} \cdot t_{23}$ and $k_{\mathrm{u}} = t_{32} \cdot t_{21}$, respectively, at a temperature T. One gets

$$k_{\mathrm{f}}(T) = \exp[\beta E_{\mathfrak{u}}(1/3 - T/T_0)]/4 \tag{1}$$

and

$$k_{\mathrm{u}}(T) = \exp(-2\beta E_{\mathfrak{u}}/3)/4, \tag{2}$$

with $\beta = 1/k_{\mathrm{B}}T$. Starting at state $\mathfrak{u}$, the average number τ_{f} of Markov steps to reach the folded state $\mathfrak{f}$ is $1/k_{\mathrm{f}}$. Likewise, the unfolding time τ_{u} is $1/k_{\mathrm{u}}$. These times are specified by our choice for the unfolding energy $E_{\mathfrak{u}} = 18k_{\mathrm{B}}T_0$.

Fig. 2 shows the resulting times τ_{f}, τ_{u}, and $\tau_{\mathrm{f}} + \tau_{\mathrm{u}}$ as functions of the temperature ratio T/T_0. Because of the purely energetic barrier $2E_{\mathfrak{u}}/3$ between the states $\mathfrak{f}$ and $\mathfrak{t}$ (cf. Table 1), the unfolding time τ_{u} decreases strongly at large temperatures T/T_0. In contrast, the folding time τ_{f} increases at elevated temperatures and converges to the limiting value $4 \cdot \exp(E_{\mathfrak{u}}/k_{\mathrm{B}}T_0) \approx 2.6 \times 10^8$ determined by the entropic difference $E_{\mathfrak{u}}/T_0$ between the states $\mathfrak{u}$ and $\mathfrak{t}$. The increase of folding times for increasing temperatures has been termed as non- or anti-Arrhenius behavior [15,16]. The time $\tau_{\mathrm{u}} + \tau_{\mathrm{f}}$ for a complete unfolding and refolding process increases with temperature for $T/T_0 > 18/(18 - \ln 2) \approx 1$. Thus, in contradiction to the common expectation of enhanced sampling, the sampling of the folding–unfolding equilibrium slows down at higher temperatures. At the mid-point temperature $T/T_0 = 1$, the folding and unfolding times are equal, i.e. $\tau_{\mathrm{f}} = \tau_{\mathrm{u}} \approx 6.5 \times 10^5$. This folding time can be used as a bridge into real time if one somewhat arbitrarily assumes that each Markov step represents a peptide dynamics lasting 10 ps. Then 6.5×10^5 Markov steps would correspond to 6.5 μs, which is a typical folding time for β-hairpin peptides at $T_0 = 300$ K [13,14]. Our model parameters then seem to catch the temporal behavior of real β-hairpin peptides. On the other hand, our three-state system is too simple to reproduce the observed temperature dependence of the folding time $\tau_{\mathrm{f}}(T)$ for all temperatures [14]. According to the quoted experimental data τ_{f} is a convex function of T with a minimum at a critical temperature, whereas it monotonously increases with T in our model (cf. Fig. 2).

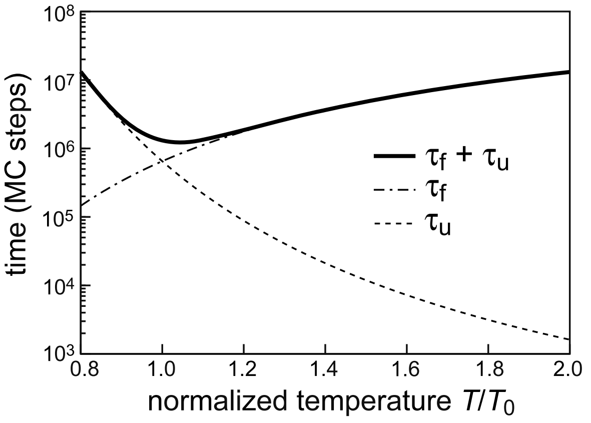

Fig. 2. Average times τ_{f} for folding (dot-dashed), τ_{u} for unfolding (dashed), and their sum $\tau_{\mathrm{f}} + \tau_{\mathrm{u}}$ (solid) as functions of the normalized temperature T/T_0.

We have applied REMC simulations [17] to our three-state Markov model. Such a REMC simulation propagates $N + 1$ copies (replicas) of the investigated system at different temperatures ($T_0 < T_1 < \cdots < T_N$). The set of trajectories of these replicas constitutes a so-called generalized ensemble. After a fixed number of simulation steps, one applies a probabilistic check whether the configuration of a replica at a higher temperature can be exchanged with the configuration of a replica at a lower temperature. If this exchange process satisfies detailed balance, the canonical ensemble at each temperature is preserved. Detailed balance is guaranteed if the exchange probability $W_{i,j}$ between the replicas i and j is calculated by the Metropolis criterion

$$W_{i,j}(X_i \rightleftarrows X_j) = \min\{1, \exp([\beta_i - \beta_j] \cdot [U(X_i) - U(X_j)])\}. \tag{3}$$

Here, $U(X_i)$ denotes the energy U of state $X \in \{\mathfrak{f}, \mathfrak{t}, \mathfrak{u}\}$ of replica i and $\beta_i = 1/k_{\mathrm{B}}T_i$.

In the time span between exchanges, each replica has to follow the pathways dictated by Fig. 1. But whenever an exchange attempt happened to be successful, states can appear in the trajectory at T_i which are not linked by a Markov step with their predecessor state. For instance, exchange can put the state $\mathfrak{u}$ directly after $\mathfrak{f}$ without setting a transition state $\mathfrak{t}$ in between. Thus, the trajectories of the replicas are characterized by the temperatures T_i and by occasional exchanges of configurations. For this reason we will call such trajectories "configurational exchange" (CE) replicas.

There is an equivalent though different point of view according to which replicas exchange temperatures instead of configurations and corresponding trajectories are exclusively composed of state sequences following existing pathways in Fig. 1. We call such trajectories "temperature exchange" (TE) replicas. The CE and TE replicas are thus characterized either by discontinuities in state (i.e. configuration) space (CE) or in temperature (i.e. momentum) space (TE). As we will see, each of these two viewpoints should be considered when discussing the convergence behavior of replica exchange sampling.

As stated in our introductory remarks, free energy differences are quantities of interest and their convergence behavior is a matter of concern. For REMC simulations of our three-state model, the corresponding quantity is the time dependent free energy difference

$$\Delta F(t) = k_{\mathrm{B}}T_0 \ln[p_{\mathfrak{f}}(t)/p_{\mathfrak{u}}(t)] \tag{4}$$

between the states $\mathfrak{u}$ and $\mathfrak{f}$ calculated from the CE replica at temperature T_0. $\Delta F(t)$ is given in terms of the relative frequencies $p_{\mathfrak{f}}(t)$ and $p_{\mathfrak{u}}(t)$ at which the states $\mathfrak{f}$ and $\mathfrak{u}$ occurred during the simulation time span $[0, t]$. For $\Delta F(t)$ the discussion of convergence is simple because its long-time limit vanishes by construction. In simulations of more complex systems the desired free energies are unknown, of course.

Nevertheless, even for such cases one can define observables with known long-time limits. An example is the ratio $q(t)$ of folding and unfolding events occurring in the generalized ensemble during the time span $[0, t]$. The long-time limit of $q(t)$ is obviously one, independently of the specific system studied. If $n_\mathfrak{f}(t')$ denotes the total number of folded states observed in the generalized ensemble at time t', the ratio $q(t)$ is given by

$$q(t) = \frac{\sum_{t'=1}^{t} \max[0, n_\mathfrak{f}(t') - n_\mathfrak{f}(t'-1)]}{\sum_{t'=1}^{t} \max[0, n_\mathfrak{f}(t'-1) - n_\mathfrak{f}(t')] + \epsilon}, \tag{5}$$

with $0 < \epsilon \ll 1$ guaranteeing that $q(t)$ is always defined. The ratio $q(t)$ can be seen as a measure for the sampling quality of the folding–unfolding equilibrium of the generalized ensemble. Therefore, one can expect that the convergence of $\Delta F(t)$ (for the CE replica at T_0) requires the convergence of $q(t)$ (in the generalized ensemble). Note that the simple mixing of existing states $\mathfrak{f}$ and $\mathfrak{u}$ among the CE replicas, due to the exchange process, does not change the composition of the generalized ensemble. Instead, transitions within the TE replicas will be necessary for the convergence of $q(t)$ and, thus, of $\Delta F(t)$.

To study the convergence of $q(t)$ and $\Delta F(t)$, we have carried out several REMC simulations of our three-state model differing from each other with respect to the initial conditions. Independently of the chosen initial conditions, all these simulations showed the same type of general behavior. Therefore, we present the results of a typical simulation. In this simulation the first five CE replicas ($T_0 < \cdots < T_4$) started at state $\mathfrak{f}$ and the remaining five at $\mathfrak{u}$.

The number of 10 replicas followed from the requirements that (i) a temperature range from T_0 up to $2T_0$ should be covered (which is a typical range for REMD simulations with $T_0 = 300$ K [9,10]) and that (ii) the upward exchange probability $W_{i,i+1}(\mathfrak{f}_i \rightleftarrows \mathfrak{u}_{i+1})$ for a folded state at T_i with an unfolded state at T_{i+1} should be $1/e$. By Eq. (3), the requirement (ii) leads to the recursive definition $T_{i+1} = E_\mathfrak{u} T_i / (E_\mathfrak{u} - k_B T_i)$ of a temperature ladder with the property that $T_9 = 2T_0$. Note that, by Eq. (3), the downward exchange probability $W_{i,i+1}(\mathfrak{u}_i \rightleftarrows \mathfrak{f}_{i+1})$ is 1. In the REMC simulation, an exchange was attempted every second MC step as described by Sugita and Okamoto [18].

Fig. 3a shows the total number of folded states $n_\mathfrak{f}$ in the generalized ensemble as a function of the simulation time. Immediately after the start of the REMC simulation, $n_\mathfrak{f}$ decreases from 5 to 3 and reaches 1 after about 10^5 time steps. Thus, 4 unfolding events occurred in this initial period of the REMC simulation. Subsequently, $n_\mathfrak{f}$ is seen to fluctuate around the value one by occasional folding and unfolding events. The temporal average of $n_\mathfrak{f}$ will thus approximate the expectation value $\sum_i P_\mathfrak{f}(T_i) = 0.89$ increasingly better. Altogether, 50 folding and unfolding events were counted within the simulation time of 5×10^6 steps (on average one expects $5 \times 10^6 \sum_i 2/[\tau_\mathfrak{f}(T_i) + \tau_\mathfrak{u}(T_i)] = 40$ events for our REMC simulation). For a conventional MC (CMC) simulation at the temperature T_0 one expects on average one folding or unfolding event every 6.5×10^5 time steps (cf. the discussion of Fig. 2). Thus, the observation of 77 such events would be expected in a CMC simulation at T_0, if this simulation takes the same computational effort ($10 \times 5 \times 10^6$ MC steps) as the REMC simulation. Therefore, in the given case the sampling provided by REMC is actually worse than that provided by a CMC simulation.

The time evolution of the ratio $q(t)$ is depicted in Fig. 3b. Apparently, the convergence of $q(t)$ is satisfactory after 5×10^6 time steps. Thus, the sampling of the folding–unfolding equilibrium in the generalized ensemble seems to be ergodic, and one expects convergence also for the free energy difference $\Delta F(t)$ at T_0. In fact, Fig. 3c demonstrates that $\Delta F(t)$ has converged excellently at the end of the simulation.

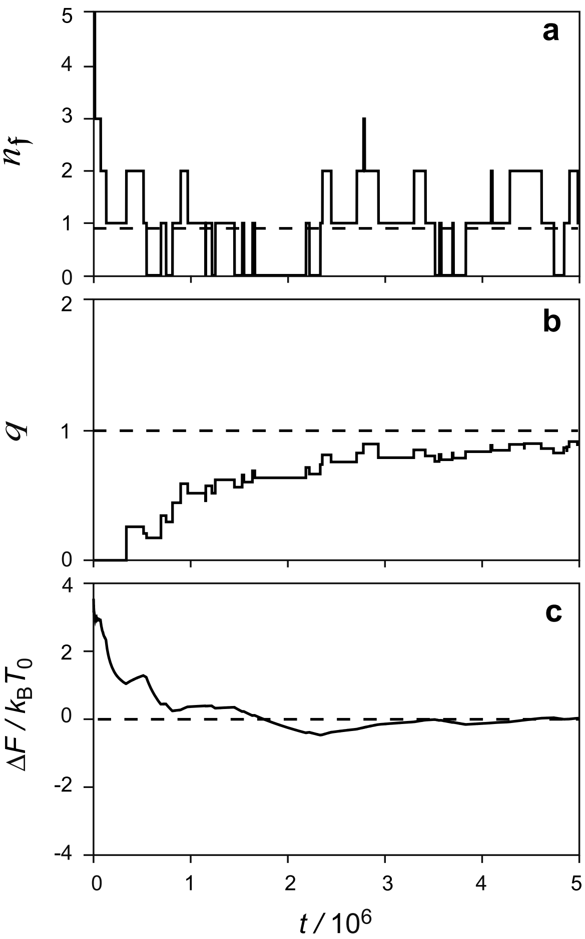

Fig. 3. (a) Number of folded states $n_\mathfrak{f}$, (b) ratio q, and (c) free energy difference ΔF as functions of the simulation time t. The dashed lines indicate the respective expectation values. See the text for a discussion.

Recalling the above critique concerning the efficiency of REMC sampling one now may ask as to whether the noted convergence of ΔF can be equivalently achieved at a smaller computational effort using a CMC simulation. Therefore we have calculated the average number of MC steps required to determine ΔF with an error smaller than one $k_B T_0$. From two sets of 100 REMC and 100 conventional MC simulations, respectively, we found average durations of about 950×10^3 steps for REMC and of about 5000×10^3 steps for the conventional one. However, since REMC employs 10 replicas a CMC simulation is by a factor of about 1.9 more efficient than a REMC simulation. This measured factor closely reproduces the corresponding expectation value which is obtained by dividing the number of folding and unfolding events expected for a CMC simulation (77) by the number (40) expected for REMC. Thus, the convergence of ΔF is directly determined by the number of folding/unfolding events observed in the generalized ensemble.

The latter statement follows from the plausible assumption that the average time which is needed by a TE replica to visit all temperatures is much shorter than the timescale on which the number $n_\mathfrak{f}(t)$ of folded states of the generalized ensemble changes. Under this condition, which we call the "mixing condition", a change of $n_\mathfrak{f}(t)$ affects all CE replicas before $n_\mathfrak{f}(t)$ changes again. If the mixing condition applies to a given RE simulation (as one can usually assume for β-hairpin folding–unfolding), the discussion of the RE efficiency becomes quite simple. Then one solely has to compare the number of folding–unfolding events expected for the generalized ensemble in a RE simulation with that expected for a CMC simulation. These expectation values can be easily calculated from the temperature dependence of the folding–unfolding time $\tau_{\mathrm{f}} + \tau_{\mathrm{u}}$ displayed in Fig. 2.

If the mixing condition applies, the dependence of the RE efficiency on the chosen model parameters is easily identified. One might ask, for instance, as to how a larger number of CE replicas covering the temperature range $[T_0, T_N]$ will affect the RE efficiency. Upon inspecting Fig. 2 one predicts a negligible effect (if the mixing condition applies also to the larger number of replicas and if the temperatures of the CE replicas are analogously distributed). For example, if we add nine temperatures $(T_i + T_{i+1})/2$ to the 10 existing ones, we expect $5 \times 10^6 \times 10/19 \sum_{i=0}^{18} 2/[\tau_{\mathrm{f}}(T_i) + \tau_{\mathrm{u}}(T_i)] = 40$ folding and unfolding events (i.e. 20 folding–unfolding events), which is (up to a difference of 0.06) the same number as the one obtained above for 10 replicas.

By the same type of reasoning one can show that the RE efficiency depends on the location of the target temperature and of the RE temperature range relative to a certain reference temperature T_M, at which the temperature dependent folding–unfolding time $\tau_{\mathrm{f}} + \tau_{\mathrm{u}}$ assumes its minimum [the minimum shown in Fig. 2 is located at $T_M = 18T_0/(18 - \ln 2)$]. There are three cases: the target temperature can be (i) smaller, (ii) equal, or (iii) larger than T_M. For the cases (i) and (iii) RE guarantees a more efficient sampling if the temperature T_N of the CE replica $N+1$ is chosen just equal to T_M. In the case (iii) this choice is quite unusual because then T_N is smaller than the target temperature ("cool replica sampling"). In the case (ii) however, which is closely matched by our example ($T_0 \approx T_M$), an efficiency reduction cannot be avoided, because the folding–unfolding times become larger both towards higher and lower temperatures, i.e. the fastest sampling is achieved by CMC at T_M. Unfortunately, the temperature T_M is generally unknown so that an optimal set-up of an RE simulation is hard to guess. Thus, by implicitly assuming T_M to be much larger than the target temperature, one usually chooses the conventional "hot replica sampling" of case (i).

Despite the simplicity of our three-state model the limited space of a letter prevents an exhaustive discussion of the parameter space. For instance, one could discuss a manifold of different models by changing the energies and entropies of the states and, thereby, aim at other systems than just hairpins. For example, consider a model in which all three states have the same entropy, the states $\mathfrak{u}$ and $\mathfrak{f}$ have identically low energies, and the transition state $\mathfrak{t}$ has a much higher energy. In such a purely "enthalpic" case one finds that $T_M \to \infty$. Therefore, the conventional RE set-up is always more efficient than CMC (if the mixing condition applies). Note, however, that with many replicas, the mixing condition can become invalid if the energy barriers measure only a few kcal/mol. As argued in Ref. [19], in this case RE can become less efficient than CMC.

Note that Nymeyer discussed the efficiency of RE in a most recent publication [21], which strongly supports the above analysis. Both analyses require that the mixing condition applies and that the generalized ensemble samples the equilibrium. Nymeyer's analytical arguments additionally rest on the assumption that the number of replicas is large. In contrast, our arguments preferentially apply to small numbers of replicas, because in this case the key mixing condition has a wider range of validity.

For our simulation, which covers a time of 5×10^6 MC steps, the conditions of mixing and equilibrium are obviously met (cf. Fig. 3). The 5×10^6 MC steps approximately correspond to a time span of 50 μs in a real-time picture. This time span is by at least three orders of magnitude larger than those REMD simulation times, which have been spent to describe the folding–unfolding equilibria of β-hairpin peptides in solution [9–11]. In these REMD simulations, the generalized ensemble will be initially far away from equilibrium. The necessity of an initial relaxation towards equilibrium likewise applies to our REMC approach. Therefore, we can address with our simulations the additional question to what extent short-time REMD simulations can show convergence towards equilibrium. We will now look at this issue by scrutinizing the first 10^4 REMC steps (approximately modeling 100 ns of REMD).

Fig. 4a shows the time evolution of $n_{\mathfrak{f}}$ during these first 10^4 MC steps. Here, the initial decay from five to three folded states occurring within the first 500 time steps is resolved. For the following 9500 time steps, neither unfolding nor folding events were observed. Thus, apart from a fast initial relaxation towards the expectation value of 0.89, no further relaxation processes happened to occur. The next unfolding event in the generalized ensemble occurred much later, i.e. after about 10^5 MC steps corresponding to 1 μs (cf. Fig. 3a).

Fig. 4b shows the associated time evolution of ΔF. Since the unfolded state $\mathfrak{u}$ did not appear in the CE replica at T_0 within the first 500 simulation steps, ΔF is not defined during this initial period. After about 2000 time steps, ΔF becomes stationary at about $3k_{\mathrm{B}}T_0$. After 10^4 time steps, more than 450 transitions between the states $\mathfrak{f}$ and $\mathfrak{u}$ were counted in the CE replica at T_0 due to the configurational exchange. Nevertheless, convergence is by no means reached because ΔF would then have to be zero (cf. Table 1) as indicated by the dashed line in Fig. 4b. Thus, after 10^4 steps the simulation is still far away from a satisfactory sampling of the folding–unfolding equilibrium ensemble.

In a usual simulation, in which the expectation value of ΔF is unknown, the stationarity observed after a fast equilibration process and the frequent changes between $\mathfrak{f}$ and $\mathfrak{u}$ in the CE replica at T_0 could lead to the erroneous assumption that ΔF is already converged. We call such an observed stationarity "pseudo-convergence". However, the erroneous interpretation of pseudo-convergence can be avoided by inspecting the ratio $q(t)$ or a related observable whose expectation value is *a priori* known. In our case, this ratio is zero instead of one during the first 10^4 simulation steps indicating the absence of real convergence.

On the other hand, one cannot be seduced to assume convergence of REMD simulations for peptide folding–unfolding equilib-

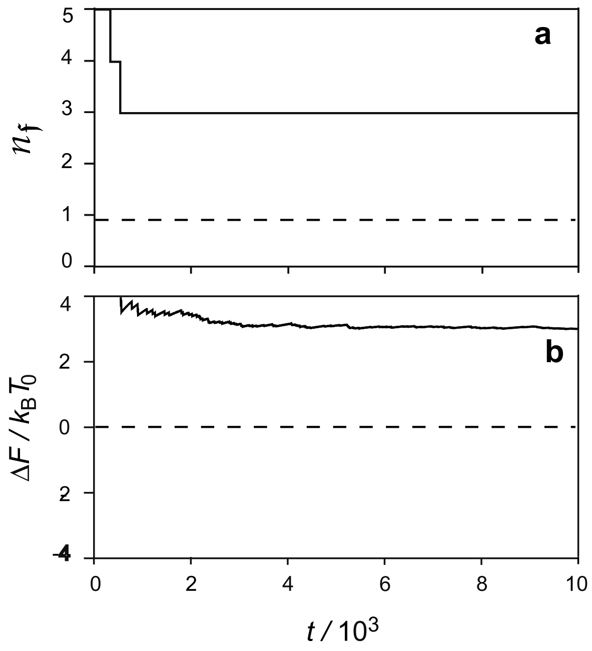

Fig. 4. Initial phase of the REMC simulation characterized by Fig. 3. Time evolutions of (a) $n_{\mathfrak{f}}$ and (b) ΔF. See the text and the caption to Fig. 3 for further information.

ria, if one compares in advance experimental folding times with durations of the applied simulations. Whenever the folding time τ_f has a given large value (e.g. μs) for all temperatures covered by the replica exchange setting, one has to take care that the simulation times are at least of the same order of magnitude as τ_f for convergence of $\Delta F(t)$, independently of how the efficiency of replica exchange compares with a conventional simulation.

Summarizing, we would like to stress the most important results of our analysis: (i) the replica exchange technique can offer a reduced sampling efficiency for peptide folding–unfolding equilibria; (ii) a sufficient sampling of the folding–unfolding equilibrium of a β-hairpin can hardly be reached with simulation times in the range of ns [9–11]; (iii) replica exchange bears the danger of misinterpreting certain stationarities as convergence which can be avoided by the tracking and counting of transitions within the TE replicas and the observation of recurrent states within these replicas.

Concerning the efficiency reduction that can be caused by replica exchange the key effect seems to be an anti-Arrhenius folding behavior, which typically occurs if the energy of the low-entropy transition state is below the energy of the high-entropy unfolded state [16]. In the case of anti-Arrhenius folding behavior (and Arrhenius like unfolding behavior), there is a specific temperature T_M for which the combined folding–unfolding time $\tau_f + \tau_u$ is minimal. An efficiency reduction by the usage of replica exchange is guaranteed if the temperature of interest is close to T_M.

Although our discussion was based on a model mimicking the folding–unfolding behavior of β-hairpin peptides, the phenomenon of pseudo-convergence is more general. Pseudo-convergence may occur in replica exchange whenever the simulation time is longer than the time between exchange trials (≈1 ps) but shorter than the timescale, on which the TE replicas switch between the relevant states (conformations). More frequent exchange trials solely accelerate the appearance of pseudo-convergence. Thus, pseudo-convergence is expected to be a widespread phenomenon in short REMD simulations. It bears the danger of wrong estimates of ensemble averages and may falsely lead to the impression of a high efficiency of replica exchange sampling.

Of course, the alleged merits of the replica exchange method have already been scrutinized by various other authors. For example, Zheng et al. [16] recently showed for a so-called kinetic network RE model that the efficiency of the replica exchange approach breaks down, if the corresponding temperatures are too far in the anti-Arrhenius temperature range. In the context of enhanced barrier crossing, Zuckerman and Lyman expressed doubt whether, specifically for biomolecules, the commonly expected gain in sampling speed at the target temperature T_0 can overcompensate the additional effort of simulating a large number of replicas [19]. Furthermore, Rhee and Pande [20] argued that short REMD simulations generally cannot yield correct ensemble averages if folding times are much larger than the applied simulation times. The sample system constructed by us now proves the correctness of their arguments.

Acknowledgement

This work was supported by the Deutsche Forschungsgemeinschaft (SFB 533/C1 and SFB 749/C4).

References

[1] U.H.E. Hansmann, Chem. Phys. Lett. 281 (1997) 140.
[2] K.Y. Sanbonmatsu, A.E. García, Proteins 46 (2002) 225.
[3] F. Rao, A. Caflisch, J. Chem. Phys. 119 (2003) 4035.
[4] J.W. Pitera, W. Swope, Proc. Natl. Acad. Sci. USA 100 (2003) 7587.
[5] M. Cecchini, F. Rao, M. Seeber, A. Caflisch, J. Chem. Phys. 121 (2004) 10748.
[6] G.S. Jas, K. Kuczera, Biophys. J. 87 (2004) 3786.
[7] A. Villa, G. Stock, J. Chem. Theory Comput. 2 (2006) 1228.
[8] A. Villa, E. Widjajakusuma, G. Stock, J. Phys. Chem. 112 (2008) 134.
[9] R. Zhou, B.J. Berne, R. Germain, Proc. Natl. Acad. Sci. USA 98 (2001) 14931.
[10] W.Y. Yang, J.W. Pitera, W.C. Swope, M. Gruebele, J. Mol. Biol. 336 (2004) 241.
[11] P.H. Nguyen, G. Stock, E. Mittag, C.-K. Hu, M.A. Li, Proteins 61 (2005) 795.
[12] T.E. Schrader, et al., Proc. Natl. Acad. Sci. USA 104 (2007) 15729.
[13] C.D. Snow, E.J. Sorin, Y.M. Rhee, V.S. Pande, Annu. Rev. Biophys. Biomol. Struct. 34 (2005) 43.
[14] D. Du, Y. Zhu, C.-Y. Huang, F. Gai, Proc. Natl. Acad. Sci. USA 101 (2004) 15915.
[15] M. Karplus, J. Phys. Chem. 104 (2000) 11.
[16] W. Zheng, M. Andrec, E. Gallicchio, R.M. Levy, Proc. Natl. Acad. Sci. USA 104 (2007) 15340.
[17] K. Hukushima, K. Nemoto, J. Phys. Soc. Jpn. 65 (1996) 1604.
[18] Y. Sugita, Y. Okamoto, Chem. Phys. Lett. 314 (1999) 141.
[19] D.M. Zuckerman, E. Lyman, J. Chem. Theory Comput. 2 (2006) 1200.
[20] Y.M. Rhee, V.S. Pande, Biophys. J. 84 (2003) 775.
[21] H. Nymeyer, J. Chem. Theory Comput. 4 (2008) 626.

3 Optimierte Replica Exchange Protokolle

Im vorangegangenen Kapitel wurde ein System untersucht, dessen Faltungszeiten sich durch Temperaturerhöhung verlangsamt. Verantwortlich für dieses sogenannte anti-Arrhenius Verhalten ist die freie Energiebarriere zwischen dem gefalteten und dem ungefalteten Zustand, die ausgehend vom ungefalteten Zustand rein entropischer Natur ist. Für Systeme, deren Dynamik durch enthalpische Barrieren dominiert sind, ist die *Replica Exchange* Methode jedoch gut geeignet, um die Abtasteffizienz einer Simulation zu erhöhen. Das Maß der Effizienzsteigerung hängt wesentlich von der Paramtereinstellung der *Replica Exchange* Methode ab.

3.1 Optimale Temperaturleitern

Im nachfolgenden Abdruck[1] des Artikels

> Robert Denschlag, Martin Lingenheil, Paul Tavan:
> „Optimal temperature ladders in replica exchange simulations“
> *Chem. Phys. Lett.* **473**, 193-195 (2009),

den ich zusammen mit Martin Lingenheil und Paul Tavan verfasst habe, wird eine Formel für eine optimale Temperaturleiter abgeleitet, die die Diffusionsgeschwindigkeit der Replikate im Temperaturraum maximiert, wobei eine konstante Wärmekapazität und die Verwendung des deterministischen „even-odd“(DEO) Austauschalgorithmus zugrunde gelegt wird.

---

[1] Mit freundlicher Genehmigung des Elsevier Verlags (Lizenznummer: 2415950020121).

Chemical Physics Letters 473 (2009) 193–195

Contents lists available at ScienceDirect

Chemical Physics Letters

journal homepage: www.elsevier.com/locate/cplett

Optimal temperature ladders in replica exchange simulations

Robert Denschlag, Martin Lingenheil, Paul Tavan *

Lehrstuhl für Biomolekulare Optik, Ludwig-Maximilians-Universität, Oettingenstr. 67, 80538 München, Germany

ARTICLE INFO

Article history:
Received 19 January 2009
In final form 20 March 2009
Available online 25 March 2009

ABSTRACT

In replica exchange simulations, a temperature ladder with N rungs spans a given temperature interval. Considering systems with heat capacities independent of the temperature, here we address the question of how large N should be chosen for an optimally fast diffusion of the replicas through the temperature space. Using a simple example we show that choosing average acceptance probabilities of about 45% and computing N accordingly maximizes the round trip rates r across the given temperature range. This result differs from previous analyses which suggested smaller average acceptance probabilities of about 23%. We show that the latter choice maximizes the ratio r/N instead of r.

© 2009 Published by Elsevier B.V.

1. Introduction

At given computer resources, the benefit of replica exchange [1–3] (RE) simulations crucially depends on the choice of certain parameters. Having chosen a temperature range $[T_{\min}, T_{\max}]$, which should be covered by the RE simulation, the optimal form of the temperature ladder $(T_1 = T_{\min}, T_2, \ldots, T_N = T_{\max})$ is an important issue [4–10]. Aiming at a minimal average round trip time of the replicas in the temperature space and assuming a constant heat capacity C, which should approximately apply to explicit solvent simulations [11], Nadler and Hansmann [9] have derived a formula

$$N \approx 1 + 0.594\sqrt{C}\ln(T_{\max}/T_{\min}) \tag{1}$$

for the number N of rungs in the temperature ladder. In Eq. (1) the (extensive) heat capacity C is given in units of the Boltzmann constant k_B and refers to the potential energy part of the total energy. As suggested by Okamoto et al. [12], from N one can determine the temperature rungs $T_i, i = 1, \ldots, N$, in the ladder by

$$T_i = T_{\min}(T_{\max}/T_{\min})^{(i-1)/(N-1)}. \tag{2}$$

This choice is generally expected [3] to provide equal exchange probabilities $p_{\mathrm{acc}}(T_i, T_{i+1}) = p_{\mathrm{acc}}(N)$ along the N-rung ladder.

Defining the function

$$\alpha(N) \equiv (T_{\max}/T_{\min})^{1/(N-1)}, \tag{3}$$

one immediately finds that the temperature rungs are given by the recursion

$$T_{i+1} = T_i\alpha(N). \tag{4}$$

Thus, for a given N, the ratio T_{i+1}/T_i is the constant $\alpha(N)$. For such a ladder and normally distributed potential energies, which is, along with a constant heat capacity, typical for explicit solvent simulation systems, the average acceptance probabilities are very well approximated [6] by

$$p_{\mathrm{acc}}(N) = \mathrm{erfc}\left[\sqrt{C}\,\frac{\alpha(N)-1}{\alpha(N)+1}\right], \tag{5}$$

where $\mathrm{erfc}(x') = 2/\sqrt{\pi}\int_{x'}^{\infty}\exp(-x^2)\mathrm{d}x$ is the complementary error function.

In summary, for a ladder spanning the temperature range $[T_{\min}, T_{\max}]$ by the exponential spacing law Eq. (2), the temperature rungs T_i are uniquely given by N. Assuming a constant heat capacity and normally distributed potential energies, such a ladder then actually provides equal average acceptance probabilities [Eq. (5)]. Therefore, temperature ladders obeying Eqs. (2) and (5) are uniquely specified by choosing either a certain number N of rungs or a certain average acceptance probability p_{acc}.

2. Methods and simulation set-up

To check whether the formula given in Eq. (1) and suggested by Nadler and Hansmann [9] actually yields RE temperature ladders with minimal round trip times, we have designed simple test systems suited for computationally inexpensive RE Monte Carlo (REMC) simulations. The systems consist of d independent one-dimensional and harmonic oscillators in the canonical ensemble (we have chosen the same potential $E = x^2$ for all oscillators). At each REMC step the coordinates of all d oscillators in a replica are randomly drawn from the associated normal distributions, the total energy E_i of the system at temperature T_i is calculated, and an exchange of systems at neighboring [3] temperatures is attempted with the Metropolis probability [13] $p(i, i+1) = \min\{1, \exp[(1/k_B T_{i+1} - 1/k_B T_i)(E_{i+1} - E_i)]\}$. We employed the standard exchange scheme [1], which alternately attempts exchanges between 'even' (T_{2i}, T_{2i+1}) and 'odd' (T_{2i-1}, T_{2i}) replica pairs. Below

---

* Corresponding author. Fax: +49 89 2180 9220.
E-mail address: tavan@physik.uni-muenchen.de (P. Tavan).

0009-2614/$ - see front matter © 2009 Published by Elsevier B.V.
doi:10.1016/j.cplett.2009.03.053

we call this RE scheme, which combines the standard exchange with the standard Metropolis criterion, the standard RE set-up.

Note the important fact that the heat capacity of our test system is independent of the temperature and is given by $C = d/2$. Therefore, it matches the conditions assumed in the derivation of Eq. (1). Note furthermore that the force constants of the harmonic oscillator potentials are of no concern because the Metropolis probability solely depends on the overlaps of the energy distributions.

First we consider the case $d = 100$. As extremal temperatures we choose $T_{\min} = 300$ K and $T_{\max} = 800$ K. With these parameters, Eqs. (1), (2), and (5) yield $N = 5$, the temperature ladder (300, 383.4, 389.9, 626.0, 800), and the average acceptance probability $p_{\mathrm{acc}} \approx 22\%$, respectively. Previously also Kone and Kofke [6] and Rathore et al. [5] have suggested an acceptance probability of about 23% to be optimal. Thus, choosing the number of rungs through Eq. (1) seems to yield a reasonable acceptance probability.

The question as to whether the above choice actually entails minimal round trip times in REMC simulations can be addressed by comparing the set-up outlined above with alternatives defined by different choices of N. We tested ladders with $N \in \{3, 4, \ldots, 9, 10, 12, \ldots, 18, 20\}$ each spanning the same temperature range [300 K, 800 K]. Every associated REMC simulation covered $S = 500\,000$ MC steps. From each of these REMC simulations we determined the number of round trips $M(N)$. Here, a round trip was counted whenever a selected replica that started at $T_{\min}$ subsequently reached $T_{\max}$ and eventually returned to $T_{\min}$. Considering instead of the round trip time $\tau(N)$ of a replica its inverse, the round trip rate $r(N) \equiv M(N)/S$, we asked which acceptance probability $p_{\mathrm{acc}}(N)$ [cf. Eq. (5)] belongs to the maximal rate $r(N)$ measured in any of our simulations.

3. Results

Fig. 1 shows the measured round trip rate r as a function $r(p_{\mathrm{acc}})$ of the average acceptance probability p_{acc}. Two data points are additionally marked by the numbers of rungs in the associated ladders ($N = 5, N = 7$). According to the graph the round trip rate r is maximal at $p_{\mathrm{acc}} \approx 0.42$ belonging to the $N = 7$ rung ladder. This result differs from the expectation voiced above that r should be maximal at $p_{\mathrm{acc}} \approx 0.22$ or $N = 5$, respectively.

This surprising result raises the question why Eq. (1) yields a prediction for the optimal N (or p_{acc}) differing from the measured one. Nadler and Hansmann [9] started the derivation of Eq. (1) by assuming for the round trip rate the plausible relation $r(p_{\mathrm{acc}}, N) = k p_{\mathrm{acc}}/N(N-1)$ with a certain constant $k > 0$. Using this assumption, one predicts that the rate $r(0.22, 5) = k0.22/5(5-1) \approx 0.011k$ should be larger than the rate $r(0.42, 7) = k0.42/7(7-1) \approx 0.010k$, which is clearly at variance with the results of our simulation. Thus, the quoted relation does not yield the correct round trip rate $r(p_{\mathrm{acc}})$ and, correspondingly, the choice of the ladder size N through Eq. (1) does not maximize r, if the standard RE set-up is used.

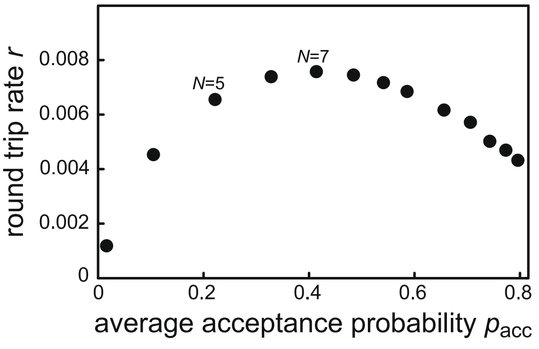

Fig. 1. Measured round trip rates r as a function of the average acceptance probability p_{acc}.

To understand how r depends on p_{acc} we introduce the average (and relative) temperature move

$$\kappa(T_i, T_{i+1}) \equiv p_{\mathrm{acc}}(T_i, T_{i+1}) \frac{T_{i+1} - T_i}{T_i} \tag{6}$$

of a replica per exchange trial (here one MC step). κ measures the average velocity of the replicas in a properly scaled temperature space. This definition is motivated by our assumption that the average replica velocity κ should be proportional to the round trip rate, i.e. that $\kappa = fr$ with a constant $f > 0$. Thus, we expect the largest round trip rates r for the largest velocities κ.

Using Eq. (4) and inverting Eq. (5) one finds for the average replica velocity

$$\kappa(p_{\mathrm{acc}}) = p_{\mathrm{acc}} \frac{2\operatorname{erfc}^{-1}(p_{\mathrm{acc}})}{\sqrt{C} - \operatorname{erfc}^{-1}(p_{\mathrm{acc}})}, \tag{7}$$

where erfc^{-1} denotes the inverse of the complementary error function. Thus, in contrast to the impression evoked by the definition in Eq. (6), κ is a constant within a given temperature ladder (because p_{acc} is a constant across each ladder).

The lines in Fig. 2 are the graphs of the function $\kappa(p_{\mathrm{acc}})$ given by Eq. (7) for systems with small and large heat capacities $C = d/2$. For $d = 100$ (solid) the velocity κ becomes maximal at $p_{\mathrm{acc}} \approx 0.42$ (i.e. at $N = 7$) and for $d = 1000$ (dashed) at $p_{\mathrm{acc}} \approx 0.44$ (i.e. at $N = 22$). Fig. 2 additionally displays scaled round trip rates fr measured for the small ($f = 9.71$) and the large system ($f = 24.6$), respectively. The good match of the scaled rates $fr(p_{\mathrm{acc}})$ (circles/squares) with the respective graphs $\kappa(p_{\mathrm{acc}})$ verifies our assumption that the average velocity $\kappa(p_{\mathrm{acc}})$ of the replicas in scaled temperature space is proportional to the round trip rate $r(p_{\mathrm{acc}})$. Note that the value of the optimal average acceptance rate, at which the round trip rate r becomes maximal, depends only weakly on the system size d.

The noted weak dependence of the optimal average acceptance probability p_{acc} on the system size $d = 2C$ can be understood by considering the limit of large systems ($C \to \infty$). Using *Mathematica* [14] we have determined the derivative $\kappa'(p_{\mathrm{acc}}) \equiv \mathrm{d}\kappa/\mathrm{d}p_{\mathrm{acc}}$ and its first order Taylor expansion $\kappa'(p_{\mathrm{acc}}) = a_0 + a_1 p_{\mathrm{acc}} + \mathcal{O}(p_{\mathrm{acc}}^2)$ at $p_{\mathrm{acc}} = 0.5$. In linear approximation κ' vanishes at $p_{\mathrm{acc}}^0 = -a_0/a_1$ which is given by

$$p_{\mathrm{acc}}^0 \approx 0.45 + g/\sqrt{C} \tag{8}$$

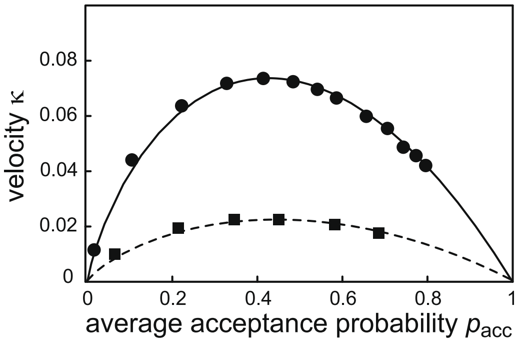

Fig. 2. Average replica velocity κ in scaled temperature space as a function of the average acceptance probability p_{acc}. The lines are graphs of $\kappa(p_{\mathrm{acc}})$ calculated from Eq. (7) for $d = 100$ (solid) and $d = 1000$ (dashed). The dots are the round trip rates r of Fig. 1 scaled by the factor $f = 9.71$. The squares are round trip rates scaled by $f = 24.6$ and resulting from REMC simulations of $d = 1000$ oscillators. Here, the rung numbers $N \in \{10, 14, 18, 22, 30, 40\}$ increase from left to right.

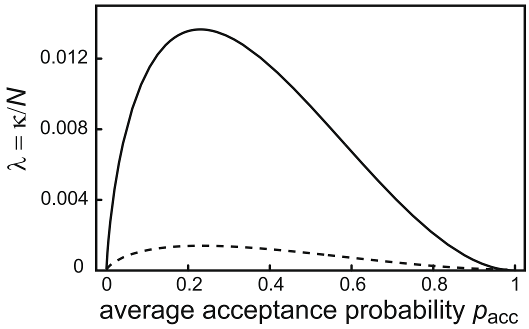

Fig. 3. $\lambda = \kappa/N$ as a function of the average acceptance probability p_{acc}. The lines are the graphs of Eq. (10) for $d = 100$ (solid) and $d = 1000$ (dashed).

with the constant g being of the order of -0.1. Thus for large systems the location p^0_{acc} of the maximum of κ approaches 0.45 from below. Note that we have also checked the limiting value 0.45 by numerically analyzing Eq. (7) for very large C.

The thus established limiting value of the optimal average acceptance probability leads to a new estimate

$$N \approx 1 + (\sqrt{C}/(2 \times 0.534) - 1/2)\ln(T_{max}/T_{min}) \tag{9}$$

for the optimal number of rungs in the associated temperature ladder. For computing Eq. (9) we have used Eq. (5), $\mathrm{erfc}^{-1}(0.45) \approx 0.534$, and $\ln[1 + 2 \times 0.534/(\sqrt{C} - 0.534)] \approx 2 \times 0.534/(\sqrt{C} - 0.534)$ for large C.

In summary, to maximize the round trip rate or minimize the round trip time, respectively, Eq. (9) has to be used instead of Eq. (1). From a practical point of view, however, instead of aiming at the maximal round trip rate, one may be content with a suboptimal rate if this choice is associated with a reduced computational effort. Instead of maximizing κ one may therefore consider the quantity

$$\lambda(p_{acc}) \equiv \kappa(p_{acc})/N(p_{acc}), \tag{10}$$

which exhibits a penalty linear in the number N of rungs. Fig. 3 shows the graphs of $\lambda(p_{acc})$ for $d = 100$ (solid line) and $d = 1000$ (dashed line). In both cases λ is maximal at $p_{acc} \approx 0.23$. Applying once again the reasoning used in the derivation of Eq. (8) one finds that the optimal p_{acc} approaches 0.234 for $C \to \infty$. This result leads to the estimate

$$N \approx 1 + (0.594\sqrt{C} - 1/2)\ln(T_{max}/T_{min}) \tag{11}$$

for the number of rungs optimizing the specific compromise $\lambda = \kappa/N$ between the round trip rate r and the number N of replicas.

Note here that Eqs. (11) and (1) become identical for large C. Thus, the number of rungs resulting from Eq. (1) effectively maximizes λ instead of κ (or, equivalently, a ladder size penalized round trip rate r/N instead of the round trip rate r). That Nadler and Hansmann [9] have effectively maximized λ instead of r can be alternatively understood by inserting the definition Eq. (6) into (10). Using subsequently Eq. (4) and the approximation $(T_{max}/T_{min})^{1/(N-1)} \approx 1 + \ln(T_{max}/T_{min})/(N-1)$, which holds for large N, one finds $\lambda \approx p_{acc}\ln(T_{max}/T_{min})/[N(N-1)]$ such that $\lambda \propto p_{acc}/[N(N-1)]$. Recall now that Nadler and Hansmann erroneously assumed a relation of this kind for the round trip rate r (i.e. for κ).

We would like to remark that our results are transferable to simulated tempering [15,16] (ST) simulations. For ST, the average acceptance probability is given by

$$p^{ST}_{acc}(N) = \mathrm{erfc}\left(\sqrt{C/2}\,\frac{\alpha(N) - 1}{\alpha(N) + 1}\right). \tag{12}$$

which is obtained from the RE expression Eq. (5) through replacing C by $C/2$ [5,17]. In the limit of large systems also $C/2$ becomes large and the optimal value of p^{ST}_{acc} is likewise at 45% or 23% depending on the optimized quantity. Similarly, the optimal N is given by Eqs. (9) or (11), respectively, through replacing C by $C/2$.

4. Summary

For simulations employing the standard RE set-up, we have derived with Eqs. (9) and (11) two formulas for the optimal sizes N of temperature ladders obeying Eqs. (2) and (5). Here, optimal means that either the round trip rate r or the compromise r/N with computational effort is maximized. We have furthermore shown that the suggestion Eq. (1) of Nadler and Hansmann [9] maximizes the compromise r/N and not r, as claimed by the authors. An optimal r is obtained with average acceptance probabilities of about 45%, whereas an optimal r/N requires values of 23% matching earlier suggestions [6,5]. As a practical consequence of our study one sees that average acceptance probabilities chosen in the range from 20% to 45% are definitely ‘good’ choices featuring, however, slightly different merits.

Acknowledgement

This work was supported by the Deutsche Forschungsgemeinschaft (SFB 533/C1 and SFB 749/C4).

References

[1] K. Hukushima, K. Nemoto, J. Phys. Soc. Jpn. 65 (1996) 1604.
[2] U.H.E. Hansmann, Chem. Phys. Lett. 281 (1997) 140.
[3] Y. Sugita, Y. Okamoto, Chem. Phys. Lett. 314 (1999) 141.
[4] C. Predescu, M. Predescu, C.V. Ciobanu, J. Chem. Phys. 120 (2004) 4119.
[5] N. Rathore, M. Chopra, J.J. de Pablo, J. Chem. Phys. 122 (2005) 024111.
[6] A. Kone, D.A. Kofke, J. Chem. Phys. 122 (2005) 206101.
[7] S. Trebst, M. Troyer, U.H.E. Hansmann, J. Chem. Phys. 124 (2006) 174903.
[8] W. Nadler, U.H.E. Hansmann, Phys. Rev. E 75 (2007) 026109.
[9] W. Nadler, U.H.E. Hansmann, J. Phys. Chem. B 112 (2008) 10386.
[10] W. Nadler, J.H. Meinke, U.H.E. Hansmann, Phys. Rev. E 78 (2008) 061905.
[11] B. Paschek, H. Nymeyer, A.E. Garcia, J. Struct. Biol. 157 (2007) 524.
[12] Y. Okamoto, M. Fukugita, T. Nakazawa, H. Kawai, Protein Eng. 4 (1991) 639.
[13] N. Metropolis, A.W. Rosenbluth, M.N. Rosenbluth, A.H. Teller, E. Teller, J. Chem. Phys. 21 (1953) 1087.
[14] Wolfram Research, Inc., Mathematica Version 5.1, Champaign, IL, 2004.
[15] A.P. Lyubartsev, A.A. Martinovski, S.V. Shevkunov, P.N. Vorontsov-Velyaminov, J. Chem. Phys. 96 (1992) 1776.
[16] E. Marinari, G. Parisi, Europhys. Lett. 19 (1992) 451.
[17] C. Zhang, J. Ma, J. Chem. Phys. 129 (2008) 134112.

3.2 Vergleich verschiedener Austauschschemata

Die im vorangegangenen Artikel entwickelte Regel für die optimale Wahl der Temperaturen setzte die Verwendung des DEO Austauschalgorithmus voraus. Der folgende Abschnitt ist ein Abdruck[1] des Artikels

> Martin Lingenheil, Robert Denschlag, Paul Tavan:
> „Efficiency of exchange schemes in replica exchange“
> *Chem. Phys. Lett.* **478**, 80-84 (2009),

in dem dieses Austauschschema mit anderen in der Literatur vorgeschlagenen Austauschalgorithmen verglichen wird. Es zeigt sich, dass unter den untersuchten Verfahren DEO die höchsten Diffusionsgeschwindigkeit der Replikate im Temperaturraum erzielt. Darüber hinaus wird die Diffusionskonstante D_{DEO} für das DEO Schema analytisch abgeleitet, wodurch auch formal gezeigt wird, dass der DEO Austauschalgorithmus eine beschleunigte Zufallsbewegung der Replikate auf der Temperaturleiter bewirkt.

---

[1] Mit freundlicher Genehmigung des Elsevier Verlags (Lizenznummer: 2415950243448).

Chemical Physics Letters 478 (2009) 80–84

Contents lists available at ScienceDirect

Chemical Physics Letters

journal homepage: www.elsevier.com/locate/cplett

Efficiency of exchange schemes in replica exchange

Martin Lingenheil, Robert Denschlag, Gerald Mathias, Paul Tavan *

Lehrstuhl für BioMolekulare Optik, Ludwig-Maximilians-Universität, Oettingenstr. 67, 80538 München, Germany

ARTICLE INFO

Article history:
Received 1 April 2009
In final form 9 July 2009
Available online 12 July 2009

ABSTRACT

In replica exchange simulations a fast diffusion of the replicas through the temperature space maximizes the efficiency of the statistical sampling. Here, we compare the diffusion speed as measured by the round trip rates for four exchange algorithms. We find different efficiency profiles with optimal average acceptance probabilities ranging from 8% to 41%. The best performance is determined by benchmark simulations for the most widely used algorithm, which alternately tries to exchange all even and all odd replica pairs. By analytical mathematics we show that the excellent performance of this exchange scheme is due to the high diffusivity of the underlying random walk.

© 2009 Elsevier B.V. All rights reserved.

1. Introduction

The replica exchange (RE) method [1–3] has become a standard approach in molecular simulation to efficiently sample the rough energy landscapes of biomolecules in solution at a target temperature T_1 (see e.g. Ref. [4]). In RE simulations, N simulation systems (replicas) are parallely propagated in time using Monte Carlo (MC) or molecular dynamics (MD) algorithms. For the standard temperature RE method in particular, the replicas $i \in \{1, \ldots, N\}$ are identical with the exception of the respective simulation temperatures T_i. At a predefined temporal spacing an exchange between two replicas i and j is attempted and is accepted with the Metropolis [5] probability

$$p_{ij} = \min\left\{1, \exp\left[(\beta_j - \beta_i)(E_j - E_i)\right]\right\}, \tag{1}$$

where E_i and E_j are the current potential energies of the replicas at the corresponding inverse temperatures $\beta_i = 1/k_B T_i$ and $\beta_j = 1/k_B T_j$, respectively. Here, k_B denotes Boltzmann's constant. The exchange probability given by Eq. (1) satisfies the detailed balance condition and therefore guarantees that the ensembles sampled by the individual replicas remain undisturbed by the exchange.

Due to the exchanges, each replica performs a random walk through the temperature space $[T_1, T_N]$. During the high temperature phases of its trajectory, a replica crosses potential energy barriers more rapidly, leading in many cases (a relevant counter example has been given in Ref. [6]) to a faster convergence, compared to a straight forward simulation, of the statistical sampling at the lower temperatures. Here it is crucial for an optimal statistical sampling at the low temperatures that the replicas cycle between low and high temperatures as frequently as possible [7–11]. As we will demonstrate below, the sizes of these round trip rates strongly depend on the detailed algorithm by which the replica pairs are selected for attempting an exchange.

A widely used exchange scheme [12–14] divides the set $\mathcal{N} \equiv \{(i, i+1) \mid i = 1, \ldots, N-1\}$ of next neighbors in the temperature ladder into the two subsets $\mathcal{E} \subset \mathcal{N}$ and $\mathcal{O} \subset \mathcal{N}$, where $\mathcal{E}$ contains all 'even' pairs $(2j, 2j+1) \in \mathcal{N}$ and $\mathcal{O}$ contains the 'odd' pairs $(2j-1, 2j) \in \mathcal{N}$. Exchanges are attempted alternatingly for the members of $\mathcal{E}$ and $\mathcal{O}$. Because of the deterministic pattern of exchange trials, we will call this method the deterministic even/odd algorithm (DEO).

We will also consider a variant of DEO which, instead of alternatingly attempting exchanges among all even and all odd replica pairs, randomly chooses with equal probability one of the subsets $\mathcal{E}$ and $\mathcal{O}$. Due to the stochastic selection of exchange sets, we call this method the stochastic even/odd algorithm (SEO). As we will show, the SEO scheme was implicitly assumed by a number of authors when theoretically deriving rules for optimal temperature ladders [7,11]. Another reason for analyzing the SEO algorithm is that an exchange scheme equivalent to SEO is the straightforward choice when implementing simulated tempering [15].

Besides DEO also other exchange schemes have been discussed in the literature. The all-pair exchange (APE) method suggested by Brenner et al. [16] considers all possible exchange pairs including non-next neighbors. Finally, the very simple random next neighbor (RNN) algorithm [16,17] chooses with equal probability at every exchange step a single pair from the set $\mathcal{N}$ of next neighbors and attempts an exchange for this pair.

Note that the DEO scheme does not permit a reverse move immediately after a successful replica swap in contrast to SEO, APE, and RNN. Therefore, it does not satisfy detailed balance and one may ask whether DEO can interfere with canonical sampling. However, Manousiouthakis and Deem [23] have shown that the equilibrium statistics, which is generated by the intermittent MD

---

* Corresponding author. Fax: +49 89 2180 9220.
E-mail address: tavan@physik.uni-muenchen.de (P. Tavan).

0009-2614/$ - see front matter © 2009 Elsevier B.V. All rights reserved.
doi:10.1016/j.cplett.2009.07.039

or MC simulation, is preserved if the sampling procedure satisfies a less strict 'balance condition'. This condition holds if each individual exchange trial satisfies local detailed balance, which is implied by the Metropolis criterion Eq. (1) for even and for odd exchanges. Thus, DEO represents a valid sampling strategy.

In this Letter we will systematically check as to how the different exchange algorithms affect the diffusion of the replicas through the temperature space. This check will provide a rule for the optimal setup of RE simulations. For this purpose we will first introduce basic notions of the RE approach and a benchmark MC system. Using the benchmark system we will then compare the round trip rates obtained with the four different exchange schemes. Because of the practical importance of the DEO algorithm, we will subsequently identify the reasons for its superior performance by analytical mathematics.

2. Theoretical basics

It is general consensus that the distances of the N rungs T_i within the temperature ladder should be chosen to yield equal average acceptance probabilities $\langle p_{i,i+1}\rangle = p_{\mathrm{acc}}$ for the exchanges between neighboring replicas i and $i+1$ [3] provided that the simulated system does not undergo a phase transition within the range of the temperature ladder [8,9]. If the system's heat capacity C is constant, which is approximately true for explicit solvent systems [18], then, following Okamoto et al. [19], the spacing law for equal average acceptance probabilities is

$$T_i = T_{\min}\cdot\alpha^{i-1}, \tag{2}$$

with the minimal temperature $T_{\min}$ and a constant ratio $\alpha = T_{i+1}/T_i$ of neighboring temperatures.

Given a certain temperature range $[T_{\min}, T_{\max}]$ to be spanned by a simulation, the choice of the number N of replicas automatically determines the temperature ratio α through

$$\alpha(N) = (T_{\max}/T_{\min})^{1/(N-1)}. \tag{3}$$

Next we assume Gaussian probability distributions

$$\rho(E_i) = \frac{1}{\sqrt{2\pi C}T_i}\exp\left[-\frac{(E_i - CT_i)^2}{2CT_i^2}\right] \tag{4}$$

for the potential energies E_i at the various temperatures T_i because these distributions are as typical for explicit solvent simulations as a constant heat capacity C. Note that, in Eq. (4), C denotes the (extensive) heat capacity in units of Boltzmann's constant k_B and refers to the potential energy part of the total energy.

With the potential energy distributions given by Eq. (4), the geometric temperature spacing by Eqs. (2) and (3), and the acceptance criterion by Eq. (1), the average acceptance probability according to Kone and Kofke [7] is

$$p_{\mathrm{acc}} = \operatorname{erfc}\left[\sqrt{C}\frac{\alpha(N)-1}{\alpha(N)+1}\right], \tag{5}$$

where $\operatorname{erfc}(x') = 2/\sqrt{\pi}\int_{x'}^{\infty}\exp(-x^2)\mathrm{d}x$ is the complementary error function.

For a predefined temperature range $[T_{\min}, T_{\max}]$, Nadler and Hansmann [11] recently derived a formula to optimize an RE simulation setup with respect to the round trip rate r, i.e., to the average number of round trips a replica performs per unit time. In this optimal ladder spanning the interval $[T_{\min}, T_{\max}]$, the average acceptance probability p_{acc} is about 23% [20]. Consistently, Kone and Kofke [7] obtained the same value for p_{acc} when optimizing the diffusion of a replica on the temperature ladder. Most recently, however, we observed in sample simulations employing the DEO scheme that the allegedly optimal value $p_{\mathrm{acc}} \approx 23\%$ led to suboptimal round trip rates [20]. This surprising observation sparked our curiosity and led us to compare different exchange schemes using a very simple benchmark simulation system.

3. Benchmark simulations

For each of the four algorithms, DEO, SEO, APE, and RNN, we performed several RE Monte Carlo (REMC) benchmark simulations with differing numbers N of replicas but with a fixed temperature range $T_{\min} = T_1 = 300$ K to $T_{\max} = T_N = 800$ K and with the temperatures T_i spaced as given by Eq. (2). In these simulations we drew the potential energies E_i of the replicas at each REMC step from the distributions given by Eq. (4) choosing $C = 500$ for the heat capacity. Then, one of the four algorithms was used to decide which exchanges should be considered, and the Metropolis criterion Eq. (1) was applied to evaluate the outcome of the exchange attempts. Every simulation comprised $S = 10^7$ REMC steps. A round trip was counted if one of the replicas had traveled the complete way from T_1 to T_N and back again. With the total number R of round trips counted during a simulation, the round trip rate is $r \equiv R/NS$.

Fig. 1 presents the measured round trip rates r as functions of $p_{\mathrm{acc}}(N)$. The shown efficiency profiles $r(p_{\mathrm{acc}})$ of the various algorithms are markedly different. The simple RNN algorithm (diamonds in Fig. 1) shows by far the weakest performance and has its maximum round trip rate $r_{\max} \approx 10^{-4}$ at $p_{\mathrm{acc}} \approx 12\%$. Because the RNN algorithm chooses only one pair from the set $\mathcal{N}$ of next neighbors for an exchange trial and because this trial is successful with an average acceptance probability p_{acc}, the average number n_{ex} of actual exchanges per REMC step is equal to p_{acc}.

Compared with the RNN scheme, the more refined APE algorithm (squares in Fig. 1) yields much higher round trip rates with a maximal performance $r_{\max} \approx 6.8\cdot10^{-4}$ at $p_{\mathrm{acc}} \approx 9\%$. At this value of p_{acc}, the average APE number of exchanges ($n_{\mathrm{ex}} = 0.55$) exceeds that of RNN ($n_{\mathrm{ex}} = 0.09$) by roughly a factor of 6. According to Fig. 1, here the APE round trip rate r is about 6.5 times higher than that of RNN. Hence, compared to RNN, the better performance of APE is mainly due to the larger value of n_{ex}, and the inclusion of non-next neighbor exchanges within APE seems to be of minor importance.

At $p_{\mathrm{acc}} \approx 23\%$ the round trip rate of the SEO algorithm assumes its maximum value $r_{\max} = 6.4\cdot10^{-4}$ (triangles in Fig. 1). At this point SEO exchanges nearly three times more pairs ($n_{\mathrm{ex}} = 1.45$) per REMC step than APE at its respective $r_{\max}$. Nevertheless, the maximal APE rate is higher than that of SEO. Interestingly, for SEO the position of $r_{\max}$ in Fig. 1 perfectly agrees with the 23% acceptance probability predicted by the optimization formula of Nadler and Hansmann [11,20] and with the point of maximal diffusivity predicted by Kone and Kofke [7].

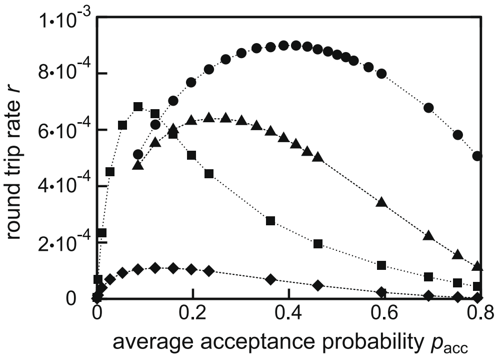

Fig. 1. The round trip rates r measured for the four different exchange schemes and a system with $C = 500$ as a function of the average acceptance probability p_{acc}: RNN (diamonds), APE (squares), SEO (triangles), DEO (circles). The dotted lines connecting the symbols are a guide for the eye.

As demonstrated by the circles in Fig. 1 the closely related DEO algorithm, performs everywhere better than SEO although both algorithms feature the same number n_{ex} of exchanges per REMC step for every choice of $p_{\mathrm{acc}}(N)$. This improved performance of DEO is particularly pronounced at large p_{acc}, i.e. at large ladder sizes N. According to Fig. 1 the maximal DEO round trip rate $r_{\max} = 9.0 \cdot 10^{-4}$ is found at $p_{\mathrm{acc}} \approx 41\%$.

These findings suggest that the theory behind the optimizations performed by Kone and Kofke [7] as well as by Nadler and Hansmann [11] does apply to SEO but not to the established and widely used DEO scheme.

4. Diffusive properties

4.1. Elementary process

To understand why DEO performs better than SEO, we analyzed the associated random walks performed by the replicas in the temperature space. A random walk is a sequence of statistically independent random experiments which we will call its elementary processes (EPs). After n EPs the displacement $X \equiv \sum_{i=1}^{n} \Delta_i$ of the random walker is the sum of the displacements Δ_i in the individual EPs. Since X is a sum of n identically distributed, statistically independent random variables Δ_i, its variance $\sigma^2(X)$ is given by $n\sigma^2(\Delta)$ [21], where $\sigma^2(\Delta)$ is the variance of the EP. If $\langle d \rangle$ is the average duration of the random walk's EP, then its diffusivity, i.e. the gain in variance per unit time, is given by

$$D = \sigma^2(\Delta)/\langle d \rangle. \tag{6}$$

4.2. Diffusivity of SEO

In the SEO scheme, the EP may have the following three outcomes: (i) The replica moves one step upward ($\Delta = +1$) on the temperature ladder with a total probability $p_{\pm} p_{\mathrm{acc}}$, where $p_{\pm} = 0.5$ is the probability of selecting the replica pair sets $\mathscr{E}$ or $\mathscr{O}$, respectively. (ii) The replica moves one step downward ($\Delta = -1$) on the ladder with the same probability. (iii) The replica does not move at all ($\Delta = 0$) with the rejection probability $1 - p_{\mathrm{acc}}$. Thus, the variance of the EP is

$$\sigma^2(\Delta) = p_{\pm} p_{\mathrm{acc}} \left[(+1)^2 + (-1)^2 \right] + (1 - p_{\mathrm{acc}})\, 0^2 = p_{\mathrm{acc}} \tag{7}$$

and its average duration is $\langle d \rangle = 1$. According to Eq. (6), the diffusivity of the SEO algorithm is then

$$D_{\mathrm{SEO}} = p_{\mathrm{acc}}. \tag{8}$$

Thus, in SEO a replica performs a simple random walk on the temperature ladder as is usually assumed in theoretical analyses of the RE approach [7,9,11,22].

4.3. Diffusivity of DEO

In contrast, the random walk imposed on a replica by the DEO algorithm is more complex. Let us first assume an infinite temperature ladder. For this situation, Fig. 2A sketches the logic of the exchanges. Assume that, in the odd REMC step j, the replica at rung i moves along the blue arrow upwards to rung $i + 1$. Then, in the following even step $j + 1$, it will be once again considered for an upward exchange toward rung $i + 2$ because DEO deterministically selects the red arrows for this exchange trial. As long as the exchange trials are successful, the replica keeps moving upward. This movement stops with the first exchange failure and, subsequently, the direction of the DEO replica movement is reversed. Thus, from the perspective of a single replica, the random walk consists of alternating upward and downward marches of variable lengths. Note that these lengths may also be zero if already the first exchange fails.

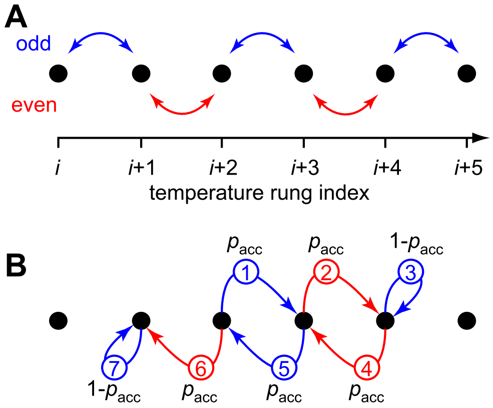

Fig. 2. (A) DEO exchanges within a temperatures ladder. The rungs $i, i+1, \ldots$ of the ladder are marked by black dots. The replica pairs which occupy the rungs joined by the blue double arrows are considered for exchange in odd REMC steps. Red double arrows refer to even REMC steps. (B) An example for an EP. The upward march consists of $k = 2$ successful steps, a failure in step 3, and of a downward march with $k' = 3$ successful steps terminated by a failure in step 7. The probability of each step is indicated at the corresponding arrow. (For interpretation of the references in colour in this figure legend, the reader is referred to the web version of this article.)

We define the EP of DEO as a pair consisting of an upward march and the following downward march. Let $k \in \mathbb{N}_0$ denote the number of successful upward steps, $k' \in \mathbb{N}_0$ the number of successful downward steps, and $l \equiv k + k'$ the sum of both. Fig. 2B shows a typical example for such an EP. This EP causes a net displacement $\Delta_{k,l} \equiv k - k' = 2k - l = -1$ and takes $d_{k,l} \equiv k + k' + 2 = l + 2 = 7$ steps. The probability of the EP shown in Fig. 2B is the product of all indicated probabilities belonging to the terminated upward $[p_{\mathrm{acc}}^2(1 - p_{\mathrm{acc}})]$ and downward marches $[p_{\mathrm{acc}}^3(1 - p_{\mathrm{acc}})]$.

The general formula for the probability of k successful upward steps, k' successful downward steps, and two unsuccessful exchange trials is

$$p_{k,l} \equiv p_{\mathrm{acc}}^{k+k'}(1 - p_{\mathrm{acc}})^2 = p_{\mathrm{acc}}^{l}(1 - p_{\mathrm{acc}})^2. \tag{9}$$

Thus, the variance of the EP is

$$\sigma^2(\Delta) = \sum_{l=0}^{\infty} \sum_{k=0}^{l} p_{k,l} \Delta_{k,l}^2 = \frac{2 p_{\mathrm{acc}}}{(1 - p_{\mathrm{acc}})^2}, \tag{10}$$

and the average duration of the EP is

$$\langle d \rangle = \sum_{l=0}^{\infty} \sum_{k=0}^{l} p_{k,l} d_{k,l} = \frac{2}{1 - p_{\mathrm{acc}}}. \tag{11}$$

From Eq. (6) we finally obtain for the DEO diffusivity

$$D_{\mathrm{DEO}} = \frac{p_{\mathrm{acc}}}{1 - p_{\mathrm{acc}}}. \tag{12}$$

A comparison with Eq. (8) demonstrates that D_{DEO} is by a factor of $1/(1 - p_{\mathrm{acc}}) > 1$ larger than D_{SEO}.

4.4. Round trip rates

The above analysis has yielded diffusivities on infinite temperature ladders. However, what we want to know are round trip rates r on finite ladders. Such a rate r is the inverse of 2τ, where τ is the mean first passage time required for a replica to diffusively cross the complete ladder. Therefore, r should be proportional [21] to the diffusivity D as long as the EPs of the underlying random walk are commensurate with the ladder size N. For the SEO scheme with its step sizes of 0 or ±1 this requirement is automatically fulfilled. However, DEO features at decreasing probabilities also EPs of arbitrarily increasing step sizes. Therefore, the proportionality $r_{\mathrm{DEO}} \propto D_{\mathrm{DEO}}$ is expected to hold only within a certain approximation.

Nadler and Hansmann [9] have calculated r assuming a SEO random walk directly from the corresponding master equation [21]. Inspection of Eq. (8) demonstrates that their result for the rate

$$r_{\mathrm{SEO}} = \frac{p_{\mathrm{acc}}}{2N(N-1)} \tag{13}$$

actually exhibits the expected proportionality $r_{\mathrm{SEO}} \propto D_{\mathrm{SEO}} = p_{\mathrm{acc}}$. If we assume such a proportionality also for DEO we get $r_{\mathrm{DEO}} = r_{\mathrm{SEO}} D_{\mathrm{DEO}}/D_{\mathrm{SEO}}$. Hence with Eqs. (8), (12), and (13), we expect for DEO the round trip rate

$$r_{\mathrm{DEO}} = \frac{p_{\mathrm{acc}}}{(1-p_{\mathrm{acc}})2N(N-1)}. \tag{14}$$

4.5. Comparison with measured rates

In Fig. 3, we compare the round trip rates $r(p_{\mathrm{acc}})$ thus analytically calculated with rates measured in our test simulations (see Fig. 1). The dashed line in Fig. 3 is the SEO prediction of Eq. (13), where we have additionally used the unique relation between N and p_{acc} given by Eqs. (5) and (3). The agreement with the measured rates (triangles in Fig. 3) is perfect as expected. Also for DEO our expectations are met. As expected, the approximation Eq. (14) (solid line) deviates only a little from the measured rates (circles).

The deviation between Eq. (14) and the measurements noted for DEO must decrease with increasing ladder size, because for large ladders all those EPs which try to reach beyond the ladder boundary become less frequent. Fig. 4 illustrates this decrease for three different average acceptance probabilities. The figure compares a round trip rate r_{RW} measured in extended DEO random walks on ladders of increasing size N with the rate r_{DEO} from Eq. (14). Due to the decrease, the depicted ratio $r_{\mathrm{RW}}/r_{\mathrm{DEO}}$ approaches the value one with growing N for all values of p_{acc}. Fig. 4 suggests that Eq. (14) is an upper limit for the actual round trip rate r_{RW} and that the overestimate of r_{RW} by r_{DEO} increases with p_{acc}. We note that at $N = 10$ and $p_{\mathrm{acc}} = 0.4$ the deviation is less than 10%.

4.6. Optimal temperature ladders

The analytical approximation Eq. (14) for the DEO round trip rate r together with the unique correspondence between p_{acc} and N (Eqs. (3) and (5)) enables us now to determine temperature ladders with a maximal r_{DEO}. Here we assume that a temperature range $[T_{\min}, T_{\max}]$ for an RE simulation and a system with known heat capacity C are given. For our benchmark system, we find the maximum of r_{DEO} at the acceptance rate $p_{\mathrm{acc}} = 40.5\%$. This prediction closely agrees with our MC measurements (Figs. 1 and 3) which identified the maximal r at the ladder size $N = 20$ corresponding to an average acceptance probability $p_{\mathrm{acc}} = 41.4\%$.

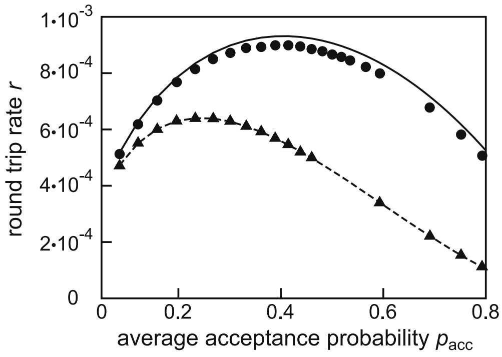

Fig. 3. Analytically calculated round trip rates r_{SEO} (Eq. (13), dashed line) and r_{DEO} (Eq. (14), solid line) as functions of the average acceptance probability p_{acc}. Values measured in our test simulations are adopted from Fig. 1. The SEO values (triangles) perfectly match Eq. (13), whereas the DEO values (circles) slightly deviate from Eq. (14).

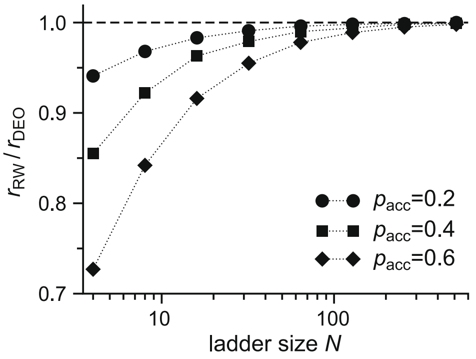

Fig. 4. Ratio of a measured round trip rate r_{RW} (calculated with a fixed acceptance probability p_{acc} from extended DEO random walks on different ladder sizes N) to the rate r_{DEO} given by Eq. (14). Ratios are shown for $p_{\mathrm{acc}} = 0.2$ (circles), $p_{\mathrm{acc}} = 0.4$ (squares), $p_{\mathrm{acc}} = 0.6$ (diamonds). The dotted lines connecting the symbols serve to guide the eye.

In a previous study [20], we found empirically for the same benchmark system that r is quite well approximated by the expression

$$r_{\kappa} \equiv c\kappa(p_{\mathrm{acc}}) \approx c' p_{\mathrm{acc}}/[N(p_{\mathrm{acc}}) - 1] \tag{15}$$

with system dependent constants c and c'. From Eqs. (15), (3), and (5) one finds that the maximum of r_{κ} is at $p_{\mathrm{acc}} = 44.4\%$, which is also close to the MC value $p_{\mathrm{acc}} = 41.4\%$.

As we have seen, the two apparently different analytical approximations Eqs. (14) and (15) yield quite similar predictions for the optimal p_{acc}. This puzzling result raises questions, which are resolved by Fig. 5. The figure shows the ratio $r_{\kappa}/r_{\mathrm{DEO}} = c'N(p_{\mathrm{acc}})(1-p_{\mathrm{acc}})$ as a function of p_{acc}. It demonstrates that for large p_{acc} the two expressions become equivalent and remain close at smaller p_{acc}. This similarity is more pronounced for very small systems (dashed line) than for larger ones (solid line). We would like to stress that the solid line is representative for all large systems with heat capacities $C > 500$ (data not shown).

By Eq. (15), r_{κ} is proportional to $1/(N-1)$, which is characteristic for a directed motion with constant velocity, whereas r_{DEO} is

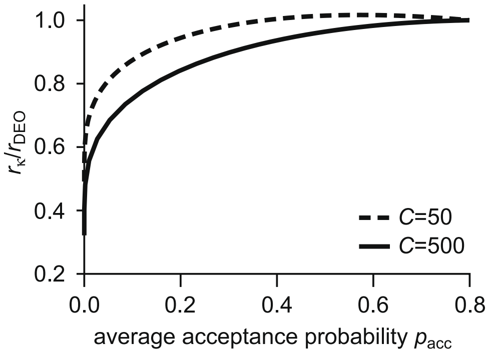

Fig. 5. The ratio $r_{\kappa}/r_{\mathrm{DEO}}$ as a function of the average acceptance probability p_{acc} for two systems with heat capacities $C = 50$ (dashed line) and $C = 500$ (solid line), respectively.

by Eq. (14) proportional to $1/[N(N-1)]$, which is typical for a diffusive motion. If the temperature ladders become so small that the EPs of the DEO random walk hit the ladder boundaries very frequently, then the approximation Eq. (14) is expected to become worse. For such small ladders one can expect that the constant velocity expression Eq. (15) becomes more accurate. To check this expectation, we calculated the p_{acc} of maximal r by Eq. (14) and Eq. (15) for the small system ($C = 50$). For this system the constant velocity expression Eq. (15) predicts 42.6%, the diffusion expression Eq. (14) yields 43.5% whereas the target value obtained through MC is 41.5% (corresponding to a ladder size $N = 7$). Thus, even for very small temperature ladders our analytical approximation r_{DEO} still predicts the location of the maximal round trip rate at nearly the same accuracy as the educated guess r_{κ} put forward in Ref. [20], while it is somewhat better for larger systems.

5. Summary

We have investigated the round trip rate performance of four different exchange algorithms. Our results demonstrate that the DEO algorithm yields the highest round rates over a wide range of average acceptance probabilities p_{acc}. Thus, using the DEO algorithm is not only a common but also a good practice in the application of replica exchange. This conclusion not only applies to replica exchange but also to simulated tempering [15]. Note, however, that according to our results (Fig. 1) the APE algorithm [16] might be an interesting alternative if one is interested in high round trip rates using minimally sized temperature ladders [20].

Examining the DEO random walk analytically we have shown that the reason for the higher DEO round trip rates compared with those of its randomized variant (SEO) is the intrinsically higher diffusivity of the corresponding random walk. Since the diffusivity advantage of DEO over SEO becomes larger with increasing p_{acc}, the acceptance probability maximizing the round trip rate is shifted from $p_{\mathrm{acc}} \approx 20\%$ (SEO) to $p_{\mathrm{acc}} \approx 40\%$ (DEO).

Finally, we have shown that the educated guess Eq. (15), which empirically had been determined to be a good optimization measure for the DEO round trip rates [20], yields results nearly equivalent to those of our analytical approximation Eq. (14).

Acknowledgement

This work was supported by the Deutsche Forschungsgemeinschaft (SFB 533/C1 and SFB 749/C4).

References

[1] K. Hukushima, K. Nemoto, J. Phys. Soc. Jpn. 65 (1996) 1604.
[2] U.H.E. Hansmann, Chem. Phys. Lett. 281 (1997) 140.
[3] Y. Sugita, Y. Okamoto, Chem. Phys. Lett. 314 (1999) 141.
[4] D.J. Earl, M.W. Deem, Phys. Chem. Chem. Phys. 7 (2005) 3910.
[5] N. Metropolis, A.W. Rosenbluth, M.N. Rosenbluth, A.H. Teller, E. Teller, J. Chem. Phys. 21 (1953) 1087.
[6] R. Denschlag, M. Lingenheil, P. Tavan, Chem. Phys. Lett. 458 (2008) 244.
[7] A. Kone, D.A. Kofke, J. Chem. Phys. 122 (2005) 206101.
[8] S. Trebst, M. Troyer, U.H.E. Hansmann, J. Chem. Phys. 124 (2006) 174903.
[9] W. Nadler, U.H.E. Hansmann, Phys. Rev. E 75 (2007) 026109.
[10] W. Nadler, J.H. Meinke, U.H.E. Hansmann, Phys. Rev. E 78 (2008) 061905.
[11] W. Nadler, U.H.E. Hansmann, J. Phys. Chem. B 112 (2008) 10386.
[12] T. Okabe, M. Kawata, Y. Okamoto, M. Mikami, Chem. Phys. Lett. 335 (2001) 435.
[13] M.J. Abraham, J.E. Gready, J. Chem. Theory Comput. 4 (2008) 1119.
[14] D. van der Spoel et al., Gromacs User Manual version 3.3, 2005. www.gromacs.org.
[15] R. Denschlag, M. Lingenheil, P. Tavan, G. Mathias, J. Chem. Theory Comput., submitted for publication.
[16] P. Brenner, C.R. Sweet, D. VonHandorf, J.A. Izaguirre, J. Chem. Phys. 126 (2007) 074103.
[17] F. Calvo, J. Chem. Phys. 123 (2005) 124106.
[18] B. Paschek, H. Nymeyer, A.E. Garcia, J. Struct. Biol. 157 (2007) 524.
[19] Y. Okamoto, M. Fukugita, T. Nakazawa, H. Kawai, Protein Eng. 4 (1991) 639.
[20] R. Denschlag, M. Lingenheil, P. Tavan, Chem. Phys. Lett. 473 (2009) 244.
[21] C.W. Gardiner, Handbook of Stochastic Methods, 2nd edn., Springer, Berlin, 1985.
[22] W. Nadler, U.H.E. Hansmann, Phys. Rev. E 76 (2007) 065701(R).
[23] V.I. Manousiouthakis, M.W. Deem, J. Chem. Phys. 110 (1999) 2753.

4 Simulated Solute Tempering

Die Geschwindigkeit, mit der die Replikate einer *Replica Exchange* Simulation durch den Temperaturraum wandern, kann über eine optimale Parameterwahl hinaus durch eine geeignete Kraftfeldskalierung positiv beeinflusst werden. Eine mögliche Skalierung des Kraftfeldes stellt das in der Einleitung beschriebene *Solute Tempering* Konzept dar, welches erstmals von Liu und Co-Autoren in Gestalt der *Replica Exchange with Solute Tempering* (REST) Methode eingeführt wurde [101] und eine deutliche Ausdünnung der Temperaturleiter bewirkt.

Aus dem vorangegangenen Kapitel geht hervor, dass (i) die ST Methode im Vergleich zu RE eine um den Faktor $1/\sqrt{2}$ geringere Anzahl an Temperatursprossen benötigt und dass (ii) die *round-trip* Zeit quadratisch mit der Anzahl der Temperatursprossen anwächst. Hieraus ergibt sich, dass die *round-trip* Zeit einer ST Simulation nur die Hälfte der *round-trip* Zeit einer entsprechenden RE Simulation beträgt. Diese Erkenntnis motivierte die im nachfolgenden abgedruckte[1] Publikation

> Robert Denschlag, Martin Lingenheil, Paul Tavan und Gerald Mathias:
> „Simulated Solute Tempering“
> *J. Chem. Theory Comput.* **5**, 2847 (2009),

die ich zusammen mit Martin Lingenheil, Paul Tavan und Gerald Mathias verfasst habe. In dieser Arbeit wird die REST spezifische Kraftfeldskalierung auf *Simulated Tempering* übertragen, woraus sich die neue *Simulated Solute Tempering* (SST) Methode ergibt. Neben einer ausführlichen Beschreibung der SST Methode, in der die akkurate Berechnung der Gewichte mit eingeschlossen ist, wird mittels einer konkreten MD Simulation die theoretische Erwartung bestätigt, dass die SST Abtasttechnik aufgrund der kürzeren *round-trip* Zeit den Konformationsraum effizienter abtastet als die REST Methode.

---

[1] Mit freundlicher Genehmigung der American Chemical Society.

J. Chem. Theory Comput. **2009,** *5,* 2847–2857

JCTC Journal of Chemical Theory and Computation

Simulated Solute Tempering

Robert Denschlag, Martin Lingenheil, Paul Tavan, and Gerald Mathias*

Lehrstuhl für Biomolekulare Optik, Ludwig-Maximilians-Universität,
Oettingenstrasse 67, 80538 München, Germany

Received May 26, 2009

Abstract: For the enhanced conformational sampling in molecular dynamics (MD) simulations, we present "simulated solute tempering" (SST) which is an easy to implement variant of simulated tempering. SST extends conventional simulated tempering (CST) by key concepts of "replica exchange with solute tempering" (REST, Liu et al. *Proc. Natl. Acad. Sci. U.S.A.* **2005**, *102*, 13749). We have applied SST, CST, and REST to molecular dynamics (MD) simulations of an alanine octapeptide in explicit water. The weight parameters required for CST and SST are determined by two different formulas whose performance is compared. For SST only one of them yields a uniform sampling of the temperature space. Compared to CST and REST, SST provides the highest exchange probabilities between neighboring rungs in the temperature ladder. Concomitantly, SST leads to the fastest diffusion of the simulation system through the temperature space, in particular, if the "even-odd" exchange scheme is employed in SST. As a result, SST exhibits the highest sampling speed of the investigated tempering methods.

Introduction

The generation of equilibrium ensembles for macromolecules by all-atom Monte Carlo (MC) or molecular dynamics (MD) simulations is a challenging task due to the huge computational effort which is generally necessary to guarantee ergodic sampling of relevant observables. The required simulation time depends on the number and on the depths of the local minima in the free energy landscape because here the simulation may get trapped for extended periods of time. If the barriers between the minima are mainly of enthalpic nature, generalized ensemble tempering techniques enable faster barrier crossings and, therefore, alleviate the sampling problem.[1,2]

Two important generalized ensemble tempering algorithms are simulated tempering (ST) and replica exchange (RE).[2] The RE method in its original form[3−5] employs several copies (replicas) of the investigated system at different temperatures $T_0 < T_1 < \cdots < T_{N\text{-}1}$. Within this temperature ladder, temperature exchanges between the replicas are periodically attempted. The corresponding probability for an exchange is given by a Metropolis criterion.[6] On the other hand, in simulated tempering,[7,8] only one "replica" diffuses along the temperature ladder, where temperature changes are determined by a Metropolis criterion slightly modified with respect to RE. Although both methods are closely related,[9] RE has attracted much more attention than ST, which is indicated by the large number of RE variants that have been suggested.[10−17] Furthermore, the RE efficiency has been the subject of many studies,[18−23] and numerous RE applications to macromolecules have been presented.[24−33] The main reason for the apparent neglect of ST is that this approach requires estimates for certain *a priori* unknown parameters, the so-called weights, to ensure a uniform sampling of the ensembles at all temperatures. In contrast, RE automatically guarantees a uniform sampling of all temperatures and is, therefore, much simpler to control.

Without prior knowledge on the properties of the simulated system an unbiased tempering algorithm should uniformly cover the chosen temperature space to generate an enhanced statistics at the temperature of interest, which usually is the lowest temperature T_0. Therefore, the average time to shuttle a replica between T_0 and the maximal temperature $T_{N\text{-}1}$ should be by orders of magnitude shorter than the simulation time. Addressing this issue, Abraham and Gready recently exam-

---

* Corresponding author phone: +49-89-2180-9228; fax: +49-89-2180-9202; e-mail: gerald.mathias@physik.uni-muenchen.de. Corresponding author address: LMU München, Lehrstuhl für BioMolekulare Optik, Oettingenstrasse 67, D-80538 München, Germany.

10.1021/ct900274n CCC: $40.75 © 2009 American Chemical Society
Published on Web 08/24/2009

ined more than forty published RE simulations for their ability to take full advantage of the tempering.[34] In most cases, they found that the simulation times were too short for a sufficiently frequent shuttling of the replicas along the temperature ladder. The reason for large shuttling times is known: This time usually scales with the square of the number of temperatures,[35] which in turn grows with the square root of the number of degrees of freedom[3] (DOF) in the simulation system. Thus, very long round trip times are expected for simulation systems with many DOF. Typical examples for such systems are macromolecules in explicit solvent. Note that such systems may additionally undergo slow phase transitions, like folding and unfolding, which may drastically increase round trip times.

Various strategies aiming at increasing the shuttling frequency were suggested for RE,[14−16,35−38] which should all be transferable to ST. A first class of strategies targets the optimization of the parameters that characterize the setup of an RE simulation. For example, Sindhikara et al.[38] recently recommended that the times between exchange trials should be as small as possible, which, however, has been disputed.[34] Additionally, rules for optimizing the temperature ladders were suggested.[35,39] A second class of strategies tries to reduce the number of DOF that are relevant for the exchange criterion, for example some strategies switch from an explicit to an implicit solvent description for the exchange trials[16] or by tempering only the areas of interest.[15] With such a reduced number of DOF, the temperature steps within the ladder can be chosen larger and, thus, a given temperature range can be covered by less rungs. As a result, the round trip times are drastically shortened. However, the quoted methods of the second class are not rigorous in terms of statistical physics because here the ensemble is modified in a somewhat arbitrary fashion. Recently, Liu et al.[14] have presented a rigorous strategy called “replica exchange with solute tempering” (REST), which largely eliminates the influence of the solvent DOF on the exchange probabilities by a temperature dependent scaling of the Hamiltonian. In this approach only the Hamiltonian at the target temperature remains unscaled and renders the desired physically meaningful ensemble. This restriction is, however, of minor importance for many applications.

An additional strategy to achieve increased shuttling frequencies is the optimal choice of the tempering method itself. For example, with accurately known weight parameters, ST is more efficient than RE because it provides larger acceptance probabilities on the same temperature ladder.[40−42] At given conditions one may equivalently state that ST requires less rungs in the temperature ladder than RE if both techniques are tuned to the same average acceptance probabilities.

The weights necessary for ST can be estimated by short preparatory simulations bearing the risk, however, that these weights are of insufficient accuracy. Addressing this issue, a recent study by Park and Pande[9] suggests that controlling an ST simulation may be less difficult than previously assumed by Mitsutake and Okamoto.[43] In contrast to the latter authors Park and Pande[9] did not stick to the rough estimates for the weights derived from a set of short preparatory simulations but instead updated the weights during the subsequent ST production run.

Here, inspired by the works of Park and Pande[9] and of Liu et al.,[14] we suggest a variant of ST called simulated solute tempering (SST), which shares key concepts with REST and its sequential variant SREST.[13] As we will demonstrate, SST has the advantages of a most simple implementation and of reducing the required number of rungs within the temperature ladder. Note, that SST should be easily transferrable to hybrid methods which combine different tempering techniques[43] or tempering with other enhanced sampling methods.[44]

We start in “Theory and Methods” with an introduction to replica exchange and its variant REST, which employs a temperature dependent scaling of the Hamiltonian. Then, we present SST along with two procedures for calculating the weights and corresponding update schemes. Subsequently, these techniques are applied to an alanine octapeptide (8ALA) solvated in water. The enthalpic barriers of 8ALA are small, and, hence, the benefit of tempering techniques is limited.[22] However, the small barriers provide fast conformational sampling which makes 8ALA ideally suited to compare different tempering strategies among each other with high statistical accuracy. In particular, we investigate the sampling efficiency and convergence of conventional ST (CST), SST, and REST. In addition, we test two temperature exchange schemes for SST to improve the method further. After the presentation and discussion of the results, we conclude the paper summarizing the key messages.

Theory and Methods

We begin by sketching the replica exchange method and the concept of solute tempering, which will lead us, when combined with simulated tempering, to the SST method.

Replica Exchange. Within both conventional temperature RE[5] (CRE) and REST,[14] N copies (replicas) of the system are simulated at temperatures $T_0 < T_1 < \cdots < T_{N-1}$ and sample the associated canonical ensembles. The set of replicas constitutes a so-called generalized ensemble. After predefined time intervals a temperature exchange between pairs of replicas is tried. A Metropolis criterion[6] determines the exchange probability

$$P_{ij} = \min[1, \exp(\Delta_{ij})] \tag{1}$$

between replicas at T_i and T_j with

$$\Delta_{ij} = \beta_i[E_i(\mathbf{x}_j) - E_i(\mathbf{x}_i)] + \beta_j[E_j(\mathbf{x}_i) - E_j(\mathbf{x}_j)] \tag{2}$$

to preserve the canonical ensembles. Here, $E_k(\mathbf{x}_l)$ is the value of the potential energy function associated with the temperature T_k, which is evaluated at a configuration $\mathbf{x}_l$ resulting from the sampling at T_l; $\beta_k = 1/k_BT_k$ is the inverse temperature where k_B is the Boltzmann constant. For CRE the potential energy is independent of the temperature, and Δ_{ij} reduces to

$$\Delta_{ij} = (\beta_i - \beta_j) \cdot [E(\mathbf{x}_i) - E(\mathbf{x}_j)] \tag{3}$$

In the case of REST, in contrast, the potential energy becomes temperature dependent and has the form

$$E_k(\mathbf{x}) = \lambda_{k,0}E^{\mathrm{pp}}(\mathbf{x}) + \lambda_{k,1}E^{\mathrm{ps}}(\mathbf{x}) + \lambda_{k,2}E^{\mathrm{ss}}(\mathbf{x}) \qquad (4)$$

where E^{pp}, E^{ps}, and E^{ss} are the solute−solute, solute−solvent, and solvent−solvent parts of the potential energy function at the target temperature T_0 of the sampling; $\lambda_{k,h}$ are parameters depending on the temperature T_k. We choose

$$\lambda_{k,0} = 1,\ \ \lambda_{k,1} = \sqrt{\beta_0/\beta_k},\ \ \lambda_{k,2} = \beta_0/\beta_k \qquad (5)$$

where $\lambda_{k,1}$ is the geometric mean of $\lambda_{k,0}$ and $\lambda_{k,2}$ instead of the arithmetic mean $(\beta_0 + \beta_k)/2\beta_k$ originally proposed by Liu et al.[14] With this choice, the required scaling of the electrostatic energy and of the corresponding forces at T_k can be achieved by simply scaling the partial charges of the solvent by a factor $(\beta_0/\beta_k)^{1/2}$. Similar considerations hold for the Lennard-Jones interactions. Thus, this choice of the $\lambda_{k,i}$ is conveniently implemented.

The advantage of the REST approach becomes apparent after a few algebraic operations. Inserting eqs 4 and 5 into eq 2 one finds

$$\begin{aligned}\Delta_{ij} &= (\beta_i - \beta_j)[E^{\mathrm{pp}}(\mathbf{x}_i) - E^{\mathrm{pp}}(\mathbf{x}_j)]\\ &\quad + (\sqrt{\beta_0\beta_i} - \sqrt{\beta_0\beta_j})[E^{\mathrm{sp}}(\mathbf{x}_i) - E^{\mathrm{sp}}(\mathbf{x}_j)]\end{aligned} \qquad (6)$$

Thus, the difference Δ_{ij}, which determines the acceptance probability eq 1, is exclusively calculated from the solute−solute and solute−solvent energies, whereas the potential energy E^{ss} of the solvent cancels.

One can quantify the benefit of REST compared with CRE by estimating the number of rungs eliminated from the temperature ladder. Assuming that the solvent DOF do not contribute to the exchange probability at all, the ratio $N_{\mathrm{REST}}/N_{\mathrm{CRE}}$ of the required rungs is estimated by the lower limit $(n_{\mathrm{p}}/(n_{\mathrm{s}} + n_{\mathrm{p}}))^{1/2}$, where n_{s} and n_{p} count the DOF of the solvent and solute, respectively. In the following we discuss how simulated tempering can further reduce the required number of rungs.

Simulated Tempering. In simulated tempering[7,8] (ST), a single system is simulated at a temperature T_i, which belongs to a given temperature ladder $T_0 < \cdots < T_{N\text{-}1}$. After given time intervals it is checked whether the system temperature T_i can be changed to T_j, where j is usually $i \pm 1$. For $i \in \{0, N - 1\}$ the transition to $j = -1$ or $j = N$ is rejected. For other transitions $i \rightarrow j$, the acceptance probability[41]

$$P_{ij} = \min[1, \exp(\Delta_{ij})] \qquad (7)$$

with

$$\Delta_{ij} = [\beta_i E_i(\mathbf{x}) - w_i] - [\beta_j E_j(\mathbf{x}) - w_j] \qquad (8)$$

represents a Metropolis criterion similar to that of RE. The weights w_k introduced in eq 8 are commonly set to the configurational parts $\beta_k\tilde{F}_k = -\ln \int \exp\,[-\beta_k E(\mathbf{x})]\mathrm{d}\mathbf{x}$ of the dimensionless free energies $\beta_k F_k$ of the simulation system at the temperatures T_k.[7,8] This choice leads to a uniform sampling of all rungs within a given temperature ladder because, in the ergodic limit, the expected ratio $\rho_k \equiv t_k/t$ of the time t_k spent by the simulation at temperature T_k to the total sampling time t is given by the Boltzmann factor of the generalized ensemble

$$\lim_{t\to\infty} \rho_k = \frac{\exp[-(\beta_k\tilde{F}_k - w_k)]}{\sum_j \exp[-(\beta_j\tilde{F}_j - w_j)]} \qquad (9)$$

leading to $\lim_{t\to\infty} \rho_k = 1/N$ for $w_j = \beta_j\tilde{F}_j$. Since the w_k are *a priori* unknown, one usually tries to estimate these weights from short preparatory simulations. Note that the w_j can be chosen differently, if a nonuniform sampling is desired.[42]

In conventional simulated tempering (CST), the potential energy function $E_k(\mathbf{x})$ is independent of the temperature T_k, and eq 8 reduces to

$$\Delta_{ij} = (\beta_i - \beta_j)E(\mathbf{x}) - (w_i - w_j) \qquad (10)$$

For the new SST method introduced here, we transfer the solute tempering concept of REST to ST and use the energy function given by eqs 4 and 5. Inserting these equations into eq 8 yields

$$\Delta_{ij} = (\beta_i - \beta_j)E^{\mathrm{pp}}(\mathbf{x}) + (\sqrt{\beta_0\beta_j} - \sqrt{\beta_0\beta_i})E^{\mathrm{ps}}(\mathbf{x}) - (w_i - w_j) \qquad (11)$$

Thus, for SST the difference Δ_{ij} is only calculated from the solute−solute and solute−solvent energies, while the potential energy E^{ss} of the solvent cancels. As we will show below the solvent−solvent contributions cancel as well in the computation of the weight differences $w_i - w_j$.

At first glance, ST (CST/SST) seems less attractive than RE (CRE/REST) because ST requires the *a priori* unknown weights w_i. However, ST provides larger average acceptance probabilities than RE[40−42] for a given temperature ladder because RE requires a simultaneous exchange of two replicas, whereas only one replica has to be considered for ST. As a result, ST needs only $1/\sqrt{2}$ times the number of rungs in the temperature ladder than RE to cover a given temperature range with the same acceptance probabilities.[39] Now, we turn to different approaches to determine the required weights w_i.

Determination of the Weights w_k. As we have seen above, a uniform sampling of the various temperatures T_k requires that the weights w_k in eq 8 are the configurational parts $\beta_k\tilde{F}_k$ of the dimensionless free energies, which can be estimated from preparatory simulations. For CST, Park and Pande have presented a formula which yields surprisingly good estimates of the w_k at a negligible computational effort (e.g., by executing a single 10 ps MD simulation at each T_k).[9] These authors replaced the potential energy $E(\mathbf{x})$ in eq 10 by the average potential energy $\langle E\rangle_i$ at T_i to get a "typical" $\Delta_{ij}^{\mathrm{typ}}$ and demanded that $\Delta_{ij}^{\mathrm{typ}} = \Delta_{ji}^{\mathrm{typ}}$, which leads to the estimate

$$w_j - w_i \approx (\beta_j - \beta_i)\frac{\langle E\rangle_i + \langle E\rangle_j}{2} \qquad (12)$$

and which has been further substantiated by Park.[41] In the Appendix we show an alternative derivation of the "trapezoid rule" eq 12 that is based on the assumption of a constant heat capacity C_V and that $\ln[1 + (T_j - T_i)/T_i]$ can be approximated by $(T_j - T_i)/T_i$.

Replacing the temperature dependent potential energies $E_i(\mathbf{x})$ and $E_j(\mathbf{x})$ in eq 8 by averages $\langle E_i\rangle_i$ and $\langle E_j\rangle_i$ transfers the trapezoid rule of CST to SST. Here, $\langle E_j\rangle_i$ is the energy function E_j evaluated for and averaged over the configurations sampled at T_i. Analogous to CST, also these SST averages yield "typical" differences $\Delta_{ij}^{\mathrm{typ}}$. Equation 5 and $\Delta_{ij}^{\mathrm{typ}} = \Delta_{ji}^{\mathrm{typ}}$ lead to

$$w_j - w_i \approx \frac{(\beta_j - \beta_i)(\langle E^{pp}\rangle_i + \langle E^{pp}\rangle_j)}{2} + \frac{(\sqrt{\beta_0\beta_j} - \sqrt{\beta_0\beta_i})(\langle E^{ps}\rangle_i + \langle E^{ps}\rangle_j)}{2} \tag{13}$$

As mentioned in the section "Simulated Tempering", $w_j - w_i$ does not depend on the solvent−solvent interactions E^{ss}. Note that one can choose $w_0 = 0$ because only differences $w_j - w_i$ matter in eq 8.

Whereas the computations of the weights w_i in CST and SST by the trapezoid rules eqs 12 and 13, repectively, are approximate, the relation

$$\exp(-w_i) = \sum_{k=0}^{N-1} \sum_{t=1}^{n_k} \frac{\exp\{-\beta_i \sum_{j=0}^{L-1} \lambda_{i,j} E^j[\mathbf{x}_k(t)]\}}{\sum_{m=0}^{N-1} n_m \exp\{w_m - \beta_m \sum_{j=0}^{L-1} \lambda_{m,j} E^j[\mathbf{x}_k(t)]\}} \tag{14}$$

presented earlier by Kumar et al.[45] for the "weighted histogram analysis method" (WHAM) is "exact" for the already sampled ensemble and provides an unbiased estimator for the true dimensionless free energies.[46] Here, N is again the number of temperatures T_k, n_k is the number of configurations $x_k(1),...,x_k(n_k)$ sampled at T_k, and L counts potential energy terms contributing to the Hamiltonian. For CST there is only one such term and one has $L = 1$, $E^0(\mathbf{x}_k) \equiv E(\mathbf{x}_k)$, and $\lambda_{i,0} = 1$. The Hamiltonian of SST eq 4 distinguishes $L = 3$ energy contributions $E^0(\mathbf{x}_k) \equiv E^{\mathrm{pp}}(\mathbf{x}_k)$, $E^1(\mathbf{x}_k) \equiv E^{\mathrm{ps}}(\mathbf{x}_k)$, and $E^2(\mathbf{x}_k) \equiv E^{\mathrm{ss}}(\mathbf{x}_k)$. With the $\lambda_{i,j}$ chosen as given by eq 5 one finds that E^{ss} cancels in eq 14 like it did in the trapezoid rule eq 13. Equation 14 has to be solved self-consistently and yields successively more and more accurate weights as the statistics is improved by an ongoing sampling. Note that Mitsutake and Okamoto[40,43] previously suggested to compute the free energies required for ST through WHAM equations, which are based on energy histograms. In contrast, eq 14 computes the free energies directly from the sampled energies and, therefore, avoids the errors introduced by the histogram discretization.[45−47]

The WHAM formula eq 14 can be used to identify the errors Δw_i of the trapezoid rules eq 12 for CST and eq 13 for SST. In the limit of ergodic sampling, the errors $\Delta w_i = w_i - w_i^{\mathrm{exact}}$ yield through eq 9 the ratios $\lim_{t\to\infty} \rho_i = \exp(\Delta w_i)/\sum_j \exp(\Delta w_j)$. These ratios will deviate from $1/N$ and, therefore, measure deviations from the desired uniformity of the sampling along the ladder of temperatures T_i. To measure this deviation in our simulations, we introduce the quantities

$$\chi_i \equiv N\frac{t_i}{t} \tag{15}$$

A uniform sampling corresponds to $\chi_i = 1.0$ at all T_i. Thus, the χ_i enable easy comparisons of the sampling uniformity achieved with differently sized temperature ladders. If the errors Δw_i are known, the long time limit of χ_i is

$$\hat{\chi}_i = N\frac{\exp(\Delta w_i)}{\sum_{j=0}^{N-1} \exp(\Delta w_j)} \tag{16}$$

For finite simulations, the χ_i exhibit statistical fluctuations which depend on the number of rungs N in the temperature ladder, on the average exchange probabilities $\bar{P}_{ij}$, and on the total number of exchange trials. For each set of these parameters, one can model an actual ST simulation by a computationally inexpensive MC simulation of a random walk along the N rungs of the temperature ladder. We will use large numbers of such MC simulations to estimate the standard deviations σ_i of the χ_i for the respective simulations. These values show to what extent one may expect convergence of sampling uniformity.

Update Schemes for the Weights w_i. Initial guesses for the weights required in ST can be obtained from short preparatory simulations using the formulas presented in the previous paragraph. The correspondingly limited statistical accuracy of the initial weights may entail a strongly nonuniform sampling along the temperature ladder in subsequent ST production runs. However, one may improve the initial guesses by utilizing the information accumulated in the course of the production run. For this purpose different adaptation schemes were suggested.[48−51]

We used a procedure based on the following considerations: Up to the first update the sampling along the temperature ladder is expected to be far off from uniformity. Consequently, a poor statistics of the potential energy distribution is obtained at some temperature rungs. To avoid an impact of this bad statistics on the estimated weights, we determine the first update by $w_i^{\mathrm{new}} = w_i^{\mathrm{old}} + \ln(t_0/t_i)$ where we set the t_i for rungs that have not been visited at all to a full exchange period. Thus, badly sampled rungs will be preferentially sampled until the next update step. By construction this strategy leads to a uniform sampling but may suffer from slow convergence. Therefore, we subsequently switch to a periodical recomputation of the weights either by the trapezoid rule (eqs 12 and 13) or by the WHAM formula (eq 14). In these recomputations, which are executed after each nanosecond of simulation, we exclusively consider the data from the production run and discarded those of the preparatory simulation.

Exchange Scheme. Having established the determination of the weights steering the exchange probabilities, we now sketch the exchange algorithms employed for ST. A straightforward exchange procedure is to choose randomly between an upward or downward exchange trial with probabilities of 50%. We call this exchange procedure "stochastic even/odd" (SEO) scheme because the corresponding exchange scheme for replica exchange is a stochastic instead of a deterministic choice between two groups of replica pairs.[52] The first group contains all "even" pairs (T_{2n},T_{2n+1}) and the second one all "odd" pairs (T_{2n-1},T_{2n}).

Table 1. Overview of Simulations Conducted[a]

label	trajectory time span/ns	temperature range/K	no. of rungs	solvent scaling	determination of weights	exchange scheme
CRE	18 × 0.1	300−500	18	no	-	DEO
CST	27	300−500	18	no	trapezoid	SEO
REST/A	4 × 0.1	300−500	4	yes	-	DEO
REST/B	5 × 0.1	300−500	5	yes	-	DEO
REST/C	4 × 12	300−500	4	yes	-	DEO
SST/A	27	300−500	4	yes	trapezoid	SEO
SST/B	27	300−500	4	yes	WHAM	SEO
SST/C	12	300−500	4	yes	WHAM	DEO
SST/D	12	300−500	5	yes	WHAM	DEO

[a] The weights for the ST simulations have been determined either by the trapezoid rule, eq 12 for CST and eq 13 for SST, respectively, or by the WHAM formula eq 14.

However, the standard exchange scheme used in replica exchange simulations is characterized by alternate exchange trials between these two groups of replica pairs,[3,34,52,53] which we have called the "deterministic even/odd" (DEO) scheme.[52] Formally, one can express the DEO exchange scheme by a relation which combines the involved temperature indices i and i' at the exchange attempt step s by $i' = i + (-1)^{i+s}$. In the framework of simulated tempering DEO alternately tries to shift the single replica at T_i to T_{i+1} (upward) or T_{i-1} (downward). In the case of a successful exchange, however, the previous exchange direction (upward or downward) is maintained for the next exchange trial and so forth until a temperature exchange fails.

We apply both exchange schemes to investigate their influence on the diffusion of the system through the temperature space. This diffusion can be measured in terms of the average round trip time τ required to travel from T_0 to T_{N-1} and back to T_0. For the SEO scheme applied to a temperature ladder with uniform average acceptance probabilities $\bar{P}_{ij} = \bar{P}$, τ in units of the time between exchange trials is related to the average acceptance probability $\bar{P}$ by[35,52,54,55]

$$\tau_{\mathrm{SEO}} = 2N(N-1)/\bar{P} \tag{17}$$

For DEO, τ is given by

$$\tau_{\mathrm{DEO}} = \tau_{\mathrm{SEO}}(1-\bar{P}) \tag{18}$$

in the limit of large N.[52] Assuming this limit, DEO always provides shorter round trip times than SEO or, equivalently, higher round trip rates τ^{-1}. Thus, the question is to what extent this expectation is confirmed for finite ladder sizes N.

Simulation System and Force Field. We have used MD simulations of a poly alanine octapeptide (8ALA), saturated with an acetyl group at the N-terminus and an *N*-methyl group at the C-terminus, to investigate the benefits of the various algorithms introduced above. The peptide was described by the CHARMM22 force field[56] and solvated in a periodic orthorhombic dodecahedron of 18 Å inscription radius containing 1112 water molecules. For the water molecules we employed the transferable three-point intermolecular potential (TIP3P),[57] modified as suggested by MacKerell et al.[56] for usage with CHARMM22. The initial 8ALA structure was generated using the Molden software[58] by setting the backbone dihedral angles to the values $\phi = -58°$ and $\psi = -47°$ to form an ideal α-helix.

MD Simulation Techniques. The software package EGO-MMVI[59] was used for all MD simulations. The electrostatic interactions were treated combining structure-adapted multipole expansions[60] with a moving-boundary reaction-field approach.[59] Here, the cutoff radius for the explicit evaluation of the electrostatic interactions was 18 Å. Beyond this radius, a dielectric continuum was assumed with a static dielectric constant $\varepsilon_s = 80$. The explicit van der Waals interactions were calculated up to a distance of 10 Å and at larger distances a mean-field approach was applied.[61] A multiple-time-step integration scheme[62] with a fastest time step of 2 fs was used. For bonds that include hydrogen atoms, the corresponding bond lengths were constrained using the M-SHAKE algorithm[63] with relative tolerance of 10^{-6}.

System Preparation. Our simulation system was equilibrated for 100 ps with two Berendsen thermostats[64] (coupling times 0.1 ps) separately keeping the solute and the solvent at 300 K. Additionally, a Berendsen barostat[64] (coupling time 1 ps) steered the system to ambient pressure (1 bar). For the subsequent tempering runs we switched from an *NPT* to an *NVT* ensemble.

Simulation Runs. As listed in Table 1 we carried out three short replica exchange simulations [CRE and REST/(A,B)] serving to estimate the initial weights for the extended simulated tempering simulations CST and SST/A-D. For CRE and CST we used the temperature ladder 300 K, 308 K, 317 K, 326 K, 336 K, 346 K, 356 K, 367 K, 378 K, 390 K, 402 K, 415 K, 428 K, 442 K, 456 K, 470 K, 485 K, and 500 K. We found average acceptance probabilities $\bar{P}_{i,i+1}$ between 5% and 14% for CRE and between 21% and 31% for CST. For REST/(A,C) and SST/A-C we used the ladder 300 K, 350 K, 415 K, and 500 K. The corresponding $\bar{P}_{i,i+1}$ range from 5% to 12% (REST) and from 19% to 28% (SST). For REST/B and SST/D, the five temperatures 300 K, 340 K, 387 K, 440 K, and 500 K were used yielding $\bar{P}_{i,i+1}$ between 15% and 19% (REST) and between 38% and 41% (SST). Exchanges were tried every 0.5 ps in all simulations. Tables S1 and S2 in the Supporting Information provide details about the average exchange probabilities along the various ladders. These values were used for setting up the MC simulations mentioned further above.

The extended simulations REST/C, CST, and SST/(A,B) serve us for comparisons of methods and address, in particular, the applicability of different adaptation schemes to SST. Furthermore, using the simulations SST/C and SST/D we will study the effects of the chosen exchange scheme (SEO vs DEO) and of the (overall) average exchange probability $\bar{P} = \langle \bar{P}_{ij} \rangle$ on the round trip rates τ^{-1} and the sampling speeds.

Sampling Speed. The main objective of tempering methods is to enhance the sampling speed of the simulation. A corresponding measure for the sampling speed is given by an algorithm recently suggested by Lyman and Zuckerman,[65] which we will denote as LZA. LZA integrates the "volume" in configurational space sampled by a trajectory. The average volume sampled during a given simulation time span provides a measure for the sampling speed.

For 8ALA we define the conformational space by the eight dihedral angles ψ_i spanned by the backbone units $N^i - C^i - C^i_\alpha - N^i$. From a trajectory of the eight-dimensional tuples $(\psi_1,...,\psi_8)$, LZA randomly chooses one tuple and removes it from the trajectory together with all other tuples lying within the sphere of predefined radius r around the chosen tuple. This procedure is repeated until all tuples of the initial trajectory have been removed. The number of steps required is a dimensionless measure for the configurational volume V_c sampled by the trajectory. Because this algorithm is nondeterministic, it is repeated m times, and the corresponding average number n_{lza} of required steps is calculated. For our analyses we choose $r = 25°\sqrt{8}$ and $m = 50$. For a fair comparison between ST and RE, we compute the sampling speed per replica, i.e. one for ST and N for RE.

Results and Discussion

At the start of an ST simulation, initial estimates for the weight parameters w_i are needed. We determined these estimates from preparatory simulations using both the approximate trapezoid rule eq 12 and the asymptotically unbiased WHAM formula eq 14. Now, a first issue is the reliability of the trapezoid rule, which we check using the 100 ps CST simulation.

Reliability of the Trapezoid Rule for CST. Table 2 compares the initial CST weights w_i determined by the trapezoid rule eq 12 from the preparatory CRE simulation with the asymptotically unbiased values calculated by the WHAM formula eq 14. For all T_i the w_i obtained by the two formulas agree quite well. The errors Δw_i of eq 12 never exceed 12% of $k_B T_i$, and, correspondingly, the uniformity measures $\hat{\chi}_i$ are all close to 1.0. Hence, one expects a nearly uniform sampling even if the weights are determined by eq 12. Thus, adaptation schemes, which are based on the trapezoid rule and on the WHAM formula, respectively, should be nearly equivalent for the given system. In the CST simulation we, therefore, applied the trapezoid rule for the periodical recomputation of the w_i.

Table 2. Weights Determined from the CRE Simulation[a]

i	T_i	w_i (trapezoid)	w_i (WHAM)	Δw_i	$\hat{\chi}_i$
0	300 K	0.0	0.0	−0.00	1.06
1	308 K	482.58	482.59	−0.01	1.05
2	317 K	991.97	991.99	−0.02	1.04
3	326 K	1468.66	1468.69	−0.03	1.03
4	336 K	1963.47	1963.49	−0.02	1.04
5	346 K	2425.14	2425.17	−0.03	1.03
6	356 K	2856.65	2856.68	−0.03	1.03
7	367 K	3299.53	3299.56	−0.03	1.03
8	378 K	3712.36	3712.41	−0.05	1.00
9	390 K	4131.64	4131.73	−0.09	0.97
10	402 K	4521.49	4521.56	−0.07	0.99
11	415 K	4913.99	4914.07	−0.08	0.98
12	428 K	5278.33	5278.44	−0.11	0.95
13	442 K	5642.42	5642.50	−0.08	0.98
14	456 K	5980.14	5980.21	−0.07	0.99
15	470 K	6294.02	6294.09	−0.07	0.99
16	485 K	6606.46	6606.55	−0.09	0.97
17	500 K	6896.68	6896.80	−0.12	0.94

[a] The weights w_i determined by the trapezoid rule eq 12 and by the WHAM formula eq 14 together with the deviations Δw_i and the correspondingly predicted (cf. eq 16) uniformity measures $\hat{\chi}_i$. The WHAM weights were employed as starting values for the CST simulation.

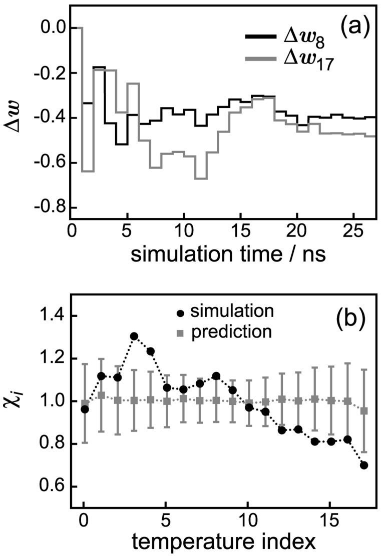

Figure 1. Uniformity of the temperature sampling in the CST simulation. (a) Time evolution of the weights w_8 and w_{17} with respect to their initial values. (b) Uniformity measures observed (χ_i, eq 15, circles) and predicted ($\hat{\chi}_i$, eq 16, squares) after 27 ns at the temperatures T_i. The standard deviations were estimated from MC trial simulations (see text for further details). The dotted lines serve as a guide for the eye.

Representative for the eighteen weights, Figure 1(a) shows the deviation of the weights w_8 and w_{17} from their initial values as a function of the simulation time. The exceptional first update $w_k^{\mathrm{new}} = w_k^{\mathrm{old}} + \ln(t_0/t_k)$, which can be seen as a special case of the update scheme proposed by Zhang and Ma,[51] sizably reduces both weights and reflects the nonuniform sampling within the preceding first nanosecond of the CST simulation. Here, the temperatures $T_8 = 378$ K and $T_{17} = 500$ K apparently have been visited more frequently than $T_0 = 300$ K. The following updates, which rely on eq 12, lead to considerable changes of the weights, which, however, become smaller toward the end of the simulation. After 27 ns the weights seem to be converged within roughly ± 0.1. This is approximately the same magnitude of error as the one introduced by the trapezoid rule.

Figure 1(b) shows the measured (circles) and expected (squares) uniformity measures χ_i and $\hat{\chi}_i$ extracted from the last 25 ns of the CST simulation as functions of the temperature. In contrast, the uniformity data shown in Table

2 had been extracted from the much shorter preparatory CRE simulation. According to eq 16 the observables $\hat{\chi}_i$ reflect the average deviations Δw_i between the trapezoid weights used during the CST simulation and WHAM weights calculated *a posteriori* from that simulation. As one sees in the figure, the expectation values $\hat{\chi}_i$ are close to one demonstrating that the trapezoid rule induces only small errors into the weights. These data confirm the claim[9] that the trapezoid rule is appropriate for choosing the weights in conventional ST simulations.

Despite the expected nearly uniform sampling of the sampling along the temperature ladder the values χ_i measured for the CST simulation deviate substantially from one, yielding a root-mean-square deviation (RMSD) from uniformity of 16%. Because the weights are calculated with a reasonable accuracy, this nonuniformity of the sampling must be due to a too short CST simulation time. We checked this issue by the simple MC model for the CST simulation described in Theory and Methods, because here the expected deviations from a uniform sampling can be reliably determined.

The gray bars in Figure 1(b) measure the standard deviations σ_i of the χ_i resulting from 1000 MC model simulations covering the same number of exchange trials as our CST simulation. One would now expect that $\mathrm{erf}(\sigma) = 68\%$ of the χ_i are found at smaller deviations than σ_i. In fact, 12 of the 18 χ_i are within the corridor marked by the σ_i, which nicely reproduces the expected statistics. Quite clearly the standard deviations σ_i can be reduced by extending the simulation time, which will then also lead to a CST sampling close to uniformity. Now the question is whether one can estimate the simulation time required for a reasonably uniform sampling. This issue can be addressed by considering the round trip rate τ^{-1} given by eq 17.

CST Round Trip Rates. From the MC model simulations we calculated an average round trip rate τ^{-1} of 0.83 ns^{-1} with a standard deviation of 0.1 ns^{-1}. Equation 17 gives an exact expression for τ applying to the SEO exchange scheme used in the CST simulation. This expression rests on the assumption of identical acceptance probabilities $\bar{P}$ for exchanges along the ladder. The $\bar{P}$ determined from the CST simulation is about 26%, and the resulting value $\tau^{-1} = 0.85$ ns^{-1} is very close to the MC result.

However, the round trip rate observed in the CST simulation is sizably smaller measuring 0.64 ns^{-1}. This deviation suggests that the time interval of 0.5 ps between subsequent exchange trials is too short to yield statistically independent configurations, i.e. that the autocorrelation time of the energy exceeds 0.5 ps. Thus, the system still has some memory of the previous exchange trial, which, however, is tolerable for most practical purposes. Furthermore, a round trip rate of 0.64 ns^{-1} means that only 16 round trips were counted during the CST simulation which is the main cause for the observed 16% RMSD from uniform sampling. To half this RMSD, a 4-fold number of round trips and, thus, a 4-fold simulation time would be necessary. Accordingly, one can estimate the number of round trips needed to achieve a desired level of uniform sampling. In turn, one can *a priori* estimate the required simulation time by multiplying this number by the predicted round trip time given in eq 17.

Table 3. Weights Determined from the REST/A Simulation[a]

i	T_i	w_i (trapezoid)	w_i (WHAM)	Δw_i	$\hat{\chi}_i$
0	300K	0.0	0.0	0.00	1.12
1	350K	−16.91	−16.89	−0.02	1.09
2	415K	−35.64	−35.52	−0.12	0.99
3	500K	−56.16	−55.83	−0.33	0.80

[a] The weights w_i were determined from the initial 100 ps of the REST/A simulation by the trapezoid rule eq 13 and the WHAM formula eq 14 together with the deviations Δw_i and the corresponding uniformity measures $\hat{\chi}_i$. The WHAM weights serve as starting values for the SST/A and SST/B simulation.

Next, we will study the sampling behavior of SST for which we will additionally examine the adaptation scheme based on the WHAM formula.

Reliability of the Trapezoid Rule for SST. Table 3 shows initial weights w_i determined from the short REST/A simulation. Because the solvent−solvent interactions do not contribute to the partition function of SST, these weights are tiny compared to those given in Table 2. Furthermore, the deviations Δw_i between the trapezoid rule eq 13 and the WHAM formula eq 14 are much larger than those listed in Table 2. The associated uniformity measures $\hat{\chi}_i$ predict that errors of this size will lead to a considerable nonuniformity of the SST sampling if the w_i are calculated by the trapezoid rule. Recall here that this rule can be derived based on two assumptions: (i) the heat capacity at consecutive temperatures T_i and T_{i+1} is constant and (ii) the logarithm $\ln(1 + \Delta T_{i+1,i}/T_i)$ is well approximated by its first order Taylor expansion. These conditions are harder to fulfill for SST than for CST because here the temperature steps $\Delta T_{i+1,i}$ are larger.

Figure 2 compares the effects of applying the trapezoid and WHAM rules, respectively, for updating the w_i during SST simulations. Figure 2(a) shows the deviation of the weight w_3 belonging to $T_3 = 500$ K during the SST/A (gray line, trapezoid) and SST/B (black line, WHAM) simulations from the initial value. The first update drastically changes w_3 in both simulations indicating that w_3 has been poorly estimated by the preparatory simulation. The subsequent updates reduce the large initial change to a final deviation of about 1.4 in both cases.

At first glance, the small difference of the resulting w_3 values suggests that the errors of the trapezoid rule are much smaller than predicted by the preparatory REST/A simulation. To check this issue, we have recalculated the weights w_i of the SST/A simulation *a posteriori* by the WHAM formula. The resulting time evolution of w_3 is depicted in Figure 2(a) by the gray dotted line. The difference of 0.22 ± 0.02 between the dotted gray and the solid gray lines is nearly constant during the simulation. Obviously, the trapezoid rule systematically underestimates w_3. A similar underestimate appears already in the initial guess for Δw_3 given in Table 2. Because of this systematic error of the trapezoid rule, the uniformity of the temperature sampling is expected to be suboptimal in SST/A.

Figure 2(b) shows the measured (circles) and predicted (squares) uniformity measures χ_i and $\hat{\chi}_i$ of the SST/A simulation. As indicated by the squares, the average deviations Δw_i between the trapezoid and the WHAM rules predict deviations of up to 13% from uniformity. The measured χ_i

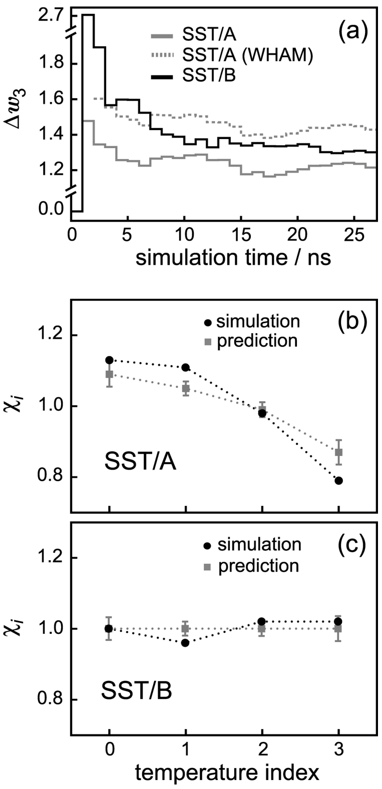

Figure 2. Uniformity of temperature sampling in SST simulations. (a) Deviation of the weight w_3 from its initial value in simulation SST/A (gray) and SST/B (black), respectively. The dotted line shows w_3' calculated a *posteriori* from SST/A using the WHAM expression eq 14. The broken w_3 axis serves to simplify the comparison with Figure 1(a). (b) Measured and predicted uniformity measures χ_i and $\hat{\chi}_i$ of SST/A and (c) of SST/B.

(circles) essentially follow these expectations but show even larger deviations from uniformity, yielding an RMSD of 14%. For instance, χ_3 happens to deviate by about two standard deviations from the respective expectation value $\hat{\chi}_3$. Like for CST, the standard deviations shown as gray bars in the figure were determined from additional MC simulations.

Figure 2(c) compares the uniformity measures of the SST/B simulation. Because the WHAM formula is the reference, the errors Δw_i vanish and eq 16 predicts a uniform sampling $\hat{\chi}_i = 1.0$ at all temperatures. In fact, the measured χ_i are close to 1.0 and show an RSMD of only 3%. Thus, SST/B exhibits an almost perfectly uniform sampling implying that the WHAM formula should be used in SST simulations for updating the w_i. The remaining deviations from uniformity are consistent with the narrow range of the statistical fluctuations estimated by our separate MC simulations. Compared with CST, the much smaller deviations of the χ_i from the predictions $\hat{\chi}_i$ indicate that many more round trips must have occurred during the SST simulations.

SST Round Trip Rates. Equation 17 predicts a round trip rate of 20 ns^{-1} for the simulations SST/(A,B), if the measured average acceptance probability $\bar{P} = 24\%$ is used. Our MC models of SST/(A,B) have reproduced this rate. For the MD simulations SST/A and SST/B, however, we found round trip rates of only 15.8 ns^{-1} and 16.5 ns^{-1}, respectively. Thus, the SST simulations apparently display the same memory effect which was already observed in the CST simulation and which reduces the round trip rates by 20%. Nevertheless, the SST round trip rates are by a factor of 26 larger than the CST rates. Correspondingly, the χ_i are much better converged in SST than in CST.

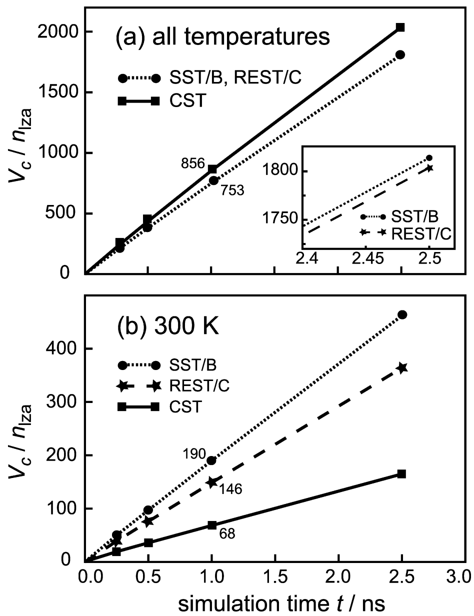

Figure 3. Volumes V_c sampled within 0.25 ns, 0.5 ns, 1 ns, and 2.5 ns by the simulations CST, SST/B, and REST/C. Due to the linearity of the shown $V_c(t)$ curves, the values at 1 ns represent the sampling speeds S in units of n_{lza}/ns. (a) Volumes $V_c(t)$ sampled by the trajectories at all temperatures. According to the inset the $V_c(t)$ curves of REST/C and SST/B are so close that they cannot be distinguished in the main plot. (b) Volume $V_c(t)$ sampled at the target temperature $T_0 = 300$ K. Note that the statistical errors of the measured volumes are smaller than the symbol sizes.

The large round trip rates and the nearly uniform sampling achieved in simulation SST/B lead to the expectation that this simulation setting leads for a peptide in solution to an improved statistics. We now will address this issue for our sample peptide 8ALA in TIP3P water.

Sampling Speed of CST, SST, and REST. The purpose of any tempering algorithm is to increase the sampling speed within the conformational space of the studied system. For our various simulation settings we determined the sampling speed using the LZA algorithm described in the Theory and Methods section. This iterative algorithm measures the volume $V_c(t)$ of the configuration space sampled within a simulation time t through an average number n_{lza} of iterations. The simulation speed $S(t)$ is then given by the time derivative of $V_c(t)$.

Figure 3(a) shows the volumes V_c sampled by the simulations CST, SST/B, and REST/C at all temperatures as functions of the simulation time t. The respective sampling speeds S are the constants $V_c(t)/t$ at $t = 1$ ns. The V_c curves of REST/C and SST/B cannot be graphically distinguished at the given scale as is documented by the inset in Figure 3(a). Apparently, CST provides the highest overall sampling speed of the three simulations. The sampling speeds of SST/B and REST/C are by about 10% smaller, which may be caused by the scaling of the solvent part of the Hamiltonian corresponding to an effectively cooler environment.

We have checked the latter conjecture by two MD simulations at 500 K (data not shown) with and without solvent scaling. Here, the effectively cooler solvent indeed reduces the sampling speed of 8ALA by about 20%. For lower temperatures we expect this effect to be correspondingly smaller. However, this small effect is tolerable if the sampling speed at the target temperature $T_0 = 300$ K is sufficiently enhanced, which is after all the aim of solute tempering methods.

Figure 3(b) compares the sampling speeds at $T_0 = 300$ K for the three methods. In contrast to the sampling speed of the generalized ensemble, at 300 K REST/C samples the peptide conformations 2.1 times faster than CST, and SST/B outperforms CST even by a factor of 2.8. Thus, SST/B samples also faster than REST/C, although the two simulations employ the same temperature ladder and the same solvent scaling. An explanation of this speedup is given by the different round trip rates of 11.1 ns^{-1} for REST/C and 16.4 ns^{-1} for SST/B. Due to the higher rate, SST delivers the structural information that is gathered at higher temperatures faster to the target temperature implying an enhanced speed of conformational sampling at T_0.

The reduced round trip rate of REST/C compared to SST/B directly results from the fact that for a given temperature ladder the average acceptance probabilities $\bar{P}_{\mathrm{RE}}$ of RE methods (including their sequential versions[13]) are smaller than the probabilities $\bar{P}_{\mathrm{ST}}$ of the corresponding ST methods.[40−42] The reason is that in RE the configurations of two replicas must simultaneously meet a certain energy criterion instead of only one replica in ST. Therefore, the average acceptance probability $\bar{P}_{\mathrm{RE}}$ should be approximately the square of $\bar{P}_{\mathrm{ST}}$. For example, the average acceptance probability of SST/B is about 26%. Thus, we expect a probability of 7% ($0.26^2 \approx 0.07$) for REST/C which is close to the measured value of 9%.

Optimal Exchange Scheme. Because the acceptance probability of REST/C is much smaller than that of SST/B, eq 17 predicts likewise different round trip rates. Compared with that expectation the round trip rate measured for REST/C (11.1 ns^{-1}) seems to be too high compared to SST/B (16.5 ns^{-1}). This large REST/C rate illustrates the advantage of the employed DEO exchange scheme compared to the SEO scheme of SST/B.[52] Furthermore, the optimal exchange probabilities $\bar{P}$ which yield the highest round trip rates are different for these two schemes. For SEO the optimal $\bar{P}$ is 23%,[52,66] whereas for DEO the optimal $\bar{P}$ is between 40% and 45% depending on the ladder size.[39,52]

To investigate the effects of the exchange scheme and the acceptance probability on the SST round trip rates we have carried out the two 12 ns simulations SST/C and SST/D. SST/C switches from SEO to DEO, and SST/D additionally uses five instead of four rungs to span the temperature range from 300 K up to 500 K (see Table 1). SST/D thereby increases $\bar{P}$ to about 40%. For SST/C we found a round trip rate of 20.0 ns^{-1} which is about 20% larger than that of SST/B. Thus, the DEO exchange scheme indeed speeds up the round trips sizably. An additional increase of $\bar{P}$ in simulation SST/D leads to a still larger round trip rate of 23.8 ns^{-1}.

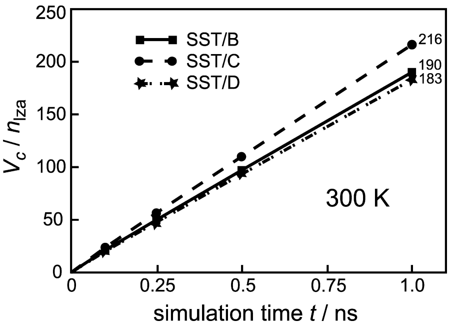

Figure 4. Sampled volumes for the simulations SST/B, SST/C, and SST/D at $T_0 = 300$ K by SST/C. Compared to SST/B the DEO exchange scheme increases the sampling speed by about 15%. This increase corresponds to the enhancement of the round trip rate. Interestingly, the sampling speed of SST/D is smaller than that of SST/B despite the much larger round trip rate. Here, the lower sampling speed is caused by the 25% reduced sampling time at 300 K due to the additional temperature rung, which is not compensated by the higher round trip rate.

Table 4. Round Trip Rates and Sampling Speeds Measured at Temperature $T_0 = 300$ K

label	round trip rates/ns^{-1}	speed/n_{lza}/ns
CST	0.63	68
REST/C	11.1	146
SST/A	15.8	204
SST/B	16.5	190
SST/C	20.0	216
SST/D	23.8	183

Figure 4 shows the effects of the round trip rates, which increase in the sequence SST/B, SST/C, and SST/D, on the sampling speed at 300 K. The highest sampling speed is achieved by SST/C. Compared to SST/B the DEO exchange scheme increases the sampling speed by about 15%. This increase corresponds to the enhancement of the round trip rate. Interestingly, the sampling speed of SST/D is smaller than that of SST/B despite the much larger round trip rate. Here, the lower sampling speed is caused by the 25% reduced sampling time at 300 K due to the additional temperature rung, which is not compensated by the higher round trip rate.

Finally, Table 4 summarizes the round trip rates and sampling speeds measured in our simulations. Using REST instead of CST speeds up the sampling by a factor of 2, whereas SST yields a speedup factor of 3. Note, however, that these factors are conservative estimates because of the particular choice of the 8ALA system. In this system the enthalpic barriers are small, and, therefore, the benefit of tempering methods is limited (see Introduction).[22] Correspondingly, the sampling speeds do not increase very much upon heating the system from the lowest to the highest temperature. However, target applications of tempering methods feature large enthalpic barriers[14,67] for which the sampling has to be accomplished mainly at high temperatures. Correspondingly, the sampling speed at T_0 should depend much stronger on the round trip rates. As a key result, SST in combination with the DEO exchange scheme should generally show much better sampling properties than REST or CST.

Conclusion

We have introduced simulated solute tempering (SST) which combines the (serial) simulated tempering method with solute tempering, i.e. the key idea of the REST approach. SST poses an efficient alternative to conventional simulated tempering and replica exchange, including REST and its sequential version SREST because it offers the largest acceptance probabilities for a given temperature ladder.

From a practical point of view, it is gratifying to note that SST can be easily implemented. For example, for rigid models of the solvent molecules only the partial charges and the van der Waals parameters have to be scaled to generate the modified Hamiltonians at higher temperatures. Furthermore, SST enables a parallel sampling of many replicas even on heterogeneous computer clusters, because all replicas travel independently through temperature space.

The necessary ingredients of SST are the weights, i.e. the dimensionless free energies of the system at the rungs of the temperature ladder. The trapezoid rule recently suggested by Park and Pande[9] for the computation of the weights is not accurate enough for SST but well suited for CST. Our rederivation of this rule has shown that it is only accurate for temperature ladders featuring small temperature differences, which is the case for CST. In SST a few rungs suffice to span a large temperature range. Due to the failure of the trapezoid rule, the SST weights should be updated using the more complex but asymptotically unbiased WHAM formula of Kumar et al.[45] Then an almost perfectly uniform sampling of the temperature rungs is guaranteed, if the simulation time exceeds the average round trip time by about 2 orders of magnitude.

Our comparison of different sampling methods (REST, CST, SST) applied to an octapeptide in explicit water has demonstrated that the SST sampling is the most efficient one as was shown by the largest round trip rate and the highest sampling speed at T_0. Finally we have shown that the round trip rates can be maximized by using the DEO instead the SEO exchange scheme and by choosing a temperature ladder that provides acceptance probabilities close to 45%.

In conclusion, the sampling efficiency of SST as well as its ease of implementation and application nourishes the hope that simulated tempering will become more popular and that we may see many exciting applications in the future.

Acknowledgment. This work was supported by the Deutsche Forschungsgemeinschaft (Grants SFB 533/C1 and SFB 749/C4). Computer time provided by Leibniz Rechenzentrum (project uh408) is gratefully acknowledged.

Appendix

For a canonical ensemble with a heat capacity C_V independent of the temperature, eq 12 can be derived by the following physical considerations. Using the shorthand notation $\Delta X_{ji} \equiv X_j - X_i$, the entropy difference $\Delta S_{ji} = C_V \ln(1 + \Delta T_{ji}/T_i)$ can be estimated by a first order Taylor expansion of the logarithm as $\Delta S_{ji} \approx C_V \Delta T_{ji}/T_i$. With $C_V = \Delta U_{ji}/\Delta T_{ji}$ one gets

$$\Delta S_{ji} \approx \frac{\Delta U_{ji}}{T_i} \tag{19}$$

With the Helmholtz free energy $F = U - TS$, where U denotes the internal energy, the free energy difference ΔF_{ji} between the systems at T_j and T_i can be written as

$$\Delta F_{ji} = \Delta U_{ji} - T_i \Delta S_{ji} - S_i \Delta T_{ji} - \Delta T_{ji} \Delta S_{ji} \tag{20}$$

Inserting eq 19 one immediately finds

$$F_j \approx F_i - S_i \Delta T_{ji} - \Delta U_{ji} \frac{\Delta T_{ji}}{T_i} \tag{21}$$

With eq 21, the dimensionless free energy difference $\Delta\phi_{ji} = F_j/k_B T_j - F_i/k_B T_i$ can be written as

$$\Delta\phi_{ji} \approx \Delta\beta_{ji}(U_i + \Delta U_{ji}) \tag{22}$$

Interchanging i and j one obtains an equally valid estimate

$$\Delta\phi_{ji} \approx \Delta\beta_{ji}(U_j - \Delta U_{ji}) \tag{23}$$

where we have used $\Delta X_{ij} = -\Delta X_{ji}$. An even better approximation is then given by the arithmetic mean

$$\Delta\phi_{ji} \approx \Delta\beta_{ji} \frac{U_i + U_j}{2} \tag{24}$$

where ΔU_{ji} cancels. Restricting the internal energy U to its configurational part, i.e., to the average potential energy $\langle E \rangle$, yields the "trapezoid" rule eq 12.

Supporting Information Available: Average acceptance probabilities $\bar{P}_{i,i\pm 1}$ for the various simulations (Tables S1 and S2). This material is available free of charge via the Internet at http://pubs.acs.org.

References

(1) Mitsutake, A.; Sugita, Y.; Okamoto, Y. *Biopolymers (Peptide Sci.)* **2001**, *60*, 96.

(2) Okamoto, Y. *J. Mol. Graphics Modell.* **2004**, *22*, 425.

(3) Hukushima, K.; Nemoto, K. *J. Phys. Soc. Jpn.* **1996**, *65*, 1604.

(4) Hansmann, U. H. E. *Chem. Phys. Lett.* **1997**, *281*, 140.

(5) Sugita, Y.; Okamoto, Y. *Chem. Phys. Lett.* **1999**, *314*, 141.

(6) Metropolis, N.; Rosenbluth, A. W.; Rosenbluth, M. N.; Teller, A. H.; Teller, E. *J. Chem. Phys.* **1953**, *21*, 1087.

(7) Lyubartsev, A. P.; Martinovski, A. A.; Shevkunov, S. V.; Vorontsov-Velyaminov, P. N. *J. Chem. Phys.* **1992**, *96*, 1776.

(8) Marinari, E.; Parisi, G. *Europhys. Lett.* **1992**, *19*, 451.

(9) Park, S.; Pande, V. S. *Phys. Rev. E* **2007**, *76*, 016703.

(10) Sugita, Y.; Kitao, A.; Okamoto, Y. *J. Chem. Phys.* **2000**, *113*, 6042.

(11) Fukunishi, H.; Watanabe, O.; Takada, S. *J. Chem. Phys.* **2002**, *116*, 9058.

(12) Affentranger, R.; Tavernelli, I. *J. Chem. Theory Comput.* **2006**, *2*, 217.

(13) Hagen, M.; Kim, B.; Liu, P.; Friesener, R. A.; Berne, B. J. *J. Phys. Chem. B* **2007**, *111*, 1416.

(14) Liu, P.; Kim, B.; Friesner, R. A.; Berne, B. J. *Proc. Natl. Acad. Sci. U.S.A.* **2005**, *102*, 13749.

(15) Kubitzki, M. B.; de Groot, B. L. *Biophys. J.* **2007**, *92*, 4262.

(16) Xu, W.; Lai, T.; Yang, Y.; Mu, Y. *J. Chem. Phys.* **2008**, *128*, 175105.

(17) Lyman, E.; Ytreberg, F. M.; Zuckerman, D. M. *Phys. Rev. Lett.* **2006**, *96*, 028105.

(18) Rao, F.; Caflisch, A. *J. Chem. Phys.* **2003**, *119*, 4035.

(19) Zhang, W.; Wu, C.; Duan, Y. *J. Chem. Phys.* **2005**, *123*, 154105.

(20) Rick, S. W. *J. Chem. Theory Comput.* **2006**, *2*, 939.

(21) Periole, X.; Mark, A. E. *J. Chem. Phys.* **2007**, *126*, 014903.

(22) Zuckerman, D. M.; Lyman, E. *J. Chem. Theory Comput.* **2006**, *2*, 1200.

(23) Denschlag, R.; Lingenheil, M.; Tavan, P. *Chem. Phys. Lett.* **2008**, *458*, 244.

(24) Zhou, R.; Berne, B. J.; Germain, R. *Proc. Natl. Acad. Sci. U.S.A.* **2001**, *98*, 14931.

(25) Sanbonmatsu, K. Y.; García, A. E. *Proteins* **2002**, *46*, 225.

(26) Pitera, J. W.; Swope, W. *Proc. Natl. Acad. Sci. U.S.A.* **2003**, *100*, 7587.

(27) Cecchini, M.; Rao, F.; Seeber, M.; Caflisch, A. *J. Chem. Phys.* **2004**, *121*, 10748.

(28) Jas, G. S.; Kuczera, K. *Biophys. J.* **2004**, *87*, 3786.

(29) Yang, W. Y.; Pitera, J. W.; Swope, W. C.; Gruebele, M. *J. Mol. Biol.* **2004**, *336*, 241.

(30) Nguyen, P. H.; Stock, G.; Mittag, E.; Hu, C.-K.; Li, M. A. *Proteins* **2005**, *61*, 795.

(31) Villa, A.; Stock, G. *J. Chem. Theory Comput.* **2006**, *2*, 1228.

(32) Schrader, T. E.; Schreier, W. J.; Cordes, T.; Koller, F. O.; Babitzki, G.; Denschlag, R.; Renner, C.; Lweneck, M.; Dong, S.-L.; Moroder, L.; Tavan, P.; Zinth, W. *Proc. Natl. Acad. Sci. U.S.A.* **2007**, *104*, 15729.

(33) Villa, A.; Widjajakusuma, E.; Stock, G. *J. Phys. Chem.* **2008**, *112*, 134.

(34) Abraham, M. J.; Gready, J. E. *J. Chem. Theory Comput.* **2008**, *4*, 1119.

(35) Nadler, W.; Hansmann, U. H. E. *J. Phys. Chem. B* **2008**, *112*, 10386.

(36) Calvo, F. *J. Chem. Phys.* **2005**, *123*, 124106.

(37) Brenner, P.; Sweet, C. R.; VonHandorf, D.; Izaguirre, J. A. *J. Chem. Phys.* **2007**, *126*, 074103.

(38) Sindhikara, D.; Meng, Y.; Roitberg, A. E. *J. Chem. Phys.* **2008**, *128*, 024103.

(39) Denschlag, R.; Lingenheil, M.; Tavan, P. *Chem. Phys. Lett.* **2009**, *473*, 193.

(40) Mitsutake, A.; Okamoto, Y. *Chem. Phys. Lett.* **2000**, *332*, 131.

(41) Park, S. *Phys. Rev. E* **2008**, *77*, 016709.

(42) Zhang, C.; Ma, J. *J. Chem. Phys.* **2008**, *129*, 134112.

(43) Mitsutake, A.; Okamoto, Y. *J. Chem. Phys.* **2004**, *121*, 2491.

(44) Bussi, G.; Gervasio, F. L.; Laio, A.; Parrinello, M. *J. Am. Chem. Soc.* **2006**, *128*, 13435.

(45) Kumar, S.; Bouzida, D.; Swendsen, R. H.; Kollman, P. A.; Rosenberg, J. M. *J. Comput. Chem.* **1992**, *13*, 1011.

(46) Shirts, M. R.; Chodera, J. D. *J. Chem. Phys.* **2008**, *129*, 124105.

(47) Kobrak, M. N. *J. Comput. Chem.* **2003**, *24*, 1437.

(48) Berg, B. A. *J. Stat. Phys.* **1996**, *82*, 323.

(49) Bartels, C.; Karplus, M. *J. Comput. Chem.* **1997**, *18*, 1450.

(50) Park, S.; Ensign, D. L.; Pande, V. S. *Phys. Rev. E* **2006**, *74*, 066703.

(51) Zhang, C.; Ma, J. *Phys. Rev. E* **2007**, *76*, 036708.

(52) Lingenheil, M.; Denschlag, R.; Mathias, G.; Tavan, P. *Chem. Phys. Lett.* 2009. in press (doi:10.1016/j.cplett.2009.07.039).

(53) Okabe, T.; Kawata, M.; Okamoto, Y.; Mikami, M. *Chem. Phys. Lett.* **2001**, *335*, 435.

(54) Gardiner, C. W. *Handbook of Stochastic Methods*, 2nd ed.; Springer, Berlin, 1985.

(55) Nadler, W.; Hansmann, U. H. E. *Phys. Rev. E* **2007**, *75*, 026109.

(56) MacKerell, A. D.; et al. *J. Phys. Chem. B* **1998**, *102*, 3586.

(57) Jorgensen, W. L.; Chandrasekhar, J.; Madura, J. D.; Impey, R. W.; Klein, M. L. *J. Chem. Phys.* **1983**, *79*, 926.

(58) Schaftenaar, G.; Noordik, J. *J. Comput.-Aided Mol. Des.* **2000**, *14*, 123.

(59) Mathias, G.; Egwolf, B.; Nonella, M.; Tavan, P. *J. Chem. Phys.* **2003**, *118*, 10847.

(60) Niedermeier, C.; Tavan, P. *J. Chem. Phys.* **1994**, *101*, 734.

(61) Allen, M. P.; Tildesley, D. J. *Computer Simulations of Liquids*; Oxford University Press: Oxford, 1987.

(62) Eichinger, M.; Grubmüller, H.; Heller, H.; Tavan, P. *J. Comput. Chem.* **1997**, *18*, 1729.

(63) Kraeutler, V.; van Gunsteren, W. F.; Hünenberger, P. H. *J. Comput. Chem.* **2001**, *22*, 501.

(64) Berendsen, H. J. C.; Postma, J. P. M.; van Gunsteren, W. F.; Dinola, A.; Haak, J. R. *J. Chem. Phys.* **1984**, *81*, 3684.

(65) Lyman, E.; Zuckerman, D. M. *Biophys. J.* **2006**, *91*, 164.

(66) Kone, A.; Kofke, D. A. *J. Chem. Phys.* **2005**, *122*, 206101.

(67) Reichold, R.; Fierz, B.; Kiefhaber, T.; Tavan, P. Submitted for publication.

CT900274N

5 Relaxation eines lichtschaltbaren Peptides

In den vorangegangenen Kaptiteln standen theoretische Methoden zur Bestimmung der kanonischen Gleichgewichtsensembles von Peptid-Lösungsmittel-Systemen im Vordergrund. Wie ich bereits in der Einleitung angesprochen habe, war der Grund für diese Untersuchungen ganz praktischer Natur, da ich zur Simulationsbeschreibung der Nicht-Gleichgewichtsdynamiken ausgewählter Modellpeptide deren Gleichgewichtsensembles benötigte. Der folgende Abschnitt ist ein Nachdruck[1] des Artikels

> Robert Denschlag, Wolfgang J. Schreier, Benjamin Rieff, Tobias E. Schrader, Florian O. Koller, Luis Moroder, Wolfgang Zinth, Paul Tavan: „Relaxation time prediction for a light switchable peptide by molecular dynamics“
> *Phys. Chem. Chem. Phys.* **12**, 6204 - 6218 (2010),

den ich zusammen mit Paul Tavan und den genannten Autoren verfasst habe. Mittels Computersimulationen und spektroskopischen Methoden werden Struktur und Dynamik eines lichtschaltbaren Peptids namens cAPB untersucht. Im Mittelpunkt der Arbeit steht die Charakterisierung der durch die *cis-trans* Isomerisierung des Farbstoffes ausgelösten Relaxationsdynamiken. Unter Verwendung der REST Methode[2] werden die strukturellen *cis-* und *trans*-Gleichgewichtsensembles simuliert, welche anschließend als Referenz zur Bestimmung des Fortschritts der lichtinduzierten Relaxation dienen. Die Ergebnisse werden mit Daten aus zeitaufgelöster IR-Spektroskopie verglichen, wobei es erstmals gelungen ist, mit Simulationen längere als die experimentell zugänglichen Zeitskalen abzudecken. Die berechnete 23 ns Relaxationszeit für den *cis-trans*-Übergang ist mithin eine Vorhersage der Theorie.

---

[1] Mit freundlicher Genehmigung der Royal Society of Chemistry.

[2] Zu Beginn dieses Projektes war die SST Abtasttechnik noch nicht ausgearbeitet.

Relaxation time prediction for a light switchable peptide by molecular dynamics†

Robert Denschlag,[a] Wolfgang J. Schreier,[b] Benjamin Rieff,[a] Tobias E. Schrader,[b] Florian O. Koller,[b] Luis Moroder,[c] Wolfgang Zinth[b] and Paul Tavan*[a]

Received 20th October 2009, Accepted 25th February 2010
First published as an Advance Article on the web 14th April 2010
DOI: 10.1039/b921803c

We study a monocyclic peptide called cAPB, whose conformations are light switchable due to the covalent integration of an azobenzene dye. Molecular dynamics (MD) simulations using the CHARMM22 force field and its CMAP extension serve us to sample the two distinct conformational ensembles of cAPB, which belong to the *cis* and *trans* isomers of the dye, at room temperature. For gaining sufficient statistics we apply a novel replica exchange technique. We find that the well-known NMR distance restraints are much better described by CMAP than by CHARMM22. In cAPB, the ultrafast *cis*/*trans* photoisomerization of the dye elicits a relaxation dynamics of the peptide backbone. Experimentally, we probe this relaxation at picosecond time resolution by IR spectroscopy in the amide I range up to 3 ns after the UV/vis pump flash. We interpret the spectroscopically identified decay kinetics using ensembles of non-equilibrium MD simulations, which provide kinetic data on conformational transitions well matching the observed kinetics. Whereas spectroscopy solely indicates that the relaxation toward the equilibrium *trans* ensemble is by no means complete after 3 ns, the 20 ns MD simulations of the process predict, independently of the applied force field, that the final relaxation into the *trans*-ensemble proceeds on a time scale of 23 ns. Overall our explicit solvent simulations cover more than 6 μs.

Introduction

Predicting the native states and the corresponding folding pathways of proteins from their amino acid sequences are the two key challenges in the computational biology of protein-folding.[1] In principle, all-atom molecular dynamics (MD) simulations employing equilibrium and non-equilibrium settings can tackle these two problems with a degree of spatial and temporal resolution unreachable by other methods.

Unfortunately, the formation of the tertiary structures building up the native state requires several microseconds in the case of fast folding proteins and at least milliseconds in other cases.[2,3] These time scales are ten to twelve orders of magnitude larger than a single MD integration step of about 1 fs used in standard simulations. Due to the progress of computer power, sampling times of small proteins in explicit solvent covering several microseconds are nowadays achievable.[4] However, because MD simulations are single molecule experiments, a multiple of the expected folding time has to be simulated for meaningful statistics.[3,5]

More statistics with the same computational effort can be produced by modeling the solvent environment implicitly instead of explicitly. Models of the "generalized Born" (GB) type[6] are particularly popular representatives of such approaches,[7–9] but an implicit solvent description may entail oversimplifications.[10,11] For example, GB is known to overstabilize salt bridges[12] and its lack of solvent viscosity can lead to wrong estimates of timescales.[9] Moreover, the foundation of GB methods lacks theoretical rigor, because it definitely does not provide for solvated proteins a solution of the Poisson equation, which is required for well-founded continuum approaches.[13–15]

On the other hand, it is not clear whether explicit solvent descriptions, which should be more accurate than implicit solvent models,[2,16,17] are precise enough for reliable predictions.[17,18] To gain an access toward scrutinizing the

---

[a] *Theoretische Biophysik, Department für Physik, Ludwig-Maximilians-Universität, Oettingenstr. 67, 80538 München, Germany. E-mail: tavan@physik.uni-muenchen.de; Fax: +49-89-2180-9202; Tel: +49-89-2180-9220*
[b] *Lehrstuhl für Biomolekulare Optik and Munich Center for Integrated Protein Science CIPSM, Ludwig-Maximilians-Universität, Oettingenstr. 67, 80538 München, Germany*
[c] *Max Planck Institut für Biochemie, Am Klopferspitz 18a, 82152 Martinsried, Germany*

† Electronic supplementary information (ESI) available: 7 tables, 7 figures, and a text explaining the additional material. The convergence of the REST simulations is illustrated by Fig. S12 and the differences induced into the free-energy landscapes of cAPB at 300 K (*cf.* Fig. 3) by the two force fields are discussed. The proton distances relevant for comparisons of NMR and REST simulation data are listed in Tables S4 and S5. The force field employed for the APB chromophore and its linkage to the peptide is specified through Fig. S13 and Tables S6–S9. Fig. S14 and S15 provide illustrations for the arguments on the temperature dependence of the RMSV contained in a corresponding section. Fig. S16 documents the temperature independence of the helicity measure H_2. Fig. S17 shows the results of our simulations on the cooling kinetics, and Table S10 adds quantitative data to the temporally resolved free energy landscapes in Fig. S11 by specifying the associated average helicities $\bar{H}_1(t)$ and $\bar{H}_2(t)$. Finally, Fig. S18 presents the relaxation data shown in Fig. 10 once again but now on a logarithmic time scale to more clearly reveal the fast processes. See DOI: 10.1039/b921803c

quality of the force fields employed in such all-atom MD simulations it is necessary to compare computational with experimental results. However, in order to actually bridge the gap between experiment and simulation, the sample system under consideration and the applied experimental techniques have to meet a series of conditions.

To be specific, the experimental techniques should offer a temporal and spatial resolution close to that of MD (fs, Å) and the sample system should be measured at (or at least near) physiological conditions. As of today, there is no experimental technique which combines a fs time resolution with an atomistic spatial resolution. On the other hand, ultra-fast pump–probe spectroscopy[19] and NMR spectroscopy[20] are techniques which separately achieve either a temporal or a spatial resolution close to that of MD. Here, ultrafast pump–probe spectroscopy enables studies of non-equilibrium dynamics and NMR spectroscopy yields structural information on equilibrium ensembles.

For ultrafast spectroscopy to work at its best, one must be able to elicit non-equilibrium peptide dynamics by a light pulse thus providing a temporally well-defined starting point. An established approach serving this purpose is a laser-induced temperature jump.[21–23] However, such a jump causes shock waves and may thus entail non-physiological system conditions.[24] A more direct way consists in covalently integrating a fast light switch into the backbone of a peptide.[25–32] The ultrafast *cis–trans* photoisomerization (200 fs) and the large geometric changes of azobenzene dyes qualify these molecules as particularly suitable photoswitches.[31] Below we will denote the corresponding constructs as azopeptides.

The limited computational resources strongly restrict the size and complexity of a chosen sample peptide, because the simulation of the necessarily large[33] solvent environment demands a huge computational effort. Thus, nowadays MD can deliver a sufficient statistics only for quite simple peptides in solution. A restricted complexity of the system is additionally important for a clear-cut interpretation of experimental data. Further below, we will also have to tackle the difficulties posed by such interpretations.

The design and synthesis of different azopeptides[26–30] has provided the material for a series of experimental[25–27,34–39] and theoretical[38–43] investigations. These studies aimed at characterizing (i) the conformational equilibria in the *cis* and *trans* states of the azobenzene switch and (ii) the light-induced dynamics transforming the perturbed *cis* ensemble into the *trans* equlibrium ensemble (or *vice versa*).

However, not all azopeptides are equally suited for simulation descriptions. For example, in light-switchable β-hairpin models[29,32,44] the folding process can be induced by the *trans* to *cis* photoisomerization of the switch. Like in any β-hairpin peptide, the folding process takes at least a few micro-seconds until completion.[38,45] Currently, such folding times cannot be covered by MD descriptions with sufficient statistics (if one employs an explicit solvent setting). Moreover, for β-hairpins the use of enhanced sampling techniques like replica exchange[46] may even slow down the sampling as recently shown by Denschlag *et al.*[47]

Much better suited for simulation descriptions is a class of azopeptides, which contains octapeptide fragments cyclized by an azobenzoic derivative.[26,28] One of these peptides is bicyclic.[26] Here, a disulfide bridge additionally restricts the conformational flexibility thus reducing the computational effort required for a statistically sufficient MD sampling. Correspondingly the bicyclic models have been extensively studied by MD.[41–43] However, when one searches for models of the conformational dynamics in native peptides, the lacking conformational flexibility clearly qualifies the bicyclic azopeptides as suboptimal. In this work we study the more flexible monocyclic azopeptide cAPB, whose chemical structure is depicted in Fig. 1.

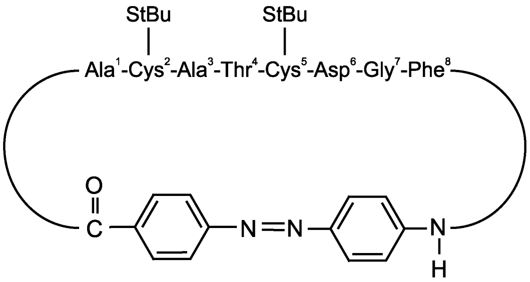

Fig. 1 Chemical structure of the model azopeptide cAPB. Here, the sequence Ala-Cys-Ala-Thr-Cys-Asp-Gly-Phe, which is part of the binding pocket of thioredoxin reductase (residues 134–141), is cyclized by (4-amino)phenylazobenzoic acid (APB). The formation of a disulfide bridge is prevented by protective S-*tert*-butylthio-groups (StBu) at the two cysteins.

Previous investigations of cAPB by NMR[26] and by MD[40] showed that the isomeric state of the chromophore, which is either *cis* or *trans*, defines two distinctly different structural ensembles of the peptide backbone. In the *trans* ensemble the backbone is restricted to extended conformations. In contrast, the *cis* ensemble features a much larger number of conformational substates. Although MD predicted multiple open-loop conformations for the *cis* ensemble, which were missing in the refined NMR structures, the MD ensembles were shown to comply with the NMR distance restraints. As a technical critique we note that the MD simulations were performed at 500 K (and thus at a much larger temperature than the NMR measurements) for the sole reason of collecting sufficient statistics at a manageable computational effort.

Furthermore, the relaxation dynamics of cAPB during the first nanosecond after *cis*/*trans* photoisomerization has been monitored by time-resolved pump–probe spectroscopy in the visible spectral range supplemented by an MD analysis of the energy relaxation.[39] In this study the UV/vis absorbtion of the azobenzene switch was used as a probe for the relaxation of the cyclic peptide. The study demonstrated fast and strongly driven structural changes in the peptide chain after the isomerization. The kinetics of the energy relaxation obtained by MD was shown to quantitatively agree with the experimental results. For the first nanosecond, within which the main processes of conformational dynamics occur near the switch, the optical spectrum of this dye was shown to be a sensitive probe of the ongoing relaxation. At a delay time of 1 ns the optical spectrum of the dye closely resembles that of the relaxed target state. For that point in time the MD simulations predicted that the relaxation of the peptide backbone is still far from being complete.[39] Thus, UV/vis pump probe spectroscopy monitoring the chromophore appears to loose its sensitivity after 1 ns.

In summary, the quoted earlier studies left several questions unanswered. First, one may wonder whether the reported agreement between MD structures and NMR distance restraints prevails, if the MD simulations serving to determine the conformational ensembles are carried out at a temperature of 300 K, which matches the conditions of the NMR measurements much more closely. Here one could speculate that lowering the temperature in the MD simulations from 500 to 300 K leads to more compact peptide structures thus modifying the prediction of open-loops as the dominant motifs in the *cis*-cAPB ensemble.[40] Concerning the relaxation of the peptide one may ask how long it actually takes for the peptide to reach the equilibrium ensemble of the *trans*-state when starting from the *cis*-ensemble.

Addressing these questions we have reinvestigated the cAPB peptide by applying various novel or revised methods:

- Instead of sampling the *cis* and *trans* ensembles by plain MD at the elevated temperature of 500 K[40] we have applied a variant[48] of the Hamilton replica exchange (HRE) approach originally suggested by Liu *et al.*,[49] which can yield the equilibrium ensembles at ambient temperature with a manageable computational effort.
- Instead of employing the total energy[39] of the peptide as a probe for the relaxation dynamics simulated by MD we now use a structural observable sensitive for the backbone conformation. Here, the equilibrium ensembles of the HRE simulations provide measures for judging the progress of the relaxation.
- Instead of using the UV/vis spectrum of the chromophore as a probe, we now apply ultrafast infrared (IR) absorption spectroscopy in the region of the amide I band of the peptide allowing us to directly and more sensitively monitor the relaxation of the backbone.

As a more technical issue we additionally check to what extent the MD results depend on the applied force field. Instead of solely using the CHARMM22 force field,[50] we have also employed its CMAP extension.[51] Comparison with experimental data will then allow a judgement on the relative performance of these two force fields. Altogether, we have spent a simulation time of more than 6 μs to cAPB solvated in dimethyl-sulfoxide (DMSO).

Theoretical methods

Replica Exchange

To sample the conformational space of the *cis* and *trans* ensembles of cAPB at 300 K we have applied a variant[48] of replica exchange with solute tempering (REST).[49] Within REST, $N + 1$ copies (replicas) of the system are simulated at different temperatures $T_0 < T_1 < \cdots < T_N$. The canonical ensembles thus generated at the temperatures T_i constitute a so-called generalized ensemble. After fixed time intervals, one checks whether the temperatures of replica pairs can be exchanged. A Metropolis criterion[52] determines the exchange probability

$$P_{ij} = \min[1,\exp(-\Delta_{ij})] \tag{1}$$

between replicas at T_i and T_j with

$$\Delta_{ij} = \beta_i\cdot[E(x_j, T_i) - E(x_i, T_i)] + \beta_j\cdot[E(x_i, T_j) - E(x_j, T_j)] \tag{2}$$

to preserve the canonical ensembles. Here, $E(x, T)$ is the potential energy of the configuration x at the temperature T and $\beta = 1/k_BT$ where k_B is the Boltzmann constant.

Within REST, the potential energy of a replica at the temperature T_i is

$$E(x, T_i) = \lambda_{i,0}E^{pp}(x) + \lambda_{i,1}E^{ss}(x) + \lambda_{i,2}E^{ps}(x) \tag{3}$$

where E^{pp}, E^{ss} and E^{ps} are the solute–solute, solvent–solvent, and solute–solvent parts of the (unscaled) potential energy function at T_0 and $\lambda_{i,h}$ are suitable parameters depending on T_i. We choose

$$\lambda_{i,0} = 1,\ \lambda_{i,1} = T_i/T_0,\ \lambda_{i,2} = \sqrt{T_i/T_0}. \tag{4}$$

Note that the form of $\lambda_{i,2}$ slightly differs from the form used in the original work[49] because our choice is particularly handy for implementations.[48] When using the CHARMM force field[50] and a rigid solvent model, *e.g.*, solely the partial charges and the Lennard-Jones energies of the solvent molecules have to be multiplied by $\sqrt{T_i/T_0}$ and T_i/T_0, respectively, to achieve the scaling required by eqn (3) and (4), which then includes even the mean field contributions[33,53] to the energy function.

The advantage of the REST approach described above becomes apparent after a few algebraic operations. With eqn (3) and (4), eqn (2) reduces to

$$\begin{aligned}\Delta_{ij} =&(\beta_i - \beta_j)\cdot[E^{pp}(x_j) - E^{pp}(x_i)]\\ &+ (\sqrt{\beta_0\beta_i} - \sqrt{\beta_0\beta_j})\cdot[E^{sp}(x_j) - E^{sp}(x_i)].\end{aligned} \tag{5}$$

Thus, the difference Δ_{ij}, which determines the acceptance probability (1), is solely calculated from the solute–solute and solute–solvent energies, while the potential energy E^{ss} of the solvent cancels. As a consequence, the number of replicas needed to cover a given temperature range is drastically reduced.

Simulation system and force-fields

The cAPB model peptide was studied by molecular dynamics (MD) simulations. As starting structures for the *cis* and *trans* states of cAPB we have chosen the respective NMR structures of lowest energy.[26] Each initial structure was placed into the center of an orthorhombic dodecahedron of 24 Å inner radius and was surrounded by 649 DMSO molecules. Thus each system contained $N = 2744$ atoms. For the peptide moiety either the CHARMM22 all-atom force-field,[50] which we will denote by the shortcut "C22" from now on, or its CMAP extension[51] were employed. Note here that the CMAP extension of C22 solely modifies the potentials of the ϕ/ψ dihedral angles within the peptide backbone. The force field required for the chromophore and for its linkages to the peptide backbone were adopted from ref. 54. These parameters are reproduced in the electronic supplementary information (ESI). A united-atom model was chosen for the DMSO molecules.[55]

MD simulation techniques

The software package EGO-MMVI[33] was used for the MD simulations. The electrostatic interactions were treated combining structure-adapted multipole expansions[56] with a moving-boundary reaction-field approach.[33] Here, the electrostatic interactions were explicitly evaluated up to a distance of about 24 Å to fulfill the minimum image convention.[53] Beyond this distance, a dielectric continuum was assumed with a static dielectric constant $\varepsilon_s = 45.8$. The van-der-Waals interactions were explicitly evaluated up to a distance of 10 Å; at larger distances a mean-field approach was applied.[53] The dynamics was integrated by a multiple-time-step scheme[57] building upon a basic time step of 1 fs. The lengths of all bonds involving hydrogen atoms were constrained using the M-SHAKE algorithm[58] with relative tolerance of 10^{-6}. Temperature T and pressure p were controlled by a Berendsen[59] thermostat and barostat with coupling constants of 0.5 and 5 ps, respectively.

System preparation

After minimizing the energy of the four simulation systems (*cis* and *trans* cAPB with and without CMAP) they were equilibrated for 400 ps by a three step MD simulation as follows: (i) within the first 100 ps the systems were tuned to ambient temperature (300 K) and pressure (1 bar) while the peptide was kept rigid so that the DMSO molecules could adapt to the solute; (ii) during subsequent 50 ps simulations the positions of the C_α atoms were softly constrained to the initial locations by harmonic restraints; (iii) the equilibrations were completed by 250 ps unconstrained simulations in which our Berendsen thermostat was separately applied to each of the two subsystems, the solute and the solvent. In all subsequent simulations serving for data collection we switched from the initial NpT ensemble to an NVT ensemble by deactivating the barostat and maintaining the resulting volume V. In these simulations we furthermore switched off the thermostat of the solute thus implementing a non-invasive solute tempering.[60]

Simulations

Table 1 summarizes our MD simulations. The equilibrium properties of cAPB were probed by four REST simulations: The simulations R/C/C22 and R/T/C22 served to explore the conformational ensembles of *cis* (C) and *trans* (T) cAPB as predicted by the standard C22 force field. In the simulations R/C/CMAP and R/T/CMAP the CMAP extension of that force field was employed. The REST simulations R/C/C22, R/T/C22, and R/T/CMAP covered a simulation time of 100.5 ns for each replica, whereas for the simulation R/C/CMAP this time was extended to 150.5 ns.

During the first 0.5 ns no exchanges were attempted. This preliminary period served to generate different initial structures for the replicas residing at the various rungs of the temperature ladder specified below. Subsequently, exchange trials were attempted every 20 ps using a deterministic even-odd exchange scheme.[46] Data for analysis were saved every 2 ps. The REST simulations covered the temperature range from 300 K to 570 K by ten rungs with the following ladder: 300, 323, 347, 372, 399, 428, 460, 495, 532, 570 K. This temperature ladder leads to an average acceptance probability (AP) of about 40% (±5%) and, thus, yields the highest round trip rates possible within the highly efficient even-odd exchange scheme employed.[61,62] In our REST simulations the replicas executed random walks yielding a nearly uniform sampling of the temperature ladder (data not shown). Thus, sampling problems like those observed earlier[63] in relatively short (5 ns) REST simulations of other peptides were absent in our peptide-solvent systems.

Table 1 Overview over the MD simulations

Label[a]	Duration[b]	Exchange[c]	Range[d]
R/C/C22	10 × 100.5 ns	20 ps	300 K–570 K
R/C/CMAP	10 × 150.5 ns	20 ps	300 K–570 K
R/T/C22	10 × 100.5 ns	20 ps	300 K–570 K
R/T/CMAP	10 × 100.5 ns	20 ps	300 K–570 K
I/C22	50 × 20 ns	—	300 K
I/CMAP	50 × 20 ns	—	300 K

[a] Name. [b] Simulation times. [c] Time between exchange trials. [d] Temperature range covered by the simulation.

To elucidate the relaxation dynamics initiated by the *cis*-to-*trans* isomerization of the chromophore, we have carried out two sets of non-equilibrium MD simulations denoted as I/C22 and I/CMAP (*cf.* Table 1). Each of these sets contains 50 separate runs differing by the initial structures randomly chosen from the REST simulations R/C/C22 and R/C/CMAP, respectively, and by the choice of the force field, of course. After a preparatory period of one picosecond, the chromophore was driven from *cis* to *trans* by activating a potential designed to mimic the photoisomerization.[39,54] After 10 ps this potential was switched off without causing perturbations, because the chromophore reaches the *trans* state much more rapidly (< 1 ps). The thus initiated relaxation dynamics of the backbone was monitored for the following 20 ns. Data for analysis were saved every 100 fs within the first 10 ps, every picosecond within the time span from 10 ps to 100 ps, and every 10 ps thereafter.

Helicity elongation score

To characterize the conformational ensembles sampled by the peptide backbone of cAPB in the *cis* and *trans* states of the chromophore and to measure the progress of the peptide's relaxation from the initial *cis* to the final *trans* ensemble, we employed the so-called helicity elongation score (HELO). This score can distinguish "extended" and "helical" conformations of the backbone. The latter class comprises, *e.g.*, the 3_{10}-, α-, and π-helices as well as various types of turns, whereas the "extended" conformations cover, *e.g.*, β-strands and polyproline I/II structures. Whenever we call a peptide structure α-helical, this narrower classification is based on applying the dictionary of protein secondary structure (DSSP).[64] However, we will generally not show the corresponding DSSP data.

For an explanation of the HELO score we note that residues involved in an α-helical structure have ψ-angles typically near $\psi_\alpha = -47°$, whereas in an extended β-strand the angles are near $\psi_\beta = \psi_\alpha + 180° = 133°$. Fig. 2 defines an α-β-scoring function $h_{\mathrm{elo}}(\psi)$, which linearly decreases from 1 to −1 as ψ changes from $\psi = \psi_\alpha$ to $\psi = \psi_\beta$. As a measure for the helicity of a sequence portion $\mathfrak{A}$ covering several residues $i \in \mathfrak{A}$ we define the HELO score

$$H_{\mathrm{ELO}}(\mathfrak{A}) = \frac{\sum_{i\in\mathfrak{A}} h_{\mathrm{elo}}(\psi_i)}{|\mathfrak{A}|} \tag{6}$$

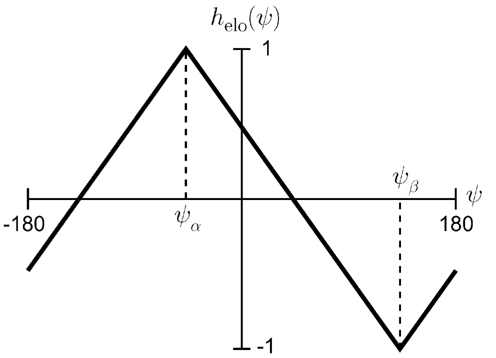

Fig. 2 The α-β-scoring function $h_{\mathrm{elo}}(\psi)$.

as the average α-β-score of the set of ψ-dihedral angles $\{\psi_i\colon i \in \mathfrak{A}\}$.

For our analysis of the cAPB peptide conformations we will use the sets $\mathfrak{A}_1 = \{1,2,8\}$ and $\mathfrak{A}_2 = \{3,4,5,6\}$, where 1 denotes alanine, 2 cysteine and so on (*cf.* Fig. 1). Thus, $H_1 \equiv H_{\mathrm{ELO}}(\mathfrak{A}_1)$ reflects the structure of the peptide in the vicinity of the chromophore and $H_2 \equiv H_{\mathrm{ELO}}(\mathfrak{A}_2)$ the structure within the core of the peptide moiety. Note, that we have omitted the residue 7 (glycine) in $\mathfrak{A}_1$ because of its high flexibility.

Free energy maps

The conformational coordinates H_1 and H_2 introduced above were used for characterizing the conformational ensembles of *cis* and *trans* cAPB by free energy maps $G(H_1,H_2)$. To compute these maps the rectangle $[-1, 1] \times [-1, 1]$ was divided into 20×20 bins and statistics over the HELO scores encountered in the REST simulations yielded bin-counts $m(H_1,H_2)$. Up to an arbitrary constant, the free energy is given by $G(H_1,H_2) = -k_BT \ln[m(H_1,H_2)/M_{\max}]$, where $M_{\max}$ is the maximal bin-count. Note that this choice for G guarantees that the minimum of G is zero. Because empty bins in the histogram density estimate would lead to infinite free energies, an upper energy cutoff $G_{\max} = -k_BT\ln(1/M_{\max})$ was introduced and G was set to $G_{\max}$ at all empty bins. A nearest neighbor smoothing was applied before generating contour plots of $G(H_1,H_2)$.

Proton distances

To compare the equilibrium ensembles computed by our REST simulations with the well-known NMR distance restraints derived from NOEs of the *cis* and *trans* isomers of cAPB,[25] we have calculated proton–proton interaction distances d_{ij} from proton–proton distances r_{ij} sampled by the simulations. Because a NOE is caused by a dipole–dipole interaction, we have calculated the interaction distances d_{ij} by the prescription[65]

$$d_{ij}(t_0,t) = (\langle r_{ij}^{-6}\rangle_{[t_0,t]})^{-1/6}. \qquad (7)$$

Here, $\langle\cdot\rangle_{[t_0,t]}$ denotes the average over the simulation time interval $[t_0,t]$ with $t > t_0$. For chemically equivalent protons $\{i_1,\ldots,i_n\}$ the geometrical center was used to compute the distance r_{ij} to proton j. In analogy to the well known root mean square deviation, we introduce the root mean square violation (RMSV)

$$\mathrm{RMSV}(t_0,t) = \sqrt{\frac{1}{|M|}\sum_{(ij)\in M} \max[0, d_{ij}(t_0,t) - d_{ij}^{\mathrm{exp}}]^2}, \qquad (8)$$

by which a simulation result violates the NOE distance restraints.[25] Here, M is the set of all proton pairs (ij), for which distances d_{ij}^{exp} were experimentally determined, and $|M|$ is the number of these distances. Note that the ESI contains a section explaining the properties and particularly the temperature dependence of the RMSV.

Experimental methods

Sample preparation

The cAPB peptides were prepared as described in ref. 26. The sample was dissolved in dimethylsulfoxide (DMSO) from Merck (Darmstadt, Germany) at a concentration of about 7 mM. In the time resolved pump probe experiments the sample was circulated through home made flow cells (pathlength 0.1 mm) with CaF_2 windows. This closed cycle system ensures the exchange of the illuminated sample volume between consecutive excitation laser pulses.

Stationary IR spectroscopy

Steady state absorption spectra were recorded using a Fourier transform infrared (FTIR) spectrometer IFS66 from Bruker (Ettlingen, Germany). No indications for sample degradation were found from stationary FTIR spectroscopy during the measurements. The *trans*-azo conformation is the thermally stable form of cAPB. At room temperature the cAPB molecules reach the *trans*-azo conformation at a timescale of some days. As a consequence, dark adapted molecules (yielding a concentration of about 100% *trans* isomers) were used for the study of the *trans* ensemble of cAPB. For the investigation of the *cis* ensemble the sample was converted to the *cis*-azo conformation by continuous UV illumination of the *trans* ππ*-absorption band with the light of a HgXe arc lamp emitting around 370 nm (LOT, Darmstadt, Germany). The lamp was equipped with filters from Schott (UG11, WG320, GG375). Taking the extinction coefficients for the *cis* and *trans* isomers into account one can estimate that about 90% of all molecules were in the *cis* form during the measurements.

Femtosecond IR spectroscopy

The structural dynamics of the *cis* to *trans* reaction have been investigated by time resolved UV pump IR probe spectroscopy. A detailed description of the experimental setup is given in ref. 66. In brief, we used the pump and probe technique with single pulses from a Ti-sapphire laser-amplifier system operated at 1 kHz. Second harmonic generation was used for excitation at 404 nm with an energy of about 2 μJ. In order to reduce excessive nonlinearities induced by the intense excitation pulses the duration of the pump pulses was increased by a quartz rod (15 cm) in front of the sample. The pump pulses had a duration of about 700 fs and were focused to a spot size of about 150 μm (FWHM) at the sample position. The IR probe pulses were generated using a two stage BBO optical parametric amplifier. The resulting near infrared pulses were used for difference frequency mixing in a $AgGaS_2$ crystal[66,67] yielding tuneable pulses in the mid IR. The resulting mid IR probe pulses had a temporal width of about 150 fs and were focused to a spot size of about 90 μm (FWHM). With a spectral bandwidth of about 150 cm^{-1} the probe pulses were tuned to several discrete central wavelengths to cover the range of the amide I and amid II bands between 1450 cm^{-1} and 1800 cm^{-1}. After the sample the probe pulses were split into two beams by a Ge plate and focused on the entrance slit of two spectrographs. Transient spectra were recorded with identical 32-element MCT detectors at a spectral resolution of about 3 cm^{-1}. In the experiment transient absorption signals with perpendicular and parallel polarizations were recorded simultaneously. All pump–probe signals shown in the figures correspond to magic angle polarization conditions calculated from the parallel and perpendicular signals. For the measurement of the time dependence of the absorption change the pump pulses were delayed with respect to the probe pulses by means of an optical delay stage allowing delay times of up to 3.5 ns.

Results and discussion

As outlined in the Introduction, the relaxation dynamics of the cAPB backbone, which is generated by the light-induced *cis*/*trans* isomerization of the APB chromophore, is in the focus of this study. The intended comparisons of a corresponding simulation description with time-resolved spectroscopic data obtained by pumping a femtosecond light flash into a room temperature equilibrium ensemble of solvated *cis*-cAPB peptides require a careful computational characterization of the equilibrium ensembles of the cAPB peptides in their *cis* and *trans* states, respectively. Here, a statistically valid description of the *cis* ensemble is required to have a proper model for the experimental ensemble present before arrival of the laser flash. A corresponding model of the *trans* equilibrium ensemble is necessary to gain a reference, which will allow to judge the progress of the simulated non-equilibrium *cis*/*trans* relaxation towards its final goal, *i.e.* the *trans* ensemble.[39,40,54]

Equilibrium ensembles at 300 K

As also mentioned in the Introduction, there has been a previous attempt to characterize the *cis* and *trans* ensembles of cAPB by MD simulation.[40] For gaining at least some statistics on the variety of conformational states sampled by cAPB in DMSO, Carstens *et al.*[40] were forced to elevate the temperature to 500 K in their 50 ns MD simulations. The resulting conformational ensembles showed a good agreement with NOE data obtained from NMR measurements.[25] Because the quoted work applied the same force field for DMSO and cAPB as we do in our approach (*e.g.* C22 for the peptide portion of cAPB), we could have employed these earlier structural ensembles for our much more extended non-equilibrium relaxation simulations.

However, it is an open question as to whether such 50 ns MD simulations of cAPB in DMSO at 500 K actually yield sufficiently accurate models for the experimental 300 K ensembles. Furthermore, the quality of the force field is always an issue of concern.[17,68] In the case of the C22 force field,[50] for instance, the CMAP extension[51] meanwhile has been argued to provide substantially improved descriptions of peptide structures.[69] Therefore, we decided to additionally address the questions of temperature and of force field quality in our following in-depth reinvestigation of the issue.

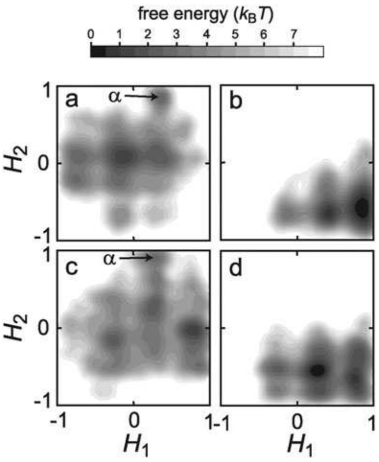

Fig. 3 Free energy landscapes $G(H_1,H_2)$ of *cis* (left) and *trans* (right) cAPB in DMSO at 300 K as obtained from the extended REST simulations characterized in Table 1. G is represented on the plane spanned by the helix-elongation measures H_i, $i = 1,2$, which are defined by eqn (6). The top row refers to the C22 and the bottom row to the CMAP force field, respectively. The measures H_i and the computation of $G(H_1,H_2)$ are explained in Methods. With the nomenclature of Table 1 the subgraphs were extracted from the REST simulations: (a) R/C/C22, (b) R/T/C22, (c) R/C/CMAP, and (d) R/T/CMAP.

Starting with the questions of how the computed conformational landscapes of *cis* and *trans* cAPB are shaped at 300 K and to what extent they are affected by the applied peptide force field we first consider Fig. 3. The figure shows four free energy landscapes $G(H_1,H_2)$, which summarize the results of the four REST simulations specified in Table 1. The conformational states sampled by the *cis* (left) and *trans* (right) cAPB peptides are characterized by the two conformational coordinates H_1 and H_2. As explained in Methods, these so-called helicity scores can distinguish helical from extended peptide conformations in different parts of the backbone. Here, values close to one signify helical structures and values close to minus one extended structures (*cf.* Fig. 2 and its discussion in the text).

In particular, H_1 is the helicity score of the peptide backbone near the covalent linkages to the chromophore (*cf.* Fig. 1). Correspondingly, values $H_1 \approx 1$ indicate the presence of turns at these locations. A comparison of the graphs at the right hand side of Fig. 3 referring to *trans* with those at the left hand side (*cis*) demonstrates that such turns are predominantly found in the simulated *trans* ensembles. In contrast, the *cis* ensembles are seen to exhibit also many extended structures near the linkages ($H_1 \approx -1$) which are completely absent for *trans*.

H_2, on the other hand, measures the helicity in the core of the peptide strand (A_3-T_4-C_5-D_6). The two distinct minima of $G(H_1,H_2)$, which are located at values $H_2 \approx 1$ and are marked by arrows in the left graphs of Fig. 3 (*cis*), thus indicate the occasional presence of a well-structured α-helix in the *cis* ensemble. In sharp contrast the *trans* graphs reveal that this ensemble is strongly dominated by extended structures in the core of the peptide ($H_2 \approx -1$). In addition, the conformational space occupied by the *cis* ensemble is seen to be much larger than in the *trans* case. The latter two results of our reinvestigation confirm previous findings[25,40] which were based on NMR and MD, respectively.

Note here, that the peptide portion of cAPB forms an α-helix in the native environment of the thioredoxin reductase from which its sequence was taken.[70] Originally, this native α-helical folding pattern had inspired the hope that the *cis*/*trans* isomerization of cAPB could provide a minimal model for force-driven helix-unfolding.[26] However, the previous 500 K MD study by Carstens *et al.*[40] had predicted that the *cis* ensemble mainly consists of various open loop structures but did not identify any conformational substates of α-helical character. Likewise, α-helical structures were absent in the set of refined NMR structures.[25] In contrast and independently of the applied force field, our 300 K REST simulations (*cf.* Fig. 3a and c) now confirm the existence of an α-helical population in the *cis*-cAPB ensemble as had been expected[26] from the thioredoxin reductase case.[70] Of course, the α-helical character of this population has been independently checked using the DSSP classifier.[64]

For a most simple characterization of the differences among the ensembles shown in Fig. 2, Table 2 lists the associated average helicities $\bar{H}_{i,\alpha}$ ($i = 1{,}2$; $\alpha \in \{c,t\}$). Comparing first for the average helicity $\bar{H}_2$ of the peptide's core the changes caused by the *cis*/*trans* isomerization, the table shows a large decrease $\Delta\bar{H}_2 \approx -0.6$ for both force fields clearly reflecting the stretching of the peptide's core toward extended conformations. Concerning the change of the average peptide helicity $\bar{H}_1$ in the linkage regions, which is enforced by the *cis*/*trans* isomerization of the azobenzene dye, the two force fields surprisingly disagree. Whereas C22 predicts a strong increase of $\Delta\bar{H}_1 \approx 0.8$ expressing a removal of extended and the appearance of turn structures at the linkages, the CMAP extension assigns nearly vanishing changes to the observable $\bar{H}_1$. Thus solely $\bar{H}_2$ is an observable, by which one can clearly distinguish the simulated *cis* and *trans* ensembles. To gain deeper insights into the surprising difference between C22 and CMAP just revealed by inspection of Table 2, one has to reconsider the free energy landscapes $G(H_1,H_2)$ shown in Fig. 3.

A corresponding detailed analysis of the differences between the conformational ensembles predicted by C22 and CMAP, respectively, is presented in the ESI together with the proof that the apparent differences are statistically significant, indeed (*cf.* Fig. S12 and the associated discussion).† This detailed analysis shows that the force fields describe the core of the peptide as measured by the observable H_2 in a very similar fashion (both for *cis* and *trans*) and predict slight but distinct differences solely for the peptide regions near the linkage to the chromophore, which are monitored by H_1.

Table 2 Average helicities $\bar{H}_1$ and $\bar{H}_2$ at 300 K

Observable[a]	C22[b]	CMAP[c]
$\bar{H}_{1,c}$	−0.09	0.38
$\bar{H}_{1,t}$	0.67	0.40
$\bar{H}_{2,c}$	0.10	0.03
$\bar{H}_{2,t}$	−0.56	−0.54

[a] The subscripts "*c*" and "*t*" label the *cis*- and *trans*-ensembles, respectively, obtained by [b] The REST simulations with the C22 or [c] The CMAP force field listed in Table 1.

Based on the above results we can start now to address the open question, which we raised further above, to what extent 50 ns MD simulations with C22 at 500 K[40] can yield valid models for the *cis* and *trans* ensembles of cAPB in DMSO at 300 K.

Conformational landscapes at high temperature

For a first answer compare Fig. 4, which shows the free energy landscapes $G(H_1,H_2)$ of the REST ensembles at 570 K, with the 300 K landscapes of Fig. 3. One immediately recognizes that raising the temperature greatly reduces the number of local minima exhibited by $G(H_1,H_2)$, *i.e.* reduces the number of distinct conformational substates. In particular, the α-helical state present at 300 K in the *cis* ensembles of C22 and CMAP disappears. When analyzing the strucures (data not shown) associated to the 570 K minima of the *cis* landscapes one recovers the open loop structures described by Carstens *et al.*[40] for their 500 K *cis* ensembles. The inspection of Fig. 4 additionally shows that the conformational space sampled by thermal fluctuations increases both for *cis* and *trans*. Furthermore, despite the smoothing of the free energy surfaces caused by the increased temperature, the differences of the C22 (top) and CMAP (bottom) landscapes, which were identified above by visual inspection of the 300 K landscapes, still persist in a weakened form at 570 K (as one can convince oneself by repeating the analysis in the ESI for the data in Fig. 4).

Interestingly, however, while CMAP predicted for 300 K that the *cis*/*trans* isomerization leaves the average helicity $\bar{H}_1$ of the linkage region nearly invariant, this invariance is gone at 570 K. For this temperature CMAP now also assigns an increase $\Delta\bar{H}_1 = 0.3$ of turn character to the linkage region, which is nearly as large as the C22 increase $\Delta\bar{H}_1 = 0.5$ at 570 K. Because the latter value is smaller than the $\Delta\bar{H}_1 = 0.8$

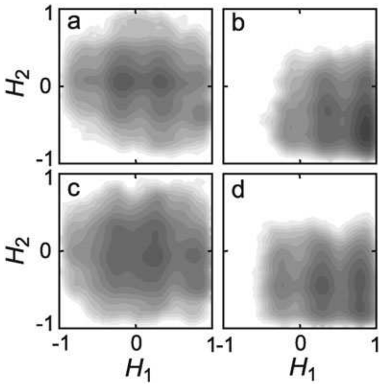

Fig. 4 Free energy landscapes $G(H_1,H_2)$ of *cis* (left) and *trans* (right) cAPB in DMSO at 570 K as obtained from our REST simulations (*cf.* Table 1). The top row refers to the C22 and the bottom row to CMAP. The subgraphs were extracted from the REST simulations: (a) R/C/C22, (b) R/T/C22, (c) R/C/CMAP, and (d) R/T/CMAP.

predicted by C22 at 300 K one concludes that raising the temperature sizably diminishes the differences between the conformational landscapes calculated by C22 and CMAP. Thus it seems that the CMAP extension affects the low-energy parts of the potential energy landscape, which are sampled at 300 K, much more strongly than the higher energy parts, which are sampled at 570 K.

Comparison with NMR data

As mentioned further above, the 500 K ensembles generated by MD with C22, which are similar to our 570 K REST ensembles (Fig. 4, top), were previously shown to explain the NMR distance restraints[25] quite well leading to the question how our 300 K ensembles perform in this respect. As a measure for the match between the computed conformational ensembles and the observed NMR distance restraints[25] we employ the root mean square violation (RMSV) between the NMR distance restraints and REST ensembles defined in Methods by eqn (7) and (8).

Fig. 5 shows the RMSVs for the two force fields C22 (squares) and CMAP (dots) for the *cis* (a) and *trans* (b) ensembles obtained by REST at 300 K as functions of the respective simulation time. All RMSVs are seen to level off after about 80 ns (*cis*) or 50 ns (*trans*) of REST simulations, respectively. To demonstrate that convergence is reached after 80 ns also for the more extended *cis* conformational space, we have extended the REST simulation R/C/CMAP to 150 ns. The associated RMSV curve (dots) in Fig. 5a is extremely flat in the time range beyond 100 ns indicating that convergence has been reached, indeed.

The most striking feature of Fig. 5 is that the RMSVs generated with the C22 force field are much larger than those produced with CMAP indicating that the CMAP ensembles agree much better with the NMR data than the C22 ensembles. Recall in this context that the conformational landscapes as characterized by Fig. 3 showed only minor differences upon exchange of the force field. Thus these small differences apparently suffice to bring the CMAP ensemble much closer to the evidence provided by NMR. According to the analysis of the properties of the RMSV presented in the ESI these small differences must consist in a few conformational sub-states, which feature small proton–proton distances for proton pairs with measured NOEs and which are present in the CMAP but absent in the C22 ensembles (both for *cis* and *trans*). This finding is in line with the analyses of van Gunsteren *et al.*[68] which imply that minor modifications of conformational ensembles may have large impacts on violations of NOE distance restraints. Furthermore, this finding is remarkable as it demonstrates that the CMAP extension of C22, which was derived mainly by quantum chemistry on small isolated model peptides,[51] provides a more realistic description for a model peptide in solution which, due to the cyclization constraints, samples unusual local conformations.

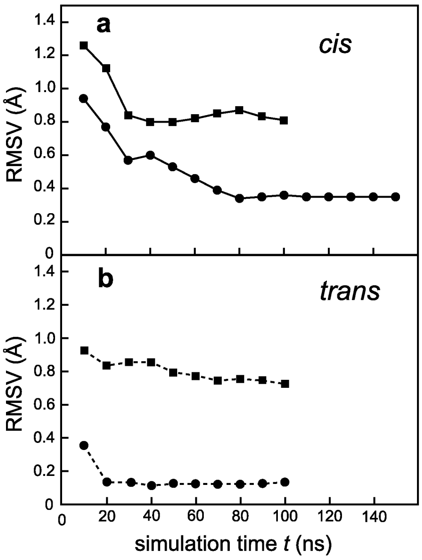

Fig. 5 RMSV(0,*t*) between the NMR distance restraints[25] and the corresponding REST ensembles at 300 K as a function of the simulation time *t* [*cf.* eqn (8)]; the squares mark C22 and dots CMAP results; the solid (*cis*) and dashed (*trans*) lines connecting the respective symbols serve as guides for the eye; (a) *cis* and (b) *trans* ensembles.

The noted strong violation of the NMR data by the 300 K ensembles obtained with C22 is a surprise and seems to contradict the previous results of Carstens *et al.*[40] who stated that their 500 K ensembles, which were also calculated with C22, agree very well with the NMR distance restraints particularly for *cis*-cAPB while exhibiting larger violations in the *trans* case (data reproduced in the ESI; see column 3 of Tables 4 and 5). To gain an understanding of this apparent contradiction we have calculated the RMSVs for the various ensembles obtained at all rungs of the REST temperature ladder. This allows to draw the RMSVs as functions of the simulation temperature. Note in this context that in REST only the peptide is "hot" whereas the surrounding solvent remains effectively "cool" due to the scaling of its Hamiltonian. In our following analysis we thus assume that the effect of the nonphysical solvent on the conformational landscape of the peptide is small. This assumption is supported by recent findings of Reichold.[69]

Fig. 6 shows that the RMSVs monotonously decrease with increasing peptide temperature for each force field as well as for *cis*- and *trans*-cAPB. As is shown in section "Temperature dependence and other properties of the RMSV" of the ESI, a monotonous decrease upon increasing temperature is a generic property of the RMSV when one considers structures with a small thermal expansion coefficient. For our cAPB peptide the cyclic closure apparently entails a sufficiently small thermal expansion.

The decrease of the RMSV in Fig. 6 is more pronounced for *cis* than for *trans* and stronger for C22 than for CMAP. For CMAP it had to be expected that the decrease is small, because the associated RMSVs are already small at 300 K and are bounded from below. For C22 and *cis*-cAPB the heating brings the RMSV from 0.81 down to 0.29, *i.e.*, close to the values 0.34 predicted by CMAP at 300 K and 0.23 calculated by us from the 500 K *cis* data of Carstens *et al.* (*cf.* Table S4 in the ESI).† As a result, the high-temperature *cis* ensembles seem to perform better than the low temperature ones (particularly for the C22 description of *cis*-cAPB). For the combination C22 and *trans* a sizable RMSV (0.45) remains at higher temperatures, which once again matches the previous 500 K MD result of 0.47 and is much larger than the CMAP result of

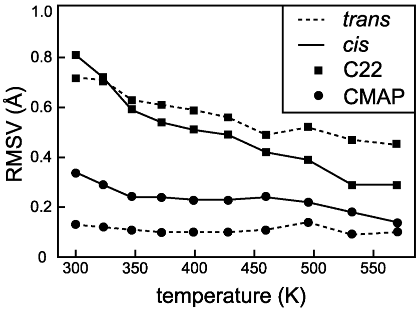

Fig. 6 RMSVs of the REST ensembles as functions of the temperature; solid lines mark *cis* and dashed lines *trans* ensembles; squares refer to C22 and dots to CMAP.

0.13 at 300 K. Thus, the strongly constrained *trans*-cAPB yields the decisive evidence for the superiority of CMAP over C22.

The smaller RMSVs observed at higher temperatures do not mean that these ensembles are more "realistic". As explained in the ESI, at these temperatures the conformational landscapes artificially extend over much larger portions of the conformational spaces and, therefore, have higher probabilities to cover also structures with vanishing NOE violations. Even a small number of such structures can strongly reduce the highly non-linear RMSV measure [*cf.* eqn (7) and (8), the ESI, and ref. 68]. Because of these high-temperature artifacts the 300 K ensembles are much more realistic. Note once again that they cover for *cis*-cAPB the native-like α-helical conformation, which disappears in a melting transition upon increase of the simulation temperature (*cf.* Fig. 3 and 4 above).

As a result, our above analysis has demonstrated that the REST simulations with the CMAP force field have provided models for the 300 K equilibrium ensembles of *cis*- and *trans*-cAPB which comply with the NMR data very well. The C22 ensembles show larger deviations although they have a considerable overlap with the CMAP ensembles. We conclude that a few conformational substates allowed by CMAP and precluded by C22 cause the much better match of the CMAP ensembles with the NMR data.

Distinguishing cAPB isomers

According to our discussion of Table 2 the isomeric states of cAPB can be distinguished by the average helicity $\bar{H}_2$ within the core of the peptide. Thus, measuring $\bar{H}_2(t)$ for an ensemble of non-equilibrium simulations can provide access to the kinetics of the photoinduced relaxation processes. In a similar way also the time resolved UV/vis pump and IR probe spectroscopy addressing this kinetics must be capable to clearly distinguish the *cis* and *trans* ensembles of cAPB.

The amide bands in the IR spectra of peptides, which originate from the normal modes of the highly polar amide groups making up the backbone, are known to change their shapes and spectral locations with the structure of the peptide[71–73] and the polarity of the solvent (see Schultheis *et al.*[74] for explanations). Thus, the amide bands of cAPB in DMSO should be capable to distinguish *cis*- and *trans*-cAPB.

In the dark, the *trans* conformation is the equilibrium state of cAPB.[26] Its IR spectrum is shown in Fig. 7a (dashed line).

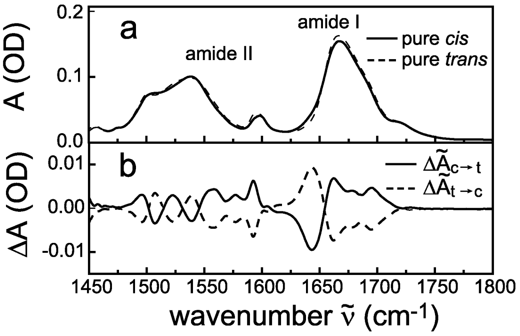

Fig. 7 IR absorption of cAPB in the spectral region of the amide I and II bands. (a) Absorption $A_c(\tilde{\nu})$ of pure *cis* (solid line) and $A_t(\tilde{\nu})$ of pure *trans* ensembles (dashed line), respectively. (b) Absorption changes $\Delta\tilde{A}_{c\to t}(\tilde{\nu})$ induced by *cis*/*trans* (solid line) and $\Delta\tilde{A}_{t\to c}(\tilde{\nu})$ by *trans*/*cis* (dashed line) isomerization of the azobenzene photoswitch elicited by illumination at $\lambda > 400$ nm and $\lambda \sim 370$ nm, respectively.

Illuminating this conformation with light of wavelengths $\lambda \approx 370$ nm yields a photostationary ensemble containing about 90% *cis*-cAPB. Because the IR spectrum $A_t(\tilde{\nu})$ of the pure *trans* state is known, one easily constructs an IR spectrum $A_c(\tilde{\nu})$ of pure *cis*-cAPB (Fig. 7a, solid line).

The spectra of the *trans*- and the *cis*-conformations are very similar. Nevertheless the differences between the two spectra can be accurately determined by recording the *cis*/*trans* difference spectra induced by illumination with light at longer wavelength ($\lambda \sim 400$ nm) (Fig. 7b, solid line). The observed absorption change is of the same order as found for other chromopeptides.[34,37,75] When the *trans* isomer is illuminated at 370 nm one can measure the *trans*/*cis* difference spectrum (Fig. 7b, dashed line). The reversibility of the photoreaction is demonstrated by the fact that the two difference spectra are (up to the sign) basically identical.

In the region of the amide I band near 1660 cm^{-1} the *trans*/*cis* conversion is seen to be associated with a shift of IR intensity toward lower frequencies. Such a redshift can be explained by amide groups becoming more strongly exposed to the polar DMSO environment.[74] In fact, according to our MD data, in *trans* the backbone is more tightly folded and, thus, less solvent accessible than in *cis*.

Monitoring the *cis*/*trans* relaxation by IR spectroscopy

Fig. 8 displays transient and stationary absorption spectra of cAPB. In the transient experiment the photostationary *cis* ensemble was excited by a 404 nm laser flash with a duration of about 700 fs. Before arrival of the laser flash the time resolved spectrum is identical to the original spectrum, thus the difference spectrum $\Delta A_{c\to t}(\tilde{\nu},t \to -\infty)$ vanishes. At very late times after excitation, converted molecules will reach the spectrum of the *trans* state. Hence, the time resolved *cis*/*trans* difference spectra $\Delta A_{c\to t}(\tilde{\nu},t)$ will approach the stationary difference spectrum $\Delta\tilde{A}_{c\to t}(\tilde{\nu})$ shown as a solid line in Fig. 7b/8c.

Fig. 8b shows a series of time resolved *cis*/*trans* difference spectra $\Delta A_{c\to t}(\tilde{\nu},t)$ obtained at selected time points $t/\text{ps} \in \{2, 10, 20, 100, 500, 3000\}$ after the 404 nm laser flash inducing the isomerization. From the picosecond to the nanosecond time

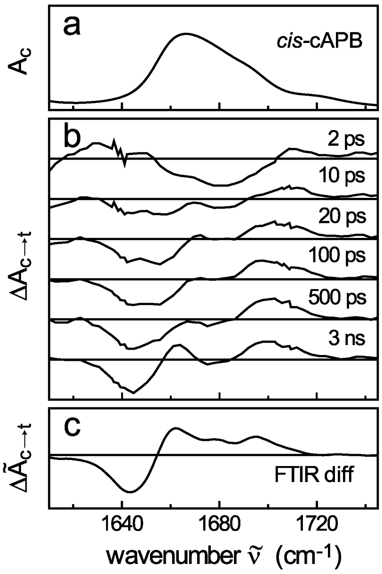

Fig. 8 IR spectra of cAPB in the amide I range given in arbitrary units. (a) IR absorption of *cis*-cAPB in DMSO. (b) Transient spectra $\Delta A_{c\to t}(\tilde{\nu},t)$ induced by *cis*/*trans* photoisomerization of the azobenzene switch. (c) Stationary difference spectrum $\Delta\tilde{A}_{c\to t}(\tilde{\nu})$.

range the transient spectra $\Delta A_{c\to t}(\tilde{\nu},t)$ are seen to undergo drastic changes. Immediately after the excitation of the azobenzene unit (see $\Delta A_{c\to t}(\tilde{\nu},t)$ at $t = 2$ ps) a redshift of the amide I band is observed as demonstrated by the bleach between 1650 and 1700 cm^{-1} and the increased absorption between 1625 and 1645 cm^{-1}. It is well established that such a redshift can be interpreted as a signature of a hot peptide exhibiting a non-thermal distribution of vibrational excitation within the amide I modes and among low frequency modes that are anharmonically coupled to the amide I modes.[34,76] The thermal excess energy within the peptide thus identified by the transient spectrum at $t = 2$ ps stems from the UV/vis photon initially absorbed by the chromophore and is generated by internal conversion (while the dye relaxes from the electronically excited state into the ground state). The noted redshift disappears within 5–10 ps and is seen to be absent after 20 ps implying that cAPB has dissipated the thermal excess energy into the DMSO environment by that time.

In the remaining time span the depicted transient spectra $\Delta A_{c\to t}(\tilde{\nu},t)$ solely reflect the conformational relaxation of cAPB's peptide moiety on its way from the *cis* toward the *trans* equilibrium ensemble. The spectra are seen to approach the stationary target spectrum $\Delta\tilde{A}_{c\to t}(\tilde{\nu})$ in Fig. 8c. However, they clearly do not reach this target completely within the recorded time span of 3 ns. As a result, after the *cis*/*trans* photoisomerization of the azobenzene switch, the relaxation of cAPB into the *trans* ensemble takes much more time than previously assumed.[39]

In this context it is important to note that the differences between the stationary spectrum $\Delta\tilde{A}_{c\to t}(\tilde{\nu})$ and the time resolved spectrum $\Delta A_{c\to t}(\tilde{\nu},t)$ at $t = 3$ ns are still sizable and are much more clearly detectable than corresponding differences previously identified for the chromophore absorption in the UV/vis spectral range.[39] Thus, as expected, our IR spectroscopy of the amide I region is actually a much more sensitive probe to structural relaxations within the peptide moiety of cAPB than the UV/vis spectroscopy, which employs the changing chromophore absorption as a probe.

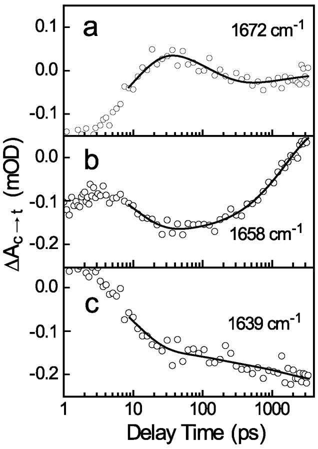

Fig. 9 Time transients $\Delta A_{c\to t}(\tilde{\nu},t)$ showing the kinetics at the indicated spectral positions $\tilde{\nu}$. The solid lines are the result of a multichannel analysis comprising frequencies $\tilde{\nu}$ regularly distributed ($\tilde{\nu} \approx 3$ cm^{-1}) over the amide I region with a sum of four exponential functions. The fit functions are drawn for delay times $t \geq 9$ ps, because our study focuses on the slow processes of conformational relaxation within the peptide part of cAPB.

The structural relaxation dynamics encoded in the time resolved transient spectra $\Delta A_{c\to t}(\tilde{\nu},t)$ for the first 3 ns after photoisomerization can be kinetically characterized by a global fit with a sum of exponentials, *i.e.* with $\sum_j a_j(\tilde{\nu})\exp(-t/\tau_j)$. Fig. 9 demonstrates the quality of such a fit for which four exponential functions have been chosen by comparing the fit with the time dependence of $\Delta A_{c\to t}(\tilde{\nu},t)$ at three selected frequencies $\tilde{\nu}$/cm^{-1} $\in \{1639, 1658, 1672\}$. For the time period starting 10 ps after the laser flash, within which the peptides should have dissipated most of their initial thermal excess energy, the fits are seen to close reproduce the experimental data at all chosen sample frequencies. The thus determined relaxation times τ_i ($i = 1,\ldots,4$) will be presented and discussed further below in connection with corresponding simulation data.

Monitoring the *cis*/*trans* relaxation by MD simulation

To obtain a description of cAPB's structural relaxation after the *cis*/*trans* isomerization of the chromophore we have carried out the two sets I/C22 and I/CMAP of non-equilibrium simulations listed in Table 1 and described in Methods. Each of the 50 simulations contained in one of the two sets starts with a simulated photoisomerization[39] depositing the energy of a UV/vis photon into a *cis*-cAPB structure, which was randomly chosen from the corresponding simulated *cis* equilibrium ensemble. Then each simulation describes the structural relaxation of this solvated molecule over a time span of 20 ns. The simulated time span is by a factor of 7 larger than the one covered experimentally by us and by a factor 20 larger than the one of the previous MD simulations.[39] The total simulation time spent for acquiring our new data covers 2 μs.

As shown further above, the ensemble average helicity measure $\bar{H}_2$ can distinguish the *cis* and *trans* equilibrium ensembles for both force fields. A time-resolved version $\bar{H}_2(t)$ of this measure is obtained at each (analysis) time point t after the simulated photoisomerization by averaging over all 50 values $H_2(t)$ contained in the respective set I/C22 or I/CMAP. The time dependent functions $\bar{H}_2(t)$ resulting for the two force fields can then be approximated with fit functions

$$h_2(t) = [\bar{H}_2(0) - \bar{H}_{2,\mathrm{t}}] \sum_j a_j \exp(-t/\tau_j) + \bar{H}_{2,\mathrm{t}} \qquad (9)$$

where $\bar{H}_{2,\mathrm{t}}$ is the average over the respective equilibrium *trans* ensemble, $\bar{H}_2(0)$ the average over the ensemble of the 50 *cis* starting structures, and $\sum_j a_j = 1$.

For the two employed force fields Fig. 10 compares the simulation results $\bar{H}_2(t)$ with fits $h_2(t)$ utilizing three exponentials. The fits are seen to reproduce the simulation data very well for both force fields. They do not require a component with an infinite relaxation time implying that the fit functions $h_2(t)$ exactly approach the respective ensemble average values $\bar{H}_{2,\mathrm{t}}$ determined by the REST simulations of the equilibrium *trans* ensembles at 300 K. Consequently, the longest time constants determined by the fits are the longest time constants in the simulated non-equilibrium ensembles which, in the long time limit, decay exponentially towards the *trans* equilibrium ensembles.

According to Fig. 10 the *trans* equilibrium ensembles are quite obviously not yet reached even after 20 ns. Nevertheless, at this point of time the relaxation is to about 75% complete. In fact, the longest time constant τ_3 entering the fits $h_2(t)$ is found to be about 23 ns for both force fields predicting that the process should be at least to 58% complete after 20 ns. Therefore, faster initial relaxations have moved the ensembles already a bit closer to their respective targets. Because we have modeled both the time resolved IR spectra $\Delta A_{c\rightarrow t}(\tilde{\nu},t)$ and the simulation data $\bar{H}_2(t)$ by exponential mixtures, one can try to compare the thus obtained relaxation times.

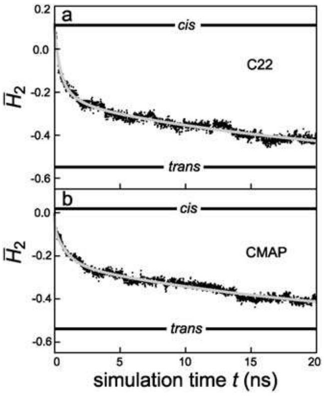

Fig. 10 Simulated relaxation dynamics induced by the *cis*/*trans* isomerization of the cAPB chromophore using (a) the C22 and (b) the CMAP force field. The relaxation is monitored by the average helicity score $\bar{H}_2(t)$ determined from the data sets I/C22 and I/CMAP comprising 50 non-equilibrium MD simulations each. The light gray lines are fits with the functions $h_2(t)$ specified in the text. The horizontal lines mark the averages $\bar{H}_2$ over the *cis* and *trans* ensembles obtained by the respective REST simulations. The ESI displays in Fig. S18 the above data additionally on a logarithmic time scale to resolve the fast processes more clearly.

Kinetics of the *cis*/*trans* relaxation

Table 3 compares the four time constants τ_j (j = 0,. . .,3) resulting from the global fit to the transient IR spectra $\Delta A_{c\rightarrow t}(\tilde{\nu},t)$ with the three time constants determined from the fits $h_2(t)$ to the simulation data $\bar{H}_2(t)$. We provide this tentative comparison of kinetic constants although it rests on the *ad hoc* assumption that the amide I spectra and the helicity score $\bar{H}_2(t)$ of the central peptide portion of cAPB are similarly sensitive to the ongoing conformational relaxation.

It would have been much more appropriate to compute the changes of the amide I bands directly from the MD trajectories using a reliable and sufficiently cost-effective method and to predict the kinetics from the calculated spectra. However, sufficiently accurate descriptions of amide bands are currently accessible only through hybrid methods combining density functional theory with molecular mechanics (see ref. 77 for a review) and such DFT/MM computations are extremely costly. In a previous analysis of the time-resolved unzipping of a light-switchable β-hairpin peptide, which also combined ultrafast IR spectroscopy with theoretical descriptions,[38] the computation of the amide I bands for a few snapshots of the solvated peptide took us several months of computer time on a linux cluster. Such DFT/MM computations are by far too costly for the given purpose of computing temporally resolved IR spectra of cAPB's *cis-trans* relaxation in DMSO. Furthermore, Stock *et al.*[43] have critically discussed the unclear relation between kinetics derived from MD conformational coordinates and time-resolved amide I spectra by considering a cyclic peptide related to the one studied by us. Here they cautiously attempted to use one of the existing (and notoriously unreliable[74]) empirical models for estimating amide I band shapes. The lack of a cost effective and accurate computational method has inspired some of us to develop a new type of polarizable force field for amide groups that aims at the (time-resolved) computation of amide bands.[74] However, currently this method is not yet fully established and ready to use. Therefore we have to resort to a plausible but by no means rigorously founded comparison of kinetics derived from different observables.

The shortest relaxation time τ_0 = 11 ps found experimentally and listed in Table 3 describes the cooling kinetics of the initially hot peptide. This time constant has no correspondence in the simulation results for the simple reason that the observable $\bar{H}_2$ is nearly independent of the temperature. In fact, when calculating the averages $\bar{H}_2$ for the REST ensembles as a function of the temperature one finds only very small changes (Fig. S16 in the ESI documents this fact).† For the MD

Table 3 Decay times τ_j from fits with n exponentials

times[a]	IR[b]	C22[c]	CMAP[d]
τ_0	11	—	—
τ_1	137	401	49
τ_2	1370	1370	981
τ_3	∞	23094	22610

[a] Times are given in ps. [b] The time resolved IR difference spectra $\Delta A_{c\rightarrow t}(\tilde{\nu},t)$ were fitted with n = 4. [c] The average helicity $\bar{H}_2(t)$ calculated from simulation I/C22 was fitted with n = 3. [d] And that from I/CMAP with n = 2.

description of the fast cooling one needs other observables, *e.g.*, the total energy[39] or directly the temperature of cAPB (see the ESI for data and discussion).

According to Table 3 the next slower relaxation time $\tau_1 = 0.14$ ns determined by IR spectroscopy differs from the fastest time constants τ_1 calculated for the relaxation of the core helicity $\bar{H}_2(t)$. Simulation I/C22 yields $\tau_1 = 0.40$ ns and I/CMAP $\tau_1 = 0.05$ ns, respectively. The statistical errors of the calculated time constants τ_1–τ_3 are about 40%, 20%, and 10%, respectively, as one can estimate by dividing the two sets of 50 relaxation trajectories into subsets comprising 25 trajectories each, by computing the fit functions eqn (9), and by evaluating standard deviations. Thus, at short times the statistical errors of the computed time scales τ are quite large.

As opposed to the case of the short 100 ps trajectories used to monitor the fast processes of heat dissipation with a very good statistics (*cf.* the ESI), computational limitations forced us to strongly limit the number of extended 20 ns simulations. Thus, instead of 500 only 50 trajectories could be calculated for each force field. Due to the multitude of conformational substates offered by *cis*-cAPB (*cf.* Fig. 3), the set of only 50 starting structures cannot adequately represent the complex *cis* ensemble perturbed by the laser flash. The α-helical substate, for instance, will be represented in this set by only very few samples (in fact, for C22 we counted two and for CMAP one α-helix). Since the unfolding of such a structure is a random experiment, the corresponding kinetics can be determined from one or two unfolding events only with huge uncertainties. Inspecting Fig. 10 once again one sees that the traces of $\bar{H}_2(t)$ show sizable fluctuations (caused by the small number of samples), which—particularly on short time scales—may distort the measurement of decay times.

Furthermore, the limited statistics of only 50 relaxation simulations for each force field does not allow us to generate smooth time dependent free energy landscapes $G[H_1,H_2,t]$ by simple counting. However, by considering each trajectory as a representative of a class, which is normally distributed in the helicity plane at each time point t (standard deviation $\sigma = 0.1$), we can expand the number of data points $[H_1(t),H_2(t)]_\rho$, $\rho = 1,\ldots,50$, delivered by the simulations through throwing the dice. Fig. 11 shows the resulting landscapes $G[H_1,H_2,t]$ at the time points $t/\mathrm{ns} \in \{0,0.2,2,20\}$. They are compared with the equilibrium ensembles obtained by REST for *cis* (top) and *trans* (bottom). The left row refers to the C22 force field, the right row to CMAP. Note that Table S10 in the ESI† lists for each of the distributions shown in Fig. 11 the average linkage and core helicities $\bar{H}_1(t)$ and $\bar{H}_2(t)$, respectively.

The landscapes $G[H_1,H_2,t]$ depicted in Fig. 11 underline our above statement on the incomplete representation of the *cis* ensemble by the 50 randomly drawn starting structures (compare the two top rows). In addition, the inspection of the figure strongly suggests that the strain-driven unfolding of the α-helical substate is one of the fastest conformational transitions elicited by the chromophore's *cis*/*trans* isomerization. This sparsely populated substate is seen to disappear within the first 0.2 ns after the photoisomerization for both force fields. Because the α-helical conformation is associated with the largest value of H_2 found in the *cis* ensemble, its disappearance will leave, despite its small population, clear traces in the time course of $\bar{H}_2(t)$. Correspondingly, the helix unfolding provides a major contribution to the fastest time constant τ_1 predicted by MD. The extremely limited statistics, by which this process is sampled (one or two events), then immediately explains the large mutual deviations of the MD values listed in Table 3 for τ_1. On the other hand, the 0.14 ns kinetics observed experimentally may well reflect the force-driven unfolding of an α-helical substate.

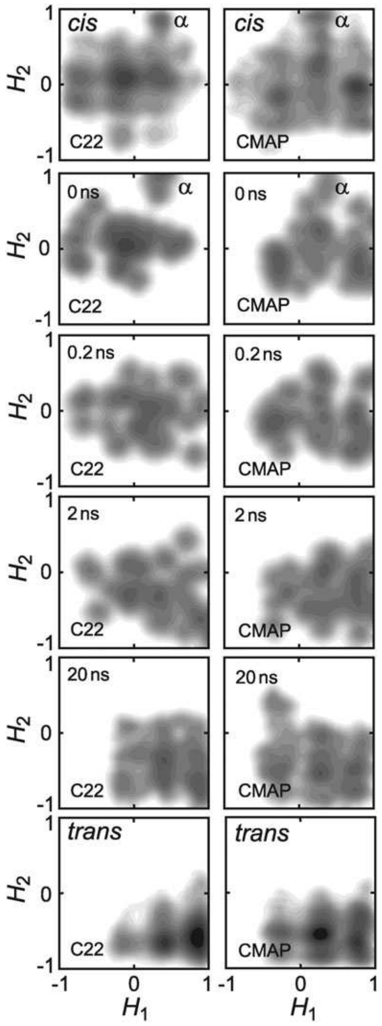

Fig. 11 Temporal evolution of ensembles. For explanation see the text.

For the next slower relaxation kinetics described by $\tau_2 \approx 1$ ns the IR and MD results exhibit a remarkable (and in part accidental) agreement (*cf.* Table 3). This decay constant is determined at a better statistics from the simulation data $\bar{H}_2(t)$ than $\tau_1 \approx 0.1$ ns. To identify the processes underlying τ_2 recall the results of Spörlein *et al.*[39] These authors have shown that the UV/vis spectrum of the chromophore, which is reached after 1 ns, closely resembles the stationary reference spectrum of the *trans* state. The spectral similarity indicates that the mechanical strain exerted by the chromophore on the peptide moiety is largely gone at that point of time. Therefore, the decay time $\tau_2 \approx 1$ ns may reflect the slowest force driven structural transitions serving to reduce the mechanical strain within the cyclic azopeptide. Comparing in Fig. 11 the time-resolved free energy landscapes reached after 2 ns with the initial landscapes one sees that all core helicities $H_2 > 0.5$ vanish within the first two nanoseconds. Within this time span the more extended *trans*-chromophore thus substantially stretches the originally quite helical peptide core.

The time-resolved IR measurements were limited to 3 ns. Because the relaxation of the peptide moiety is far from being complete after 3 ns, the associated spectral fits contain a fourth time constant $\tau_3 = \infty$. In contrast, the fits $h_2(t)$ to the simulation data $\bar{H}_2(t)$ do not require an additional offset for $t \to \infty$ because the known limiting value $h_2(t \to \infty) = \bar{H}_{2,\mathrm{t}}$ has been built into the fit function eqn (9). As a result and independently of the chosen force field, the simulation data definitely predict that the relaxation toward the *trans* ensemble is complete on the computed time scale $\tau_3 \approx 23$ ns (*cf.* Table 3).

According to the arguments given above, the slow 23 ns kinetics, by which the equilibrium *trans* ensemble is reached, most likely does not anymore serve to relieve mechanical stress. Instead, it should be associated to a stochastic search within the conformational space that transforms the *cis*-related non-equilibrium ensemble, which is reached after a few nanoseconds, eventually into the equilibrium *trans* ensemble (*cf.* Fig. 11). This stochastic search involves thermally driven flips of the amide groups around the dihedral angles ψ_i at the C_α atoms of the residues *i*. As a result, the helicities H_1 in the linkage regions and H_2 in the core of the peptide will approach the *trans* distribution which should resemble the distributions shown at the bottom of Fig. 11b for C22 (left) and for CMAP (right).

The surprising similarity of the time constant τ_3 determined with the two force fields then indicates that the energy barriers, which are associated with the mentioned flips, have similar heights. This result corroborates our earlier hypothesis that the CMAP extension hardly modifies the high energy regions of the C22 potential energy landscape (see our discussion of Fig. 3 and 4).

Conclusion

We have reinvestigated the *cis*/*trans* photoisomerization of the monocyclic azopeptide cAPB in DMSO by combining ultrafast UV/vis pump IR probe spectroscopy with nonequilibrium MD simulations. Because these simulations require the knowledge of cAPB's conformational equilibria in the *cis* and *trans* states of the APB chromphore, we have calculated these equilibria by applying the novel REST technique.[48,49]

Here, we have compared two different force fields. We found that the CMAP extension[51] describes the well-known NMR distance restraints of *cis*- and *trans*-cAPB[25] much better than the original C22 force field.[50] Furthermore we have demonstrated that the CMAP extension mainly modifies the low-energy regions of the C22 energy landscape while leaving the sizes of the energy barriers nearly invariant. Both force fields predict the presence of an α-helical substate in the 300 K ensembles of the *cis* conformation, whose predominance had been one of the objectives during the design of cAPB.[26] This α-helical substate had been absent in the set of refined NMR structures[25] and in the high-temperature *cis* ensemble computed earlier by a 50 ns MD simulation.[40]

We would like to stress however that, despite the differences of cAPB's conformational *cis* and *trans* ensembles identified by us between low (300 K) and high (≈500 K) temperatures, the key conclusions of the earlier MD study remain valid. The study correctly explains the shortcomings of the usual NMR structure refinement when applied to flexible peptides. Here the refinement erroneously predicts artificially compact structures.[40,68]

As shown by us, the *cis* and *trans* conformational ensembles of cAPB at 300 K can be experimentally distinguished by the shapes of the amide I bands in the IR spectra. In the simulation data they can be distinguished by considering the ensemble average helicity in the core region (A_3-T_4-C_5-D_6) of the peptide moiety. The transient IR difference spectra, which monitor the peptide relaxation over a 3 ns time span after the photoisomerization, reveal a cooling process with a decay time of 11 ps which is overlooked by the helicity measure because the latter is largely independent of temperature. In addition, the observed time-resolved IR spectra and the simulated helicity time series identify two further relaxation time constants $\tau_1 \approx 0.1$ ns and $\tau_2 \approx 1$ ns. The MD simulations suggest that both time constants belong to force driven relaxations relieving the mechanical strain that had been built up within the cyclic azopeptide by the stretching of the chromophore during *cis*/*trans* photoisomerization. Here, τ_1 is associated with the fast stretching of peptide conformations, which feature very high core helicities and include the α-helical substate mentioned above. Furthermore, τ_2 represents the time scale at which the forces exerted by the chromophore on the peptide are finally relieved.

After the first few nanosconds of strain reduction a non-equilibrium conformational ensemble remains. The thermal relaxation of this ensemble toward the target equilibrium ensemble of the *trans* state is outside the limited time window of our experimental setup. The ensembles of MD simulations, however, which have been generated for the C22 and the CMAP force fields, respectively, and cover the time span of 20 ns, unanimously predict that this relaxation proceeds with a decay time $\tau_3 \approx 23$ ns. It will be interesting to see whether this prediction can be confirmed by temporally more extended measurements.

When trying to bridge the gap between theory and experiment in the field of biomolecular simulation one usually has been confronted with the problem that the time scales covered by the experimental studies are too large for simulation descriptions because of computational limitations. Interestingly, the small cAPB model compound has now been demonstrated to provide an example for which the reverse is true: The simulation could cover time scales inaccessible to the experimental setup due to technical restrictions.

Acknowledgements

This work was supported by the Deutsche Forschungsgemeinschaft (Grants SFB 533/C1, SFB 749/A5/C4, Forschergruppe 526). Computer time provided by Leibniz Rechenzentrum (project uh408) is gratefully acknowledged.

References

1 A. Liwo, M. Khalili and H. A. Scheraga, *Proc. Natl. Acad. Sci. U. S. A.*, 2005, **102**, 2362–2367.

2 Y. Duan and P. A. Kollman, *Proc. Natl. Acad. Sci. USA*, 1998, **282**, 740–744.

3 J. Kubelka, J. Hofrichter and W. A. Eaton, *Curr. Opin. Struct. Biol.*, 2004, **14**, 76–88.

4 P. L. Freddolino, F. Liu, M. Gruebele and K. Schulten, *Biophys. J.*, 2008, **94**, L75–L77.

5 C. Dobson and M. Karplus, *Curr. Opin. Struct. Biol.*, 1999, **9**, 92–101.

6 W. C. Still, A. Tempczyk, R. C. Hawley and T. Hendrickson, *J. Am. Chem. Soc.*, 1990, **112**, 6127–6129.

7 B. Zagrovic, E. J. Sorin and V. Pande, *J. Mol. Biol.*, 2001, **313**, 151–169.

8 D. Satoh, K. Shimizu, S. Nakamura and T. Terada, *FEBS Lett.*, 2006, **580**, 3422–3426.

9 H. Lei and Y. Duan, *J. Mol. Biol.*, 2007, **370**, 196–206.

10 R. Zhou and B. J. Berne, *Proc. Natl. Acad. Sci. U. S. A.*, 2002, **99**, 12777–12782.

11 H. Nymeyer and A. E. García, *Proc. Natl. Acad. Sci. U. S. A.*, 2003, **100**, 13934–13939.

12 R. Geney, M. Layten, R. Gomperts, V. Hornak and C. Simmerling, *J. Chem. Theory Comput.*, 2006, **2**, 115–127.

13 B. Egwolf and P. Tavan, *J. Chem. Phys.*, 2003, **118**, 2039–2056.

14 M. Stork and P. Tavan, *J. Chem. Phys.*, 2007, **126**, 165105.

15 M. Stork and P. Tavan, *J. Chem. Phys.*, 2007, **126**, 165106.

16 M. Levitt and R. Sharon, *Proc. Natl. Acad. Sci. U. S. A.*, 1988, **85**, 7557–7561.

17 P. Tavan, H. Carstens and G. Mathias, *Protein Folding Handbook. Part I.*, Wiley-VCH, Weinheim, 2005, ch. 33, pp. 1170–1195.

18 H. J. C. Berendsen, *Science*, 1998, **282**, 642–643.

19 J. Breton, J. Martin, A. Migus, A. Antonetti and A. Orszag, *Proc. Natl. Acad. Sci. U. S. A.*, 1986, **83**, 5121–5125.

20 K. Wüthrich, *NMR of Proteins and Nukleic Acids*, Wiley, New York, 1986.

21 S. Williams, T. P. Causgrove, R. Gilmanshin, K. S. Fang, R. H. Callender, W. H. Woodruff and R. B. Dyer, *Biochemistry*, 1996, **35**, 691.

22 R. M. Ballew, J. Sabelko and M. Gruebele, *Proc. Natl. Acad. Sci. U. S. A.*, 1996, **93**, 5759–5764.

23 W. A. Eaton, V. Munoz, S. J. Hagan, G. S. Jas, L. J. Lapidus, E. R. Henry and H. J., *Annu. Rev. Biophys. Biomol. Struct.*, 2000, **29**, 327–359.

24 P. Hamm, J. Helbing and J. Bredenbeck, *Annu. Rev. Phys. Chem.*, 2008, **59**, 291–317.

25 C. Renner, R. Behrendt, S. Spörlein, J. Wachtveitl and L. Moroder, *Biopolymers*, 2000, **54**, 489–500.

26 R. Behrendt, C. Renner, M. Schenk, F. Q. Wang, J. Wachtveitl, D. Oesterhelt and L. Moroder, *Angew. Chem., Int. Ed.*, 1999, **38**, 2771.

27 J. R. Kumita, O. S. Smart and G. A. Woolley, *Proc. Natl. Acad. Sci. U. S. A.*, 2000, **97**, 3803–3808.

28 L. Ulysse, J. Cubillos and J. Chmielewski, *J. Am. Chem. Soc.*, 1995, **117**, 8466–8467.

29 S.-L. Dong, M. Löweneck, T. Schrader, W. Schreier, W. Zinth, L. Moroder and C. Renner, *Chem.–Eur. J.*, 2006, **12**, 1114–1120.

30 A. Aemissegger and D. Hilvert, *Nat. Protoc.*, 2007, **2**, 161–167.

31 C. Renner, U. Kusebauch, M. Löweneck, A. G. Milbradt and L. Moroder, *J. Pept. Res.*, 2005, **65**, 4–14.

32 A. Aemissegger, V. Kräutler, W. F. van Gunsteren and D. Hilvert, *J. Am. Chem. Soc.*, 2005, **127**, 2929–2936.

33 G. Mathias, B. Egwolf, M. Nonella and P. Tavan, *J. Chem. Phys.*, 2003, **118**, 10847–10860.

34 J. Bredenbeck, J. Helbing, A. Sieg, T. Schrader, W. Zinth, C. Renner, R. Behrendt, L. Moroder, J. Wachtveitl and P. Hamm, *Proc. Natl. Acad. Sci. U. S. A.*, 2003, **100**, 6452–6457.

35 J. Wachtveitl, S. Spörlein, H. Satzger, B. Fonrobert, C. Renner, R. Behrendt, D. Oesterhelt, L. Moroder and W. Zinth, *Biophys. J.*, 2004, **86**, 2350–2362.

36 G. A. Woolley, *Acc. Chem. Res.*, 2005, **38**, 486–493.

37 J. A. Ihalainen, J. Bredenbeck, R. Pfister, J. Helbing, L. Chi and I. H. M. van Stokkum, *Proc. Natl. Acad. Sci. U. S. A.*, 2007, **104**, 5383–5388.

38 T. E. Schrader, W. J. Schreier, T. Cordes, F. O. Koller, G. Babitzki, R. Denschlag, C. Renner, M. Löweneck, S.-L. Dong, L. Moroder, P. Tavan and W. Zinth, *Proc. Natl. Acad. Sci. U. S. A.*, 2007, **104**, 15729–15734.

39 S. Spörlein, H. Carstens, H. Satzger, C. Renner, R. Behrendt, L. Moroder, P. Tavan, W. Zinth and J. Wachtveitl, *Proc. Natl. Acad. Sci. U. S. A.*, 2002, **99**, 7998–8002.

40 H. Carstens, C. Renner, A. G. Milbradt, L. Moroder and P. Tavan, *Biochemistry*, 2005, **44**, 4829–4840.

41 P. H. Nguyen, Y. MU and G. Stock, *Proteins: Struct., Funct., Bioinf.*, 2005, **60**, 485–494.

42 P. H. Nguyen and G. Stock, *Chem. Phys.*, 2006, **323**, 36–44.

43 P. H. Nguyen, R. D. Gorbunov and G. Stock, *Biophys. J.*, 2006, **91**, 1224–1234.

44 M. Erdelyi, A. Karlen and A. Gogoll, *Chem.–Eur. J.*, 2006, **12**, 403–412.

45 D. Du, Y. Zhu, C.-Y. Huang and F. Gai, *Proc. Natl. Acad. Sci. U. S. A.*, 2004, **101**, 15915–15920.

46 K. Hukushima and K. Nemoto, *J. Phys. Soc. Jpn.*, 1996, **65**, 1604–1608.

47 R. Denschlag, M. Lingenheil and P. Tavan, *Chem. Phys. Lett.*, 2008, **458**, 244–248.

48 R. Denschlag, M. Lingenheil, P. Tavan and G. Mathias, *J. Chem. Theory Comput.*, 2009, **5**, 2847–2857.

49 P. Liu, B. Kim, R. A. Friesner and B. J. Berne, *Proc. Natl. Acad. Sci. U. S. A.*, 2005, **102**, 13749–13754.

50 A. D. MacKerell, D. Bashford, M. Bellott, R. L. Dunbrack, J. D. Evanseck, M. J. Field, S. Fischer, J. Gao, H. Guo, S. Ha, D. Joseph-McCarthy, L. Kuchnir, K. Kuczera, F. T. K. Lau, C. Mattos, S. Michnick, T. Ngo, D. T. Nguyen, B. Prodhom, W. E. Reiher, B. Roux, M. Schlenkrich, J. C. Smith, R. Stote, J. Straub, M. Watanabe, J. Wiorkiewicz-Kuczera, D. Yin and M. Karplus, *J. Phys. Chem. B*, 1998, **102**, 3586–3616.

51 A. D. MacKerell, M. Feig and C. L. Brooks, III, *J. Comput. Chem.*, 2004, **25**, 1400–1415.

52 N. Metropolis, A. W. Rosenbluth, M. N. Rosenbluth, A. H. Teller and E. Teller, *J. Chem. Phys.*, 1953, **21**, 1087–1092.

53 M. P. Allen and D. J. Tildesley, *Computer Simulations of Liquids*, Oxford University Press, Oxford, 1987.

54 H. Carstens, *Dissertation*, Fakultät für Physik, Ludwig-Maximilians-Universität München, 2004.

55 P. Bordat, J. Sacristan, D. Reith, S. Girard, A. Glattli and F. Müller-Plathe, *Chem. Phys. Lett.*, 2003, **374**, 201–205.

56 C. Niedermeier and P. Tavan, *J. Chem. Phys.*, 1994, **101**, 734–748.

57 M. Eichinger, H. Grubmüller, H. Heller and P. Tavan, *J. Comput. Chem.*, 1997, **18**, 1729–1749.

58 V. Kraeutler, W. F. van Gunsteren and P. H. Hünenberger, *J. Comput. Chem.*, 2001, **22**, 501–508.

59 H. J. C. Berendsen, J. P. M. Postma, W. F. van Gunsteren, A. Dinola and J. R. Haak, *J. Chem. Phys.*, 1984, **81**, 3684–3690.

60 M. Lingenheil, R. Denschlag, R. Reichold and P. Tavan, *J. Chem. Theory Comput.*, 2008, **4**, 1293–1306.

61 R. Denschlag, M. Lingenheil and P. Tavan, *Chem. Phys. Lett.*, 2009, **473**, 193–195.

62 M. Lingenheil, R. Denschlag and P. Tavan, *Chem. Phys. Lett.*, 2009, **478**, 80–84.

63 X. Huang, M. Hagen, B. Kim, R. A. Friesner, R. Zhou and B. J. Berne, *J. Phys. Chem. B*, 2007, **111**, 5405–5410.

64 W. Kabsch and C. Sander, *Biopolymers*, 1983, **22**, 2577–2637.

65 X. Daura, K. Gademann, H. Schäfer, B. Jaun, D. Seebach and W. F. van Gunsteren, *J. Am. Chem. Soc.*, 2001, **123**, 2393–2404.

66 T. Schrader, A. Sieg, F. Koller, W. Schreier, Q. An, W. Zinth and P. Gilch, *Chem. Phys. Lett.*, 2004, **392**, 358.

67 P. Hamm, R. A. Kaindl and J. Stenger, *Opt. Lett.*, 2000, **25**, 1798.

68 W. F. van Gunsteren, D. Bakowies, R. Baron, I. Chandrasekhar, M. Christen, X. Daura, P. Gee, D. P. Geerke, A. Glättli, P. H. Hünenberger, M. A. Kastenholz, C. Oostenbrink, M. Schenk, D. Trzesniak, N. F. A. van der Vegt and H. B. Yu, *Angew. Chem., Int. Ed.*, 2006, **45**, 4064–4092.

69 R. Reichold, *Dissertation*, Fakultät für Physik, Ludwig-Maximilians-Universität München, 2009.

70 T. N. Gustafsson, T. Sandalova, J. Lu, A. Holmgren and G. Schneider, *Acta Crystallogr., Sect. D: Biol. Crystallogr.*, 2007, **63**, 833–843.

71 D. M. Byler and H. Susi, *Biopolymers*, 1986, **25**, 469–487.

72 F. Siebert, *Methods Enzymol.*, 1995, **246**, 501–526.

73 A. Barth and C. Zscherp, *Q. Rev. Biophys.*, 2002, **35**, 369–430.

74 V. Schultheis, R. Reichold, B. Schropp and P. Tavan, *J. Phys. Chem. B*, 2008, **112**, 12217–12230.

75 J. Bredenbeck, J. Helbing, J. R. Kumita, G. A. Woolley and P. Hamm, *Proc. Natl. Acad. Sci. U. S. A.*, 2005, **102**, 2379–2384.

76 P. Hamm, S. M. Ohline and W. Zinth, *J. Chem. Phys.*, 1997, **106**, 519.

77 M. Schmitz and P. Tavan, *Modern Methods for Theoretical Physical Chemistry of Biopolymers*, Elsevier, Amsterdam, 2006, ch. 8, pp. 157–177.

Supplementary Material for PCCP

Supporting information to the manuscript

Relaxation time prediction for a light switchable peptide by molecular dynamics

Robert Denschlag*, Wolfgang J. Schreier†, Benjamin Rieff*,
Tobias E. Schrader†, Florian O. Koller†, Luis Moroder‡, Wolfgang Zinth†,
and Paul Tavan*§

*Theoretische Biophysik, Department für Physik,
†Lehrstuhl für Biomolekulare Optik and Munich Center for Integrated Protein Science CIPSM,
*†Ludwig-Maximilians-Universität, Oettingenstr. 67, 80538 München, Germany

‡Max Planck Institut für Biochemie, Am Klopferspitz 18a, 82152 Martinsried, Germany

§corresponding author, email: tavan@physik.uni-muenchen.de,
phone: +49-89-2180-9220, fax: +49-89-2180-9202

Convergence of REST free energy maps

To study the convergence of the REST simulations listed in table 1 we have divided for each simulation the set of 10 replicas into two subsets each containing five replicas. 300 K data were collected for each of these subsets, whenever one of its replicas happened to visit the 300 K temperature rung. Thus, the two replica swarms $\kappa = 1,2$ generated two independent 300 K data sets for which the conformational landscapes $G_\kappa(H_1,H_2)$ were calculated as described in Methods.

Already a first visual comparison of the various graphs labeled with the subscripts 1 and 2 in Figure 12 demonstrates a close similarity between the free energy landscapes $G_\kappa(H_1,H_2)$ extracted from the two different swarms $\kappa = 1,2$ at 300 K. For the C22 force field (Figs. 12a$_\kappa$,b$_\kappa$) the match between the landscapes $G_\kappa(H_1,H_2)$ associated to the swarms κ is very good apart from small differences between the depths of the various local minima. For CMAP (Figs. 12c$_\kappa$,d$_\kappa$) the match of the data from the two subsets is not quite as impressive but still pretty good. The modifications of the landscapes induced by the application of different force fields, which are discussed in the paper in connection with Fig. 3, are clearly retained in the swarm landscapes. For instance, both C22 swarms predict for the *cis* ensemble nearly no occupancy in the region $H_1 > 0.6$ (cf. Figs. 12a$_1$,a$_2$) and substantial occupation of the region $H_1 > -0.6$, whereas the CMAP swarms show the opposite behavior (cf. Figs. 12c$_1$,c$_2$). Thus, the differences of the conformational landscapes attributed in the paper to differences between the force fields are definitely not artifacts of insufficient statistics. Furthermore, the sampling of the conformational spaces as expressed by the complete data sets seems to be pretty exhaustive.

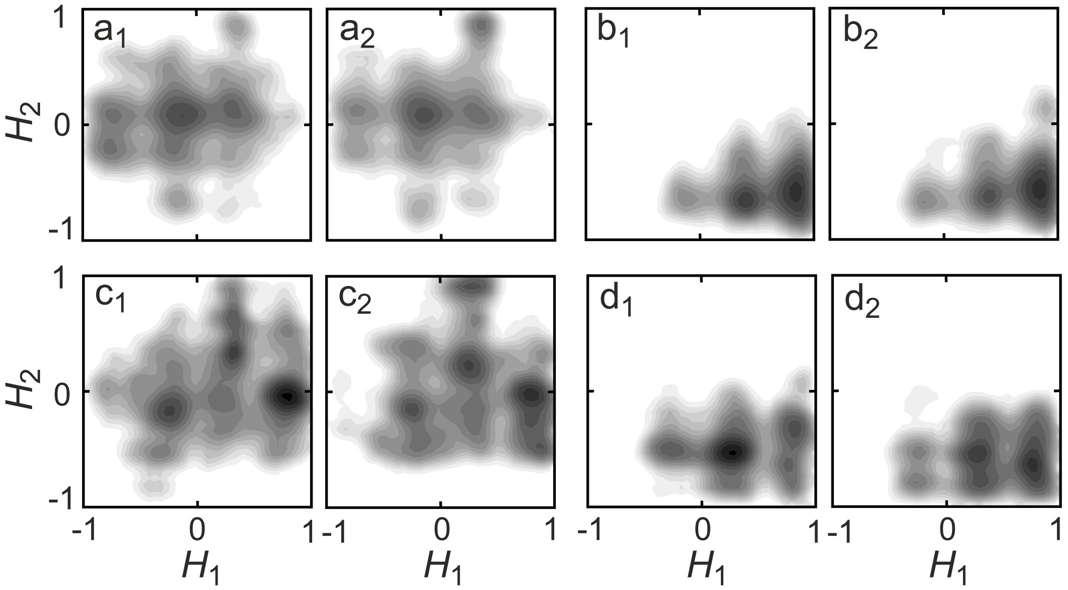

Figure S12: Free energy landscapes $G_\kappa(H_1,H_2)$ obtained at 300 K from two different swarms $\kappa = 1,2$ covering five replicas each. Swarm 1 contains the replicas with initial temperatures in the range [300 K,399 K], and swarm 2 those from [428 K,570 K]. Results of swarm κ are depicted in the graphs labeled with the subscript κ. With the nomenclature of table 1 the graphs refer to the following simulations: (a$_\kappa$) R/C/C22, (b$_\kappa$) R/T/C22, (c$_\kappa$) R/C/CMAP, and (d$_\kappa$) R/T/CMAP.

Differences of the force fields. The C22 and CMAP force fields yield different predictions for 300 K equilibrium ensembles of cAPB in the *cis*- and *trans*-states. Because Fig. S12 has demonstrated that all our REST simulations (cf. table 1) yield well-converged the free energy landscapes $G_\kappa(H_1,H_2)$, the differences between the two predictions can be identified by a visual comparison between the top (C22) and bottom (CMAP) rows of Fig. 3 (or equivalently of Fig. S12). All differences, which are discussed in detail below and are detectable in Fig. 3, are statistically significant, indeed.

For the *trans* ensemble (Figs. 3b,d or Figs. 12b$_\kappa$,d$_\kappa$) both force fields apparently agree that the central part of the peptide backbone is largely extended ($H_2 < 0$). Correspondingly, the averages $\bar{H}_{2,\mathrm{t}}$ have very similar values (cf.

table 2). Slight conformational differences are predicted by C22 and CMAP, respectively, for the peptide backbone near the covalent linkages to the chromophore. Within the dominant conformational substate resulting from C22, this portion of the backbone is seen to exhibit sharper turns ($H_1 \approx 0.8$) than in the corresponding CMAP state ($H_1 \approx 0.3$). Similarly the ensemble average $\bar{H}_1$ is by about 0.3 larger for C22 than for CMAP.

With respect to the conformational coordinate H_1 the *cis* ensembles show the opposite behavior: CMAP predicts that highly populated conformational substates are located in the region $H_1 > 0.6$, which corresponds to substantial turns at the linkages (cf. Fig. 3c). Thus also the average $\bar{H}_1 = 0.38$ is positive and close to the value of 0.40 found for the CMAP *trans* ensemble. In contrast, C22 predicts that the "turn" region $H_1 > 0.6$ of the conformational space is essentially empty (cf. Fig. 3a). Instead the region $H_1 < -0.6$ signifying extended structures at the linkages is well-populated. As a result, for C22 the average value $\bar{H}_1$ is shifted to the smaller value of -0.09. In contrast, CMAP assigns only a very small population to the "extended" region $H_1 < -0.6$. Concerning the helicity of the core of the peptide (as measured by H_2) the Figs. 3a,c reveal no significant differences for the two force fields. This visual impression is validated by the values of $\bar{H}_{2,\mathrm{c}}$ which are very similar indeed (cf. table 2).

As a result, the two force fields predict slightly different conformational ensembles for *cis*- and *trans*-cAPB at 300 K with the differences being largely confined to the linkage regions within which the peptide is covalently attached to chromophore.

Proton distances

In the following two tables S4 and S5 the proton distances from experiment,[1] earlier MD simulations[2] and our REST simulations are listed. Table S4 contains the *cis* data and table S5 the *trans* data.

Force Field:			—	C22			CMAP	
Temperature:			300 K	500 K	300 K	570 K	300 K	570 K
Atom 1	-	Atom 2[a]	r^b_{exp}	r^c_{MD}	r^d_{MD}	r^d_{MD}	r^e_{MD}	r^e_{MD}
APB:0:H2,H4	-	ALA:1:HN	4.52	2.69	2.73	2.72	2.73	2.72
APB:0:H1,H5	-	ALA:1:HN	6.71	4.72	4.77	4.75	4.78	4.75
ALA:1:HA	-	CYS:2:HN	3.01	2.79	2.54	2.55	2.75	2.58
ALA:1:HB*	-	CYS:2:HN	4.07	2.86	2.93	2.93	3.44	3.37
ALA:1:HB*	-	ALA:3:HN	5.08	4.82	4.56	4.45	4.87	4.46
CYS:2:HA	-	ALA:3:HN	2.88	2.58	2.56	2.70	2.70	2.54
CYS:2:HN	-	ALA:1:HN	3.11	2.67	3.18	2.81	2.63	2.44
ALA:3:HA	-	THR:4:HN	2.81	2.63	2.63	2.60	2.40	2.50
ALA:3:HB*	-	THR:4:HN	4.32	3.03	2.99	3.02	3.66	3.47
ALA:3:HB*	-	APB:0:H1,H5	7.86	6.15	10.55	7.87	5.86	6.42
ALA:3:HB*	-	APB:0:H6,H10	8.03	6.16	11.06	8.08	5.53	6.81
ALA:3:HB*	-	APB:0:H7,H9	7.21	5.34	9.52	6.56	4.30	5.73
ALA:3:HN	-	CYS:2:HN	3.09	2.67	2.61	2.34	2.31	2.33
THR:4:HA	-	CYS:5:HN	2.77	2.62	2.58	2.48	2.57	2.47
THR:4:HB	-	CYS:5:HN	3.30	2.78	2.65	2.61	3.18	3.02
THR:4:HG2*	-	APB:0:H1,H5	8.02	6.80	7.64	7.52	7.78	7.72
THR:4:HG2*	-	APB:0:H6,H10	7.33	6.67	6.87	7.83	7.42	7.70
THR:4:HG2*	-	APB:0:H7,H9	6.79	5.90	5.63	7.34	6.23	6.74
THR:4:HN	-	ALA:3:HN	3.28	2.84	2.72	2.58	2.74	2.44
THR:4:HN	-	CYS:5:HN	3.20	2.70	2.76	2.65	2.28	2.45
ASP:6:HA	-	GLY:7:HN	2.94	2.56	2.61	2.53	2.73	2.52
ASP:6:HB1	-	THR:4:HG1	4.80	6.22	6.94	6.47	6.38	5.66
ASP:6:HB2	-	THR:4:HG1	4.80	5.24	5.61	5.18	5.91	4.86
ASP:6:HB1	-	GLY:7:HN	5.30	2.74	2.68	2.57	3.33	3.05
ASP:6:HB1	-	PHE:8:HPHE*	7.10	5.47	5.58	6.06	5.96	5.81
ASP:6:HB2	-	PHE:8:HPHE*	7.10	5.81	6.10	6.57	6.28	6.26
ASP:6:HB1	-	APB:0:H7,H9	6.20	6.05	6.46	5.90	6.70	5.96
ASP:6:HB2	-	APB:0:H7,H9	6.78	6.43	7.04	6.10	7.56	6.88
GLY:7:HA1	-	ASP:6:HA	4.90	4.51	4.54	4.52	4.76	4.57
GLY:7:HA2	-	ASP:6:HA	5.02	4.57	4.59	4.54	4.62	4.53
GLY:7:HA1	-	PHE:8:HN	3.24	2.47	2.47	2.41	2.88	2.59
GLY:7:HA2	-	PHE:8:HN	3.24	2.72	2.55	2.69	2.97	2.67
GLY:7:HN	-	ASP:6:HN	3.00	2.67	2.56	2.51	2.64	2.35
PHE:8:HA	-	APB:0:H7,H9	6.01	4.24	4.23	4.29	4.48	4.35
PHE:8:HA	-	APB:0:HN	2.53	2.49	2.47	2.54	2.85	2.65
PHE:8:HB1	-	APB:0:H7,H9	6.92	4.68	4.80	4.70	4.77	4.71
PHE:8:HB2	-	APB:0:H7,H9	6.78	4.38	4.20	4.29	4.23	4.23
PHE:8:HB1	-	APB:0:HN	3.47	2.78	2.94	2.77	2.78	2.75
PHE:8:HB2	-	APB:0:HN	3.80	2.60	2.45	2.52	2.50	2.46
PHE:8:HN	-	APB:0:HN	3.35	2.68	2.78	2.49	2.45	2.47
PHE:8:HPHE*	-	APB:0:HN	6.54	4.79	5.21	5.07	5.49	5.14
RMSV[f]:			-	0.23	0.81	0.29	0.34	0.14

Table S4: Proton distances r for *cis*-cAPB. [a]Names of the involved Atoms using the following nomenclature: Residue:Number:Atom(s) - Residue:Number:Atom(s). A star indicates a set of (chemically) equivalent protons. [b]experiment.[1] [c]Carstens et al.[2] [d]REST simulation R/T/C22. [e]REST simulation R/T/CMAP. [f]RMSV. All distances are given in Å.

Force Field:			—		C22		CMAP	
Temperature:			300 K	500 K	300 K	570 K	300 K	570 K
Atom 1	-	Atom 2[a]	r^b_{exp}	r^c_{MD}	r^d_{MD}	r^d_{MD}	r^e_{MD}	r^e_{MD}
APB:0:H2,H4	-	ALA:1:HN	4.70	2.65	2.72	2.71	2.71	2.71
ALA:1:HB*	-	CYS:2:HN	4.02	2.90	2.91	2.95	3.44	3.30
ALA:1:HB*	-	ALA:3:HN	5.80	5.25	5.21	5.15	5.68	5.37
CYS:2:HA	-	ALA:3:HN	2.64	3.11	2.99	3.14	2.60	2.70
CYS:2:HB1	-	ALA:3:HN	3.19	2.58	2.53	2.49	3.07	3.08
CYS:2:HB2	-	ALA:3:HN	3.42	2.74	2.60	2.65	3.16	3.17
CYS:2:HN	-	ALA:1:HN	2.63	2.29	2.38	2.25	2.27	2.14
ALA:3:HB*	-	CYS:2:HA	5.22	5.37	5.45	5.47	5.18	5.22
ALA:3:HB*	-	CYS:2:HN	5.42	5.50	5.41	5.20	5.10	4.82
ALA:3:HB*	-	THR:4:HN	3.96	2.99	2.97	2.94	3.40	3.28
ALA:3:HB*	-	APB:0:H1,H5	7.02	7.31	7.93	6.32	5.07	4.81
THR:4:HA	-	CYS:5:HN	2.56	2.51	2.54	2.43	2.32	2.36
THR:4:HA	-	APB:0:H1,H5	6.04	4.03	3.71	3.84	4.33	4.44
THR:4:HB	-	CYS:5:HN	3.09	2.88	3.18	2.73	3.73	3.15
THR:4:HB	-	ASP:6:HN	4.35	6.35	7.06	5.17	4.53	4.25
THR:4:HG2*	-	ASP:6:HN	5.09	5.55	6.21	5.23	3.82	4.21
THR:4:HG2*	-	APB:0:H6,H10	6.42	5.14	5.04	5.10	4.96	5.37
CYS:5:HB1	-	ASP:6:HN	3.28	2.64	2.37	2.47	3.39	2.93
CYS:5:HB2	-	ASP:6:HN	3.63	2.92	3.01	2.72	3.41	3.22
CYS:5:HB1	-	APB:0:H6,H10	6.29	4.10	4.98	4.31	5.07	4.64
CYS:5:HB2	-	APB:0:H6,H10	6.06	4.39	3.70	3.95	4.71	4.41
CYS:5:HB2	-	APB:0:H7,H9	6.83	5.01	4.27	4.36	5.21	4.79
ASP:6:HA	-	GLY:7:HN	2.82	2.36	2.39	2.45	2.29	2.41
ASP:6:HB1	-	THR:4:HG1	4.79	6.55	7.59	6.66	4.36	5.29
ASP:6:HB2	-	THR:4:HG1	4.63	5.95	7.47	5.74	4.18	4.52
ASP:6:HB1	-	GLY:7:HN	3.60	2.54	2.36	2.40	2.76	2.65
ASP:6:HB2	-	GLY:7:HN	3.64	2.87	3.27	2.70	3.67	3.11
ASP:6:HB1	-	APB:0:H6,H10	7.20	6.63	7.18	5.92	4.79	5.56
ASP:6:HB2	-	APB:0:H6,H10	7.20	6.59	7.25	5.58	4.71	5.13
ASP:6:HB1	-	APB:0:H7,H9	6.80	5.47	5.89	5.19	3.68	4.60
ASP:6:HB2	-	APB:0:H7,H9	6.80	5.75	6.40	4.98	4.23	4.54
ASP:6:HB1	-	APB:0:HN	5.62	4.98	5.53	4.64	3.22	3.96
GLY:7:HN	-	ASP:6:HN	3.86	3.40	3.96	2.92	3.27	2.53
GLY:7:HA1	-	ASP:6:HA	4.67	4.46	4.56	4.50	4.42	4.45
GLY:7:HA2	-	ASP:6:HA	4.40	4.49	4.46	4.52	4.41	4.51
GLY:7:HA1	-	PHE:8:HN	2.71	2.25	2.19	2.27	2.52	2.35
GLY:7:HA2	-	PHE:8:HN	3.13	3.18	3.22	3.12	3.18	2.99
GLY:7:HA1	-	APB:0:HN	4.28	3.91	3.82	3.93	4.34	4.05
GLY:7:HA2	-	APB:0:HN	4.58	4.96	5.08	5.03	4.90	4.95
PHE:8:HB1	-	APB:0:HN	3.64	2.75	2.59	2.70	2.50	2.76
PHE:8:HB2	-	APB:0:HN	3.79	2.78	2.72	2.62	2.69	2.63
PHE:8:HN	-	APB:0:HN	2.86	2.36	2.29	2.30	2.43	2.39
PHE:8:HPHE*	-	APB:0:HN	6.50	5.31	5.77	5.49	5.68	5.44
RMSV[f]:			-	0.47	0.72	0.45	0.13	0.10

Table S5: Proton distances *r* for *trans*-cAPB. [a]Names of the involved Atoms using the following nomenclature: Residue:Number:Atom(s) - Residue:Number:Atom(s). A star indicates a set of (chemically) equivalent protons. [b]experiment.[1] [c]Carstens et al.[2] [d]REST simulation R/T/C22. [e]REST simulation R/T/CMAP. [f]RMSV. All distances are given in Å.

Force field parameters of the chromophore

The following four tables S6, S7, S8, and S9 contain the force field parameters for the APB switch and for its covalent linkage to the peptide. Fig. S13 shows the chemical structure of the APB chromophore. The mapping between the atom names given in the figure and the atom types required for specifying the force field is given in table S6.

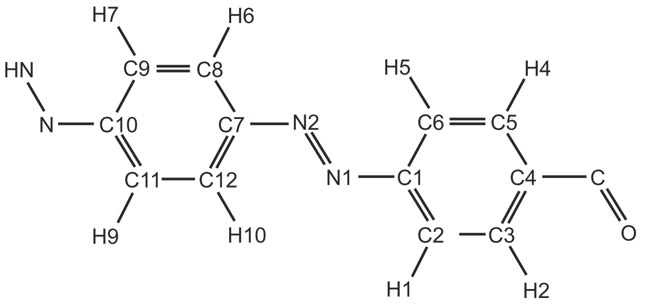

Figure S13: Chemical structure of the APB chromophore. The mapping between atom names and atom types is given in table S6.

Name	Atom type	Charge	Name	Atom type	Charge
C1	CAZ	0.4028	C2	CAZ	-0.2561
C3	CAZ	-0.0145	C4	CAZ	-0.1647
C5	CAZ	-0.0145	C6	CAZ	-0.2561
N1	NAZ	-0.2439	N2	NAZ	-0.2439
C7	CAZ	0.4028	C8	CAZ	-0.1803
C9	CAZ	-0.2389	C10	CAZ	0.3665
C11	CAZ	-0.2389	C12	CAZ	-0.1803
H1	HAZ	0.1202	H2	HAZ	0.0836
H4	HAZ	0.0836	H5	HAZ	0.1202
H6	HAZ	0.1202	H7	HAZ	0.1654
H9	HAZ	0.1654	H10	HAZ	0.1202
N	NH1	-0.5293	HN	H	0.3192
C	C	0.5930	O	O	-0.5017

Table S6: Partial charges derived by DFT.[3]

Type 1	Type 2	k_b	b_0
CAZ	CAZ	419.4	1.398
NAZ	CAZ	341.7	1.419
HAZ	CAZ	404.7	1.086
NAZ	NAZ	716.8	1.261
C	CAZ	250.0	1.504
NH1	CAZ	320.0	1.405
CT2	CAZ	230.0	1.526

Table S7: Atom types, force constant k_b (kcal mol^{-1} Å^{-2}), and equilibrium distance b_0 (Å)defining the covalent bond energy terms.[3]

Type 1	Type 2	Type 3	k_ϕ	ϕ_0
CAZ	CAZ	CAZ	40.0	120.0
HAZ	CAZ	CAZ	34.4	120.0
NAZ	CAZ	CAZ	60.2	120.0
NAZ	NAZ	CAZ	121.1	114.8
C	CAZ	CAZ	45.8	120.0
O	C	CAZ	80.0	121.0
NH1	C	CAZ	80.0	116.5
NH1	CAZ	CAZ	70.0	120.0
H	NH1	CAZ	35.0	114.8
C	NH1	CAZ	50.0	120.0
HA	CT2	CAZ	49.3	107.5
CT2	CAZ	CAZ	45.8	120.0
NH1	CT2	CAZ	50.0	116.3

Table S8: Atom types, force constant k_ϕ (kcal mol^{-1} rad^{-2}), and equilibrium angle ϕ_0 (deg) defining the angles energy terms.[3]

Type	Type	Type	Type	k_{ϕ_n}	n	ϕ_n
CAZ	NAZ	NAZ	CAZ	12.47	2	180.0
NAZ	NAZ	CAZ	CAZ	2.03	2	180.0
				0.18	4	0.0
CAZ	CAZ	C	X	0.55	2	180.0
				0.13	4	0.0
C	CAZ	CAZ	CAZ	3.10	2	180.0
CAZ	C	NH1	CT1	1.60	1	0.0
				2.50	2	180.0
CAZ	C	NH1	H	2.50	2	180.0
CAZ	CAZ	NH1	X	0.71	2	180.0
				0.13	4	0.0
NH1	CAZ	CAZ	CAZ	3.10	2	180.0
CT1	C	NH1	CAZ	1.60	1	0.0
				2.50	2	180.0
O	C	NH1	CAZ	2.50	2	180.0
CAZ	NAZ	NAZ	CAZ	20.62	2	180.0
				3.19	4	0.0

Table S9: Atom types, force constant k_{ϕ_n} (kcal/mol), periodicity n, and phase shift (deg) for dihedral energy terms defining the dihedral energy terms. The parameters for the dihedral CAZ-NAZ-NAZ-CAZ given at the bottom of the table are used in the MD/ISOM3 simulation.[3]

Temperature dependence and other properties of the RMSV

Based on a very simple model we explain, why the observable RMSV, which is defined by Eq. (8) and is used to measure the agreement between NMR proton-proton distances d_{ij}^{exp} and simulation data, is expected to be a monotonously decreasing function of the simulation temperature T (as is apparent in Fig. 6).

Assume that a peptide is in the solid state, i.e., that the peptide atoms i thermally fluctuate around fixed average positions $\langle \mathbf{r}_i \rangle$. If the fixing is harmonic, then the standard deviation of the fluctuations increases with $\sqrt{T}$ (in the limit of small amplitudes) and the positions $\mathbf{r}_i(t)$ are normally distributed. Therefore, also the distances $r_{ij}(t)$ between the atoms will be normally distributed

$$p(r_{ij}|\sigma_{ij}) = \frac{1}{\sqrt{2\pi}\sigma} \exp\left[\frac{-(r_{ij} - \langle r_{ij}\rangle)^2}{2\sigma_{ij}^2}\right] \tag{1}$$

around average distances $\langle r_{ij} \rangle$ with standard deviations σ_{ij} increasing monotonously with $\sqrt{T}$. Then the so-called interaction distances[4] d_{ij}, which are defined by Eq. (7) and serve for comparisons of simulation data with NOE distance restraints d_{ij}^{exp}, can be estimated through

$$d_{ij} \equiv \left[\left\langle \frac{1}{r_{ij}^6} \right\rangle\right]^{-1/6} \approx \left[\int_{r_{\min}}^{\infty} \frac{p(r_{ij}|\sigma_{ij})}{r_{ij}^6} dr_{ij}\right]^{-1/6} \tag{2}$$

where the minimal distance $r_{\min}$ models a hard-sphere exclusion applicable to close atoms. Because the widths σ_{ij} of the distance distributions $p(r_{ij})$ are functions of T, also the interaction distances d_{ij} depend on T.

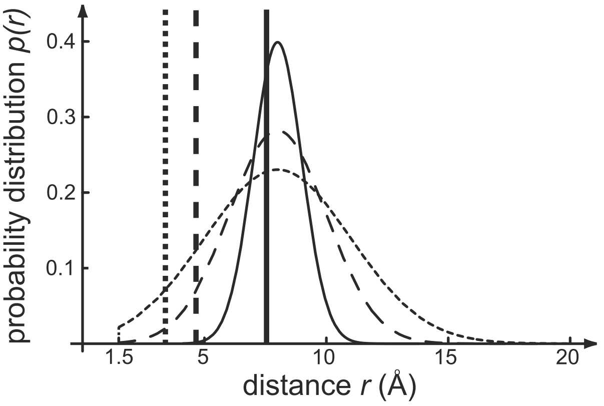

Figure S14: Distance distributions $p(r_{ij}|\sigma_{ij})$ of two hydrogen atoms in a putative rigid model structure for three different temperatures T_κ. Low temperature T_1: solid; intermediate temperature T_2: dashed; high temperature T_3: dotted. Also indicated through the vertical bars are the associated NMR interaction distances $d_{ij,\kappa}$.

As a specific example, consider two hydrogen atoms for which a NOE signal has been measurable. Then the experimental distance d_{ij}^{exp} of these atoms will be not much larger than about 5 Å, because NOE signals of more distant atoms become very weak. Now suppose that the average distance $\langle r_{ij} \rangle$ in the simulated (rigid) structure is 8 Å and that the contact distance $r_{\min}$ is 1.5 Å. Consider furthermore three different temperatures T_κ, $\kappa = 1, 2, 3$, as measured by the three different widths $\sigma_{ij,\kappa} = 1$, 2, 3 Å, and assume that the average distances $\langle r_{ij} \rangle$ are independent of temperature as is approximately the case for solids with a small thermal expansion coefficient. Then the corresponding interaction distances $d_{ij,\kappa}$ resulting from the three different distance distributions shown in Fig. S14 are 7.51, 4.66, and 3.29 Å, respectively. Thus, the interaction distances $d_{ij,\kappa}$ monotonously decrease with increasing temperatures T_κ although the average structure is invariant ($\langle r_{ij} \rangle = 8$ Å).

Next suppose that the measured distance d_{ij}^{exp} is 4 Å. Then the contributions $\max[0, d_{ij,\kappa} - d_{ij}^{\mathrm{exp}}]^2$ of the three interaction distances $d_{ij,\kappa}$ to the RMSV are 12.3 Å^2, 0.4 Å^2, and 0, respectively (cf. the definition of the RMSV in

Eq. (8)). Thus, although the average structures in the three simulations are identical, the low temperature simulation correctly signifies a large deviation for this particular distance whereas the high temperature simulation signifies no violation at all. High temperature simulations like those in Ref. 2 can therefore give the incorrect impression of a good match with NMR data. This artifact is avoided by choosing the experimental temperature in the simulations.

In summary, the simple model of a harmonically fixed and, thus, **rigid peptide structure** clearly explains why one should expect a monotonously decreasing RMSV, if one simulates the system at increasing temperatures. Note in this context that the experimental distances d_{ij}^{exp} should have the same temperature dependence as the interaction distances d_{ij} derived from a simulation implying that one will measure smaller values with increasing T (as long as the structure remains rigid). If one wants to use the RMSV as an absolute measure for judging the quality of a model structure, one has to make sure that the thermal fluctuations in the experimental and simulated systems are of equal size.

The above example has also shown that the interaction distances d_{ij} decrease, if more small values r_{ij} are contained in the ensemble of sampled distances. For a **multimodal** distance distribution $p(r_{ij})$ featuring many substates, which is the generic case for **flexible peptides**, this property implies that the interaction distance d_{ij} is dominated by the substates exhibiting small distances. If one finds, e.g., nine times the value $r_{ij} = 8$ Å and once the value $r_{ij} = 2$ Å, then Eq. (7) predicts an interaction distance $d_{ij} \approx 3$ Å.

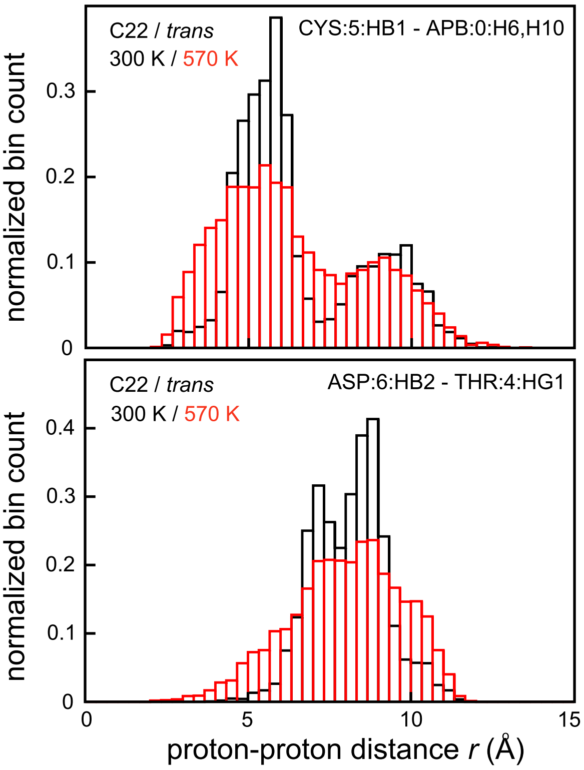

Figure S15: Histograms of distance distributions $p(r_{ij}|\sigma_{ij})$ for hydrogen atoms observed in REST simulations of *trans*-cAPB at two different temperatures.

Finally we want to demonstrate that the simple model actually applies to cAPB. In Figure 15 we provide examples for the temperature dependencies of two randomly selected proton-proton distance distributions, for which NOE's were actually observed in *trans*-cAPB (see table S5 for the corresponding interaction distances d_{ij}). The two histograms both show broadenings of the respective distributions upon heating and nearly invariant locations, around which they are centered. In particular, both distributions feature an increasing number of small distances upon heating which explains, why the associated interaction distances decrease from 4.98 to 4.31 Å for the top histogram and from 7.47 to 5.74 Å for the bottom histogram with increasing T. Because in the former case the observed distance is 6.29 Å and, thus, larger than the MD interaction distances at both temperatures, the contributions to the RMSV vanish in both cases (cf. Eq. 8). In the latter case, however, it is small measuring only 4.63 Å and, hence, the contribution to the RMSV decreases with T. Because relatively small distances are frequent among the NMR data, the monotonous decrease of the total RMSV with increasing T is readily understood.

Note here that the bimodal distribution (top) reflects the existence of at least two conformations in the simulated ensemble. As mentioned above, the NOE interaction distance is 6.29 and, thus, right at the location of the first maximum of the 300 K distance distribution shown in the top graph of Fig. S15 indicating again that NOE distances overlook substates with large proton-proton distances.

Temperature dependence of average helicity scores

Whereas the shapes of the amide I bands in the spectra of peptides are highly sensitive to the temperature, the ensemble average helicity $\bar{H}_2$ of *cis*-cAPB is nearly independent of temperature. This fact is proven by Fig. S16 for the CMAP force field, which shows the variation of $\bar{H}_2$ within the generalized REST ensemble as a function of the temperature.

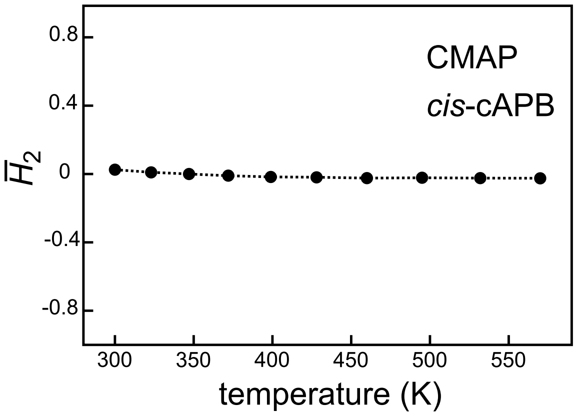

Figure S16: The ensemble average helicity $\bar{H}_2$ of *cis*-cAPB as a function of temperature within the REST simulation R/C/CMAP.

Fast cooling processes monitored by MD

Because the observable $\bar{H}_2(t)$ is insensitive to the temperature and senses the structural alteration of the chromophore, which is caused by its *cis/trans* isomerization, only with a delay of about 100 ps, the faster relaxation processes are overlooked by $\bar{H}_2(t)$. In contrast, the peptide's temperature directly maps the initial deposition of heat into the peptide and its subsequent dissipation into the surrounding solvent. For an ensemble of 500 short (100 ps) simulations of the cAPB photoisomerization in DMSO, where the peptide was described by the C22 force field, we have monitored the ensemble average time course of cAPB's temperature $\bar{T}(t)$.

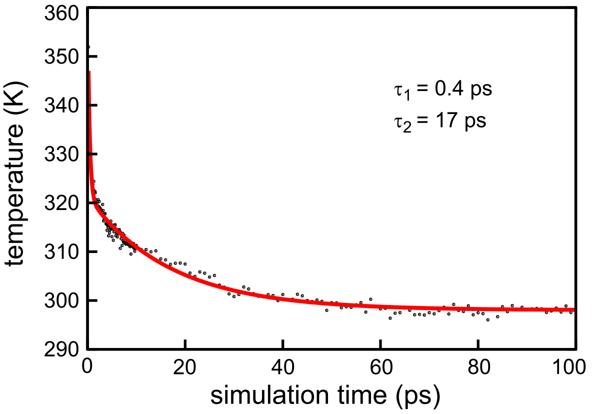

Figure S17: Temporal evolution $\bar{T}(t)$ of cAPB's average temperature extracted from an ensemble of 500 short simulations of the *cis/trans* photoisomerization.

Fig. S17 shows these data together with a fit using a sum of two exponential functions. This fit yields a fast decay of 0.4 ps corresponding to the immediate ballistic dissipation of energy during the chromophore's isomerization and a slower cooling process occurring on a time scale of 17 ps. The former time constant roughly agrees with the 0.3 ps kinetics extracted from cAPBs total energy calculated in earlier MD simulations and with the 0.2 ps time constant determined by ultrafast pump-probe spectroscopy in the UV/vis region for the chromophore isomerization.[5] The latter time constant nicely agrees with the 11 ps kinetics observed in the time resolved amide I spectra of cAPB (see table 3) and with earlier measurements of such cooling kinetics by optical pump-probe spectroscopy,[6] which determined a cooling time of 15 ps for hot azobenzene in ethanol.

Slow relaxation processes monitored by MD

Fig. S11 in the paper shows the time resolved landscapes $G[H_1, H_2, t]$ at the time points $t/\text{ns} \in \{0, 0.2, 2, 20\}$. For a simple numerical representation of these distributions we additionally provide in table 10 the average linkage and core helicities $\bar{H}_1(t)$ and $\bar{H}_2(t)$, respectively. The table demonstrates once again that only $\bar{H}_2(t)$ is suited to distinguish *cis* and *trans*.

	C22^a		CMAP^b	
time/ns	$\bar{H}_1$	$\bar{H}_2$	$\bar{H}_1$	$\bar{H}_2$
$-\infty$	−0.09	0.10	0.38	0.03
0.2	0.13	−0.02	0.28	−0.12
2.0	0.30	−0.26	0.43	−0.22
20	0.47	−0.44	0.31	−0.40
∞	0.67	−0.56	0.40	−0.54

Table S10: Temporal evolution of average helicities $\bar{H}_i(t)$, $i = 1, 2$. ^{a}From simulation I/C22 for $|t| < \infty$, R/C/C22 for $t = -\infty$, and R/T/C22 for $t = \infty$. ^{b}From I/CMAP for $|t| < \infty$, R/C/CMAP for $t = -\infty$, and R/T/CMAP for $t = \infty$.

Supplementary Material for PCCP
This journal is © The Owner Societies 2010

Relaxation plotted on a logarithmic time scale

The simulated kinetics of the *cis/trans* relaxation of cAPB as monitored by the average helicity score $\bar{H}_2(t)$ in the core of the peptide has been presented on a linear time axis in Fig. S10. This linear plot clearly reveals the slow ($\tau_3 = 23$ ns) exponential decay but does not resolve the fast processes associated with τ_1 and τ_2. Therefore we plot in Fig. S18 the same data once again on a logarithmic time scale.

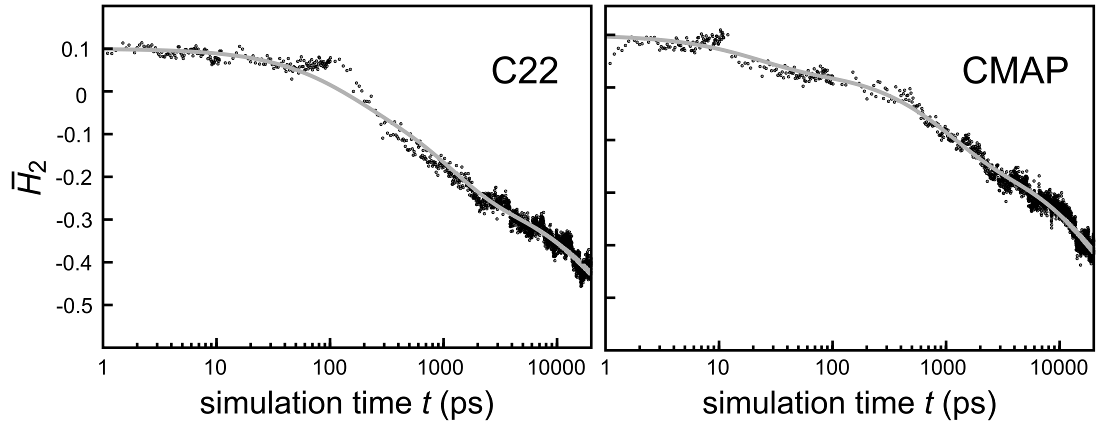

Figure S18: Data on the simulated *cis/trans* relaxation of cAPB from Fig. S10 presented on a logarithmic time scale to clearly resolve the fast events.

For the C22 force field, the average core helicity $\bar{H}_2(t)$ is essentially invariant during the first 150 ps, although the isomerization is finished after 0.3 ps, and cooling as well as important conformational changes occur within this time in the vicinity of the chromophore.[5] This observation demonstrates that it takes a certain amount of time until the stretching of the chromophore propagates to the core of the peptide. After about 150 ps the average helicity score $\bar{H}_2(t)$ of the peptide core suddenly drops indicating the force-driven unfolding of the one α-helix in the *cis*-ensemble.

For CMAP the results are qualitatively similar, but the first unfolding of one of the two α-helices in the *cis*-ensemble occurs already after 10 ps. A second sharp drop after about 150 ps indicates the sudden breaking of the hydrogen bonds stabilizing the second α-helix in the ensemble. The fact that the fast processes mainly involve individual unfolding events explains, why the very fast time constants τ_1 determined by the multi-exponential fits bear large statistical uncertainties.

References

[1] C. Renner, R. Behrendt, S. Spörlein, J. Wachtveitl and L. Moroder, *Biopolymers*, 2000, **54**, 489–500.

[2] H. Carstens, C. Renner, A. G. Milbradt, L. Moroder and P. Tavan, *Biochemistry*, 2005, **44**, 4829–4840.

[3] H. Carstens, *Dissertation*, Fakultät für Physik, Ludwig-Maximilians-Universität München, 2004.

[4] X. Daura, K. Gademann, H. Schafer, B. Jaun, D. Seebach and W. F. van Gunsteren, *J. Am. Chem. Soc.*, 2001, **123**, 2393–2404.

[5] S. Spörlein, H. Carstens, H. Satzger, C. Renner, R. Behrendt, L. Moroder, P. Tavan, W. Zinth and J. Wachtveitl, *Proc. Natl. Acad. Sci. USA*, 2002, **99**, 7998–8002.

[6] T. Naegele, R. Hoche, W. Zinth and J. Wachtveitl, *Chem. Phys. Lett.*, 1997, **272**, 489–495.

6 Resümee und Ausblick

Nicht nur die Simulationen der schon in der Einleitung ausführlich vorgestellten lichtschaltbaren Azopeptide, sondern auch weitere Simulationsprojekte aus der Arbeitsgruppe wie die Beschreibung der Chromophor-Konformerenensmebles in Bakteriorhodopsin[102] oder die Untersuchung des Einflusses der Umgebungspolarität auf die Stabilität der Helix 1 im zellulären Prionprotein [55] warfen die Frage auf, wie die meist knappen Computerresourcen möglichst optimal genutzt werden können. Daher bekam ich zu Beginn meiner Dissertation den Arbeitsauftrag, die äußerst populäre RE Methode zu untersuchen und gegebenenfalls zu implementieren.

Hier stellte sich recht schnell heraus, daß die RE Methode in ihrer ursprünglichen Fassung nur sehr bedingt für den Einsatz in unserer Arbeitsgruppe geeignet ist. Dies liegt an der großen Anzahl an Temperatursprossen, die notwendig sind, um einen hinreichend großen Temperaturbereich aufzuspannen, wenn das Lösungsmittel explizit berücksichtigt wird. Entsprechend beinhaltet eine RE Simulation gewöhnlich dutzende parallel laufende Simulationen. Da aber meistens nur die Daten bei der Zieltemperatur T_0 von Interesse sind, ist es durchaus fraglich, ob RE wirklich eine effizienteres Abtasten verglichen zu herkömmlichen Simulationen bewirkt [85].

Man kann es als eine glückliche Fügung ansehen, dass just zu der Zeit, in der meine ersten Untersuchungen zu RE liefen, Liu und Co-Autoren die sog. *Replica Exchange with Solute Tempering* (REST) Methode publizierten [101]. Da diese RE Methode mit ihrem schon in der Einleitung näher beschriebenen *Solute Tempering* Konzept die Anzahl der Temperatursprossen drastisch reduziert, sahen mein Betreuer, Paul Tavan, und ich das oben angesprochene Problem als gelöst an.

Nachdem ich die REST Methode in Form von Shell-Skripten implementiert hatte, wendete ich die Methode auf die beiden in der Einleitung dieser Arbeit vorgestellten Azopeptide an. Im Falle des zyklischen Azopeptids cAPB stellten die so ermittelten Gleichgewichtsensembles die Grundlage für die in Kapitel 5 abgedruckte Publikation dar. Bei der REST Behandlung des β-Haarnadelpeptids schien die Simulation schon nach wenigen Nanosekunden konvergiert zu sein, was bei mir anfänglich Begeisterung hervorrief. Nach einer kritischen Sichtung der Daten ergab sich aber, dass die RE Methode einem naiven Anwender eine scheinbare Konvergenz vorgaukeln kann. Diese Erkenntnis war der Ausgangspunkt für die Untersuchungen, die zu dem in Kapitel 2 abgedruckten Artikel führten.

Um das Konvergenzverhalten der β-Haarnadel Simulation genauer zu untersuchen, konstruierte ich ein 3-Zustands Markovmodell für ein β-Haarnadelpeptid, dessen drei Zustände gerade den gefalteten Zustand, einen Übergangszustand und den ungefalteten Zustand eines Haarnadelpeptids repräsentieren. Mit diesem Modellsystem führte ich RE Simulationen durch und untersuchte das Konvergenzverhalten dieser Simulationen bezüglich der freien Energiedifferenz zwischen dem gefalteten und ungefalteten Zustand. Das Modellsystem wurde so konstruiert, dass diese freie Energiedifferenz bei der Zieltemperatur T_0 gerade verschwindet. Auf ein reales β-Haarnadelpeptid übertragen bedeutet dies, dass im Ensemble bei T_0 =300 K etwa 50% der Haarnadelpeptide gefaltet sind, was eine durchaus realistische Annahme ist [11].

Neben der scheinbaren Konvergenz, die in der zitierten Publikation als Pseudokonvergenz bezeichnet wurde, legten die RE Simulationen eine ernste Schwachstelle der RE Methode offen: Entgegen der Erwartung, dass eine Temperaturerhöhung die Faltungs-Entfaltungsdynamik des Modellsystems beschleunigt, trat genau das Gegenteil ein. Zwar beschleunigte eine Temperaturerhöhung den Entfaltungsprozess, gleichzeitig verlangsamte sie aber den Faltungsprozess dermaßen, dass die durchschnittliche Zeit für eine Entfaltung und nachfolgende Rückfaltung mit steigender Temperatur anwuchs. Dieses überraschende Verhalten hat seine Ursache darin, dass die Barriere zwischen dem entfalteten Zustand und dem Übergangszustand entropischer Natur ist. Tatsächlich wurde dieses Verhalten auch schon bei experimentellen Messungen zur Faltungsdynamik an β-Haarnadelpeptiden beobachtet [110], was ein gutes Indiz für die Realitätsnähe des verwendeten 3-Zustandsmodells darstellt. Da für das von mir zu untersuchende β-Haarnadelpeptid Faltungszeiten im Bereich von Mikrosekunden gemessen wurden [16], gab ich das Vorhaben, das strukturelle Gleichgewichtsensemble dieses Peptids mittels MD-Simulationen zu bestimmen, als rechentechnisch unhandhabbar auf.

Sind hingegen enthalpische Barrieren für langsame Abtastgeschwindigkeiten verantwortlich, so können auf Temperaturerhöhung basierende Strategien wie RE die Abtastgeschwindigkeit steigern [111]. Dabei hängt die Abtasteffizienz der RE Methode nicht alleine von den Eigenschaften des zu simulierenden Systems ab, sondern auch davon, wie bestimmte, der Methode innewohnende Parameter gewählt werden. Zu diesen Parametern zählt beispielsweise die Zieltemperatur T_0 und die maximale Temperatur T_{N-1}. Während für die Zieltemperatur meist standardmäßig $T_0 = 300$ K gewählt wird, kann die Frage nach der Temperatur T_{N-1} nicht pauschal beantworten werden. Oft richtet sich die Wahl von T_{N-1} nach der Anzahl an Temperatursprossen und damit nach der Anzahl an Replikaten, die man gleichzeitig aufgrund der verfügbaren Rechnerresourcen simulieren kann. Hat man sich für eine maximale Temperatur T_{N-1} entschieden, stellt sich die Frage, wie die einzelnen Temperaturen T_k einer Temperaturleiter zu wählen sind. Ein mögliches Kriterium für die Güte einer Temperaturleiter ist die Zeit, die ein Replikat im Schnitt benötigt, um von T_0 nach T_{N-1} und zurück zu wandern. Diese Zeit wird als *round-trip* Zeit τ bezeichnet und sollte durch eine optimale Temperaturleiter minimiert werden.

Stutzig machte mich nun, dass es in der Literatur sich widersprechende Aussagen gab, wie eine auf die *round-trip* Zeit optimierte Temperaturleiter zu konstruieren ist. So fanden Predescu und Co-Autoren, dass eine optimale Temperaturleiter einhergeht mit einer mittleren Akzeptanzwahrscheinlichkeit von etwa 40% zwischen in der Temperatur benachbarten Replikate [112]. Abweichend hierzu gaben Nadler und Hansmann eine mittlere Akzeptanzwahrscheinlichkeit von rund 20% an. Diese Autoren gaben darüber hinaus auch erstmals eine einfache Formel an, mit deren Hilfe die einzelnen Sprossen T_k einer optimalen Temperaturleiter bestimmt werden können, sobald $T_{\min} = T_0$ und $T_{\max} = T_{N-1}$

sowie die Wärmekapazität C des Simulationssystems bekannt sind [113].

Um zu klären, welche mittlere Akzeptanzwahrscheinlichkeit tatsächlich zur kürzesten *round-trip* Zeit führt, untersuchte ich den Sachverhalt an einem einfachen Modellsystem aus harmonischen Oszillatoren. Ein solches Oszillatorensystem benötigt ähnlich wie das 3-Zustandsmodell für das β-Haarnadelpeptid sehr wenig Rechenleistung und verfügt darüber hinaus über eine von der Temperatur des Systems unabhängige Wärmekapazität. Letztere Eigenschaft war deswegen wichtig, weil Nadler und Hansmann in ihrer Herleitung eine konstante Wärmekapazität vorausgesetzt hatten — eine Bedingung, die für Simulationssysteme mit explizitem Lösungsmittel meist in guter Näherung erfüllt ist [113].

Abweichend zu den theoretischen Resultaten von Nadler und Hansmann ergaben meine RE Rechnungen an dem Oszillatorsystem, dass, je nach Systemgröße, mittlere Akzeptanzwahrscheinlichkeiten zwischen 40% und 45% zu minimalen *round-trip* Zeiten führen. Hieraus resultierte eine zu Nadler und Hansmann abweichende Formel zur Bestimmung der Temperatursprossen T_k. Diese Formel stellt den Kern der ersten in Kapitel 3 abgedruckten Publikation dar, wobei darüber hinaus dort erstmals eine weitere Vorschrift zur Konstruktion einer optimierten ST Temperaturleiter angegeben wurde. Aus der letztgenannten Vorschrift geht hervor, dass eine solche ST Leiter eine um den Faktor $1/\sqrt{2}$ kleinere Anzahl an Temperatursprossen benötigt als eine entsprechende RE Leiter.

Obwohl die Ergebnisse meiner Rechnungen sowohl der Prüfung durch meinen Kollegen Martin Lingenheil als auch der finalen Prüfung durch meinen Betreuer Paul Tavan standhielten und außerdem im Wesentlichen mit den Resultaten von Predescu und Co-Autoren übereinstimmten, bestand dennoch der Verdacht, dass wir eventuell noch nicht alles bis ins letzte Detail verstanden haben. Dieser Verdacht lag darin begründet, dass die Berechnungen von Nadler und Hansmann auf vernünftigen Annahmen basierten und auch sonst keine Fehler zu erkennen waren. Tatsächlich stellte sich im Rahmen der nun folgenden genauen Analyse heraus, dass das dem Austauschprozess zugrundeliegende Austauschschema für die unterschiedlichen Resultate verantwortlich ist.

Typischerweise wird der Austausch der Temperaturen im Wechsel mit allen „geraden“ Temperaturpaaren $\ldots,(T_{2i},T_{2i+1}),(T_{2i+2},T_{2i+3}),\ldots$ und allen „ungeraden“ Temperaturpaaren $\ldots,(T_{2i+1},T_{2i+2}),(T_{2i+3},T_{2i+4}),\ldots$ durchgeführt [112, 114, 115]. Dieses Schema lag auch unseren RE Simulationen zugrunde. Da man diesem Austauschschema noch keinen Namen gegeben hatte, wurde es von uns mit DEO bezeichnet, wobei diese Bezeichnung für *Deterministic Even-Odd* steht. Auch Predescu und Co-Autoren verwendeten das DEO Schema, während die Arbeit von Nadler und Hansmann indirekt ein zufälliges anstatt eines abwechselnden Austauschens zwischen den geraden und ungeraden Paaren unterstellt. Wir gaben diesem im Vergleich zum DEO leicht abgewandelten Austauschschema den Namen SEO (*Stochastic Even-Odd*).

In der zweiten im Kapitel 3 abgedruckten Publikation wurden daher unterschiedliche Austauschschemata bezüglich ihres Einflusses auf die *round-trip* Zeiten untersucht. Es stellte sich heraus, dass das DEO Austauschschema mit Abstand zu den kürzesten *round-trip* Zeiten führt. Zwar bewirkt das DEO Schema, im Unterschied zum SEO Schema, keine einfache, sondern eine abgewandelte Zufallsbewegung (*Random Walk*) der Replikate auf der Temperaturleiter, dennoch gilt auch für das DEO Schema, dass die mittleren *round-*

trip Zeiten proportional zum Quadrat der Anzahl N der Temperatursprossen sind. Dieser quadratische Zusammenhang bedeutet, dass die ST Methode im Vergleich zu RE wegen $N_{\mathrm{ST}} = N_{\mathrm{RE}}/\sqrt{2}$ um einen Faktor 1/2 kürzere *round-trip* Zeiten liefert, solange beide Verfahren das gleiche Austauschschema verwenden.

Letztere Erkenntnis führte mich dazu, das *Solute Tempering* Konzept, welches ursprünglich von Liu und Co-Autoren nur auf RE angewendet wurde [101], auch auf die ST Methode zu übertragen. Die hieraus resultierende ST Variante namens SST wurde in der Publikation des Kapitel 4 vorgestellt und auf ein konkretes MD System angewandt. Unter anderem zeigte sich, dass SST gegenüber REST höhere Abtastgeschwindigkeiten liefert. Dabei wurde für die SST Simulationen das DEO Austauschschema meines Wissens zum ersten mal auf eine ST Methode angewendet. Dass in der Vergangenheit der Unterschied zwischen den *round-trip* Zeiten von RE und entsprechenden ST Simulationen nie besonders stark ausgefallen ist, kann vermutlich auch darauf zurückgeführt werden, dass RE Simulationen mit dem DEO Austauschschema betrieben wurden, während für ST Simulationen das für diese Abtasttechnik näherliegende, aber unterlegene SEO Schema verwendet wurde.

Obwohl die SST Methode höhere Abtastgeschwindigkeiten als REST liefert, wurde im Kapitel 5 zur Bestimmung des strukturellen Gleichgewichtsensembles des cAPB Modellpeptids die REST Methode verwendet, da zum Startzeitpunkt der REST Simulationen die SST Methode noch nicht ausgearbeitet war. Dass konventionelle MD bei Raumtemperatur zur Bestimmung der strukturellen Gleichgewichtsensembles von cAPB ungeeignet ist, hatte schon mein Vorgänger, Heiko Carstens, festgestellt, indem er die Häufigkeit von Diederwinkelflips der ϕ/ψ Diederwinkel analysierte [3]. Die beobachteten Flips waren derart selten, dass er dazu überging, die Gleichgewichtssimulationen bei 500 K durchzuführen.

Obwohl die bei 500 K erzeugten Gleichgewichtsensembles für *cis*- und *trans*-cAPB sehr gut mit den Proton-Proton Abständen aus NMR Messungen übereinstimmten, war es ein Teilergebnis der Publikation aus Kapitel 5, dass diese Übereinstimmung keineswegs eine Garantie für realistische Gleichgewichtsensembles darstellt. Die dort vorgestellten REST Simulationen wurden für zwei unterschiedliche Kraftfelder (CHARMM22 und CHARMM22/CMAP) durchgeführt und lieferten neben den strukturellen Gleichgewichtsensembles bei Raumtemperatur auch nichtphysikalische Hochtemperaturensembles. So wichen die aus den REST Simulationen bei 570 K mit dem CHARMM/CMAP Kraftfeld ermittelten strukturellen Hochtemperaturensembles stark von den bei Raumtemperatur ermittelten Ensembles ab, obwohl die Strukturdaten sowohl für 570 K als auch für 300 K im Einklang mit den experimentellen NMR Daten standen. Interessanterweise standen die strukturellen Ensembles, die mit REST unter Verwendung des CHARMM Kraftfeldes berechnet wurden, weit weniger gut im Einklang mit den NMR Daten, was darauf hindeutet, dass die Erweiterung des CHRAMM Kraftfeldes durch die CMAP Korrekturkarte tatsächlich ein realistischeres Kraftfeld liefert.

Im Vordergrund der in Kapitel 5 abgedruckten Publikation stand jedoch die Frage, auf welchen Zeitskalen die durch lichtinduzierte *cis-trans* Isomerisierung ausgelöste Relaxation des cAPB Peptids abläuft. Die Bestimmung der strukturellen *cis*- und *trans*-Gleichgewichtsensembles mittels REST diente primär dazu, die Start- und Endpunkte der lichtinduzierten Dynamiken genau zu bestimmen, um dadurch den Fortschritt der lichtinduzierten Dynamik verfolgen zu können. Für jedes der beiden schon für die REST Simulationen verwendeten Kraftfelder wurden jeweils 50 Startstrukturen aus dem entsprechenden *cis*-Gleichgewichtsensemble zufällig ausgewählt, um an ihnen MD Nichtgleichgewichtssimulationen durchzuführen, indem zu Beginn jeder Simulation durch die *cis-trans* Isomerisierung des integrierten Farbstoffes die Relaxation hin zum entsprechenden *trans*-Ensemble ausgelöst wurde.

Die Ergebnisse dieser Simulationen wurden mit den aus IR *pump-probe* Messungen ermittelten Relaxationszeiten der Arbeitsgruppe Zinth verglichen. Dabei konnten für die kürzesten durch IR bestimmten Relaxationszeiten von 11 ps und 137 ps entsprechende Zeiten weder aus den CHARMM noch aus den CHARMM/CMAP Nichtgleichgewichtssimulationen extrahiert werden. Dies liegt wohl hauptsächlich daran, dass die verwendete Observable $\bar{H}_2$ zur Untersuchung sehr schneller Dynamiken nicht geeignet ist, da $\bar{H}_2$ in den ersten 100 ps sich nur sehr wenig ändert und damit nicht besonders sensitiv in diesem initialen Zeitraum ist. Dies spiegelt sich auch in den recht großen statistischen Fehlern der mittels MD bestimmten Kurzzeitdynamiken wider. Tatsächlich hatte ich die $\bar{H}_2$ Observable eingeführt, um die langsamsten, bislang auch experimentell nicht bekannten Relaxationszeiten zu bestimmen und nicht, wie es mein Vorgänger schon getan hatte [3, 7], die kurzen Zerfallszeiten.

Für die längste experimentell gemessene Zerfallszeit von etwa 1,4 ns lieferten die MD Simulationen für beide Kraftfelder (CHARMM und CHARMM/CMAP) dann auch eine erstaunlich gute Übereinstimmung mit den experimentellen Daten. Da die IR *pump-probe* Messungen aus technischen Gründen nur ein Zeitfenster von 3 ns abdeckten, konnten damit keine längeren Relaxationszeiten ermittelt werden. Andererseits war anhand des nach 3 ns beobachteten Differenzspektrums klar, dass der Relaxationsprozess zu diesem Zeitpunkt noch nicht beendet ist.

Um die Nachfolgeprozesse zu analysieren, dehnte ich daher die Nichtgleichgewichtssimulationen auf 20 ns aus und fand eine Relaxationszeit von etwa 23 ns, unabhängig vom verwendeten Kraftfeld. Diese Relaxationszeit konnte eindeutig als die langsamste Zerfallszeit identifiziert werden, womit die Frage nach der Dauer der *cis-trans* Relaxationsdynamik aus theoretischer Sicht beantwortet werden konnte. Dennoch bleibt es eine spannende Frage, ob die berechnete Langzeitdynamik auch durch das Experiment bestätigt werden kann. Leider ist mittlerweile der Vorrat an cAPB aufgebraucht, so dass die Beantwortung dieser Frage davon abhängt, ob in der Zukunft noch einmal eine ausreichende Menge an cAPB hergestellt wird.

Unabhängig davon wird jedoch sicherlich das cAPB Peptid in MD Simulationen als Modellpeptid weiterhin von Interesse sein. Beispielsweise kann an diesem Modellpeptid das in der Entwicklung befindliche implizite Lösungsmittelmodell durch den Vergleich von freien Energielandschaften getestet werden, die einerseits durch das implizite Lösungsmittelmodell und andererseits, wie in Kapitel 5 geschehen, durch explizites Lösungsmittel bestimmt wurden. Angemerkt sei, dass die Verwendung eines impliziten Lösungsmittelmodells das *Solute Tempering* Konzept keineswegs bedeutungslos werden lässt, da sich dieses Konzept auch auf Teilbereiche des zu untersuchenden Moleküls anwenden lässt [102].

Das *Solute Tempering* Konzept hat in Verbindung mit RE (REST) und ST (SST) neben der bloßen Einsparung an Temperatursprossen vermutlich einen weiteren, bislang in der Literatur nicht erwähnten Vorteil: Wir vermuten, dass REST sowie SST in Verbindung mit einem sog. Berendsen Thermostaten [116] verwendet werden darf, ohne dadurch die Gültigkeit der kanonischen Ensemblestatistik zu verletzen. Hierzu muss man wissen, dass der Berendsen Thermostat sehr häufig in RE Simulationen verwendet wird, obwohl er kein echtes kanonisches Ensemble erzeugt [117] und daher streng genommen nicht in RE bzw. ST Simulationen eingesetzt werden darf [118, 119]. Erste Voruntersuchungen an einem kleinen Oktapeptid mittels MD ergaben, dass solange ausschließlich das Lösungsmittel und nicht das gelöste Molekül an den Thermostaten gekoppelt ist, der im Austauschkriterium berücksichtigte Energieanteil kanonisch verteilt ist. Dies wurde von uns schon länger vermutet [118] und war ein Grund dafür, dass das cAPB Peptid in den in Kapitel 5 vorgestellten Simulationen nicht an den Berendsen Thermostaten gekoppelt wurde. Mittlerweile hat sich Sebastian Bauer diesem Thema gewidmet und man darf in naher Zukunft von ihm gesicherte Resultate erwarten.

Ein weiteres Projekt, das ich auf Initiative von Gerald Mathias am Ende meiner Doktorandenzeit begonnen hatte, hat das Ziel, ein neues Austauschschema zu entwickeln, das den bislang aus Kapitel 3 bekannten Austauschschemata überlegen ist. Obwohl ich auch hier nicht mehr die Zeit fand, dieses Projekt erfolgreich abzuschließen, sind erste vorläufige Resultate durchaus erfolgsversprechend. Entsprechend wird dieses Projekt von Gerald Mathias weitergeführt und auch hier darf man in naher Zukunft Ergebnisse erwarten.

Wie ich bereits weiter oben erwähnt habe, kann man unter bestimmten Bedingungen *round-trip* Zeit optimierte Temperaturleitern berechnen, sobald man die Wärmekapazität sowie die minimale und maximale Temperatur T_0 und T_{N-1} vorgibt. Welche maximale Temperatur T_{N-1} in einer RE bzw. ST Simulation zu optimalen Ergebnissen führt, kann bislang jedoch nicht angegeben werden. Tatsächlich wird man diese Frage wohl auch in der Zukunft nicht pauschal beantworten können. Allerdings könnten die Erkenntnisse aus den Kapiteln 2 und 3 dazu führen, wenigstens Regeln zur Bestimmung einer optimalen Temperatur T_{N-1} für wohldefinierte Grenzfälle zu finden. Erste Ideen hierzu existieren zwar bereits, deren Qualität muss aber erst noch durch geeignete Simulationen überprüft werden.

Leider stellt auch der beste Austauschalgorithmus in Verbindung mit einer optimalen Temperaturleiter noch keine Garantie für kurze *round-trip* Zeiten dar. Vielmehr hängt die *round-trip* Zeit in einer realen RE Simulation wesentlich davon ab, wie stark die potentiellen Energien der einzelnen Systemzustände (Konformationen) voneinander abweichen. Durch den Austauschprozess werden nämlich Replikate, die sich in einer Konformation mit niedriger potentieller Energie befinden, bevorzugt zu niedrigen Temperaturen ausgetauscht, während Replikate mit hohen potentiellen Energien zu hohen Temperaturen befördert werden. Solange Replikate in ihrer Konformation verharren und große energetische Unterschiede zwischen den Konformationen der einzelnen Replikate bestehen, werden die Replikate vergleichsweise lange für einen *round-trip* benötigen und die in Kapitel 3 angegebene Formel zur Bestimmung der *round-trip* Zeit ist dann nicht mehr gültig[1]. Dieses Problem tritt typischerweise bei Phasenübergängen von gefalteten zu ungefalteten Systemzuständen auf, wobei der Energiesprung je nach RE Variante unterschiedlich stark ausgeprägt sein kann.

Will man also beispielsweise REST oder SST zum Abtasten des Konformationsraumes verwenden, ist es empfehlenswert, durch initiale Testrechnungen erst einmal abzuschätzen, ob das *Solute Tempering* Konzept dieses Problem lindert oder gar verschärft, weil das skalierte Kraftfeld bei T_{N-1} im Vergleich zum unskalierten Kraftfeld kleinere oder eventuell größere Energieunterschiede zwischen gefalteten und ungefalteten Zuständen hervorruft. Tatsächlich findet sich in der Literatur eine Arbeit von Huang und Co-Autoren, in der das *Solute Tempering* Konzept vermutlich die dort beobachtete schlechte Durchmischung der Replikate im Temperaturraum aufgrund des hier beschriebenen Sachverhaltes verursacht hat [120].

Andererseits lässt sich die an einem Phasenübergang gehemmte Durchmischung der Replikate durch verschiedene Ansätze steigern. Ein solcher Ansatz stammt von Trebst und Co-Autoren [121], und beruht darauf, dass die *round-trip* Zeit deutlich verkürzt werden kann, wenn die Anzahl der Temperatursprossen in der Umgebung der kritischen Temperatur deutlich erhöht wird. Ein weiterer, von Kamberaj und van der Vaart vorgestellter Ansatz besteht darin, die Energiefunktion mittels des Wang-Landau Algorithmus [122] derart zu modifizieren, dass alle Replikate in etwa die gleiche mittlere Energie aufweisen. Damit verschwindet der Energiesprung im Bereich der kritischen Temperatur, was zu einem *Random Walk* der Replikate im Temperaturraum führt. Für ein System mit relativ wenigen Freiheitsgraden wurde dieser Ansatz schon erfolgreich getestet [123]. Dennoch steht der Nachweis noch aus, ob letzterer Ansatz auch für komplexe Systeme praktikabel ist: Zum Einen wird die Bestimmung einer hinreichend „flachen“ Energiefunktion mit einem erheblichen Aufwand verbunden sein und zum Anderen ändert die Modifikation der Energiefunktion die Besetzungswahrscheinlichkeiten der einzelnen Zustände, was im Extremfall dazu führen kann, dass wesentliche Zustände in einer solchen Simulation nicht mehr vorkommen, und somit auch eine Regewichtung der Daten keine akkuraten Ergebnisse liefern kann.

---

[1] Tatsächlich wird dort eine Formel für die inverse *round-trip* Zeit, die sog. *round-trip* Rate angegeben.

Literaturverzeichnis

[1] A. L. Lehninger. *Grundkurs Biochemie*. Walter de Gruyter, Berlin, 1985.

[2] L. Stryer. *Biochemie*. Spektrum Akademischer Verlag, Heidelberg, 1991.

[3] H. Carstens. *Konformationsdynamik lichtschaltbarer Peptide: Molekulardynamiksimulationen und datengetriebene Modellbildung*. Dissertation, Fakultät für Physik, Ludwig-Maximilians-Universität München, 2004.

[4] S. Spörlein, H. Carstens, H. Satzger, C. Renner, R. Behrendt, L. Moroder, P. Tavan, W. Zinth, and J. Wachtveitl. Ultrafast spectroscopy reveals subnanosecond peptide conformational dynamics and validates molecular dynamics simulation. *Proc. Natl. Acad. Sci. USA*, 99:7998–8002, 2002.

[5] H. Carstens, C. Renner, A. G. Milbradt, L. Moroder, and P. Tavan. Multiple loop conformatuions of peptides predicted by molecular dynamics simulations are compatible with NMR. *Biochemistry*, 44:4829–4840, 2005.

[6] A. R. Fersht and V. Daggett. Protein folding and unfolding at atomistic resolution. *Cell*, 108:573–582, 2002.

[7] P. Tavan, H. Carstens, and G. Mathias. Molecular dynamics simulations of proteins and peptides: Problems, achievements, and perspectives. In Johannes Buchner and Thomas Kiefhaber, editors, *Protein Folding Handbook. Part I.*, chapter 33, pages 1170–1195. Wiley-VCH, 2005.

[8] W. F. van Gunsteren and J. Dolenc. Biomolecular simulations: Historical picture and future perspectives. *Biochem. Soc. Trans.*, 36:11–15, 2008.

[9] C. Renner, R. Behrendt, S. Spörlein, J. Wachtveitl, and L. Moroder. Photomodulation of conformational states. I. Mono- and bicyclic peptides with (4-amino)phenylazobenzoic acid as bockbone constituent. *Biopolymers*, 54:489–500, 2000.

[10] R. Denschlag, W. J. Schreier, B. Rieff, T. E. Schrader, O. Koller, L. Moroder, W. Zinth, and P. Tavan. Relaxation time prediction for a light switchable peptide by molecular dynamics. *Phys. Chem. Chem. Phys.*, 12:6204–6218, 2010.

[11] S.-L. Dong, M. Löweneck, T. E. Schrader, W. J. Schreier, W. Zinth, L. Moroder, and C. Renner. A photocontrolled beta-hairpin peptide. *Chem.-Eur. J.*, 12:1114–1120, 2006.

[12] M. Karplus and J. A. McCammon. Molecular dynamics simulations of biomolecules. *Nature Struct. Biol.*, 9:646–652, 2002.

[13] G. Mathias, B. Egwolf, M. Nonella, and P. Tavan. A fast multipole method combined with a reaction field for long-range electrostatics in molecular dynamics simulations: The effects of truncation on the properties of water. *J. Chem. Phys.*, 118:10847–10860, 2003.

[14] E. Lindahl, B. Hess, and D. van der Spoel. Gromacs 3.0: A package for molecular simulation and trajectory analysis. *J. Mol. Mod.*, 7:306–317, 2001.

[15] R. Denschlag, M. Lingenheil, and P. Tavan. Efficiency reduction and pseudo-convergence in replica exchange sampling of protein folding-unfolding equilibria. *Chem. Phys. Lett.*, 458:244–248, 2008.

[16] T. E. Schrader, W. J. Schreier, T. Cordes, F. O. Koller, G. Babitzki, R. Denschlag, C. Renner, M. Löweneck, S.-L. Dong, L. Moroder, P. Tavan, and W. Zinth. Light-triggered β-hairpin folding and unfolding. *Proc. Natl. Acad. Sci. USA*, 104:15729–15734, 2007.

[17] P. L. Freddolino, F. Liu, M. Gruebele, and K. Schulten. Ten-microsecond molecular dynamics of fast-folding ww domain. *Biophys. J.*, 94:L75–L77, 2008.

[18] K. Hukushima and K. Nemoto. Exchange Monte Carlo method and application to spin glass simulations. *J. Phys. Soc. Jpn.*, 65:1604–1608, 1996.

[19] U. H. E. Hansmann. Free energy landscape and folding mechanism of a β-hairpin in explicit water: A replica exchange molecular dynamics study. *Chem. Phys. Lett.*, 281:140–150, 1997.

[20] Y. Sugita and Y. Okamoto. Replica-exchange molecular dynamics method for protein folding. *Chem. Phys. Lett.*, 314:141–151, 1999.

[21] C. M. Dobson. Protein folding and misfolding. *Nature*, 426:884–890, 2003.

[22] J. L. Sohl, S. S. Jaswal, and Agard D. A. Unfolded conformations of α-lytic protease are more stable than its native state. *Nature*, 395:817–819, 1998.

[23] Z. Wang, J. Mottonen, and E. J. Goldsmith. Kinetically controlled folding of the serpin plasminogen activator inhibitor 1. *Biochemistry*, 35:16443–16448, 1996.

[24] C. B. Anfinsen, E. Haber, M. Sela, and F. H. White Jr. The kinetics of formation of native ribonuclease during oxidation of the reduced polypeptide chain. *Proc. Natl. Acad. Sci. USA*, 47:1309–1314, 1961.

[25] C. J. Epstein, R. F. Goldberger, and C. B. Anfinsen. The genetic control of tertiary protein structure: Studies with model systems. *Cold Spring Harbor Symp. Quant. Biol.*, 28:439–449, 1963.

[26] C. B. Anfinsen. Principles that govern the folding of protein chains. *Science*, 181:223–230, 1973.

[27] C. M. Dobson. Experimental investigation of protein folding and misfolding. *Methods*, 34:4–14, 2004.

[28] J. P. Taylor, J. Hardy, and K. H. Fischbeck. Toxic proteins in neurodegenerative disease. *Science*, 296:1991–1995, 2002.

[29] F. U. Hartl and M. Hayer-Hartl. Molecular chaperones in the cytosol: from nascent chain to folded protein. *Science*, 295:1852–1858, 2002.

[30] L. Pauling, R. B. Corey, and H. R. Branson. The structure of proteins: Two hydrogen-bonded helical configurations of the polypeptide chain. *Proc. Natl. Acad. Sci. USA*, 37:235–240, 1951.

[31] L. Pauling and R. B. Corey. The pleated sheet, a new layer configuration of polypeptide chains. *Proc. Natl. Acad. Sci. USA*, 37:251–256, 1951.

[32] W. A. Eaton, V. Munoz, P. A. Thompson, E. R. Henry, and J. Hofrichter. Kinetics and dynamics of loops, α-helices, β-hairpins, and fast-folding proteins. *Acc. Chem. Res.*, 31:745–753, 1998.

[33] C. D. Snow, N. Nguyen, S. Pande, and M. Gruebele. Absolute comparison of simulated and experimental protein-folding dynamics. *Nature*, 420:102–106, 2002.

[34] W. Y. Yang and M. Gruebele. Folding at the speed limits. *Nature*, 423:193–197, 2003.

[35] U. Mayor, N. R. Guydosh, C. M. Johnson, Grossmann J. G., S. Sato, G. S. Jas, S. M. V. Freund, D. O. V Alonso, V. Daggett, and A. R. Fersht. The complete folding pathway of a protein from nanoseconds to microseconds. *Nature*, 421:863–867, 2003.

[36] L. L. Qiu, S. A. Pabit, A. E. Roitberg, and S. J. Hagen. Smaller and faster: The 20-residue trp-cage protein folds in 4 μs. *J. Am. Chem. Soc.*, 124:12952–12953, 2002.

[37] J. A. McCammon. Protein dynamics. *Rep. Prog. Phys.*, 47:1–46, 1984.

[38] W. A. Eaton, V. Munoz, S. J. Hagen, G. S. Jas, L. J. Lapidus, E. R. Henry, and J. Hofrichter. Fast kinetics and mechanisms in protein folding. *Annu. Rev. Biophys. Biomol. Struct.*, 29:327–359, 2000.

[39] S. Geibel, J. H. Kaplan, E. Bamberg, and T. Friedrich. Conformational dynamics of the Na^+/K^+–ATPase probed by voltage champ flourometry. *Proc. Natl. Acad. Sci. USA*, 100:964–969, 2003.

[40] D. W. Green, V. M. Ingram, and M. F. Perutz. The structure of haemoglobin IV. Sign determination by the isomorphous replacement method. *Proc. Roy. Soc. A*, 225:287–307, 1954.

[41] J. C. Kendrew, G. Bodo, H. M. Dinitzis, R. G. Parrish, H. Wyckoff, and D. C. Phillips. A three-dimensional model of the myoglobin molecule obtained by X-ray analysis. *Nature*, 181:662–666, 1985.

[42] B. Nölting. Mechanism of protein folding. *Proteins*, 41:288–298, 2000.

[43] R. Rowan III, J. A. McCammon, and B. D. Sykes. A study of the distances obtained from nuclear magnetic resonance nuclear Overhauser effect and relaxation time measurements in organic structure determination. Distances involving internally rotating methyl groups. Application to *cis*- and *trans*-crotonaldehyde. *J. Am. Chem. Soc.*, 96:4773–4780, 1974.

[44] K. Wüthrich. *NMR of Proteins and Nukleic Acids*. Wiley, New York, 1986.

[45] C. K. Woodward. Hydrogen exchange rates and protein folding. *Current Opinion in Struct. Biol.*, 4:112–116, 1994.

[46] A. K. Bhuyan and J. B. Udgaonkar. Real-time NMR measurements of protein folding and hydrogen exchange dynamics. *Current Science*, 10:942–952, 1999.

[47] A. Weiss. Fluorescence spectroscopy of single biomolecules. *Science*, 283:1676 – 1683, 1999.

[48] L. Nilsson and B. Halle. Molecular origin of time-dependent fluorescence shifts in proteins. *Proc. Natl. Acad. Sci. USA*, 102:13867–13872, 2005.

[49] F. Schotte, M. Lim, T. A. Jackson, A.V. Smirnov, J. Soman, J. S. Olson, G. N. Phillips, M. Wulff, and P. A. Anfinrud. Watching a protein as it functions with 150-ps time-resolved X-ray crystallography. *Science*, 300:1944–1947, 2003.

[50] J. Bredenbeck, J. Helbing, J. R. Kumita, G. A. Woolley, and P. Hamm. α-helix formation in a photoswitchable peptide tracked from picoseconds to microseconds by time-resolved IR spectroscopy. *Proc. Natl. Acad. Sci. USA*, 102:2379–2384, 2005.

[51] E. Chen, M. J. Wood, A. L. Fink, and D. S. Kliger. Time-resolved Circular Dichroism studies of protein folding intermediates of cytochrome c. *Biochemistry*, 37:5589–5598, 1998.

[52] O. Bieri, J. Wirz, B. Hellrung, M. Schutkowski, M. Drewello, and T. Kiefhaber. The speed limit for protein folding measured by triplet-triplet energy transfer. *Proc. Natl. Acad. Sci. USA*, 96:9597–9601, 1999.

[53] M. Stork, A. Giese, H. A. Kretzschmar, and P. Tavan. MD simulations indicate a possible role of parallel α-helices in seeded aggregation of poly-Gln. *Biophys. J.*, 88:2442–2451, 2005.

[54] T. Hirschberger, M. Stork, B. Schropp, K. F. Winkelhofer, J. Tatelt, and P. Tavan. Structural instability of the prion protein upon M205S/R mutations revealed by molecular dynamics simulations. *Biophys. J.*, 90:3908–3918, 2006.

[55] M. Lingenheil, R. Denschlag, and P. Tavan. Highly polar environments catalyze the unfolding of PrPC helix 1. *Europ. Biophys. J.*, 2010. *DOI: 10.1007/s00249-009-0570-6*.

[56] S. B. Oskan, G. A. Wu, J. D. Chodera, and K. A. Dill. Protein folding by zipping and assembly. *Proc. Natl. Acad. Sci. USA*, 104:11987–11992, 2007.

[57] K. A. Dill, S. B. Ozkan, T. R. Weikl, J. D. Chodera, and V. A. Voelz. The protein folding problem: when will it be solved? *Current Opinion in Struct. Biol.*, 17:1–5, 2007.

[58] O. M. Becker, A. D. MacKerell, B. Roux, and Watanabe M. *Computational Biochemistry and Biophysics*. Marcel Decker Inc., New York, 2001.

[59] J. A. McCammon, B. R. Gelin, and M. Karplus. Dynamics of folded proteins. *Nature*, 267:585–590, 1977.

[60] M Levitt and S. Lifson. Refinement of protein conformations using a macromolecular energy minimization procedure. *J. Mol. Biol.*, 46:269–279, 1969.

[61] B. R. Brooks, R. E. Bruccoleri, B. D. Olafson, D. J. States, S. Swaminathan, and M Karplus. CHARMM: A program for macromolecular energy, minimization, and dynamics calculations. *J. Comput. Chem.*, 4:187–217, 1983.

[62] A. D. MacKerell, D. Bashford, M. Bellott, R. L. Dunbrack, J. D. Evanseck, M. J. Field, S. Fischer, J. Gao, H. Guo, S. Ha, D. Joseph-McCarthy, L. Kuchnir, K. Kuczera, F. T. K. Lau, C. Mattos, S. Michnick, T. Ngo, D. T. Nguyen, B. Prodhom, W. E. Reiher, B. Roux, M. Schlenkrich, J. C. Smith, R. Stote, J. Straub, M. Watanabe, J. Wiorkiewicz-Kuczera, D. Yin, and M. Karplus. All-atom empirical potential for molecular modeling and dynamics studies of proteins. *J. Phys. Chem. B*, 102:3586–3616, 1998.

[63] D. A. Pearlman, D. A. Case, J. W. Caldwell, W. S. Ross, T. E. Cheatham, S. Debolt, D. Ferguson, G. Seibel, and P. Kollman. AMBER, a package of computer programs. *Comput. Phys. Commun.*, 91:1–41, 1995.

[64] W. R. P. Scott, P. H. Hünenberger, I. G. Tironi, A. E. Mark, S. R. Billeter, J. Fennen, A. E. Torda, T. Huber, P. Krüger, and W. F. van Gunsteren. The GROMOS biomolecular simulation program package. *J. Phys. Chem.*, 103:3596–3607, 1996.

[65] W. L. Jorgensen, D. S. Maxwell, and Tirado-Rives J. Development and testing of the OPLS all-atom force field on conformational energetics and properties of organic liquids. *J. Am. Chem. Soc.*, 118:11225–11236, 1996.

[66] L. Verlet. Computer "experiments" on classical fluids. I. Thermodynamical properties of Lennard-Jones molecules. *Phys. Rev.*, 159:98–103, 1967.

[67] M. P. Allen and D. J. Tildesley. *Computer Simulations of Liquids*. Oxford University Press, Oxford, 1987.

[68] N. Metropolis, A. W. Rosenbluth, M. N. Rosenbluth, A. H. Teller, and E. Teller. Equation of state calculation by fast computing machines. *J. Chem. Phys.*, 21:1087–1092, 1953.

[69] M. Yoneya, H. J. C. Berendsen, and Hirasawa K. A noniterative matrix method for constraint molecular-dynamics simulations. *Molecular Simulation*, 13:395–405, 1994.

[70] A. D. MacKerell, M. Feig, and C. L. Brooks, III. Extending the treatment of backbone energetics in protein force fields: Limitations of gas-phase quantum mechanics in reproducing protein conformational distributions in molecular dynamics simulations. *J. Comput. Chem.*, 25:1400–1415, 2004.

[71] A. Kitao, K. Yonekura, S. Maki-Yonekura, F.A. Samatey, K. Imada, K. Namba, and N. Go. Switch interactions control energy frustration and multiple flagellar filament structures. *Proc. Natl. Acad. Sci. USA*, 103:4894–4899, 2006.

[72] P. L. Freddolino, A. S. Arkhipov, S. B. Larson, A. McPherson, and K. Schulten. Molecular dynamics simulations of the complete satellite tobacco mosaic virus. *Structure*, 14:437–449, 2006.

[73] P. Maragakis, K. Lindorff-Larsen, M. P. Eastwood, R. O. Dror, J. L. Klepeis, I. T. Arkin, M. O. Jensen, H. Xu, N. Trbovic, R. A. Friesener, A. G. Palmer, and D. E. Shaw. Microsecond molecular dynamics simulation shows effect of slow loop dynamics on backbone amide order parameters of proteins. *J. Phys. Chem. B*, 112:6155–6158, 2008.

[74] W. C. Still, A. Tempczyk, R. C. Hawley, and T. Hendrickson. Semianalytical treatment of solvation for molecular mechanics and dynamics. *J. Am. Chem. Soc.*, 112:6127–6129, 1990.

[75] V. A. Voelz, G. R. Bowman, K. Beauchamp, and V. S. Pande. Molecular simulation of *ab initio* protein folding for a millisecond folder NTL9(1-39). *J. Am. Chem. Soc.*, 132:1526–1528, 2010.

[76] Hugh Nymeyer and Angle E. García. Simulation of the folding equilibrium of α-helical peptides: A comparison of the generalized born approximation with explicit solvent. *Proc. Natl. Acad. Sci. USA*, 100:13934–13939, 2003.

[77] R. Zhou and B. J. Berne. Can a continuum model reproduce the free energy landscape of a β-hairpin folding in water? *Proc. Natl. Acad. Sci. USA*, 99:12777–12782, 2002.

[78] R. Geney, M. Layten, R. Gomperts, V. Hornak, and C. Simmerling. Investigation of salt bridge stability in a generalized born solvent model. *J. Chem. Theory Comput.*, 2:115–127, 2006.

[79] H. Lei and Y. Duan. Two-stage folding of HP-35 from *ab initio* simulations. *J. Mol. Biol.*, 370:196–206, 2007.

[80] J. D. Jackson. *Classical Electrodynamicss*. John Wiley and Sons, New York, second edition, 1975.

[81] M. Stork and P. Tavan. Electrostatics of proteins in dielectric solvent continua: I. Newton's third law marries qe forces. *J. Chem. Phys.*, 126:165105, 2007.

[82] B. Egwolf and P. Tavan. Continuum description of solvent dielectrics in molecular-dynamics simulations of proteins. *J. Chem. Phys.*, 118:2039–2056, 2003.

[83] M. Stork and P. Tavan. Electrostatics of proteins in dielectric solvent continua: I. newton's third law marries qe forces. *J. Chem. Phys.*, 126:165105, 2007.

[84] M. Stork and P. Tavan. Electrostatics of proteins in dielectric solvent continua: II. first applications in molecular dynamics simulations. *J. Chem. Phys.*, 126:165106, 2007.

[85] D. M. Zuckerman and E. Lyman. A second look at canonical sampling of biomolecules using replica exchange simulation. *J. Chem. Theory Comput.*, 2:1200–1202, 2006.

[86] Y. Okamoto. Generalized-ensemble algorithms: Enhanced sampling techniques for Monte Carlo and molecular dynamics simulations. *J. Mol. Graph. Model.*, 22:425–439, 2004.

[87] S. Kumar, D. Bouzida, R. H. Swendsen, P. A. Kollman, and J. M. Rosenberg. The weighted histogram analysis method for free-energy calculations on biomolecules. I. the method. *J. Comput. Chem.*, 13:1011–1021, 1992.

[88] G. M. Torrie and J. P. Valleau. Nonphysical sampling distributions in Monte Carlo free-energy estimation - umbrella sampling. *J. Comput. Phys.*, 23:187–199, 1977.

[89] G. H. Paine and H. A. Scheraga. Prediction of the native conformation of a polypeptide by a statistical-mechanical procedure. I. Backbone structure of enkephalin. *Biopolymers*, 24:1391–1436, 1985.

[90] M. Mezei. Adaptive umbrella sampling: Self-consistent determination of the non-Boltzmann bias. *J. Comput. Phys.*, 68:237–248, 1987.

[91] C. Bartels and M. Karplus. Multidimensional adaptive umbrella sampling: Applications to main chain and side chain peptide conformations. *J. Comput. Chem.*, 18:1450–1462, 1997.

[92] B. A. Berg and T. Neuhaus. Multicanonical algorithms for first order phase transitions. *Phys. Lett. B*, 267:249–253, 1991.

[93] B. A. Berg and T. Neuhaus. Multicanonical ensemble: A new approach to simulate first-order phase transitions. *Phys. Rev. Lett.*, 68:9–12, 1992.

[94] H. Fukunishi, O. Watanabe, and S. Takada. On the Hamilton replica exchange method for efficient sampling of biomolecular systems: Application to protein structure prediction. *J. Chem. Phys.*, 116:9058–9067, 2002.

[95] R. Affentranger and I. Tavernelli. A novel Hamiltonian replica exchange MD protocol to enhance protein conformational space sampling. *J. Chem. Theory Comput.*, 2:217–228, 2006.

[96] S. Kannan and M. Zacharias. Folding of trp-cage mini protein using temperature and biasing potential replica exchange molecular dynamics simulations. *Int. J. Mol. Sci.*, 10:1121–1137, 2009.

[97] H. S. Hansen and P. H. Hünenberger. Using the local elevation method to construct optimized umbrella sampling potentials: calculation of the relative free energies and interconversion barriers of glucopyranose ring conformers in water. *J. Comput. Chem.*, 31:1–23, 2010.

[98] R. E. Bruccoleri and M. Karplus. Conformational sampling using high-temperature molecular dynamics. *Biopolymers*, 29:1847–1862, 1990.

[99] A. P. Lyubartsev, A. A. Martinovski, S. V. Shevkunov, and P. N. Vorontsov-Velyaminov. New approach to Monte Carlo calculation of the free energy: Method of expanded ensembles. *J. Chem. Phys.*, 96:1776–1783, 1992.

[100] E. Marinari and G. Parisi. Simulated tempering: A new Monte Carlo scheme. *Europhys. Lett.*, 19:451–458, 1992.

[101] P. Liu, B. Kim, R. A. Friesner, and B. J. Berne. Replica exchange with solute tempering: A method for sampling biological systems in explicit water. *Proc. Natl. Acad. Sci. USA*, 102:13749–13754, 2005.

[102] G. Babitzki, R. Denschlag, and P. Tavan. Polarization effects stabilize bacteriorhodopsin's chromophore binding pocket: A molecular dynamics study. *J. Phys. Chem.*, 113:10483–10495, 2009.

[103] R. Denschlag, M. Lingenheil, P. Tavan, and G. Mathias. Simulated solute tempering. *J. Chem. Theory Comput.*, 5:2847–2857, 2009.

[104] M. Kastner. Monte Carlo methods in statistical physics: Mathematical foundations and strategies. *Commun. Nonlinear Sci. Numer. Simul.*, 15:1589–1602, 2010.

[105] S. Park and V. S. Pande. Choosing weights for simulated tempering. *Phys. Rev. E*, 76:016703, 2007.

[106] D. A. Kofke. On the acceptance probability of replica-exchange Monte Carlo trials. *J. Chem. Phys.*, 117:6911–6914, 2002.

[107] K. A. Dill and S. Bromberg. *Molecular driving forces: statistical thermodynamics in chemistry and biology*. Garland Science, Taylor and Francis Group, New York, 2003.

[108] D. J. Earl and M. W. Deem. Parallel tempering: Theory, applications, and new perspectives. *Phys. Chem. Chem. Phys.*, 7:3910–3922, 2005.

[109] R. Reichold. *Rechnergestützte Beschreibung der Struktur und Dynamik von Peptiden und ihren Bausteinen*. Dissertation, Fakultät für Physik, Ludwig-Maximilians-Universität München, 2009.

[110] D. Du, Y. Zhu, C.-Y. Huang, and F. Gai. Understanding the key factors that control the rate of β-hairpin folding. *Proc. Natl. Acad. Sci. USA*, 101:15915–15920, 2004.

[111] A. Mitsutake, Y. Sugita, and Y. Okamoto. Generalized-ensemble algorithms for molecular simualtions of biopolymers. *Biopolymers*, 60:96–123, 2001.

[112] C. Predescu, M. Predescu, and C. V. Ciobanu. On the efficiency of exchange in parallel tempering Monte Carlo simulations. *J. Phys. Chem. B*, 109:4189–4196, 2005.

[113] W. Nadler and U. H. E. Hansmann. Optimized explicit-solvent replica exchange molecular dynamics from scratch. *J. Phys. Chem. B*, 112:10386–10387, 2008.

[114] T. Okabe, M. Kawata, Y. Okamoto, and M. Mikami. Replica-exchange Monte Carlo method for the isobaric-isothermal ensemble. *Chem. Phys. Lett.*, 335:435–439, 2001.

[115] M. J. Abraham and J. E. Gready. Ensuring mixing efficiency of replica-exchange molecular dynamics simulations. *J. Chem. Theory Comput.*, 4:1119–1128, 2008.

[116] H. J. C. Berendsen, J. P. M. Postma, W. F. van Gunsteren, A. Dinola, and J. R. Haak. Molecular dynamics with coupling to an external bath. *J. Chem. Phys.*, 81:3684–3690, 1984.

[117] Tetsuya Morishita. Fluctuation formulas in molecular-dynamics simulations with the weak coupling heat bath. *J. Chem. Phys.*, 113:2976–2982, 2000.

[118] M. Lingenheil, R. Denschlag, and P. Tavan. The "hot-solvent/cold-solute" problem revisited. *J. Chem. Theory Comput.*, 4:1293–1306, 2008.

[119] E. Rosta, N.-V. Buchete, and G. Hummer. Thermostat artifacts in replica exchange Molecular Dynamics simulations. *J. Chem. Theory Comput.*, 5:1393–1399, 2009.

[120] X. Huang, M. Hagen, B. KIM, R. A. Friesner, Zhou R., and Berne B. J. Replica exchange with solute tempering: Efficiency in large scale systems. *J. Phys. Chem.*, 111:5405–5410, 2007.

[121] S. Trebst, M. Troyer, and U. H. E. Hansmann. Optimized parallel tempering simulations of proteins. *J. Chem. Phys.*, 124:174903, 2006.

[122] F. Wang and D. P. Landau. Determining the density of states for classical models: A random walk algorithm to produce a flat histogram. *Phys. Rev. E*, 64:056101, 2001.

[123] H. Kamberaj and A. van der Vaart. An optimized replica exchange molecular dynamics method. *J. Chem. Phys.*, 130:074906, 2009.

Danksagung

Mein vornehmlicher Dank am Gelingen dieser Arbeit gebührt meinem Betreuer und Doktorvater Prof. Paul Tavan, der mir trotz meiner fünfjährigen Tätigkeit in einer Bank und der damit verbundenen Physikabstinenz die Gelegenheit zur Promotion gab. Danke auch für deine Unterstützung und Schulung im wissenschaftlichen Schreiben und Präsentieren, das entgegengebrachte Vertrauen und die damit verbundene Möglichkeit eigenverantwortlich zu arbeiten.

Großer Dank geht auch an meinen Kollegen, Freund und „Sparringspartner“ Dr. Martin Lingenheil für die tolle und fruchtbare Zusammenarbeit. Unsere nicht selten unüberhörbaren Diskussionen werde ich sehr vermissen, wenngleich der ein oder anderen Zimmernachbar weniger wehmütige Gedanken damit verbinden wird. Entsprechend gilt mein Dank allen im C-Flügel ansässigen Kollegen für die hohe „Lärmtoleranz“.

Leider viel zu kurz war meine Zusammenarbeit mit Dr. Gerald Mathias. Danke für deine wertvollen Ratschläge und Anregungen und nicht zuletzt für deine Unterstützung beim Publizieren. Unschätzbar war und ist auch die Arbeit unseres Systemadiminstrators Sebastian Bauer, ohne dessen Einsatz das Computernetzwerk sicherlich nicht halb so gut funktionieren würde. In diesem Zusammenhang sei auch Dr. Rudolf Reichold und Dr. Bernhard Schropp gedankt.

Über die Arbeitsgruppe hinaus gilt mein besonderer Dank Herrn Prof. Zinth und seinen beiden Mitarbeitern Dr. Tobias Schrader und Dr. Wolfgang Schreier für die unkomplizierte und – wie ich glaube – erfolgreiche Zusammenarbeit. An dieser Stelle danke ich auch gerne den immer freundlichen und hilfsbereiten Sekretärinnen, Frau Michaelis und Frau Widmann-Diermeier, sowie dem Akademischen Rat Dr. Karl-Heinz Mantel. Darüber hinaus richte ich ein Dankeschön an alle Mitglieder des BMO für die tolle Atmosphäre. Das jeden Sommer wiederkehrende Eisbachschwimmen oder der gepflegte Fußball-Kick im Englischen Garten werden mir fehlen. Zu guter Letzt gebührt auch großer Dank meiner Familie und meinem Freundeskreis für den all zu leicht als selbstverständlich empfundenen sozialen Rückhalt, welcher mir unabdingbar für das Gelingen des Projekts Dissertation erscheint.

Lebenslauf

Name:	Robert Denschlag
Geburtsdatum:	19.5.1972
Geburtsort	Worms

seit 2009	Lehrer an der Albert-Schäffle-Schule in Nürtingen
2005 – 2009	Doktorand in der Arbeitsgruppe Tavan (LMU München)
2000 – 2004	Anwendungsinformatiker innerhalb der Dresdner Bank
1999	Physik Diplom
1995	Mathematik Vordiplom
1994	Physik Vordiplom
1992 – 1999	Studium der Physik und Mathematik an der TH Karlsruhe
1991 – 1992	Grundwehrdienst
1991	Abitur
1989 – 1991	Besuch des Rudi-Stephan Gymnasium Worms
1982 – 1989	Besuch der Karmeliter Realschule Worms
1978 – 1982	Besuch der Kerschensteiner Grundschule Worms